



SAPIENZA
UNIVERSITÀ DI ROMA



PH.D. IN ASTRONOMY, ASTROPHYSICS AND SPACE SCIENCE

CYCLE XXXII

CONSTRAINTS ON COSMOLOGICAL PARAMETERS FROM FUTURE CMB EXPERIMENTS AND LENSING SURVEYS

FABRIZIO RENZI

A.Y. 2018/2019

SUPERVISOR : ALESSANDRO MELCHIORRI

COORDINATOR : PAOLO DE BERNARDIS

DEPUTY COORDINATOR : NICOLA VITTORIO

CONTENTS

Thesis project	xi
Abstract	xv
Introduction	xvii
I FLRW cosmology	1
1 Cosmological Models and Inflation	3
1.1 The Homogeneous and Isotropic Universe	4
1.2 FLRW spacetime	7
1.2.1 Geodesic equation and particle motion	8
1.2.2 Particle Horizon	10
1.2.3 Redshift	12
1.2.4 Distance in Cosmology	12
1.3 The dynamics of the FLRW background	14
1.3.1 The stress-energy tensor	14
1.3.2 Friedmann Equations	16
1.4 The fine-tuning problem of the Hot Big Bang Cosmology	19
1.4.1 The flatness problem	19
1.4.2 The horizon problem	19
1.5 Classical Inflation	20
1.5.1 A solution to all problems	20
1.5.2 Slow-roll single field inflation	22
2 Universe Thermodynamics	27
2.1 Thermal History	27
2.1.1 Equilibrium Thermodynamics	30
2.1.2 Density, Pressure and Entropy conservation	31
2.2 Cosmic Neutrino Background	33
2.3 Recombination	34

II	From inhomogeneities to anisotropies	39
3	The inhomogeneous Universe	41
3.1	Cosmological Perturbation Theory	42
3.1.1	Perturbations of the FLRW metric	42
3.1.2	Matter perturbations	43
3.1.3	Fixing the gauge	44
3.1.4	Evolution and conservation equations	45
3.1.5	Setting Initial Conditions	47
3.2	Initial condition from Inflation	48
3.2.1	Primordial gravity waves	51
3.3	Inhomogeneities	52
3.3.1	Collisionless Boltzmann equation	53
3.3.2	Collision term for Thomson scattering	54
3.3.3	Photon Boltzmann equation	56
3.3.4	Neutrinos	58
3.4	CMB anisotropies	59
3.4.1	Anisotropies from inhomogeneity	60
3.4.2	Transfer function	62
3.4.3	Diffusion Damping	68
3.4.4	CMB polarization	68
III	Scientific Research Results	71
4	Magnetic Fields and Gravitational Waves	73
4.1	Introduction	73
4.2	Primordial Magnetic Fields	75
4.2.1	Magnetic Parameters	75
4.2.2	Impact of PMFs on CMB spectra and fiducial model	78
4.3	Method	81
4.4	Results	84
4.4.1	Results from MCMC	84
4.4.2	Delensing	88
4.4.3	Importance of small-scale B-mode measurements	89
4.5	Constraints from Faraday rotation	91
4.6	Discussion and Conclusion	95

CONTENTS

5	Cornering the Planck Lensing Tension with Future CMB data	97
5.1	Introduction	97
5.2	Current status of the A_{lens} anomaly	99
5.3	Method	100
5.4	Results	102
5.4.1	Future constraints on A_{lens}	102
5.4.2	Testing A_{lens} in different spectra and frequency channels	104
5.4.3	Using B modes to test the A_{lens} anomaly.	105
5.4.4	Future constraints on angular scale dependence of A_{lens}	108
5.5	Conclusions	109
6	Make Lensing Strong Again	111
6.1	Introduction	111
6.2	Cosmology with Time Delay Measurements	114
6.2.1	Theory of Gravitational Lensing Time Delays	114
6.2.2	Lens Mass Model and Mass-Sheet degeneracy	116
6.2.3	Stellar Dynamics Modelling	117
6.3	Analysis method and mock datasets	118
6.3.1	Mock Catalogues	121
6.4	Forecasts for cosmological parameters	123
6.4.1	Figure of Merit for Strong Lensing Time Delay	126
6.5	A smoking gun for dark energy?	128
6.6	Conclusions	130
7	Standard Sirens Impact on Future Hubble Parameter Constraints	133
7.1	Introduction	134
7.2	Method	136
7.2.1	Extended Models	136
7.2.2	Forecasts for CMB	137
7.2.3	Forecasts for BAO	139
7.2.4	Forecast for gravitational wave standard sirens	140
7.3	Results	142
7.3.1	$\Lambda\text{CDM} + \Omega_k + \Sigma m_v + N_{\text{eff}} + w$ model	142
7.3.2	$\Lambda\text{CDM} + \Omega_k + \Sigma m_v + w_0 + w_a$ model	149
7.3.3	Figure of Merit	153
7.4	Conclusions	155

IV	Appendix	161
A	Measuring anisotropies in the Faraday rotation angle	163
B	Constraints on cosmological parameters from SLTD	165
	REFERENCES	167

LIST OF FIGURES

1	ΔN_{eff} as a function of decoupling temperature	xviii
1.1	CMB spectrum from FIRAS data	5
1.2	Planck map of the CMB	5
1.3	SDSS map	6
1.4	Example of slow-roll inflationary potential	23
2.1	Evolution of $g_{\star}(T)$ in the Standard Model	35
2.2	Evolution of X_e predicted by the Saha equation	36
3.1	Planck 2018 temperature power spectrum	67
4.1	Comparison between primary and magnetic contribution to CMB power spectra	79
4.2	Comparison between the B-mode spectrum of magnetic and infla- tionary modes	80
4.3	Forecasted constraints for $B_{1 \text{ Mpc}}$ vs. r for PIXIE, LiteBIRD, Stage- 3 and CMB-S4	86
4.4	Impact of delensing for LiteBIRD, CMB-S4 and CORE-M5	88
4.5	Signal to noise ratio for LiteBIRD and CMB-S4	89
4.6	Impact of varying ℓ_{max} on CMB-S4 constraints	91
4.7	B-mode angular spectrum from Faraday rotation for several fre- quencies	92
4.8	Expected noise for LiteBIRD and CORE-M5	94
5.1	Forecasted constraints for CMB-S4 at 90 GHz	105
5.2	Forecasted constraints for CMB-S4 at 150 GHz	106
5.3	Forecasted constraints for CMB-S4 at 220 GHz	107
5.4	Future constraints on A_{lens} scale dependance from CMB-S4	108
6.1	The schematic view of a strongly lensed system	115
6.2	10 lenses mock datasets for time delay and velocity dispersion . .	123
6.3	Constraints for the Λ -mock datasets - I	124
6.4	Constraints for the Λ -mock datasets - II	125

LIST OF FIGURES

6.5	Constraints for the Λ -mock datasets - III	126
6.6	FoM plots for strong lensing time delay results for several cosmological models	127
6.7	Marginalized means and error estimate for H_0 using w CDM mock dataset	129
6.8	Constraints in different redshift bins for w CDM mock dataset . . .	130
7.1	Forecasted constraints on extended model for LiteBIRD, Stage-3 and CMB-S4 - I	145
7.2	Forecasted constraints on extended model for LiteBIRD, Stage-3 and CMB-S4 - II	146
7.3	Forecasted constraints on extended model for LiteBIRD, Stage-3 and CMB-S4 - III	147
7.4	Forecasted constraints on extended model for LiteBIRD, Stage-3 and CMB-S4 - IV	148
7.5	Forecasted constraints on extended model for LiteBIRD, Stage-3 and CMB-S4 - V	151
7.6	Forecasted constraints on extended model for LiteBIRD, Stage-3 and CMB-S4 - VI	152
7.7	FoM plot for LiteBIRD, Stage-3 and CMB-S4	155

LIST OF TABLES

1.1	Solutions of the Eq.(1.46) for a flat Universe dominated by matter (MD), radiation (RD) and a cosmological constant (Λ D).	18
4.1	Cosmological and magnetic field parameters assumed for the fiducial model	77
4.2	Experimental specifications for the several CMB experiments . . .	81
4.3	Delensing factor α for the various experiments described in Tab. 7.1.	81
4.4	95% C.L. constraints on $B_{1\text{Mpc}}$ and $\log_{10}(\eta_v/\eta_B)$ for the PIXIE, LiteBIRD and CORE-M5 experiments	85
4.5	As in Tab. 4.4 for the Stage-3 (deep and wide configurations) and CMB-S4 experiments.	86
4.6	95% C.L. constraints on $B_{1\text{Mpc}}$, $\log_{10}(\eta_v/\eta_B)$ and r for the PIXIE, LiteBIRD and CORE-M5 experiments.	87
4.7	As in Tab. 4.6 for the Stage-3 (deep and wide configurations) and CMB-S4 experiments.	88
4.8	S/N ratio for the detection of a nearly scale-invariant PMF of 1.08 nG through FR.	93
5.1	Constraints at 68% c.l. on cosmological parameters from pre-Planck and Planck datasets	100
5.2	Experimental specifications for the several configurations considered in the forecasts.	101
5.3	Cosmological Parameters assumed for the fiducial model.	101
5.4	Expected constraints on A_{lens} for a fiducial model assuming $A_{lens} = 1.000$	103
5.5	Expected constraints on A_{lens} and B_{lens} from Planck real data and Stage-IV simulated data	110
6.1	Prior ranges on the cosmological and nuisance parameters sampled in our analysis.	121
6.2	Fiducial values for the mock lens parameters.	121
7.1	Specifications for the different experimental configurations	138

LIST OF TABLES

7.2	Specifications for the forecast DESI data, obtained by [1].	140
7.3	Forecasted constraints on extended model for LiteBIRD, Stage-3 and CMB-S4 - I	145
7.4	Forecasted constraints on extended model for LiteBIRD, Stage-3 and CMB-S4 - II	146
7.5	Forecasted constraints on extended model for LiteBIRD, Stage-3 and CMB-S4 - III	147
7.6	Forecasted constraints on extended model for LiteBIRD, Stage-3 and CMB-S4 - IV	148
7.7	Forecasted constraints on extended model for LiteBIRD, Stage-3 and CMB-S4 combined with a pessimistic GWSS prior - I	149
7.8	Forecasted constraints on extended model for LiteBIRD, Stage-3 and CMB-S4 - V	151
7.9	Forecasted constraints on extended model for LiteBIRD, Stage-3 and CMB-S4 - VI	152
7.10	Forecasted constraints on extended model for LiteBIRD, Stage-3 and CMB-S4 combined with a pessimistic GWSS prior - II	153
7.11	FoM values for simulated CMB data for different combination of datasets	153
B.1	Mean marginalized values and their 68% confidence level bounds for the three DE model considered. We show here the results for the ideal case for 10, 100 and 1000 lenses.	165
B.2	Mean marginalized values and their 68% confidence level bounds for the three DE model considered. We show here the results for the realistic case for 10, 100 and 1000 lenses.	166

THESIS PROJECT

This is a summary of my thesis project and of the other research works I have done during my Ph.D. that are not included in this manuscript.

Thesis work

The intent of this thesis is to forecast constraints from future experiments on cosmological parameters in non- Λ CDM cosmologies and to study the possibility of the next decade of cosmological observations to constraint new physics beyond that of standard cosmology.

The standard cosmological model, also known as Hot Big Bang cosmology or Λ CDM model, is based on the assumption that the Universe is composed only of three “ingredients” : a cosmological constant associated with Dark Energy (DE) and denoted by Λ and matter in the form of either Cold Dark matter (composing the 90% of the matter in the Universe and denoted with CDM) or ordinary matter (such as electrons and protons).

The Planck satellite has provided a great confirmation of the Λ CDM paradigm and showed that the whole history of the Universe can be described only by 6 parameters, assuming General Relativity as the correct theory of gravity and the validity of the cosmological principle and of inflation. However, not everything has gone in its place: few tensions between different experiments and within Planck itself are appearing. Most notably the tension between late and early Universe measurements of the Hubble constant H_0 has now grown to a statistical significance of $\sim 5\sigma$ [2]. Of course this could be the results of some unresolved systematics but most interestingly this tension could indicate that we need to abandon the Λ CDM paradigm. This is motivated by the fact that the value of H_0 inferred from the observation of the Cosmic Microwave Background (CMB) depends on the assumed cosmological model while late time observations do not strongly depend on any assumption about the background cosmology (typically Supernovae Ia calibrated using Cepheids as an anchor [3, 4]). For example, new physics in the dark energy or neutrino sectors can significantly undermine the Planck constraints on the Hubble constant, solving the current tension on H_0 (see *e.g.* [3, 5–25]). Clearly and independent and accurate determination of H_0 from a

future observation will be crucial to confirm or reject the possibility of new physics beyond Λ CDM. In this thesis within the various possible observables that can lead to constraints on H_0 we consider two of the most promising: gravitational waves standard sirens and strong lensing time delay.

Along with the Hubble tension, the most relevant anomaly, at least from the statistical point of view, concerns the amount of lensing in the CMB angular power spectra. In [26] a phenomenological parameter, called A_{lens} was introduced to rescale the amplitude of lensing in the CMB spectra. This parameter is mainly used to test theoretical assumptions and systematics and in principle has no physical meaning. However, Planck 2015 analysis has reported $A_{\text{lens}} = 1.15^{+0.13}_{-0.12}$ at 95% C.L. about 2σ larger than the expected value ($A_{\text{lens}} = 1$) with significant impact in the parameter extraction [27]. In the latest Planck results this tension has grown worse touching the 3σ level and showing that a better understanding of this parameter is needed.

One of the main goals of future experiments is to measure the so-called “smoking gun” of inflation, *i.e.* the signature in CMB polarization produced by vacuum fluctuations of the metric (tensor modes) during inflation. Current constraints on tensor modes only give an upper bound on their amplitude at the level of $\sim 10^{-1}$ [28]. Next generation experiments, like LiteBIRD [29], have been designed to reach a sensibility on the amplitude of tensor mode around two orders of magnitude better than the current bound. However a primordial magnetic field with a scale invariant spectrum and amplitude within the current Planck bound (see e.g. [27]) can produce exactly the same spectrum produced by inflationary gravitational waves preventing future experiments from claiming a detection of a non-zero amplitude of the tensor modes. This leads to a degeneracy in the parameter space between the amplitude of the magnetic field and that of the primordial gravitational waves which must be taken properly into account to disentangle the two signature from one another.

During my Ph.D. I have studied these topics in four of my research works:

1. In [Phys. Rev. D97 \(2018\) no.12, 123534](#) we have shown that primordial magnetic fields can cause a contamination of a possible signal from primordial gravitational waves. Experiments targeting primordial tensor modes at the level of 10^{-3} will need to distinguish this signature from that generated by a primordial magnetic field of amplitude ~ 1 nG. We show that a clean way to break the degeneracy rely on measuring the small scale features of the magnetic spectrum. In fact, conversely to primordial tensor modes, the magnetic field generates vector perturbations with a spectrum peaked around $\ell \sim 1000$. Therefore experiments with sufficient angular resolution, as CORE-M5 or CMB-S4, will be able to distinguish a tensor mode produced

by inflation from that of a primordial magnetic field. Furthermore we show that another possible way to break the degeneracy is to rely on the anisotropies in the Faraday rotation angle.

2. In [Phys.Rev. D97 \(2018\) no.12, 123534](#) it was shown that future experiments will have the possibility of confirm/falsify the A_{lens} tension found in Planck data at the level of 10 standard deviations when considering a CMB-S4 like experiment. With a CMB-S4 like probe also a possible scale dependence for A_{lens} could be investigated leading to a better understanding of its physical nature. Therefore CMB-S4 would have the potential to falsify the current tension on the amount of lensing in CMB power spectra and test a possible scale dependence with incredible precision.
3. In [arXiv:1910.03566 \[astro-ph.CO\]](#) we study the possibility of constraining the Dark Energy (DE) equation of state using future measurements of the strong lensing time delay (SLTD) between the images of multiply lensed quasar. Experiments like the Large Synoptic Survey Telescope (LSST) are expected to detect a large number of lensed quasar systems and to extract from many of them time delay measurements of good enough quality to obtain cosmological constraints. We show that the constraint on the DE parameter strongly depends on the number of lensed systems in our dataset and worsen a factor of two when considering a dynamical DE equation of state. However in the most optimistic case w can still be constrained to the 2% accuracy confirming that SLTD is a promising and powerful observable to test our assumptions on the DE equation of state.
4. In [Phys. Rev. D98 \(2018\) no.8, 083523](#) we discuss the ability of future cosmological data to constrain the Dark Energy (DE) equation of state when combined with a measurement of H_0 coming from gravitational waves standard sirens (GWSS). We show that, provided that GWSS can measure H_0 with a 1% accuracy, the bound on the DE parameter w may reach the 3% and 7% level for a constant and a time-varying dark energy equation of state respectively.

Other works

Only the four works listed above have been report in this thesis. For completeness the remaining publications produced during my Ph.D. are the following:

- M. Shokri, F. Renzi and A. Melchiorri. “*Cosmic Microwave Background constraints on non-minimal couplings in inflationary models with power law*

potentials". Phys. Dark Univ. 24 (2019) 100297 [arXiv:1905.00649](#) [astro-ph.CO]

- F. Renzi, M. Shokri and A. Melchiorri. "What is the amplitude of the Gravitational Waves background expected in the Starobinski model ?". [arXiv:1909.08014](#) [astro-ph.CO]
- N. Carlevaro, G. Montani and F. Renzi. "Study of MRI in stratified viscous plasma configuration" EPL 117 (2017) 49001 [arXiv:1608.08849](#) [astro-ph.CO]

ABSTRACT

Anisotropies in the angular power spectra of the Cosmic Microwave Background (CMB) temperature and polarization have confirmed that we live in a Universe that agree with the theoretical predictions of the Λ CDM cosmology with great accuracy. Nevertheless there are many issues that have not yet found a solution, such as the H_0 and A_{lens} tension, measuring the B-modes of Cosmic Microwave Background polarization and understanding the physics of dark energy. Future cosmological probes, like CMB-S4, LiteBIRD, Stage-III and CORE-M5, will have to deal with all of these. In the first part of this thesis we study the possibility of future experiments to constrain efficiently the amplitude of primordial tensor modes in presence of a primordial magnetic field. In the second part we discuss how they would be able to falsify the A_{lens} tension and test a possible scale dependence of this parameter. In the last part instead we discuss the constraints that could be achieved on the dark energy equation of state combining together gravitational waves, CMB and strong lensing data.

INTRODUCTION

The standard cosmological model (or Hot Big Bang cosmology) assumes the Universe to have negligible curvature and to be composed mainly of Cold Dark matter and of a Dark Energy associated to a constant energy density denoted by Λ . The flat Λ CDM model, as it is more commonly referred to, has been found to be almost in perfect agreement with the measurements of the anisotropies of the Cosmic Microwave Background (CMB) provided by the Planck satellite [30]. So far, the Planck mission has provided an astonishing confirmation of the flat Λ CDM model:

- The six parameters that describes the Λ CDM model have been constrained with incredible accuracy. All but one - the optical depth at reionization - of these six parameters are known with sub-percent precision [28].
- A deviation from the scale invariant Harrison-Zeldovich spectrum has been detected at the level of 5σ pointing towards inflation as the mechanism generating it. Furthermore, a combination of Planck and BICEPS2/Keck Array [31] has significantly improved the upper bound on the tensor-to-scalar ratio leading to disfavour many large-field inflationary models [32].
- Further evidences of the presence of dark matter (DM) and dark energy (DE) (which make up the 95% of the Universe energy density today) have been provided

Nevertheless many open questions have not yet found an answer, for example :

- Inflation predicts the generation of metric perturbations (gravitational waves) that imprint the B-mode polarization spectrum of the CMB. A detection of this signature in the B-mode spectrum would be a “a smoking gun” for inflation and it is indeed one of the main goals of future CMB experiments, like CMB-S4 [33] and LiteBIRD [29], which are expected to bring the sensitivity on the amplitude of tensor modes in the range $\delta r = 0.01 - 0.001$. However there exists other effects that could generate B-modes polarization (*e.g.* topological defects, galactic foregrounds, primordial magnetic fields and so on) therefore these experiments will be able to claim a detection of tensor perturbations of the metric only if these spurious contributions can be identified and removed.

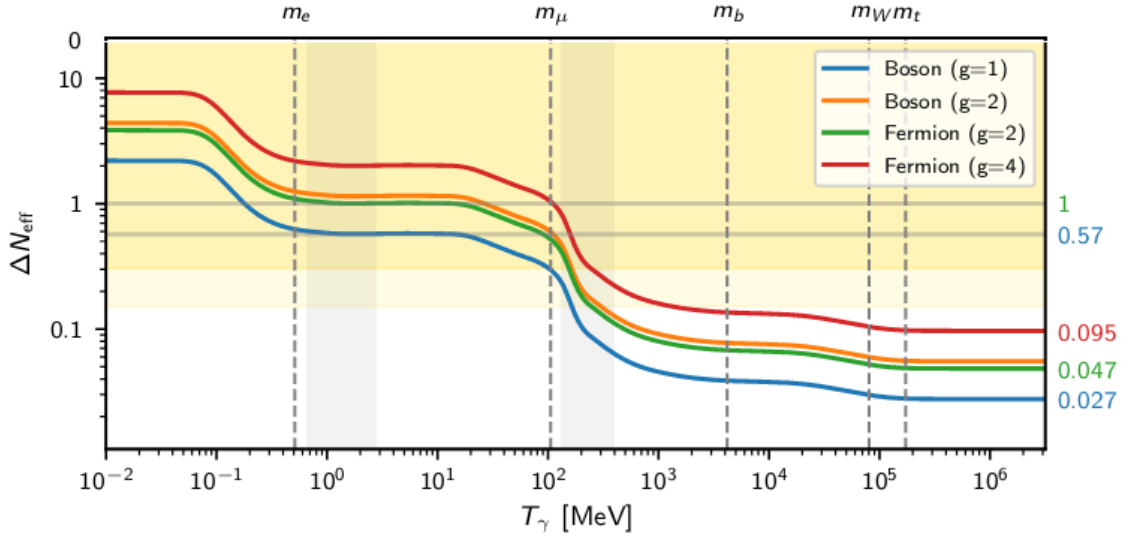


Figure 1: Expected ΔN_{eff} today for species decoupling from thermal equilibrium as a function of the decoupling temperature. Dashed vertical lines denote some mass scales at which corresponding particles annihilate with their antiparticles. One-tailed 68% and 95% regions excluded by PlanckTT,TE,EE+lowE+lensing+BAO are shown in gold [28]

- Is there any other relativistic species beyond those predicted by the Standard Model ? The Standard Model predicts $N_{\text{eff}} \gtrsim 3$ assuming three neutrinos species and the current bound from the Planck satellite $N_{\text{eff}} = 2.99 \pm 0.17$ is in good agreement with this prediction. However a deviation from the standard value may arise if new physics at high energies leads to additional weakly coupled species, see *e.g.* Fig.1.
- What is the value of the sum of neutrino masses ? Particle physics experiments on neutrino flavors have shown that neutrinos do possess small but non-zero masses. When the Planck data are analysed, the total mass scale of neutrinos is assumed to be the minimal mass scale in a normal mass hierarchy *i.e.* $\sum m_\nu = 0.06 \text{ eV}$ (see *e.g.* [27, 28]) but the total neutrino mass is indeed unknown and there are no strong evidences to prefer one over the others (see *e.g.* [34–38]). Therefore allowing for a varying $\sum m_\nu$ in analysing CMB data is one of the most well-motivated extensions of the Λ CDM model.
- What are the properties of DM and DE ? In particular, it is still unclear how DM interacts with the Standard Model (What is its annihilation cross section ? Can it decay into Standard Model particles? What kind of particle compose it ? and so on) or if the Universe acceleration is driven by vacuum energy or some modification of General relativity.
- How Gaussian is the statistics of primordial perturbations ? Even tough the

assumptions of Gaussian fluctuations has been proved to be in agreement with current data, there is still space for non-Gaussianities [39]. Detecting such feature will give insights on the physics of inflation but the primordial signal is often negligible compared to the contribution of the late-time evolution of the gravitational potential.

This thesis focus on understanding how future experiments will address some of these open questions and it is structured in the following way:

FIRST PART contains a review of the basis of the Friedmann-LeMaitre-Robertson-Walker (FLRW) cosmology. We derive the equations describing the evolution of the matter-energy density of the several species that make up our Universe. Along with it, we describe the fine-tuning problems of the standard cosmological model and how inflation can overcome them. Finally we briefly discuss the early Universe thermodynamics.

SECOND PART contains a review of perturbation theory in cosmology and of how the anisotropies in the CMB temperature are computed

THIRD PART contains the scientific research carried out during my Ph.D.

- I start by presenting a study on how well future experiments that will aim to measure the inflationary tensor modes could resolve a spurious contribution from a primordial magnetic field with a scale invariant spectrum carried out in [40]. Then I proceed with a study on possible solution of the A_{lens} tension with the upcoming CMB experiments. This work was carried out in [41]
- In the last part I will present two works dedicated to study the future impact of gravitational waves and strong lensing surveys in improving our knowledge of the DE equation of state parameter which were carried out in [42, 43].

PART I

FLRW COSMOLOGY

1 COSMOLOGICAL MODELS AND INFLATION

In this Chapter we are going to describe the main features of *Hot Big Bang cosmology*. We start with an introduction about the observational confirmations of the cosmological principle. We proceed describing how this translates into the mathematical properties of the Friedmann-Lemaitre-Robertson-Walker (FLRW) metric. Then we discuss the solution of Einstein equations in a FLRW background and the implication for the dynamics of the Universe. In the last part of the Chapter we discuss the inconsistencies of the Big Bang theory and how those can be resolved with an early accelerated expansion phase called inflation. This Chapter is mainly based on [44–47]

Contents

1.1	The Homogeneous and Isotropic Universe	4
1.2	FLRW spacetime	7
1.2.1	Geodesic equation and particle motion	8
1.2.2	Particle Horizon	10
1.2.3	Redshift	12
1.2.4	Distance in Cosmology	12
1.3	The dynamics of the FLRW background	14
1.3.1	The stress-energy tensor	14
1.3.2	Friedmann Equations	16
1.4	The fine-tuning problem of the Hot Big Bang Cosmology	19
1.4.1	The flatness problem	19
1.4.2	The horizon problem	19
1.5	Classical Inflation	20
1.5.1	A solution to all problems	20
1.5.2	Slow-roll single field inflation	22

1.1 The Homogeneous and Isotropic Universe

When describing any problem in physics, one should focus on the right assumptions to capture the essence of the problem and get rid of any irrelevant and unwanted details. The Universe is not different in this respect. The main assumption in the field of cosmology is the so-called *Cosmological Principle* stating that :

On a sufficiently large scale, the properties of the Universe are the same for all observers. Therefore the Universe is homogeneous and isotropic *i.e.* it has the same properties at every point and in every direction

Note that the statement of the cosmological principle refers only to the spacial properties of the Universe. As we will see later in this manuscript, the Universe is neither homogeneous nor isotropic in time. This assumption, which could seem very limiting in practice, is actually able to glance much of the properties of the Universe on large scales.

The validity of the cosmological principle can be also tested through observations. Fortunately our assumptions about the Universe stood up quite well at this trial. There are two main pieces of evidence supporting the cosmological principle: the cosmic microwave background and the tridimensional distribution of the galaxies.

THE COSMIC MICROWAVE BACKGROUND

The cosmic microwave background is the afterglow of the Big Bang, a snapshot of the Universe when it was only 300000 years old. It is made by an almost uniform sea of photon emitting a black body radiation at the temperature of $T \approx 2.7\text{K}$. First discovered by Penzias and Wilson in 1965 [48] (and subsequently granted them the nobel prize in 1978), it was found to match perfectly the theoretical prediction by the Far InfraRed Absolute Spectrophotometer (FIRAS) [49, 50] installed on the COBE satellite [51] (see Fig.1.1) and confirmed the extreme smoothness of our Universe. However the CMB is not completely uniform. There are extremely small fluctuations in temperature with a characteristic amplitude of $\delta T/T_{\text{CMB}} \sim 10^{-5}$. While the discovery of fluctuations in the microwave background paved the way for the study of CMB anisotropies it also confirmed again that only extremely tiny deviation from smoothness were present in the early Universe. We will return in Chapter 3 on how these fluctuations are produced and on the properties of the anisotropies of the CMB

1. COSMOLOGICAL MODELS AND INFLATION

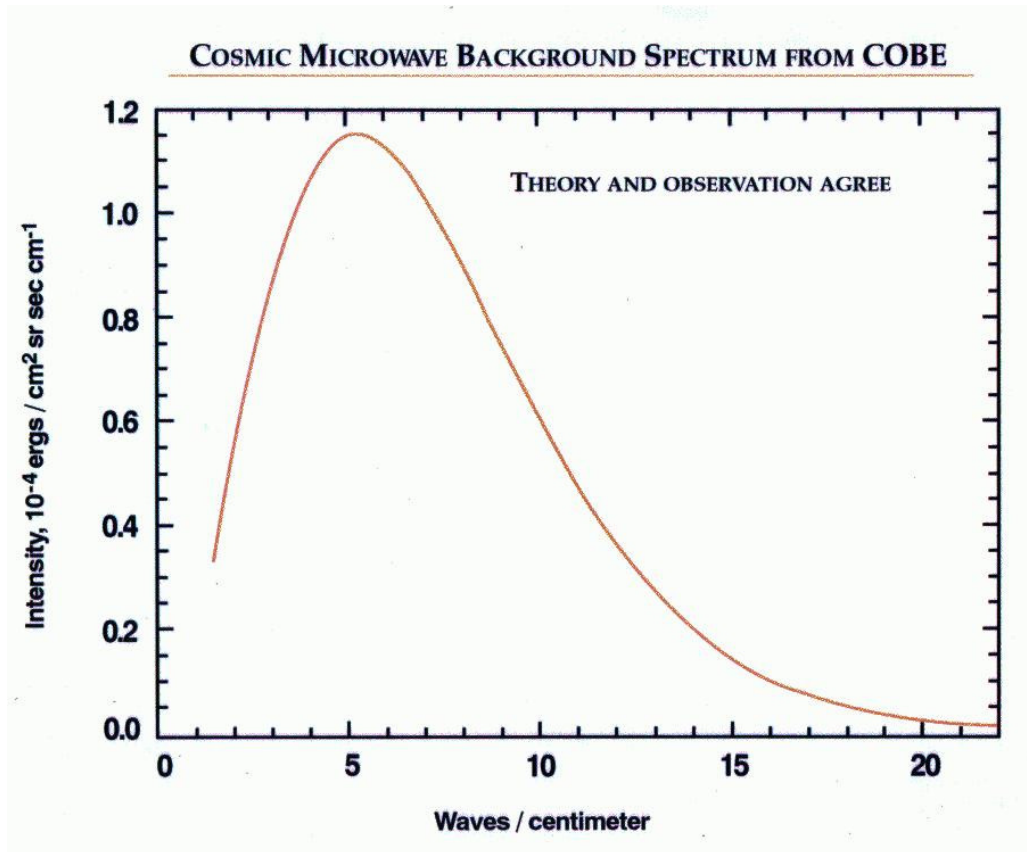


Figure 1.1: The cosmic microwave background spectrum plotted in waves per centimeter vs intensity. The plot is realized with the data collected with the Far InfraRed Absolute Spectrophotometer (FIRAS) an instrument on the COBE satellite [51]. The FIRAS data matched so well the theoretical prediction of a blackbody spectrum at $T \approx 2.7\text{K}$ that is impossible to distinguish the data from the fit ! [49, 50]

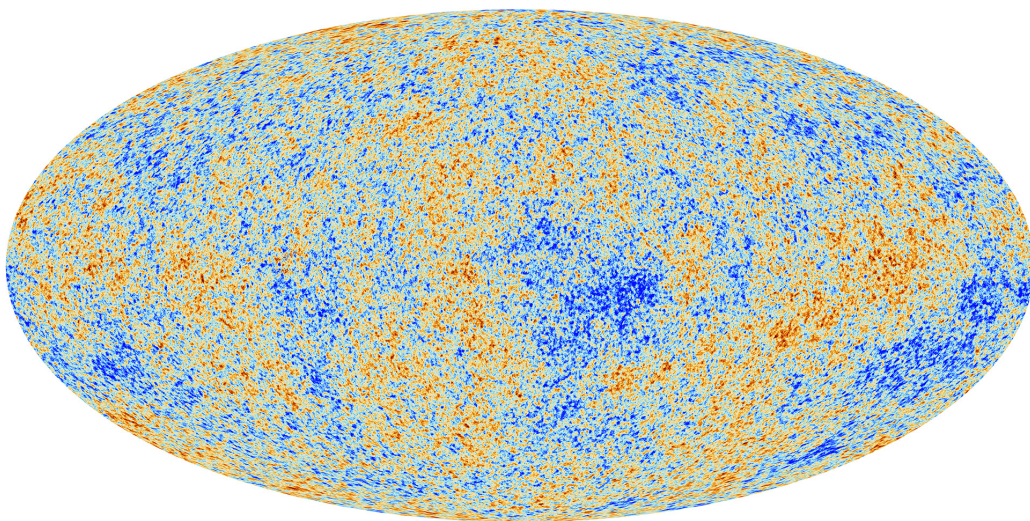


Figure 1.2: The most recent picture of the fluctuations of the CMB as measured by the Planck satellite [30, 52]

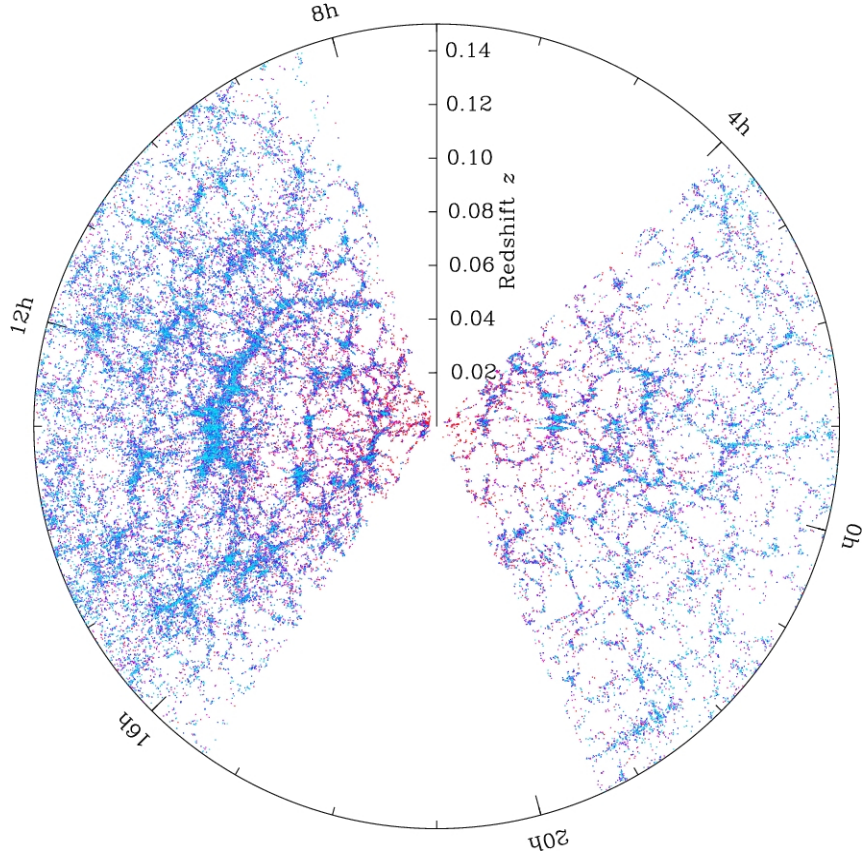


Figure 1.3: The SDSS's map of the Universe [56]. Each dot is a galaxy and there are more than one million points in the map. As reported in the figure the surveys extended up to $z = 0.15$ corresponding to ~ 435 Mpc

GALAXY SURVEYS

A further proof to support the cosmological principle comes from the mapping of the distribution of galaxies around us. A number of galaxy surveys (most recently eBOSS [53], APOGEE-2 [54] and MANGA survey [55]) have provided a tridimensional map of more than one million galaxies composing what is known as the Sloan Digital Sky Surveys (SDSS) [56], the most detailed 3D map of the Universe ever made. In Fig. 1.3 we report the most up to date 3D map of the galaxies around us provided by SDSS. The SDSS's map confirms that, while clumpy on small scales, the distribution of galaxies is roughly homogeneous for distance greater than ~ 100 Mpc ($z \sim 0.04$) and becomes increasingly smooth on larger scales. Yet, galaxies are clearly not randomly distributed, they are grouped into large scale structures of different size. We will see that the tiny fluctuations of the CMB are the seeds that formed these structures but to understand how this have happened we should allow to deviate from smoothness.

We have shown in this Section that there are strong observational evidences to support the validity of the cosmological principle. However we have also seen

1. COSMOLOGICAL MODELS AND INFLATION

that tiny deviations from smoothness were already present when the Universe was really young and those inhomogeneities have grown into the rich variety of structures we observe today. But this is not the end of the story. If we have answered the question of how to describe the geometry of our Universe and we have placed a strong principle to sustain it, much more questions need to be answered : “Why the Universe is so smooth ?”, “What generated the fluctuations we observe in the CMB?”, “What is the Universe made of ?” and “How are galaxies formed in such a smooth Universe ?”. Remarkably, all these questions have an answer that can be found employing only fundamental physics and our knowledge of the early Universe. Even more interestingly these answers can be tested with observations.

1.2 FLRW spacetime

Mathematically the cosmological principle implies that, on scale larger than 100 Mpc, our Universe is described by the Friedmann-Lemaitre-Robertson-Walker (FLRW) metric [44, 57–60]. In spherical coordinates $\{r, \theta, \phi\}$ the FLRW metric assumes the form (throughout this thesis we will always assume $c = \hbar = 1$ unless otherwise stated) :

$$ds^2 = g_{\mu\nu}(t, \vec{x})dx^\mu dx^\nu = -dt^2 + a^2(t) \left[\frac{dr^2}{1 - kr^2} + r^2(d\theta^2 + \sin^2 \theta d\phi^2) \right] \quad (1.1)$$

There are some features of Eq.(1.1) that is worth mentioning before moving on:

- The symmetries of the Universe *i.e.* homogeneity and isotropy, have reduced the ten independent components of the metric $g_{\mu\nu}(t, \vec{x})$ to a single function of time, the scale factor $a(t)$, and a constant, the curvature parameter k .
- FLRW metric admits a foliation with “cosmic time” coordinate t and space-like hypersurfaces Σ_t of constant time. The hypersurfaces Σ_t are both translationally invariant (homogeneous) and rotationally invariant (isotropic). In other words, the assumptions of the cosmological principle are translated in the mathematical properties of the hypersurfaces in which the spacetime is foliated into.
- The parameter k parametrizes the curvature of the hypersurfaces Σ_t : positively curved hypersurfaces will have $k > 0$, while flat and negative curved hypersurfaces will have $k = 0$ and $k < 0$ respectively.
- The FLRW metric has a rescaling symmetry :

$$a \rightarrow \lambda a \quad ; \quad r \rightarrow r/\lambda \quad ; \quad k \rightarrow \lambda^2 k \quad (1.2)$$

this means that the geometry of the Universe will be the same if we rescale r , a and k at the same time. This freedom can be exploited to set the scale factor to unity at the present time, t_0 , *i.e.* $a(t_0) \equiv 1$. If this is the case, the scale factor $a(t)$ becomes a dimensionless quantity while r and $k^{-1/2}$ inherit the dimension of length.

- The coordinate r is called comoving coordinate. The comoving coordinate is related to the physical coordinate by the scale factor *i.e.* $r_{\text{phys}} = a(t)r$, in other words an observer looking at an object at fixed comoving distance r will measure a physical distance from it that depends on time.

The physical velocity of an object is then obtained taking the time derivative of r_{phys} :

$$v_{\text{phys}} \equiv \frac{dr_{\text{phys}}}{dt} = a(t) \frac{dr}{dt} + r \frac{da}{dt} \equiv v_{\text{pec}} + H r_{\text{phys}} \quad (1.3)$$

As we can see from Eq.(1.3), the physical velocity is composed of two terms:

1. The *Hubble flow* due to the expansion of the Universe, $H r_{\text{phys}}$, where $H \equiv \dot{a}/a$ is the Hubble parameter
2. *Peculiar velocity*, $v_{\text{pec}} \equiv a(t) \frac{dr}{dt}$, which is the velocity associated with the motion of an object with respect to the cosmological Hubble flow (*i.e.* is the velocity measured by an observer at rest with the Hubble flow, called comoving observer)

However, peculiar velocities are typically very small compared to the Hubble flow and can be safely neglected at the background level.

We see therefore that the evolution of the metric in an FLRW spacetime is entirely dictated by the evolution of the scale factor $a(t)$ whose evolution will be related to the energy momentum tensor via Einstein field equations (see Section 1.3). Before describing the dynamics of the scale factor, however, we will describe the kinematics properties of the FLRW background.

1.2.1 Geodesic equation and particle motion

In the absence of additional non-gravitational forces freely falling particles in curved spacetime move along special trajectories called *geodesic*. For massive particles a geodesic is a timelike curve $X^\mu(\tau)$ which minimizes the proper time $\Delta\tau$ between two points in the spacetime. It is possible to show that the extremal path satisfies the so-called *geodesic equation* (we do not give here a formal derivation of the geodesic equation but we remind the interested reader to the literature on

1. COSMOLOGICAL MODELS AND INFLATION

the basics of General Relativity [57–60]):

$$\frac{d^2 X^\mu}{d\tau^2} = -\Gamma_{\alpha\beta}^\mu \frac{dX^\alpha}{d\tau} \frac{dX^\beta}{d\tau} \quad (1.4)$$

where $\Gamma_{\alpha\beta}^\mu$ are called *Christoffel symbols* and are defined through the metric $g_{\mu\nu}$ as:

$$\Gamma_{\alpha\beta}^\mu = \frac{1}{2} g^{\mu\gamma} (g_{\gamma\beta,\alpha} + g_{\gamma\alpha,\beta} - g_{\alpha\beta,\gamma}) \quad (1.5)$$

where we have used the convention $\partial_\rho g_{\mu\nu} \equiv g_{\mu\nu,\rho}$ to indicate partial derivative with respect to X^ρ . The geodesic equation can be rewritten in a more compact form introducing the *four-velocity* of the particle, $U^\mu \equiv dX^\mu/d\tau$:

$$\frac{dU^\mu}{d\tau} = -\Gamma_{\alpha\beta}^\mu U^\alpha U^\beta \quad (1.6)$$

Noting that $d/d\tau \equiv dX^\alpha/d\tau \, d/dX^\alpha$ the above equation can be written as:

$$U^\alpha \nabla_\alpha U^\mu = 0 \quad (1.7)$$

where $\nabla_\alpha U^\mu = U_{,\alpha}^\mu + \Gamma_{\alpha\beta}^\mu U^\beta$ is the covariant of the four-velocity. The above equation can be also written in terms of the particle *four-momentum*, since for a massive particle $P^\mu = mU^\mu$, as :

$$P^\alpha \nabla_\alpha P^\mu = 0 \quad (1.8)$$

For massless particles instead, we cannot define the geodesic in terms of the proper time since this is zero and therefore $U^\mu U_\mu = 0$. However, we can simply define the momentum of massless particles as dx^μ/ds where s is an affine parameter such that the geodesic equation takes exactly the form of Eq.(1.8). With this definition Eq.(1.8) holds both for massive and massless particles. Now that we have an equation describing the propagation of massless and massive particles we can make a step further and solve it. To evaluate the r.h.s of Eq.(1.8) what we need is to compute the Christoffel symbols for the FLRW metric. Fortunately, all Christoffels with two time the same indices vanish *i.e.* $\Gamma_{00}^\mu = \Gamma_{0\beta}^0 \equiv 0$, the only non vanishing components are:

$$\Gamma_{ij}^0 = a\dot{a}\gamma_{ij}, \quad \Gamma_{0j}^i = \frac{\dot{a}}{a}\delta_j^i, \quad \Gamma_{jk}^i = \frac{1}{2}\gamma^{il}(\gamma_{kl,j} + \gamma_{jl,k} - \gamma_{jk,l}) \quad (1.9)$$

or are related to this by symmetry (note that the Christoffels are symmetric on the bottom indices $\Gamma_{\alpha\beta}^\mu = \Gamma_{\beta\alpha}^\mu$). The homogeneity of the FLRW background implies that $\partial_i P^\mu = 0$ so that Eq.(1.8) rewrites:

$$P^0 \frac{dP^\mu}{dt} = -\left(2\Gamma_{0j}^\mu P^0 + \Gamma_{ij}^\mu P^i\right) P^j \quad (1.10)$$

Now, to solve Eq.(1.10) we have to distinguish between massive and massless particles:

- A particle initially at rest in the comoving frame will remain at rest since the r.h.s of Eq.(1.10) vanish if $P^j = 0$ and therefore $dP^\mu/dt = 0$
- From the zero component of Eq.(1.10) we see that :

$$E \frac{dE}{dt} = -\Gamma_{ij}^0 P^i P^j = -\frac{\dot{a}}{a} p^2 \quad (1.11)$$

where $p^2 \equiv -g_{ij}P^iP^j = a^2\gamma_{ij}P^iP^j$ is the *physical* three-momentum. The components of P^i satisfies the constraint $g_{\mu\nu}P^\mu P^\nu = m^2$ (or $E^2 - p^2 = m^2$ with $m = 0$ for massless particles). It follows $E dE = p dp$ and then:

$$\frac{\dot{p}}{p} = -\frac{\dot{a}}{a} \quad (1.12)$$

For a massless particle this implies that the energy decays with the expansion of the Universe since $p^2 = E^2$ *i.e.*

$$\frac{\dot{E}}{E} = -\frac{\dot{a}}{a} \quad (1.13)$$

For a massive particle instead this implies :

$$P^i = \frac{mv^i}{\sqrt{1 - g_{\mu\nu}v^\mu v^\nu}} \propto \frac{1}{a} \quad \text{with } i = 1, 2, 3 \quad (1.14)$$

where $v^i = dx^i/d\tau$ is the comoving peculiar velocity. Then a freely-falling massive particle will converge on the Hubble flow

1.2.2 Particle Horizon

In General Relativity the causal structure of the space-time is determined by how far light can travel in a certain amount of time. In order to describe the propagation of light (photons) in an FLRW background it is useful to introduce the conformal time η :

$$d\eta = \frac{dt}{a(t)} \quad (1.15)$$

and to redefine the radial coordinate of the FLRW metric employing the transformation $d\chi \equiv dr/\sqrt{1 - kr^2}$, such that the metric could be rewritten as :

$$ds^2 = -dt^2 + a^2(t) [d\chi^2 + S_k^2(\chi)d\Omega^2] \quad (1.16)$$

where :

$$S_k(\chi) \equiv \frac{1}{\sqrt{k}} \begin{cases} \sinh(\sqrt{k}\chi) & k < 0 \\ \sqrt{k}\chi & k = 0 \\ \sin(\sqrt{k}\chi) & k > 0 \end{cases} \quad (1.17)$$

and $d\Omega^2 \equiv d\theta^2 + \sin^2\theta d\varphi^2$ is the infinitesimal solid angle element. Since the spacetime is isotropic, we can always define a coordinate systems in which light travels only in the radial direction (*i.e.* $\theta = \varphi = \text{const}$), so that the photon trajectories are described by a two-dimensional line elements:

$$ds^2 = a^2(\eta)(-d\eta^2 + d\chi^2) \quad (1.18)$$

Since, photons travel along null geodesics, $ds^2 = 0$, their path is defined by:

$$\Delta\chi = \pm\Delta\eta \quad (1.19)$$

where the plus sign is for outgoing photons and the minus sign for incoming ones. Following Eq.(1.19), the maximum comoving distance light could have traveled between an initial time t_i and a time t is simply given by the difference in conformal time *i.e.* $\Delta\eta = \eta(t) - \eta(t_i)$. Hence, we can define the comoving particle horizon as:

$$\chi_p(t, t_i) = \int_{t_i}^t \frac{dt'}{a(t')} \quad (1.20)$$

If we assume that the Big Bang¹ “started” with a singularity at time $t_i = 0$, then the greatest comoving distance from which an observer at time t could receive light signal is given by:

$$\chi_p(t, 0) = \int_0^t \frac{dt'}{a(t')} \quad (1.21)$$

The physical particle horizon will be then obtained simply multiplying this quantity by the scale factor *i.e.* $d_p(t, 0) = a(t)\chi_p(t, 0)$. Therefore, observer separated by a distance larger than $d_p(t, 0)$ could have never communicate with each other. One may expect that as time proceed more and more regions of the spacetime come into causal contact (*i.e.* they fall into the horizon of one another) but this need not to be the case. Infact, the time evolution of the FLRW metric (and then its causal structure) depends on the matter-energy contents of the Universe, as we will see in Section 1.3, and the value of η could both increase or decrease depending on the matter-energy content of the Universe.

¹*It is worth stressing that the Big Bang singularity is a point in time, but not in space. It happens everywhere in space.*

1.2.3 Redshift

In Section 1.2.1 we have seen that massless particles loose energy with time because the Universe is expanding. This property of the FLRW metric leads to the concept of *redshift*: classically this can be seen as a stretching of the wavelength of an electromagnetic waves propagating freely due to the Hubble flow. The concept of redshift plays a key role in cosmology since everything that we know about the Universe is inferred through the light emitted by distant sources and must be taken into account when analysing observational data. The expression of redshift can be derived either classically or quantum mechanically, here we follow the latter (a more detailed discussion can be found on [58, 59]). From a quantum mechanical point of view, the wavelength of a photon is related to its momentum by $\lambda = 2\pi/p$. Since for photons the momentum is inversely proportional to the scale factor, light emitted at time t_1 with wavelength λ_1 is observed at time t_0 with wavelength:

$$\lambda_0 = \frac{a(t_0)}{a(t_1)} \lambda_1 \quad (1.22)$$

Since $a(t_0) > a(t_1)$ it is also $\lambda_0 > \lambda_1$. It is conventional to define the *redshift* parameter as the fractional shift in wavelength of a photon observed at t_0 and emitted at $t_1 < t_0$,

$$z \equiv \frac{\lambda_0 - \lambda_1}{\lambda_1} \implies 1 + z = \frac{1}{a(t_1)} \quad (1.23)$$

where in the last equality we have made use of $a(t_0) \equiv 1$.

1.2.4 Distance in Cosmology

When speaking of distance in cosmology we have to be careful about what we mean with “distance”. We already encountered two definitions of distance, the *metric distance*, $S_k(\chi)$, of Eq.(1.17) and the *comoving distance*,

$$\chi(z) = \int_{t_1}^{t_0} \frac{dt'}{a(t')} = \int_0^z \frac{dz}{H(z)} \quad (1.24)$$

that we used to define the particle horizon in Eq.(1.20). Note that for a flat Universe the metric and comoving distances coincide. These distances however cannot be observed but are useful in defining the observable distances.

LUMINOSITY DISTANCE

One way to infer distance in astronomy is to measure the flux, F , of a source of known luminosity, L . In a non-expanding Universe, the observed flux F at a distance d from a source of known luminosity L can be simply written as:

$$F = \frac{L}{4\pi d^2} \quad (1.25)$$

1. COSMOLOGICAL MODELS AND INFLATION

since the total luminosity on a spherical shell with area $4\pi d^2$ is constant. In flat spacetime, this is generalized replacing the distance d with the metric distance $S_k(\chi)$ *i.e.*

$$F = \frac{L(\chi)}{4\pi S_k^2(\chi)} \quad (1.26)$$

where now $L(\chi)$ is the luminosity through a (comoving) spherical shell with radius S_k^2 . To generalise this to a FLRW spacetime, we should take into account that:

1. In a fixed time the number of photons crossing a shell will be smaller today than at the emission time by a factor $(1+z)^{-1}$. Therefore the luminosity $L(\chi)$ is dimmed by the same amount being the energy multiplied by the number of photons passing the shell per unit time.
2. The energy of the photons will be smaller today than at emission by, again, a factor $(1+z)^{-1}$ because of expansion.

These effects add up so that the observed flux in a FLRW Universe is:

$$F = \frac{L(\chi)}{4\pi (1+z)^2 S_k^2} \equiv \frac{L(z)}{4\pi d_L^2(z)} \quad (1.27)$$

where we have introduced the luminosity distance $d_L(z) = (1+z) S_k$. Objects of known luminosity are sometimes referred to as *standard candles*, one example are Supernovae of Type Ia [61].

ANGULAR DIAMETER DISTANCE

Another way to determine distances is to measure the angle θ subtended by an object of known size l . This kind of objects is known as *standard ruler*, one example are the Baryon Acoustic Oscillations (BAO) [62]. Assuming the angle θ to be small, the distance to the object is simply:

$$d_A = \frac{l}{\theta} \quad (1.28)$$

this quantity is known as *angular diameter distance*. In an expanding Universe, the comoving size of an object is l/a while the angle subtended is $\theta = (l/a)/S_k(\chi)$ so that:

$$d_A = a S_k(\chi) = \frac{S_k(\chi)}{1+z} \quad (1.29)$$

It is worth noting that d_A is equal to the comoving distance for $z \rightarrow 0$ but it decreases at very large redshift, then objects at large redshift will appear bigger than they would at intermediate redshift.

Supernovae standard candles and BAO have played an important role in proving that the Universe is into an accelerated expansion phase which have led to the

discovery that the dominant form of matter-energy today is the Dark Energy [62–64]. We will return to the concept of Dark Energy in the next Section where we discuss the dynamics of an FLRW Universe.

1.3 The dynamics of the FLRW background

The dynamics of the Universe is determined by the Einstein equation,

$$G_{\mu\nu} = 8\pi G T_{\mu\nu} \quad (1.30)$$

relating the Einstein tensor, $G_{\mu\nu}$, determined by the spacetime geometry (*i.e.* by the metric $g_{\mu\nu}$) and the stress-energy tensor $T_{\mu\nu}$ determined by the matter-energy content of the Universe. In the next Sections we are going to use these equation to solve for the evolution of the scale factor $a(t)$ as a function of the “energy budget” of the Universe.

1.3.1 The stress-energy tensor

The requirement of isotropy and homogeneity force the stress-energy tensor to be that of a *perfect fluid* (fluid energy and momentum are conserved and there are no anisotropic stress, see also [57, 59, 60]),

$$T_{\mu\nu} = (\rho + P)U_\mu U_\nu - P g_{\mu\nu} \quad (1.31)$$

or with mixed indices:

$$T^\mu_\nu = (\rho + P)U^\mu U_\nu - P \delta^\mu_\nu \quad (1.32)$$

U^μ is the relative four-velocity between the fluid and the observer (for a comoving observer $U^\mu = (1, 0, 0, 0)$ and we would have $T^\mu_\nu = \text{diag}(\rho, -P, -P, -P)$) while ρ and P are the energy density and pressure in the *rest-frame* of the fluid. To describe the evolution in time of density and pressure¹ we make use of the conservation equation of T^μ_ν , which reads:

$$\nabla_\mu T^\mu_\nu = \partial_\mu T^\mu_\nu + \Gamma^\mu_{\nu\lambda} T^\lambda_\mu - \Gamma^\lambda_{\mu\nu} T^\mu_\lambda = 0 \quad (1.33)$$

The evolution of the energy density is determined by the “zero” component of this equation *i.e.*

$$\frac{d\rho}{dt} + \Gamma^\mu_{\mu 0} \rho - \Gamma^\lambda_{\mu 0} T^\mu_\lambda = 0 \quad (1.34)$$

where we have used the fact that $T^i_0 = 0$ due to isotropy. Now, making use of Eq.(1.9) we find:

$$\dot{\rho} + 3\frac{\dot{a}}{a}(\rho + P) = 0 \quad (1.35)$$

¹spatial homogeneity and isotropy require that ρ and P are function of the time only

1. COSMOLOGICAL MODELS AND INFLATION

which is the *continuity equation* for a fluid in an expanding Universe. We can now use Eq.(1.35) to glean information about the evolution of different matter-energy components in the Universe. We start rewriting Eq.(1.35) as :

$$a^{-3} \frac{\partial(\rho a)}{\partial t} = -3 \frac{\dot{a}}{a} P \quad (1.36)$$

We proceed then classifying the different components by their contribution to the pressure:

- **Matter**

Throughout this work we will use “matter” to indicate all form of energy for which the pressure is much smaller than the energy density $|P| \ll \rho$ so that we can neglect the pressure contribution of this component. Setting $P = 0$ in Eq.(1.36) we have $\rho \propto a^{-3}$. This dilution reflects the fact that particle number density scale with the inverse of the volume $V \propto a^3$ i.e. $n = dN/dV \propto a^{-3}$. This scaling for the density, as we will see in the next Chapter, is verified for a gas of non-relativistic particles where the energy density is dominated by the mass. In the standard picture matter is made of two components *dark matter*, which compose most of the matter density of the Universe but is “invisible” since do not interact with photons, and *baryons*, which in cosmology is used to indicate ordinary matter (nuclei and electrons)

- **Radiation**

We will use “radiation” instead to refers to species for which the pressure satisfies $\rho = 3P$. In this case Eq.(1.36) implies:

$$\rho \propto a^{-4} \quad (1.37)$$

The dilution now takes into account the redshifting of the energy of massless particles, $E \propto a^{-1}$, along with the dilution caused by the increasing of the Universe volume due to expansion. In the standard picture, radiation is made up of *photons* which, being massless, have always been relativistic (today we detect those photons as the CMB), and *neutrinos*, which behaved like radiation for most of the Universe history and only recently they have started to behave as matter due to their small masses.

- **Dark Energy**

As we have seen in the previous Section Supernovae measurements have shown that the Universe is in a accelerated expansion phase. Matter and radiation are not enough to describe the acceleration, another component has to be added in the energy budget. This is a mysterious negative pressure component with $P = -\rho$. From Eq.(1.36) we see that the energy density do

not dilute with the expansion *i.e.* it is constant $\rho \propto a^0$, therefore energy has to be created as the Universe expands. Because of this feature dark energy has been associated to the concept of vacuum energy of quantum field theory which ground state corresponds to a stress-energy tensor of the form:

$$T_{\mu\nu}^{vac} = \rho_{vac} g_{\mu\nu} \quad (1.38)$$

This form of $T_{\mu\nu}$ implies that $P_{vac} = -\rho_{vac}$. Unfortunately, quantum field theory predicts a value for the vacuum energy which is completely off from the observed one $\rho_{vac}/\rho_{obs} \sim 10^{120}$. However, Eq.(1.30) is not uniquely defined, one can add on the l.h.s. a term of the form $-\Lambda g_{\mu\nu}$, for some constant Λ^2 , without changing the conservation law of the stress-energy tensor. In other words, we could have written Eq.(1.30) as:

$$G_{\mu\nu} - \Lambda g_{\mu\nu} = 8\pi G T_{\mu\nu} \quad (1.39)$$

Nowadays, this contribution to Einstein equations is treated as an additional term in the stress-energy tensor with the same form of Eq.(1.38):

$$T_{\mu\nu}^{(\Lambda)} = \frac{\Lambda}{8\pi G} g_{\mu\nu} \equiv \rho_{\Lambda} g_{\mu\nu} \quad (1.40)$$

1.3.2 Friedmann Equations

Until now we have concentrated on the r.h.s. of Eq.(1.30), to solve for the evolution of the scale factor we need to explicitate the form of the Einstein tensor for the FLRW metric. Due to the symmetries of the FLRW metric, the only non-zero components of the Einstein tensor are:

$$G_0^0 = 3 \left[\left(\frac{\dot{a}}{a} \right)^2 - \frac{k}{a^2} \right] \quad (1.41a)$$

$$G_j^i = \delta_j^i \left[2 \frac{\ddot{a}}{a} + \left(\frac{\dot{a}}{a} \right)^2 + \frac{k}{a^2} \right] \quad (1.41b)$$

Combining these relations with the definition of the stress-energy tensor we get the *Friedmann equations*:

$$\left(\frac{\dot{a}}{a} \right) = \frac{8\pi G}{3} \rho - \frac{k}{a^2} \quad (1.42a)$$

$$\frac{\ddot{a}}{a} = -\frac{4\pi G}{3} (\rho + 3P) \quad (1.42b)$$

²The constant Λ is also known as cosmological constant

1. COSMOLOGICAL MODELS AND INFLATION

where $\rho \equiv \sum_i \rho_i$ and $P \equiv \sum_i P_i$ are the sum of all the contributions to pressure and radiation in the Universe. The first Friedmann equation is often written in terms of the Hubble parameter,

$$H^2 = \frac{8\pi G}{3} \rho - \frac{k}{a^2} \quad (1.43)$$

This implies that, for a flat Universe with $k = 0$, the density today has a precise value called *critical density*:

$$\rho_{crit,0} = \frac{3H_0^2}{8\pi G} = 2.8 \times 10^{11} h^2 M_\odot \text{ Mpc}^{-3} \quad (1.44)$$

where we have made use of the definition of the reduced Hubble constant $H_0 h^{-1} = 100 \text{ km s}^{-1} \text{ Mpc}^{-1}$. The critical density can then be used to define the dimensionless density parameters:

$$\Omega_{i,0} \equiv \frac{\rho_{i,0}}{\rho_{crit,0}} \quad (1.45)$$

where the subscript i runs over all the species (photons, dark matter, etc.). Using Eq.(1.45) we can rewrite the first Friedmann equation in terms of the $\Omega_{i,0}$:

$$H^2(a) = H_0^2 \left[\Omega_{r,0} \left(\frac{a_0}{a} \right)^4 + \Omega_{m,0} \left(\frac{a_0}{a} \right)^3 + \Omega_{k,0} \left(\frac{a_0}{a} \right)^2 + \Omega_{\Lambda,0} \right] \quad (1.46)$$

here, $\Omega_{k,0} \equiv -k/(a_0 H_0)^2$ is the ‘‘curvature’’ density parameter. As commonly done in the literature we drop the subscript ‘‘0’’ to denote the density parameter today, so that *e.g.* Ω_r is the radiation density today in terms of the critical density today. Using this convention and employing Eq.(1.23) we can rewrite the above equation as:

$$H^2(z) = H_0^2 \left[\Omega_r (1+z)^4 + \Omega_m (1+z)^3 + \Omega_k (1+z)^2 + \Omega_\Lambda \right] \quad (1.47)$$

Evaluating the above equation at the present time, a relation between the Ω of different species is found *i.e.*

$$\sum_i \Omega_i + \Omega_k = 1 \quad (1.48)$$

Current observations from CMB and Large scale structure (LSS) have lead to strong constraints on the density parameters Ω_i [27, 28]:

$$\Omega_b h^2 = 0.0224 \pm 0.0001 \quad \Omega_c h^2 = 0.120 \pm 0.001 \quad (1.49)$$

$$\Omega_m = 0.315 \pm 0.007 \quad \Omega_\Lambda = 0.6847 \pm 0.0073 \quad (1.50)$$

where Ω_b and Ω_c are the baryons and cold dark matter density respectively and h is the reduced Hubble constant. These results shows that $\Omega_k \approx 0$, we will assume

Phase	w	$a(t)$	$a(\eta)$
RD	1/3	$t^{2/3}$	η^2
MD	0	t^1	η
Λ D	-1	e^{Ht}	$-\eta^{-1}$

Table 1.1: Solutions of the Eq.(1.46) for a flat Universe dominated by matter (MD), radiation (RD) and a cosmological constant (Λ D).

therefore in the rest of the present work the Universe to be *flat*³. These results also show that the Universe today is composed of:

- 5% of ordinary matter
- 27% of (cold) dark matter
- 68% of a dark energy component with $w \approx -1$

SINGLE COMPONENT SOLUTION OF THE FRIEDMANN EQUATION

We have now all the tools to solve Eq.(1.46) and describe the evolution of the scale factor $a(t)$. We start by noting that due to the different redshift scaling of energy density species in Eq.(1.47), the history of the Universe has been a succession of epochs dominated by a single energy density species. First radiation then matter and the cosmological constant at late time. In the case of a single species Eq.(1.47) can be analytically solved to find the time evolution of the scale factor $a(t)$. We define the equation of state of a single species as:

$$P = w\rho \quad (1.51)$$

where w is a constant which value depends on the species we are considering. Using Eq.(1.51) in the continuity equation Eq.(1.36), we can find a solution for the evolution of the density ρ :

$$\rho(a) \propto a^{-3(1+w)} \quad (1.52)$$

Inserting the above equation into Eq.(1.46) we obtain the time dependence of the scale factor:

$$a(t) \propto \begin{cases} t^{2/3(1+w)} & w \neq -1 \\ e^{Ht} & w = -1 \end{cases} \quad (1.53)$$

A summary of the solutions is given in Tab.1.1

³This constraints have been found fitting cosmological data with a standard Λ CDM parametrization [27]. We refer to [27, 28] for an analysis of the constraints on the curvature parameter in extended (i.e. non- Λ CDM) cosmologies

1.4 The fine-tuning problem of the Hot Big Bang Cosmology

The Hot Big Bang cosmology described in the previous Sections has been found to be extremely successful when compared with observations but, the description we have made is still incomplete. We have not already specified what initial conditions have made the Universe appears as it is today. We are going to see that the Universe requires a particularly fine-tuned set of initial condition to evolve into its current state.

1.4.1 The flatness problem

Consider the definition of the curvature density that we have made in Eq.(1.46) as a function of redshift:

$$\Omega_k(z) \equiv \frac{-k^2}{a^2 H^2} = \Omega_k \frac{(1+z)^2}{E^2(z)} \quad (1.54)$$

For a truly flat Universe $\Omega_k = 0$ at all time, but otherwise assuming for simplicity a single component Universe, one finds:

$$\Omega_k(z) = \frac{\Omega_k}{\Omega_i(1+z)^{1+3w}} \quad (1.55)$$

so that during matter and radiation dominance $|\Omega_k|$ is an increasing function of time. Then, even though curvature density is very close to zero today, it was even closer to zero at earlier times. The Universe therefore should have started out remarkably close to be flat. Recall also that, to a flat Universe is associated a total energy density equal to the critical density. Therefore having an extremely tiny curvature at early times is equivalent to assume that the energy density of the Universe was extremely fine tuned to be close to the critical density at that time.

1.4.2 The horizon problem

In order to discuss the horizon problem we start by writing the comoving particle horizon of Eq.(1.20) as:

$$\chi_p(a) = \int_{\ln a_i}^{\ln a} (aH)^{-1} d \ln a \quad (1.56)$$

where $a_i \equiv 0$ corresponds to the Big Bang singularity (BBs). The causal structure of the Universe is related to the quantity $(aH)^{-1}$, the *comoving Hubble radius*. Assuming a perfect fluid with equation of state given by Eq.(1.51), one finds:

$$(aH)^{-1} = H_0^{-1} a^{(1+3w)/2} \quad (1.57)$$

The *strong energy condition* i.e. $1 + 3w > 0$ is verified for all familiar energy sources (radiation and matter) and leads to the conclusion that the Hubble radius increases as the Universe expansion goes on. We can therefore rewrite the particle horizon as:

$$\chi_p(\eta) = \frac{2H_0^{-1}}{1 + 3w} \left(a^{(1+3w)/2} - a_i^{(1+3w)/2} \right) \equiv \eta - \eta_i \quad (1.58)$$

These definitions make evident two important features of the comoving horizon:

- $\chi_p(a)$ receives the largest contributions from late time, since $\eta_i \rightarrow 0$ as $a_i \rightarrow 0$
- the comoving horizon is a finite quantity,

$$\chi_p(t) = \frac{2H_0^{-1}}{1 + 3w} a(t)^{(1+3w)/2} = \frac{2}{1 + 3w} (aH)^{-1} \quad (1.59)$$

and it is proportional to the Hubble radius $\chi_p \propto (aH)^{-1}$

We have seen in Section 1.1 that the relic radiation of the Big Bang, the CMB, is almost perfectly isotropic with anisotropies of one part in one hundred thousand. The finiteness of the conformal time implies however that most part of the CMB have never been in causal contact. In particular, the characteristic angular scale of the CMB anisotropies is the angle at which the horizon is seen at recombination,

$$\theta \approx \frac{\eta_{rec}}{\eta_0} \approx 1^\circ \quad (1.60)$$

where $\eta_{rec} = \eta(t_{rec})$ is the value of the conformal time when the CMB is emitted. We see indeed that the CMB temperature is the same for region separated by more than 1° , so that at recombination the Universe was made up of $(\eta_{rec}/\eta_0)^{-3} \approx 10^4$ causally disconnected patches (see also Fig. 1.2).

If these regions have never had time to communicate (i.e. were never in causal contact) why they have the same temperature ?

This corresponds to the so-called *horizon problem*. A possible solution is that the initial density perturbations were exactly that required to observe the right degree of uniformity in the CMB and possessed the right degree of fluctuations to explain the formation of the structures we observe today. As for the flatness problem this explanation corresponds to have very fine-tuned initial conditions. We will see shortly that the an accelerated expansion phase at early time (called *inflation*) can solve all these problems without the necessity of any fine-tuning.

1.5 Classical Inflation

1.5.1 A solution to all problems

Both the horizon and the flatness problem are a results of the behavior of the Hubble radius, $(aH)^{-1}$, which as we have seen because of the strong energy condition grows

1. COSMOLOGICAL MODELS AND INFLATION

at the same rate of the particle horizon. However there are no reasons to assume that the strong energy condition cannot be violated. If we conjecture that $1 + 3w < 0$, we find that the Hubble radius decreases with time,

$$\frac{d}{dt}(aH)^{-1} < 0 \quad (1.61)$$

At present time then the comoving horizon appears much larger than the Hubble radius so that particles cannot communicate today but were in causal contact at earlier time. This constitutes the solution of the horizon problem. A similar argument is also able to solve the flatness problem. Infact the curvature density, $|\Omega_k| = |k|/(aH)^2$, is now also a decreasing function of time. So, no matter what was the initial curvature of the Universe since it get closer and closer to zero while expansion is occurring. Before going into the details of the physics that can lead to the shrinking of the Hubble radius, it is worth discussing the consequences of this assumption:

- The shrinking of the comoving radius implies an *accelerated expansion*,

$$\frac{d}{dt}(aH)^{-1} = -\frac{\ddot{a}}{(\dot{a})^2} < 0 \Rightarrow \ddot{a} > 0 \quad (1.62)$$

Therefore inflation is commonly defined as a period of acceleration.

- We have seen in the previous Section that an accelerated expansion corresponds to a constant Hubble rate therefore:

$$\frac{d}{dt}(aH)^{-1} = -\frac{\dot{a}H + a\dot{H}}{(aH)^2} = -\frac{1}{a}(1 - \epsilon_H) \quad (1.63)$$

where we have defined $\epsilon_H \equiv -\dot{H}/H^2$. Therefore inflation also corresponds to the requirement,

$$\epsilon_H = -\frac{\dot{H}}{H^2} < 1 \quad (1.64)$$

If we also define another quantity N defined by, $dN/dt \equiv -H$, which measure the number of *e-folds* of inflation. Then, the condition on the Hubble radius can be translated into a condition on ϵ_H , *i.e.*

$$\epsilon_H = \frac{d \log H}{dN} < 1 \quad (1.65)$$

- As we discussed above, the strong energy condition is violated if $(aH)^{-1}$ decreases in time. Using Eq.(1.36) and Eq.(1.46) we find:

$$\epsilon_H = -\frac{\dot{H}}{H^2} = \frac{3}{2}(1 + w) < 1 \quad (1.66)$$

inflation, then, is associated to a dominant form of energy with negative pressure or $w < -1/3$.

1.5.2 Slow-roll single field inflation

The simplest way to mathematically address all the features that are required for inflation to happen is to associate inflationary dynamics to that of a scalar field $\phi(t)$, dubbed the inflaton¹. The stress-energy tensor associated with the scalar field can be written as :

$$T^{\mu\nu} = \partial_\mu \phi \partial_\nu \phi - g_{\mu\nu} \left(\frac{1}{2} g^{\alpha\beta} \partial_\alpha \phi \partial_\beta \phi - V(\phi) \right) \quad (1.67)$$

From this definition we can easily derive the pressure and energy density associated with the scalar field ϕ :

$$T_0^0 = \rho_\phi \Rightarrow \rho_\phi = \frac{1}{2} \dot{\phi}^2 + V(\phi) \quad (1.68)$$

$$T_j^i = -P_\phi \delta_j^i \Rightarrow P_\phi = \frac{1}{2} \dot{\phi}^2 - V(\phi) \quad (1.69)$$

while the Friedmann equations can be written in terms of the scalar field as:

$$H^2 = \frac{1}{3} \frac{1}{M_{pl}^2} \left(\frac{1}{2} \dot{\phi}^2 + V \right) \quad (1.70a)$$

$$\dot{H} = -\frac{1}{2} \frac{\dot{\phi}^2}{M_{pl}^2} \quad (1.70b)$$

where $M_{pl}^2 = (8\pi G)^{-1}$ is the Planck mass. We see therefore that the evolution of the Hubble parameter is determined entirely by the kinetic term. Combining Eq.(1.70a) and Eq.(1.70b), one finds that the inflaton evolves accordingly to a Klein-Gordon equation of the form:

$$\ddot{\phi} + 3H\dot{\phi} + V'(\phi) = 0 \quad (1.71)$$

where $V' = dV/d\phi$. Instead, the equation of state parameter w_ϕ associated to the inflaton is simply:

$$w_\phi = \frac{P_\phi}{\rho_\phi} = \frac{\frac{1}{2} \dot{\phi}^2 - V(\phi)}{\frac{1}{2} \dot{\phi}^2 + V(\phi)} \quad (1.72)$$

The requirement to have an accelerated expansion, *i.e.* $w \approx -1$, is verified only if $\dot{\phi}^2/2 \ll V(\phi)$ or in other words we can have an acceleration driven by the inflaton only if the inflationary potential dominates over the kinetic term.

How we can satisfy this requirement ?

The common way to go around this issue is to assume a shallow slope for the

¹In principle the inflaton could be a function of both space and time coordinates $\phi(x, t)$ but the symmetries of the FLRW metric require the inflaton to depends only on time.

1. COSMOLOGICAL MODELS AND INFLATION

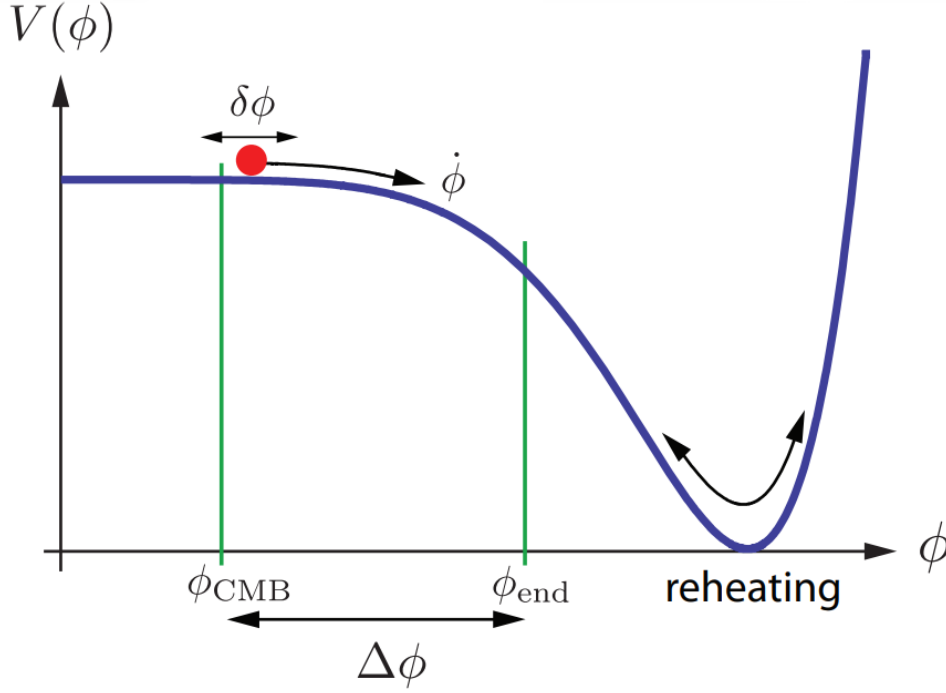


Figure 1.4: Example of a inflaton potential. The accelerated phase occurs when the potential energy of the field $V(\phi)$ dominates the total energy of the inflaton. Inflation ends when the kinetic energy $1/2\dot{\phi}^2$ become comparable with the potential energy. CMB fluctuations are produced at ϕ_{CMB} around 60 e-folds before the end of inflation. After inflation ends, the inflaton starts to oscillate around the minimum of the potential converting its energy density in radiation. This process is called commonly reheating

potential leading to its minimum: the field would have slowly evolved towards the potential minimum maintaining small the kinetic energy and allowing for $\ddot{a} > 0$ (see Fig.1.4). This condition is known as the *slow-roll regime*, while the requirement that the potential energy dominates over the kinetic terms is known as the *slow-roll approximation*. One can easily see that in the slow-regime also the condition $\epsilon_H < 1$ is verified. Infact, using Eq.(1.64) and Eq.(1.70b) one finds:

$$\epsilon_h = \frac{\dot{\phi}^2}{M_{pl}^2 H^2} = \frac{3}{1 + 2V/\dot{\phi}^2} \quad (1.73)$$

so if the potential contribution to the energy density dominates over the kinetic term we always have $\epsilon_H < 1$. In the slow-roll regime $\epsilon_H \ll 1$ and $\rho_\phi \sim -P_\phi$ hence inflation follows a quasi de Sitter expansion while the potential falls into its minimum.

What remains to be answered is : How long inflation should last in order to have enough time to solve both the horizon and the flatness problem ?

What we need is that the condition $\epsilon_H < 1$ is verified for a sufficiently large number of Hubble times. We therefore introduce another parameter to take this into account:

$$\eta_H = -\frac{d \log \epsilon_H}{dN} = 2\epsilon_H + \frac{2\ddot{\phi}}{H\dot{\phi}} \quad (1.74)$$

This parameter must also satisfy the same condition as of ϵ_H , *i.e.* $|\eta_H| < 1$ (or $|\eta_H| \ll 1$ in the slow-roll regimes). These conditions on ϵ_H and $|\eta_H|$ can be reformulated as constraints on the shape of the inflationary potential leading to the definition of the so-called *slow-roll parameters*²:

$$\epsilon_V \equiv \frac{M_{pl}^2}{2} \left(\frac{V'}{V} \right)^2 \quad \eta_V \equiv M_{pl}^2 \frac{V''}{V} \quad (1.75)$$

As for ϵ_H and $|\eta_H|$, the slow-roll parameters, ϵ_V and $|\eta_V|$, have to be small for inflation to happen *i.e.* $\{\epsilon_V, |\eta_V|\} \ll 1$. In the slow-roll regime, the two set of parameters are also related by the following identities:

$$\epsilon_H \approx \epsilon_V \quad (1.76a)$$

$$\eta_H \approx -2\eta_V + 4\epsilon_V \quad (1.76b)$$

Finally, inflation ends when acceleration ceases (*i.e.* $\ddot{a} = 0$) corresponding to $\epsilon_H = 1$ ($\epsilon_V \approx 1$) and a violation of the slow-roll approximation. We can then estimate the number of “e-folds” required for inflation as:

$$N(t) = \log \frac{a_{\text{end}}}{a(t)} = \int_t^{t_{\text{end}}} H(t') dt' \quad (1.77)$$

where t_{end} corresponds to the time where $\epsilon_H = 1$. In the slow-roll regime the following relations hold,

$$H dt = \frac{H}{\dot{\phi}} d\phi \approx \frac{1}{M_{pl}^2} \frac{V(\phi)}{V'(\phi)} d\phi \quad (1.78)$$

where in the last equality we have assumed $\dot{\phi} > 0$, and Eq.(1.77) can be written as an integral over the field space of the inflaton:

$$N(t) = \frac{1}{M_{pl}^2} \int_{\phi(t)}^{\phi_{\text{end}}} d\phi \frac{V(\phi)}{V'(\phi)} \quad (1.79)$$

From Eq.(1.79), we see that the number of e-folds associated with inflation depends on the specific form of the potential that is driving it. However, we can estimate the approximate value of N for inflation with the following argument. The Hubble radius at the onset of inflation must have been larger than the largest scale observable at the present time, or in other words than the current Hubble radius. Assuming that after inflation the Universe is radiation dominated (considering the

² ϵ_H and $|\eta_H|$ are generally referred to as the Hubble slow-roll parameters

1. COSMOLOGICAL MODELS AND INFLATION

matter dominance phase add only a small correction) we have that $H \propto a^{-2}$. The Hubble radius at the end of inflation can be then estimated from:

$$a_{\text{end}} = \frac{a_0 H_0}{a_{\text{end}} H_{\text{end}}} = \frac{T_0}{T_{\text{end}}} \quad (1.80)$$

Assuming that $T_{\text{end}} = 10^{15}$ GeV and recalling that $T_0 = 2.7$ K = 10^{-3} eV then $a_{\text{end}} \sim 10^{-28}$. So the comoving Hubble radius after inflation was 28 orders of magnitude smaller than today. Then the inflationary picture works only if this condition is satisfied. To translate this into a constraint on the number of e-folds, recall that during inflation the Hubble parameter is nearly a constant and the Universe experiences a de Sitter-like expansion, therefore:

$$\frac{a(t)}{a_{\text{end}}} = e^{H\Delta t} \approx e^{N(t)} \implies N \gtrsim 60 \quad (1.81)$$

So, we need at least 60 e-folds for inflation to solve the issues of the Hot Big Bang scenario. We conclude this Chapter stressing out that a microscopic interpretation of inflation is still unknown but there are many models whose predictions fall well inside the observational bounds (see *e.g.* [32]). For a more detailed discussion on inflationary physics instead we refer to [47].

1. COSMOLOGICAL MODELS AND INFLATION

2 UNIVERSE THERMODYNAMICS

As we have seen in the previous Chapter, the Universe emerged in a very hot and dense state after the end of inflation. The rate of interactions between particles was so fast that thermodynamic equilibrium was established, and the state of the Universe was that of a plasma at a single temperature T . As the Universe expanded, the plasma cooled down, and the first light elements (hydrogen, helium and lithium) formed. At some point, the temperature had dropped enough that electrons recombine and the first atoms get formed. At this point the efficiency of the interactions that bounded photons and plasma particles is so low that they start to stream freely and the Universe becomes transparent to radiation becoming what we see now as the CMB.

In this Chapter, we are going to review briefly the thermal history of the Hot Big Bang, with a glance at neutrino decoupling and recombination. This Chapter is mainly based on [44, 46]

Contents

2.1	Thermal History	27
2.1.1	Equilibrium Thermodynamics	30
2.1.2	Density, Pressure and Entropy conservation	31
2.2	Cosmic Neutrino Background	33
2.3	Recombination	34

2.1 Thermal History

In order to understand the thermal history of our Universe, one has to compare the *rate of interactions* Γ with the expansion rate H . Indeed, when the rate of interactions is much bigger than the expansion rate ($\Gamma \gg H$), the time scale of particle interactions is much smaller than the characteristic expansion time scale and local thermal equilibrium is reached before the effect of expansion become relevant. However, as the Universe cools down the interaction rate typically decreases much faster than the Hubble rate and when $\Gamma \sim H$ then the particles start to decouple from the thermal bath. In the standard model the rate of interaction

between to particle species can be written as

$$\Gamma \equiv n\langle\sigma v\rangle \quad (2.1)$$

where n is the particles number density and we have assumed that both species have the same density, σ is the interaction cross Section and v is the relative velocity between the two species of particles. The brackets indicate instead an average over the velocity distribution. In the Standard Model, interactions are mediated by gauge bosons therefore one can write $T \sim \alpha^2/T^2$ with $\alpha \equiv g^2/4\pi$ being the generalized structure constant associated with a generic gauge bosons. Assuming that all the species involved are ultra-relativistic (which is well motivated for $T \gtrsim 100$ GeV), we can set $v \sim 1$. The number density of particles scales as the inverse of the Universe volume so approximately we have $n \sim a^{-3} \sim T^3$. Therefore, we can write the rate of interactions as:

$$\Gamma = n\langle\sigma v\rangle \sim \alpha^2 T \quad (2.2)$$

The expansion rate instead is estimated through the Friedmann equation and remembering that for relativistic species we have $\rho \sim a^{-4} \sim T^4$, hence:

$$H \sim \frac{T^2}{M_{pl}^2} \quad (2.3)$$

Then, taking the ratio of Eq.(2.2) and Eq.(2.3) we have:

$$\frac{\Gamma}{H} \sim \frac{\alpha^2 M_{pl}}{T} \sim \frac{10^{16} \text{ GeV}}{T} \quad (2.4)$$

where we used $\alpha \sim 10^{-2}$. We see therefore from Eq.(2.4) that the condition $\Gamma \gg H$ is satisfied for temperatures $100 \text{ GeV} \lesssim T \lesssim 10^{16} \text{ GeV}$. Below $T \lesssim 100 \text{ GeV}$ the electroweak symmetry is broken and the cross Section of interactions become that of the weak force *i.e.* $\sigma \sim G_F^2 T^2$ where $G_F \sim 1.17 \times 10^{-5} \text{ GeV}^{-2}$ is the Fermi constant. Then, we have:

$$\frac{\Gamma}{H} \sim \left(\frac{T}{1 \text{ MeV}} \right)^3 \quad (2.5)$$

The strength of weak interactions decreases as the temperature of the Universe drops, for $T \sim 1 \text{ MeV}$ the ratio becomes $O(H)$ and particles that interacts with the primordial plasma only through weak interactions decouple at this temperature. In the next Sections we are going to describe how the breaking of particles equilibrium caused by cooling of our Universe has shaped the cosmological history. We conclude this introduction with a summary of the key thermal epochs of the Universe (for a detailed discussion of the various epoch see [65]).

2. UNIVERSE THERMODYNAMICS

- **Baryogenesis**

This is the epoch where the asymmetry between baryons and anti-baryons was generated. Particles and anti-particles annihilate with process of the form $e^+ + e^- \rightarrow 2\gamma$ *i.e.* two antiparticles annihilate into a pair of photons. If initially the Universe was filled with equal amount of particles and anti-particles then we expect to end up with a Universe filled only with radiation. However we observe today an excess of matter (baryons) over anti-matter with a density with respect to photons (γ) of $n_b/n_\gamma \sim 10^{-9}$.

- **Electroweak phase transition**

For temperature around 100 GeV particles acquire masses through the Higgs mechanism, as we have seen above, leading to a drastic change in the strength of weak interactions.

- **QCD phase transition**

Around $T \sim 150$ MeV strong interactions between quarks and gluons become important and baryons (three quarks systems) and mesons (quark anti-quark pair) start to form and began the relevant degree of freedom after the QCD transition.

- **Dark Matter Freeze-out**

Dark matter interacts very weakly with ordinary matter so it is expected to decouple relatively early. If it is made of WIMP (weakly interactive massive particles) then dark matter decouple (and its density freeze to a constant value) from the primordial plasma for $T \gtrsim 1$ MeV.

- **Neutrino Decoupling**

Neutrinos interacts only through weak interactions therefore they will decouple when $T \lesssim 1$ MeV as we have discussed above.

- **Electron-Positron Annihilation**

For $T \approx m_e \sim 0.5$ MeV photons are not energetic enough to keep the positron-electron pair annihilation process in equilibrium. Positron and electrons then annihilate transferring their energy to the thermal bath and heating it up. Neutrinos are instead not affected since they have already decoupled.

- **Big Bang Nucleosynthesis**

At $T \approx 0.1$ MeV, around three minutes after the Big Bang, light elements were formed.

- **Recombination**

This is the epoch during which neutral hydrogen was formed.

- **Photon Decoupling**

Before recombination photons are coupled with the other particles forming the primordial plasma through Compton scattering ($e^- + \gamma \rightarrow e^- + \gamma$). After recombination, however, the free electron density drops sharply and the Compton scattering become inefficient. Photons decouples from the plasma, their mean free path becoming longer than the horizon. They have since freely streamed through the Universe and we observe them today as the CMB

2.1.1 *Equilibrium Thermodynamics*

When talking about thermal equilibrium in early stage of the Universe history, we are actually referring to a statistical equilibrium between a huge number of particles of different species. The system is then described by a *distribution function* $f(\mathbf{x}, \mathbf{p}, t)$ in phase space [58]. Because of homogeneity, the distribution function has to be independent of the position \mathbf{x} . Furthermore, isotropy requires that the momentum dependence in f comes only through the magnitude of the momentum and not through its orientation in space, *i.e.* $p \equiv |\mathbf{p}|$. The number density of particle in the phase space is then simply given by [44, 58]:

$$n = \frac{g}{(2\pi)^3} \int f(p) d^3p \quad (2.6)$$

where g is the internal number of degrees of freedom (*e.g.* the spin) and $(2\pi)^3$ is the density of states in the phase space volume. The energy density is found simply weighting the number density with the particle energy $E(p)$ ¹:

$$\rho = \frac{g}{(2\pi)^3} \int d^3p f(p) E(p) \quad (2.7)$$

with similar arguments one finds that the pressure is defined as:

$$P = \frac{g}{(2\pi)^3} \int d^3p f(p) \frac{p^2}{3E(p)} \quad (2.8)$$

Before moving on, it is worth introducing three important concept that we will need to describe the thermal history of the Universe.

- **Kinetic Equilibrium**

A system of particles is in kinetic equilibrium if the particles exchange energy and momentum efficiently. This leads the system to a state of maximum

¹To a good approximation, particles in the early Universe were weakly interacting, therefore their energy is a function of the magnitude of the momentum only, *i.e.* $E^2 = p^2 + m^2$

2. UNIVERSE THERMODYNAMICS

entropy in which the distribution function is given by the *Fermi-Dirac* (for fermions) and *Bose-Einstein* distribution (for bosons):

$$f(p) = \frac{g}{e^{(E-\mu)/T} \pm 1} \quad (2.9)$$

where μ is the chemical potential

- **Chemical Equilibrium**

A system of particles is in chemical equilibrium with respect to some reaction if the rate of direct and inverse reaction is the same. Consider for example a generic interactions $x_1 + x_2 + \dots \rightleftharpoons y_1 + y_2 + \dots$, chemical equilibrium is reached when the condition,

$$\sum_{x_i} \mu_{x_i} = \sum_{y_i} \mu_{y_i} \quad (2.10)$$

is satisfied.

- **Thermal Equilibrium**

When a system of particles is both in chemical and kinetic equilibrium is said to be in thermal equilibrium. All the particles of the system share therefore the same temperature.

2.1.2 Density, Pressure and Entropy conservation

We now can make a step further and explicitly compute the density and pressure of a system of particles in a FLRW Universe. Recalling that $E(p) = p^2 + m^2$ and assuming chemical equilibrium, it is straightforward to show that:

- In the ultra-relativistic limit $T \gg m$, the integrals Eqs.(2.6 - 2.7) can be done in terms of the Riemann function, ζ :

$$n = \frac{g\zeta(3)}{\pi^2} T^3 \times \begin{cases} 1 & \text{bosons} \\ \frac{3}{4} & \text{fermions} \end{cases} \quad (2.11a)$$

$$\rho = \frac{\pi^2}{30} g T^4 \times \begin{cases} 1 & \text{bosons} \\ \frac{7}{8} & \text{fermions} \end{cases} \quad (2.11b)$$

$$P = \frac{1}{3} \rho \quad (2.11c)$$

- In the non-relativistic limit ($m \gg T$), instead the integrals become:

$$n = g \left(\frac{mT}{2\pi} \right)^{2/3} e^{-m/T} \quad (2.12a)$$

$$\rho = mn \quad (2.12b)$$

$$P = nT \gg \rho \quad (2.12c)$$

Comparing Eqs.(2.11) with Eqs.(2.12), we see that when temperature drops below m all quantities of the system get an exponential suppression. This is a consequence of the annihilation of particles and antiparticles: as the temperature decreases particle species become non-relativistic, particles energy is not high enough for pair production and annihilation cannot be balanced any more. Through Eqs.(2.11) it is also possible to define the so-called *effective number of relativistic species*, $g_\star(T)$. When $T \gtrsim 100$ GeV, all particles of the Standard Model are relativistic so that they all contribute to the radiation energy density ρ_r . Assuming T to be the temperature of a photon gas, the total radiation energy density would be the sum of the energy density of all the species involved, *i.e.*

$$\rho_r = \sum_i \rho_i = \frac{\pi^2}{30} g_\star(T) T^4 \quad (2.13)$$

The sum of Eq.(2.13) may receive contributions of two types:

1. Contribution from relativistic species ($T \gtrsim m$) which are in equilibrium with photons, in this case g_\star has the form:

$$g_\star^{th} = \sum_{i=b} g_i + \frac{7}{8} \sum_{i=f} g_i \quad (2.14)$$

when the temperature drops below the mass threshold m_i of a particle species, it becomes non-relativistic and its contribution is removed from the sum.

2. Relativistic species that are not in thermal equilibrium with the photons so that $T_i \neq T \gg m_i$. For those decoupled species g_\star can be written as:

$$g_\star^{dec}(T) = \sum_{i=b} g_i \left(\frac{T_i}{T} \right)^4 + \frac{7}{8} \sum_{i=f} g_i \left(\frac{T_i}{T} \right)^4 \quad (2.15)$$

If there are decoupled particles which are still relativistic in the thermal bath, we need to estimate their temperature in order to calculate their contribution to g_\star . This can be done using a conserved quantity, the total entropy of the Universe. From the second law of Thermodynamics we know that the entropy of the Universe can only increase or stay constant and it is conserved in equilibrium. Since there 10^9 photons per baryons the entropy of the Universe is dominated by that of the photon bath (at least as long as the Universe is sufficiently uniform). Any entropy production from non-equilibrium processes is therefore completely insignificant relative to the total entropy. Then, to a good approximation, we can treat the expansion as adiabatic so that the total entropy is constant even beyond equilibrium. Assuming there is no chemical work, $\mu = 0$, from the second law we can write:

$$dS = d \left(\frac{\rho + P}{T} V \right) = d(sV) \quad (2.16)$$

2. UNIVERSE THERMODYNAMICS

where we have defined the *entropy density*, $s = (P + \rho)/T$. Taking the time derivative, we can see that this is a conserved quantity:

$$\frac{dS}{dt} = \frac{V}{T} \left(\frac{d\rho}{dt} + \frac{1}{V} \frac{dV}{dt} (\rho + P) \right) + \frac{V}{T} \left(\frac{dP}{dt} - \frac{\rho + P}{T} \frac{dT}{dt} \right) = 0 \quad (2.17)$$

The first term vanishes because of the continuity equation Eq.(1.36), the second term vanishes because, in the absence of chemical work, $\partial P / \partial T = (\rho + P)/T$. Then the total entropy is conserved and $s \propto a^{-3} \propto T^3$. Using Eqs.(2.11), we see that the entropy density can be written as:

$$s = \sum_i \frac{\rho_i + P_i}{T_i} \equiv \frac{2\pi^2}{45} g_{\star,S}(T) T^3 \quad (2.18)$$

where we have defined $g_{\star,S} = g_{\star,S}^{th} + g_{\star,S}^{dec}$. In thermal equilibrium we clearly have $g_{\star,S} = g_{\star}^{th}$, but for decoupled species since $s \propto T^3$ we have:

$$g_{\star,S}^{dec} \equiv \sum_{i=b} g_i \left(\frac{T_i}{T} \right)^3 + \frac{7}{8} \sum_{i=f} g_i \left(\frac{T_i}{T} \right)^3 \neq g_{\star}^{dec} \quad (2.19)$$

Therefore g_{\star} and $g_{\star,S}$ are equivalent only if all species are in equilibrium at the same temperature. There are however two important implications of the conservation of entropy:

1. Since $s \propto a^{-3}$, the number of particles in a comoving volume is simply $N_i \equiv n_i/s$. If particles are not produced or destroyed then $n_i \propto a^{-3}$ and N_i is a constant.
2. Eq.(2.18) implies that :

$$g_{\star,S}(T) T^3 a^3 = \text{const} \implies T \propto g_{\star,S}(T)^{-1/3} a^{-1} \quad (2.20)$$

Away from particles mass threshold $g_{\star,S}$ is nearly constant and $T \propto a^{-1}$. The factor $g_{\star,S}(T)^{-1/3}$ accounts for the fact that whenever a particle species becomes non-relativistic, its entropy is transferred to the other relativistic species still present in the thermal plasma, causing T to decrease slightly less slowly than a^{-1} . We will see in next Section that this has important consequences for the formation of the CMB and the cosmic neutrino background (CvB).

2.2 Cosmic Neutrino Background

Neutrinos interact with the primordial plasma only via weak interaction. We have seen in Section 2.1 that when the temperature drops below 1 MeV particles

that interact through the weak force decouple from the thermal bath (a precise calculation gives $T_w^{dec} \approx 0.8 \text{ MeV}$). After decoupling, neutrinos move freely along geodesic preserving the relativistic Fermi-Dirac distribution. Their entropy will be conserved therefore $T_\nu \propto a^{-1}$. If $g_{\star,S}$ is constant then the photon temperatures will scale in the same way and photons and neutrinos would have the same temperature $T_\nu = T_\gamma$. However, if some annihilation process happens the temperature decrease more slowly than a^{-1} . For neutrinos this is indeed the case. After neutrino decoupling, infact, $e^+ - e^-$ pairs start to annihilate when the temperature drops below the electron mass and energy is injected into the plasma. The photon bath is therefore heated up by the electron-positron annihilation process and $T_\gamma > T_\nu$. Using the fact that $g_\gamma = g_e^+ = g_e^- = 2$ we have that:

$$g_{\star,S}^{th} = \begin{cases} 2 + \frac{7}{8} \times 4 = \frac{11}{2} & T \gtrsim m_e \\ 2 & T < m_e \end{cases} \quad (2.21)$$

Since $g_{\star,S}^{th}(aT_\gamma)^3$ remains constant in equilibrium we have:

$$T_\nu = \left(\frac{4}{11} \right)^3 T_\gamma \quad (2.22)$$

When $T \ll m_e$ the effective number of relativistic species is:

$$g_\star = 2 + \frac{7}{8} \times 2N_{\text{eff}} \left(\frac{4}{11} \right)^{4/3} = 3.38 \quad (2.23a)$$

$$g_{\star,S} = 2 + \frac{7}{8} \times 2N_{\text{eff}} \left(\frac{4}{11} \right) = 3.94 \quad (2.23b)$$

where we have introduced the parameter N_{eff} the so-called *effective number of neutrino species*. For an instantaneous decoupling $N_{\text{eff}} = 3$. However, neutrinos were still decoupling when the $e^+ - e^-$ annihilation began, so some of the energy released did leak to neutrinos. Accounting for this raises the value to $N_{\text{eff}} = 3.046$. The evolution of $g_\star(T)$ is shown in Fig.2.1

2.3 Recombination

Until now we have assumed kinetic equilibrium for the systems of particles we were considering, so that their distribution function were described by the Fermi-Dirac or Bose-Einstein distribution. However there are many processes in the early Universe for which this assumption does not hold. One of such processes is the epoch of *recombination* when the first atoms were formed. For $T > 1 \text{ eV}$, the primordial plasma was composed of free electrons, photons (tightly coupled

2. UNIVERSE THERMODYNAMICS

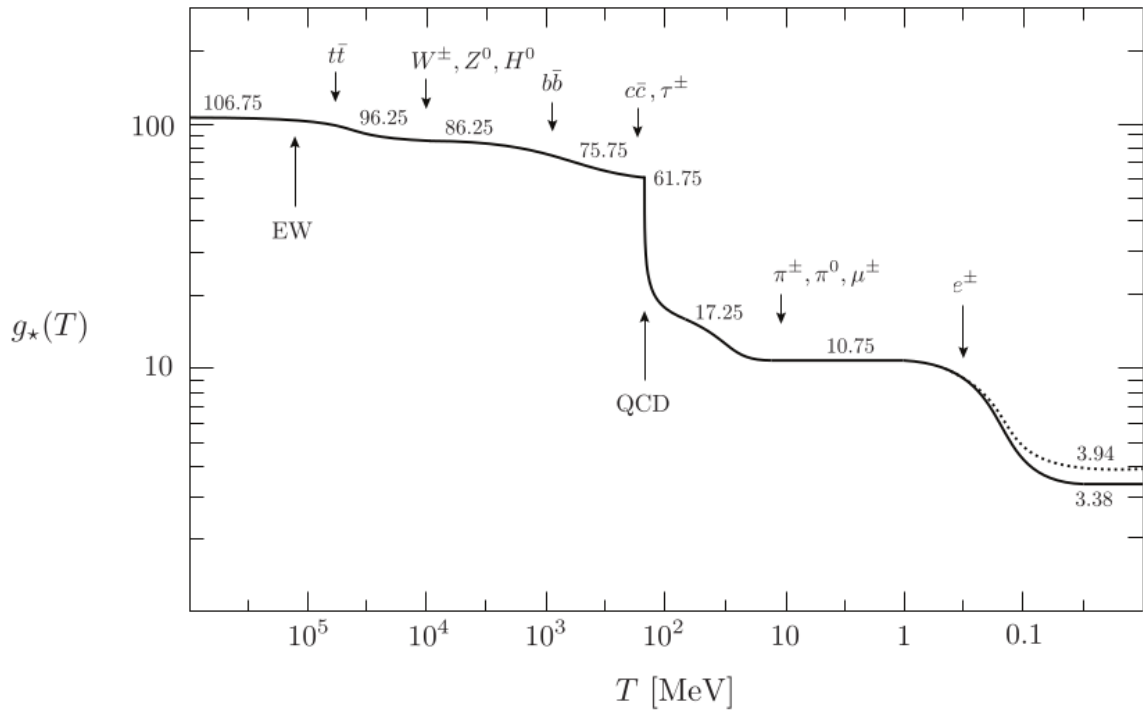


Figure 2.1: Evolution of the relativistic degree of freedom $g_*(T)$ assuming the Standard Model particle content. The dotted line represent $g_{*,s}(T)$ [44]

to electrons via Compton scattering) and protons (coupled to the electrons via Coulomb scattering). When the temperature becomes low enough the formation of neutral hydrogen became viable since the reaction



is not efficient enough to maintain the hydrogen ionized. Then, the density of free electrons dropped sharply and photons mean free path became longer than the horizon distance. The Universe became transparent to radiation. To understand when this happens we have to track the evolution of the fraction of free electron w.r.t. baryons $X_e \equiv n_e/n_b$. When baryons and photons are still in equilibrium ($T > 1 \text{ eV}$) we have the following equilibrium abundances:

$$n_i^{eq} = g_i \left(\frac{m_i T}{2\pi} \right)^{3/2} \exp \left(\frac{\mu_i - m_i}{T} \right) \quad (2.25)$$

where $i = \{e, p, \text{H}\}$ and we have used $T_i < m_i$. Recall also that $\mu_e + \mu_p = \mu_{\text{H}}$ following from the equilibrium of Eq.(2.24) (since $\mu_\gamma = 0$). To get rid of the chemical potential, we consider the ratio of the abundances of free protons and electrons w.r.t. that of neutral hydrogen.

$$\left(\frac{n_{\text{H}}}{n_e n_p} \right) \Big|_{eq} = \frac{g_{\text{H}}}{g_e g_p} \left(\frac{2\pi}{T} \frac{m_{\text{H}}}{m_e m_p} \right)^{3/2} e^{(m_p + m_e - m_{\text{H}})/T} \quad (2.26)$$

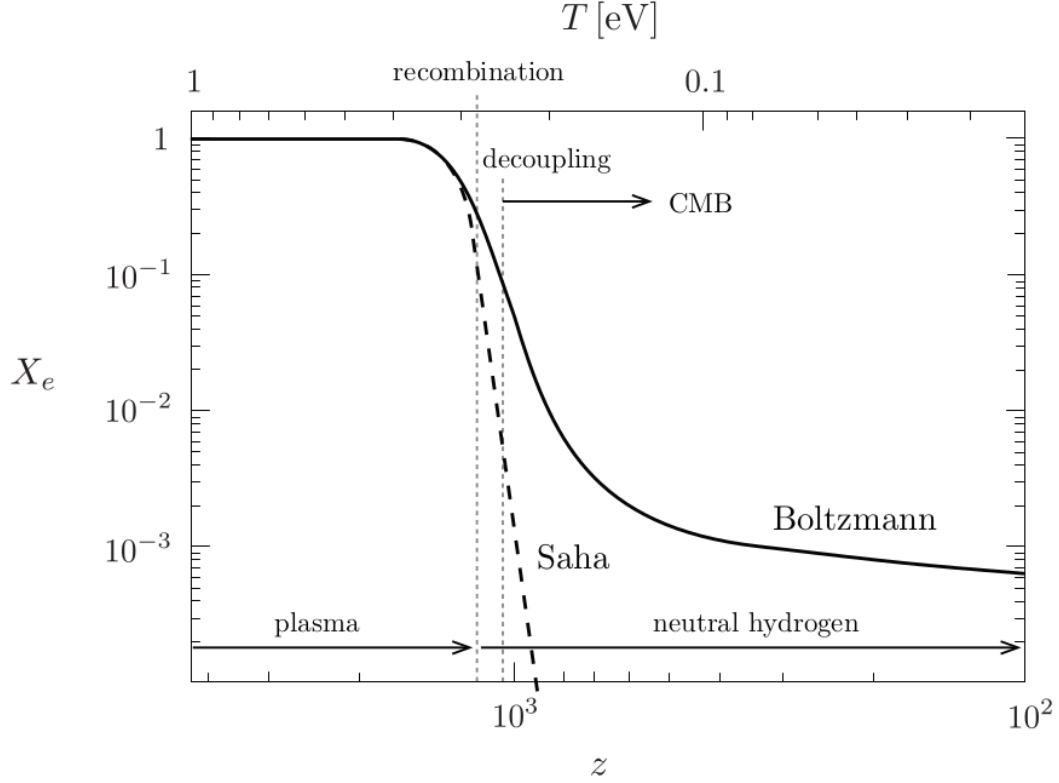


Figure 2.2: Evolution of the electron fraction X_e as a function of redshift. The dashed curve shows the evolution of X_e predicted by the Saha equation, the solid line instead represents the calculation made with a more exact numerical treatment (involving the Boltzmann equation, see also next Chapter)

Using the fact that $g_p = g_e = 2$ and $g_H = 4$, introducing the binding energy $B_H \equiv m_e + m_p - m_H = 13.6$ eV and taking $n_e = n_p$ (since the Universe is not electrically charged) we end up with:

$$\left. \frac{n_H}{n_e^2} \right|_{eq} = \left(\frac{2\pi}{m_e T} \right)^{3/2} e^{\frac{B_H}{T}} \quad (2.27)$$

Using the fact that the baryon density is:

$$n_b = \eta_b n_\gamma = \eta_b \frac{2\zeta(3)}{\pi^2} T^3 \quad (2.28)$$

where $\eta_b = 5.5 \times 10^{-10} (\Omega_b h^2 / 0.020)$ is the *baryon-to-photon ratio*. Considering only protons (which compose the 90% of the primordial abundance of nuclei) and ignoring all other nuclei, the baryon density can be written as $n_b \approx n_p + n_H = n_e + n_H$ and hence:

$$\frac{1 - X_e}{X_e^2} = \frac{n_H}{n_e^2} n_b \quad (2.29)$$

Substituting the above equation in Eq.(2.27) we arrive at the *Saha equation*:

$$\left(\frac{1 - X_e}{X_e^2} \right)_{eq} = \frac{2\zeta(3)}{\pi^2} \eta_b \left(\frac{2\pi}{m_e T} \right)^{3/2} e^{\frac{13.6 \text{ eV}}{T}} \quad (2.30)$$

2. UNIVERSE THERMODYNAMICS

As we see from Fig.2.2, the Saha equation, which assumes that the electron abundance is the equilibrium one, gives a good prediction of the temperature of recombination T_{rec} and decoupling T_{dec} however a calculation involving the Boltzmann equation (see next Chapter) is needed to calculate the relic density of electrons after freeze-out.

We proceed defining T_{rec} as the temperature where 90% of the electrons have combined with protons so that $X_e = 0.1$. Using Eq.(2.30), we find:

$$T_{rec} \approx 0.3 \text{ eV} \approx 3600 \text{ K}$$

Recombination occurs at $T_{rec} \ll B_H$, the reason is that the baryon fraction is really small $\eta_b \ll 1$ and there are around 10^9 photons for each hydrogen atom. Even when the temperature drops below B_H , the high energy tail of the photon distribution contains still a lot of photon with energy greater than B_H which can ionize newly formed hydrogen atoms.

Using $T_{rec} = T_0(1 + z_{rec})$ with $T_0 = 2.7 \text{ K}$, we find $z_{rec} \approx 1320$. Since the matter-radiation equality happens at $z_{eq} \approx 3500$, recombination occurs in the matter-dominated era. Therefore, $a \propto t^{-3/2}$ and

$$t_{rec} \sim 2.9 \times 10^5 \text{ y}_s$$

As shown Fig.2.2, photon decoupling happens slightly after recombination. Photons decouples from the plasma when their interaction rate is comparable to the Hubble rate, *i.e.* $\Gamma_Y(T_{dec}) \sim H_0(T_{dec})$. Photons are coupled to the plasma through electrons Thomson scattering with $\Gamma_Y \approx n_e \sigma_T$ where $\sigma_T \approx 2 \times 10^{-3} \text{ MeV}$. Using:

$$\Gamma_Y(T_{dec}) = n_b X_e(T_{dec}) \sigma_T = \frac{2\zeta(3)}{\pi^2} \eta_b \sigma_T X_e(T_{dec}) T_{dec}^3 \quad (2.31a)$$

$$H(T_{dec}) = H_0 \sqrt{\Omega_m} \left(\frac{T_{dec}}{T_0} \right)^{3/2} \quad (2.31b)$$

we get,

$$X_e(T_{dec}) T_{dec}^{3/2} \sim \frac{\pi^2}{2\zeta(3)} \frac{H_0 \sqrt{\Omega_m}}{\eta_b \sigma_T T_0^{3/2}} \quad (2.32)$$

Therefore using Eq.(2.30) we finally obtain the value of $T_{dec} \sim 0.27 \text{ eV}$. While the redshift and time of photons decoupling are:

$$z_{dec} \approx 1100$$

$$t_{dec} \approx 3.8 \times 10^5 \text{ y}_s$$

This is the moment in which the Cosmic Microwave Background was formed. We conclude this Section with a few remarks:

- Even though $T_{dec} \sim T_{rec}$, the ionization fraction decreases significantly between recombination and decoupling (see also Fig.2.2) *i.e.* $X_e(T_{rec}) = 0.1$ and $X_e(T_{dec}) = 0.01$. Indeed a high degree of neutrality is needed for the Universe to become transparent to photon propagation.
- Recombination happens after matter-radiation equality but the ratio Ω_r/Ω_m is still high enough to leave observable signature in the CMB, through the early ISW effect [44].

PART II

FROM INHOMOGENEITIES TO ANISOTROPIES

3 THE INHOMOGENEOUS UNIVERSE

Until now we have treated the Universe as perfectly homogeneous and isotropic, however to understand the formation and evolution of large scale structure (LSS) we have to introduce inhomogeneities. In this Chapter we will develop the formalism of cosmological perturbation theory and discuss how inflation sets the initial conditions to solve the perturbation equations. In the last part of the Chapter we use the perturbation theory we have drawn to connect the fluctuations in the energy density with the anisotropies we observe in the CMB.

This Chapter is mainly based on [44, 46]

Contents

3.1	Cosmological Perturbation Theory	42
3.1.1	Perturbations of the FLRW metric	42
3.1.2	Matter perturbations	43
3.1.3	Fixing the gauge	44
3.1.4	Evolution and conservation equations	45
3.1.5	Setting Initial Conditions	47
3.2	Initial condition from Inflation	48
3.2.1	Primordial gravity waves	51
3.3	Inhomogeneities	52
3.3.1	Collisionless Boltzmann equation	53
3.3.2	Collision term for Thomson scattering	54
3.3.3	Photon Boltzmann equation	56
3.3.4	Neutrinos	58
3.4	CMB anisotropies	59
3.4.1	Anisotropies from inhomogeneity	60
3.4.2	Transfer function	62
3.4.3	Diffusion Damping	68
3.4.4	CMB polarization	68

3.1 Cosmological Perturbation Theory

3.1.1 Perturbations of the FLRW metric

In order to avoid unnecessary technical details, we will take the background metric to be the flat FLRW metric. The perturbed spacetime metric can then be written:

$$ds^2 = a^2(\eta) \left((1 + 2A)d\eta^2 - 2B_i dx^i d\eta - (\delta_{ij} + h_{ij})dx^i dx^j \right) \quad (3.1)$$

It will be useful to perform a scalar-vector-tensor (SVT) decomposition of the perturbations. In fact, Einstein equations for the different components do not mix at linear order and can be treated separately. Furthermore, it is worth stressing that these fluctuations are produced during inflation (as we will see briefly in Section 3.1.5) therefore inflationary dynamics sets the initial condition needed to solve the perturbation equations. However vector perturbations are not produced during inflation and even if they are, they would decay quickly with the expansion of the Universe (see e.g. [66] and reference therein). The SVT decomposition allow then to neglect vector perturbations and deal only with scalar and tensor ones.

We proceed by decomposing the degree of freedom of the perturbed metric using the SVT approach. For the vector terms, B_i , this means we can decompose it into the gradient of a scalar and a divergenceless term:

$$B_i = \partial_i B + \hat{B}_i \quad (3.2)$$

with $\partial^i \hat{B}_i = 0$. In similar fashion, a rank-2 tensor can be decomposed as:

$$h_{ij} = 2C\delta_{ij} + 2\partial_{\langle i}\partial_{j\rangle}E + 2\partial_{(i}\hat{E}_{j)} + 2\hat{E}_{ij} \quad (3.3)$$

where we have defined:

$$\partial_{\langle i}\partial_{j\rangle}E \equiv \left(\partial_i\partial_j - \frac{1}{3}\delta_{ij}\nabla^2 \right) E \quad (3.4)$$

$$\partial_{(i}\hat{E}_{j)} \equiv \frac{1}{2} \left(\partial_i\hat{E}_j + \partial_j\hat{E}_i \right) \quad (3.5)$$

As for B_i , hatted quantities are divergenceless while the tensor \hat{E}_{ij} is traceless, $\hat{E}_i^i = 0$. We need to face the fact unfortunately that metric perturbations (as well as matter perturbations, see next Section) are not uniquely defined but depends on the particular choice of the coordinate systems or “gauge choice”. Making a different choice of coordinates can change the values of the perturbation variables or it can results in introducing fictitious perturbations. In particular choosing a transformation of the form:

$$X^\mu \rightarrow X^\mu \equiv \tilde{X}^\mu + \xi^\mu(\eta, \mathbf{x}) \quad (3.6)$$

3. THE INHOMOGENEOUS UNIVERSE

where $\xi^0 \equiv T$ and $\xi^i \equiv L^i = \partial^i L + \hat{L}^i$ and we have decomposed the spatial shift L^i in its scalar and vector components, and using the equivalence of the metric element ds^2 in the two coordinate systems, one can show that the perturbation variables are transformed as:

$$A \rightarrow A - T' - \mathcal{H}T \quad (3.7)$$

$$B \rightarrow B + T - L' \quad \hat{B}_i \rightarrow \hat{B}_i - L'_i \quad (3.8)$$

$$C \rightarrow C - \mathcal{H}T - \frac{1}{3}\nabla^2 L \quad (3.9)$$

$$E \rightarrow E - L \quad \hat{E}_i \rightarrow \hat{E}_i - \hat{L}_i \quad \hat{E}_{ij} \rightarrow \hat{E}_{ij} \quad (3.10)$$

where \mathcal{H} is the Hubble parameter in conformal time and $'$ denotes derivative w.r.t. conformal time. Before looking at how the problem of choosing the gauge can be resolved we are going to see how the gauge choice affects the perturbations of the stress energy tensor.

3.1.2 Matter perturbations

We start noting that the components of the stress-energy tensor can be written as:

$$T_0^0 = \bar{\rho} + \delta\rho \quad (3.11)$$

$$T_0^i = v^i (\bar{\rho} + \bar{P}) \quad (3.12)$$

$$T_j^i = -(\bar{P} + \delta P) \delta_i^j - \Pi_j^i \quad (3.13)$$

where an over-bar denotes background quantities and v^i is the bulk velocity and Π_j^i is the transverse and traceless anisotropic stress tensor. It is useful to introduce a new quantity, the *momentum density* $q^i = v^i (\bar{\rho} + \bar{P})$. The momentum density and the anisotropic stress can be also decomposed in their scalar, vector and tensor parts as:

$$q^i = \partial_i q + \hat{q}_i \quad (3.14a)$$

$$\Pi^{ij} = \partial_{\langle i} \partial_{j \rangle} \Pi + \partial_{\langle i} \hat{\Pi}_{j \rangle} + \hat{\Pi}_{ij} \quad (3.14b)$$

Using these relations and employing the transformation rule for rank-2 tensors on T_μ^ν , one can show that under coordinate transformation of the form of Eq.(3.6) the

matter perturbations variables transform as :

$$\delta\rho \rightarrow \delta\rho - T\bar{\rho}' \quad (3.15)$$

$$\delta P \rightarrow \delta P - T\bar{P}' \quad (3.16)$$

$$q^i \rightarrow q_i + (\bar{\rho} + \bar{P})L'_i \quad (3.17)$$

$$v_i \rightarrow v_i + L'_i \quad (3.18)$$

$$\Pi_{ij} \rightarrow \Pi_{ij} \quad (3.19)$$

3.1.3 Fixing the gauge

We have seen in the previous two sections that the matter and metric perturbations are gauge dependant, a wrong choice of the coordinates system can therefore make real perturbations to disappear or fake perturbations to appear. To avoid fixing a specific gauge one can also define gauge invariant quantity through special combination of the metric perturbations, these quantities are known as *Bardeen variables*: (see *e.g.* [57, 58, 60] for a detailed discussion of gauge freedom in general relativity).

$$\Psi \equiv A + \mathcal{H}(B + E') + (B - E')' \quad (3.20a)$$

$$\Phi \equiv -C - \mathcal{H}(B - E') + \frac{1}{3}\nabla^2 E \quad (3.20b)$$

$$\Phi_i \equiv \hat{E}'_i - \hat{B}_i \quad (3.20c)$$

$$\hat{E}_{ij} \quad (3.20d)$$

where prime denotes derivatives w.r.t. conformal time and $\mathcal{H} \equiv a'/a$ is the Hubble parameter in conformal time. In this thesis, we will not use gauge invariant quantities but instead we will fix the gauge in order to make physics more evident. In what follows we will only make use of the following gauge choice:

- *Newtonian gauge*

In the Newtonian gauge we fix $\mathbf{B} = \mathbf{E} = 0$. This leads to the following perturbed metric:

$$ds^2 = a^2(\eta) \left((1 + 2\Psi) - \left[(1 - 2\Phi)\delta_{ij} + h_{ij} \right] \right) \quad (3.21)$$

where $\Psi \equiv A$ is the gravitational potential and $\Phi \equiv C$ is the local perturbations of the average scale factor and h_{ij} is the transverse and traceless tensor. For now we will study only scalar perturbations and set $h_{ij} = 0$.

3. THE INHOMOGENEOUS UNIVERSE

- *Spatially Flat gauge*

In the Spatially flat gauge we fix $C = E = 0$, we will make use of this gauge when discussing inflationary perturbations.

Before moving on, there are some few remarks that is worth making about the Newtonian gauge:

- The choice of $B = 0$ is equivalent to require that hypersurface of constant time are orthogonal to the observer worldlines at rest in the coordinates.
- Induced geometry on constant time hypersurfaces is isotropic since $E = 0$.
- In absence of anisotropic stress $\Phi \equiv \Psi$ and the metric would resemble that of the weak field limit of GR about Minkowski spacetime

3.1.4 Evolution and conservation equations

As we have seen in the previous chapter the equations of motion for the variables describing the matter-radiation component of the Universe are given by the continuity equation $\nabla_\mu T^{\mu\nu} = 0$. If there are several contributions to the stress-energy tensor then they simply add up *i.e.* $T_{\mu\nu} = \sum_a T_{\mu\nu}^{(a)}$ which implies that also the fluid variables sums up as:

$$\delta\rho = \sum_a \delta\rho_a \quad \delta P = \sum_a \delta P_a \quad q^i = \sum_a q_{(a)}^i \quad \Pi^{ij} = \sum_a \Pi^{ij} \quad (3.22)$$

If there is no momentum or energy transfer between the different species composing the stress-energy tensor then the species are separately conserved and we also have $\nabla^\mu T_{\mu\nu}^{(a)} = 0$. Using this, the perturbed conservation equations assume the form:

$$\delta'_a = - \left(1 + \frac{\bar{P}_a}{\bar{\rho}_a} \right) (\partial_i v_a^i - 3\Phi') - 3\mathcal{H} \left(\frac{\delta P_a}{\bar{\rho}_a} - \frac{\bar{P}_a}{\bar{\rho}_a} \delta_a \right) \quad (3.23a)$$

$$v_a^i = - \left(\mathcal{H} + \frac{\bar{P}'_a}{\bar{\rho}_a + \bar{P}_a} \right) v_a^i - \frac{1}{\bar{\rho}_a + \bar{P}_a} \left(\partial^i \delta P_a - \partial_j \Pi_a^{ij} \right) - \partial^i \Psi \quad (3.23b)$$

where $\delta_a = \delta\rho_a/\bar{\rho}_a$ is the density contrast. The different matter components are gravitationally coupled through the metric fluctuations, these equations are determined via the Einstein equations by the total perturbed stress-energy tensor. From the components of Einstein equations we find (for a detailed derivation see

e.g. [44, 47, 57–60]):

$$00\text{-component} \quad \nabla^2 \Phi - 3\mathcal{H}(\Phi' + \mathcal{H}\Psi) = 4\pi G a^2 \delta\rho \quad (3.24a)$$

$$ij\text{-component} \quad \nabla^2(\Phi - \Psi) = -8\pi G a^2(\bar{\rho} + \bar{P})\sigma \quad (3.24b)$$

$$0i\text{-component} \quad \Phi' + \mathcal{H}\Phi = -4\pi G a^2 q \quad (3.24c)$$

$$ij\text{-tracepart} \quad \Phi'' + 3\mathcal{H}\Phi' + (2\mathcal{H} + \mathcal{H}^2)\Phi = 4\pi G a^2 \delta P \quad (3.24d)$$

where in deriving Eq.(3.24b) we have used the decomposition of the anisotropic stress in Fourier space *i.e.* $\Pi_{ij} = -(\bar{\rho} + \bar{P}) \left(\hat{k}^i \hat{k}^j - 1/3 \delta^{ij} \right) \sigma$.

To solve the coupled system of equations made by Eqs.(3.23) and Eqs.(3.24) we need to provide initial conditions for the perturbed variables. We will see that perturbations are generated during inflation through quantum fluctuations of the inflaton, and then they are promoted to classical fluctuations during the acceleration phase when the Hubble radius shrinks and perturbations exit the horizon. We will see therefore that inflation naturally provides a mechanism to generate cosmological fluctuations and set their initial conditions. Before moving on to discuss how to properly sets initial conditions for the perturbation equations, it is worth making some few comments on the equations we have introduced in this section:

- Eqs.(3.23) are not enough to describe the evolution of the four perturbations $\{\delta_a, \delta\rho_a, \delta P_a, \Pi_a^{ij}\}$. However, perfect fluids are characterized by strong interactions which keeps the pressure isotropic then one can set $\Pi_a^{ij} = 0$. In addition pressure perturbations are related to density perturbations through the adiabatic speed of sound $c_{s,a}^2$ *i.e.* $\delta P_a = c_{s,a}^2 \delta\rho_a$. The perturbations of a perfect fluid are therefore described by only two variables δ_a and v_a and Eqs.(3.23) are sufficient to describe their evolution. Assuming also that the background equation of state is constant for all species $\bar{P}_a/\bar{\rho}_a \equiv w_a$, we can rewrite Eq.(3.23a) as:

$$\delta'_a = -(1 + w_a)(\partial_i v_a^i - 3\Phi') - 3\mathcal{H}\delta_a(c_{s,a}^2 - w_a) \quad (3.25)$$

We note however that decoupled or weakly-interacting species such as neutrinos cannot be described by a perfect fluid and the above assumptions do not apply. In this case one need to solve the Boltzmann equation. We will return on this when describing CMB anisotropies and spectra at the end of the Chapter.

- Eq.(3.24a) is the relativistic generalization of the *Poisson equation*. Inside the Hubble radius the Fourier mode of the perturbations satisfy $k \gg \mathcal{H}$ therefore

3. THE INHOMOGENEOUS UNIVERSE

$\nabla^2\Phi$ dominates the r.h.s of Eq.(3.24a) and we return to the classical Poisson equation for the gravitational potential Φ *i.e.* $\nabla^2\Phi \approx 4\pi G a^2 \delta\rho$. Relativistic corrections will be therefore important only for scales comparable to the Hubble radius *i.e.* $k \lesssim \mathcal{H}$

- Eq.(3.24b) is sourced by the reduced anisotropic stress tensor σ but for perfect fluids $\sigma = 0$ therefore $\Psi \approx \Phi$. This is indeed a well motivated assumption. Baryons and dark matter can be described as a perfect fluids so they do not contribute to the anisotropic stress. Photons start to develop an anisotropic stress only during the matter dominance when their contribution to the total energy density can be ignored. The only exception is represented by free-streaming neutrinos which cannot be described by a perfect fluid, however their effect is also relatively small and we will neglect it.

3.1.5 Setting Initial Conditions

At sufficient early time ($\eta \rightarrow 0$) all scales of interest for observations were outside the horizon. We will see in next Section that inflation sets up the initial condition for the Newtonian potential Φ on super-horizon scales, then the super-horizon limit ($k \ll \mathcal{H}$) of Eq.(3.24a) can be used to infer the initial condition for the density contrast δ .

ADIABATIC PERTURBATIONS

In the rest of this thesis, we will only consider adiabatic initial conditions since this assumption is consistent with current data and in single field slow-roll inflation this are the only kind of perturbations that can be excited. This initial condition satisfies:

$$I_{ij} \equiv \frac{\delta_i}{1+w_i} - \frac{\delta_j}{1+w_j} = 0 \quad \forall i, j \quad (3.26)$$

thus for adiabatic perturbations, all matter component have the same fractional density since $w_m = 0$. Radiation perturbations instead follow,

$$\delta_r = \frac{4}{3}\delta_m \quad (3.27)$$

since $w = 1/3$ for relativistic species. This means that the total energy density $\delta\rho = \sum_a \delta\rho_a \delta_a$ is dominated by the species that carries the dominant energy contribution. At early times the Universe is radiation dominated so that the fractional density is that of radiation δ_r . We see from Eq.(3.24d) that on super-horizon scale $\Phi \approx \text{const}$ and Eq.(3.24a) implies:

$$\delta \approx \delta_r = -2\Phi = \text{const} \quad (3.28)$$

Therefore, all matter perturbations are given in terms of the super-Hubble value of the potential Φ .

However the gravitational potential Φ is constant on super horizon scales only if the equation of state of the background is constant. When the equation of state evolves, *e.g.* in the transition from radiation to matter dominance, also the potential evolves. Therefore it is convenient to define a quantity that remains constant on large scales even when the equation of state changes. This variable is the so-called *comoving curvature perturbation*:

$$\mathcal{R} = -\Phi + \frac{\mathcal{H}}{\bar{\rho} + \bar{P}} \delta q \quad (3.29)$$

The quantity \mathcal{R} has also another advantage: it is gauge invariant *i.e.* it does not change under a coordinate transformation (see *e.g.* [44, 57]). In the next section we will see how inflation predicts the value of the curvature perturbation at the onset of the radiation dominated phase.

3.2 Initial condition from Inflation

We have seen in Section 1.5 how inflation can resolve the problems of Hot Big Bang scenario and bring the singularity back to infinite past $\eta \rightarrow -\infty$. In this Section we will see how inflation provides a natural mechanism to seed the fluctuations of the CMB and sets the initial conditions for the evolution of perturbations in the radiation and matter dominated phase. The mechanism behind the generation of perturbations during inflation is rather simple: the evolution of the inflaton field $\phi(t)$ governs the total energy density $\rho(t)$ and hence controls when inflation ends. Essentially, the inflation acts as a local “clock” reading off the amount of inflationary expansion still to occur. In quantum mechanics precise timing is not possible because of the uncertainties principle *i.e.* quantum-mechanical clocks always have some variance. This translate into having spatially varying fluctuations of the inflaton $\delta\phi(t, \mathbf{x})$. Hence, at the end of inflation there will be local differences in time $\delta t(\mathbf{x})$. These differences in the local expansion histories lead to a differences in the local densities after inflation $\delta\rho(t, \mathbf{x})$ and to curvature perturbations $\mathcal{R}(\mathbf{x})$. In the following we will give a brief review of the calculation that allows to connect the variance of the inflaton with that of the curvature perturbation, for a more detailed derivation we refer to [44, 47]

In the spatially flat gauge ($g_{ij} = -a^2\delta_{ij}$) the inflationary action is:

$$S = \int d^3\eta d^3x \sqrt{-g} \left[\frac{1}{2} g^{\mu\nu} \partial_\mu \phi \partial_\nu \phi - V(\phi) \right] \quad (3.30)$$

in this gauge the information are carried by the inflaton perturbation $\delta\phi$ and the metric perturbations $\delta g_{0\mu}$ and the two quantities are related by Einstein equations.

3. THE INHOMOGENEOUS UNIVERSE

Furthermore in the spatially flat gauge $\delta g_{0\mu}$ are suppressed w.r.t. inflaton fluctuations by a factor of the order of the slow-roll parameter ϵ_H . At leading order we can then ignore fluctuations of the geometry and perturb the scalar field independently.

Evaluating Eq.(3.30) on an unperturbed FLRW background we find:

$$S = \int d^3\eta d^3x \left[\frac{1}{2}a^2 \left(\phi'^2 - (\nabla\phi)^2 \right) - a^4 V(\phi) \right] \quad (3.31)$$

We expand the inflaton as $\phi(\eta, \mathbf{x}) = \bar{\phi}(\eta) + a^{-1}F(\eta, \mathbf{x})$ and we look for the linearized equations for $F(\eta, \mathbf{x})$. To do this we expand the action Eq.(3.31) to second order in F , *i.e.*

$$S_{(2)} = \int d^3\eta d^3x \frac{1}{2} \left[(F'^2 - (\nabla F)^2) - \frac{a''}{a} F^2 \right] \quad (3.32)$$

which implies the following equation of motion:

$$F_k'' + (k^2 - \frac{a''}{a})F_k = 0 \quad F_k(\eta) \equiv \int \frac{d^3\mathbf{x}}{(2\pi)^{3/2}} F(\eta, \mathbf{x}) e^{-ik \cdot \mathbf{x}} \quad (3.33)$$

In a quasi-deSitter background $a''/a \approx 2/\eta^2$ and we have:

$$F_k'' + (k^2 - \frac{2}{\eta^2})F_k = 0 \quad (3.34)$$

At sufficient early times all modes where inside the horizon, $|k\eta| \gg 1$, in this limit Eq.(3.34) reduces to:

$$F_k'' + k^2 F_k = 0 \quad (3.35)$$

During inflation the Hubble radius shrinks and eventually a mode of given k crosses the horizon when $|k\eta| \sim 1$. At this moment we one can switch to a description in terms of the comoving curvature perturbation \mathcal{R} which become constant outside the horizon $|k\eta| \ll 1$. The variance of \mathcal{R} at horizon crossing will then become the initial condition of perturbations in the post-inflationary FLRW Universe.

We start noting that Eq.(3.35) is just the equation for a simple harmonic oscillator, therefore it has two independent solution $F_k \propto e^{\pm ik\eta}$. We are interested only to the $-$ solution which corresponds to the ground state of the Hamiltonian of the oscillator [47]. In practice this mean solving Eq.(3.34) with the initial condition:

$$\lim_{\eta \rightarrow \infty} F_k(\eta) = \frac{1}{\sqrt{2k}} e^{-ik\eta} \quad (3.36)$$

Assuming a slow-roll inflation, it is sufficient to study the solutions of Eq.(3.34) in a deSitter spacetime which read:

$$F_k(\eta) = \frac{e^{-ik\eta}}{\sqrt{2k}} \left(1 - \frac{i}{k\eta} \right) \quad (3.37)$$

where we have made use of the initial condition, Eq.(3.36), to get rid of the solution $\propto e^{ik\eta}$.

Finally we evaluate the variance of the mode function F_k , to determine the perturbations of the scalar field. This is done by promoting the function F to a quantum operator \hat{F} and evaluating its variance over the ground state of the harmonic oscillator. After some manipulation one finds:

$$\langle |\hat{F}|^2 \rangle = \int d \ln k \frac{k^3}{2\pi^2} |F_k(\eta)|^2 \quad (3.38)$$

We are now going to connect this solution with the curvature perturbation \mathcal{R} . First of all we define the dimensionless *power spectrum* as:

$$\Delta_F^2(k, \eta) \equiv \frac{k^3}{2\pi^2} |F_k(\eta)|^2 \quad (3.39)$$

Using Eq.(3.37) we have:

$$\Delta_{\delta\phi}^2(k, \eta) = a^{-2} \Delta_F^2(k, \eta) = \left(\frac{H}{2\pi} \right)^2 \left(1 + \left(\frac{k}{aH} \right)^2 \right) \quad (3.40)$$

At horizon crossing this is simply:

$$\Delta_{\delta\phi}^2(k, \eta) = \frac{H^2}{2\pi} \Big|_{k=aH} \quad (3.41)$$

We are now in place to connect the fluctuations of the inflaton with the curvature perturbation. Recall from Eq.(3.29) that

$$\mathcal{R} = -\Phi + \frac{H}{\bar{\rho} + \bar{P}} \delta q \quad (3.42)$$

As discussed we neglect the spatial variation of the metric w.r.t. the fluctuation of the inflaton therefore $\Phi = 0$. The perturbed stress-energy tensor is instead:

$$\delta T_j^0 = g^{0\mu} \partial_\mu \phi \partial_j \delta \phi = \frac{\bar{\phi}'}{a^2} \partial_j \delta \phi = -\partial_j \delta q \quad (3.43)$$

Using $\bar{\rho} + \bar{P} = a^{-2} \bar{\phi}'^2$, we have:

$$\mathcal{R} = \frac{\mathcal{H}}{\bar{\phi}'} \delta \phi = -H \frac{\delta \phi}{\bar{\phi}} = -H \delta t \quad (3.44)$$

confirming our assumption that the curvature perturbation is induced by the time shift at the end of inflation. The power spectrum of \mathcal{R} at horizon crossing is then easily found to be:

$$\Delta_{\mathcal{R}}^2(k) = \frac{H^2}{2\pi \bar{\phi}} \Big|_{k=aH} = \frac{1}{8\pi^2 \epsilon_H} \frac{H^2}{M_{pl}^2} \Big|_{k=aH} \quad (3.45)$$

3. THE INHOMOGENEOUS UNIVERSE

The form of the spectrum is generally approximated with a power law of the form:

$$\Delta_{\mathcal{R}}^2(k) = A_s \left(\frac{k}{k_s} \right)^{n_s-1} \quad (3.46)$$

where the spectral index n_s is connected to the slow-roll parameters by the following relation:

$$n_s - 1 = -2\epsilon_H - \eta_H \quad (3.47)$$

The most recent observation have placed a very tight constraint on the value of the scalar spectral index showing a percent-level deviation from a scale invariant spectrum ($n_s = 1$) *i.e.* $n_s = 0.965 \pm 0.004$ [28]. This is indeed a strong confirmation of the time dependence in the inflationary dynamics and of the quantum nature of primordial fluctuations.

3.2.1 Primordial gravity waves

In this Section we are going to sketch the logic (identical to that of the scalar case) behind the evolution of tensor perturbations during inflation but we will not go through the details of the quantum production of tensor fluctuations (more details on the production of gravity waves during inflation can be found in [44, 47]).

We start by the spatial metric for tensor perturbations:

$$ds^2 = a^2(\eta)[d\eta^2 - (\delta_{ij} + 2h_{ij})dx^i dx^j] \quad (3.48)$$

Substituting this in the Einstein-Hilbert action and expanding to second order gives:

$$S_{(2)} = \frac{M_{pl}^2}{8} \int d\eta d^3x a^2 [h'_{ij} - (\nabla h_{ij})^2] \quad (3.49)$$

it is convenient to divide the degree of freedom in the metric (the polarization of the gravitational waves) using:

$$\frac{M_{pl}}{2} a h_{ij} \equiv \frac{1}{\sqrt{2}} \begin{pmatrix} f_+ & f_\times & 0 \\ f_\times & -f_+ & 0 \\ 0 & 0 & 0 \end{pmatrix} \quad (3.50)$$

so that the perturbed action rewrites:

$$S_{(2)} = \frac{M_{pl}^2}{8} \int d\eta d^3x \left[f_\lambda'^2 - (\nabla f_\lambda)^2 + \frac{a''}{a} f_\lambda^2 \right] \quad (3.51)$$

This is are just two copies of the action in Eq.(3.32), one for each polarization mode of the gravitational wave, $f_{\times,+}$. The power spectrum for tensor modes can

therefore be directly inferred from the results for scalar perturbations,

$$\Delta_h^2(k, \eta) = 2 \times \left(\frac{2}{aM_{pl}} \right)^2 \Delta_F^2(k, \eta) \quad (3.52)$$

which at horizon crossing reads:

$$\Delta_h(k, \eta)^2 = \frac{2}{\pi^2} \frac{H^2}{M_{pl}^2} \Big|_{k=aH} \quad (3.53)$$

We notice that the tensor amplitude, conversely to the scalar one, depends only on H and it is therefore a direct measure of the expansion rate during inflation. The form of the tensor power spectrum is also commonly approximated as a power law,

$$\Delta_h^2(k) = A_t \left(\frac{k}{k_t} \right)^{n_t} \quad (3.54)$$

where the spectral index is given by $n_t = -2\epsilon_H$. Generally the tensor amplitude is given in terms of the scalar amplitude A_s at the tensor pivot scale k_t defining the so called *tensor-to-scalar ratio*:

$$r \equiv \frac{\Delta_{\mathcal{R}}^2(k_t)}{\Delta_h^2(k_t)} \quad (3.55)$$

It is commonly assumed that the pivot scale of tensor and scalar is the same *i.e.* $k_s = k_t$ so that r is defined independently of the scalar spectral index and pivot scale:

$$r = \frac{A_s}{A_t} = 16\epsilon_H \quad (3.56)$$

The most recent constraint on the value of r , achieved combining Planck, BICEP2 and BAO data gives only an upper limit $r < 0.07$ [28, 32]. More stringent constraints on r require the measurement of polarization B-modes which are a direct trace of quantum fluctuations of the metric produced during inflation (see Section 3.4.4. Measuring polarization B-modes is indeed one of the main goal of future experiments such as CMB-S4 [33] and LiteBIRD [29])

3.3 Inhomogeneities

Metric perturbations couple gravitationally to all matter perturbations at early times when the Universe is filled with a plasma made of photons, baryons and electrons. Baryons and electrons are in turn coupled to each other via Coulomb scattering while electrons and photons interact via Thomson scattering. When electron density drops at recombination, Thomson scattering become inefficient

3. THE INHOMOGENEOUS UNIVERSE

and photons decouple from the primordial plasma and start to stream freely. In turn Coulomb scattering efficiency is not affected and electrons and baryons can be treated as a single tightly coupled fluid. To derive the fluctuations in the CMB, we need to follow the complicated set of interactions between all matter components until recombination. To do this we will need to employ the *Boltzmann equation*.

$$\frac{df_a}{d\eta} = \frac{\partial f_a}{\partial \eta} + \frac{\partial f_a}{\partial \mathbf{x}} \cdot \frac{\partial \mathbf{x}}{\partial \eta} + \frac{\partial f_a}{\partial \ln \epsilon} \frac{d \ln \epsilon}{d\eta} + \frac{\partial f_a}{\partial \hat{\mathbf{p}}} \cdot \frac{d\hat{\mathbf{p}}}{d\eta} = C[\{f_b\}] \quad (3.57)$$

where $\epsilon = a(t)E$ is the *comoving energy* and $\hat{\mathbf{p}}$ is direction of propagation of photons. For each species a then there will be an evolution equation for the species distribution function f_a coupled to the distribution function of the other species b through the collision term $C[\{f_b\}]$. Since we are interested in the evolution of the distribution function for photons only f_γ we will drop the subscript and refer to it simply as f . Photons interacts mainly with electrons therefore the collision term will depend only on the photon and electron distribution function *i.e.* $C[\{f, f_e\}]$.

3.3.1 Collisionless Boltzmann equation

We will start by studying the l.h.s. of Eq.(3.57) and for the moment we will set the collision term to zero. This leads to:

$$\frac{d}{d\eta} f(\eta, E, \mathbf{x}, \hat{\mathbf{p}}) = 0 \quad (3.58)$$

which states that, in absence of scattering, the number of particles in a given element phase space does not change with time. We note that the last term in Eq.(3.57) is a second order term: in fact the Bose-Einstein distribution depends only on photon momentum \mathbf{p} and not on the direction of propagation $\hat{\mathbf{p}}$ therefore $\partial f / \partial \hat{\mathbf{p}}$ is non-zero only at first order and the same is true for $\partial \hat{\mathbf{p}} / d\eta$ which is non-zero only if there are perturbations to the gravitational potential. Thus the last term is the product of two first order terms and can be neglected at linear order. With a similar argument one can show that also $\partial f / \partial \mathbf{x}$ and $\partial \ln \epsilon / \partial \eta$ are first order terms, therefore we can write Eq.(3.58) as:

$$\frac{\partial f}{\partial \eta} + \hat{\mathbf{p}} \cdot \nabla f + \frac{\partial \bar{f}}{\partial \ln \epsilon} \frac{d \ln \epsilon}{d\eta} = 0 \quad (3.59)$$

where we have used $d\mathbf{x}/d\eta = \hat{\mathbf{p}}$ and \bar{f} is zero-order distribution function. At order zero this implies that $\partial \bar{f} / \partial \eta = 0$ and therefore the zero-order distribution function depends only on ϵ , this is consistent with Eq.(2.9) as long as $T \propto a^{-1}$,

$$\bar{f}(\epsilon) \propto \left[\exp \left(\frac{\epsilon}{T_0} \right) - 1 \right]^{-1} \quad (3.60)$$

where $T_0 = 2.7255\text{K}$ is the present CMB temperature. To study the effect of perturbations we introduce the fractional temperature perturbation $\Theta(\eta, \mathbf{x}, \hat{\mathbf{p}})$ which we assume to be independent from ϵ *i.e.* the temperature perturbations is the same at all frequencies and does not lead to spectral distortion. The perturbed distribution function is rewritten as:

$$f(\eta, \mathbf{x}, \epsilon, \hat{\mathbf{p}}) = \left[\exp \left(\frac{\epsilon}{a\bar{T}(\eta)[1 + \Theta(\eta, \mathbf{x}, \hat{\mathbf{p}})]} \right) - 1 \right]^{-1} \quad (3.61)$$

Assuming Θ to be a small perturbation we can rewrite Eq.(3.59) as:

$$-\frac{d\ln \bar{f}(\epsilon)}{d\ln \epsilon} \left(\frac{d\Theta}{d\eta} - \frac{d\ln \epsilon}{d\eta} \right) = 0 \quad (3.62)$$

In the absence of collisions, the evolution of the temperature perturbations is therefore directly related to the evolution of the comoving photon energy which is described by the geodesic equation. Recalling that for photons $g_{\mu\nu}P^\mu P^\nu = 0$, in the Newtonian gauge we have:

$$P^\mu = \frac{\epsilon}{a^2} [1 - \Psi, (1 + \Phi)\hat{\mathbf{p}}] \quad (3.63)$$

Using Eq.(1.4) and $d\eta/d\lambda = \epsilon/a^2(1 - \Psi)$, the geodesic equation can be rewritten in conformal time as:

$$(1 - \Psi)\frac{\epsilon}{a^2}\frac{dP^\mu}{d\eta} + \Gamma_{\nu\rho}^\mu P^\nu P^\rho = 0 \quad (3.64)$$

The 00-component of this equation is then:

$$\frac{d\ln \epsilon}{d\eta} = -\frac{d\Psi}{d\eta} + (\dot{\Psi} + \dot{\Phi}) \quad (3.65)$$

the photon energy evolves along the geodesic in presence of metric perturbations due to variation of Ψ along the path and by the evolution of the potentials. As expected, in absence of perturbations photon energy is conserved.

3.3.2 Collision term for Thomson scattering

The dominant scattering effect close to recombination is the Thomson scattering of the photons off the free electrons in the plasma. This is the only scattering process we need to take into account to calculate the r.h.s of Eq.(3.57)

Let us start in the rest frame of a single electron. In this frame, an incoming photon has energy ϵ'_{in} and 3-momentum $\mathbf{p}'_{in} = \epsilon'_{in}\hat{\mathbf{p}}_{in}$. Since Thomson scattering is an elastic process it does not change the photon energy so that the scattered photon has energy ϵ'_{in} and 3-momentum $\mathbf{p}' = \epsilon'_{in}\hat{\mathbf{p}}'$. The *differential cross-section*

3. THE INHOMOGENEOUS UNIVERSE

for Thomson scattering of unpolarized radiation (*i.e.* the rate at which electrons scatter photons per solid angle, per unit incident photon flux) is:

$$\frac{d\sigma}{d\Omega} = \frac{\sigma_T}{4\pi} \quad (3.66)$$

where σ_T is the Thomson cross section. Now, we can write the scattering rate with respect to the proper time τ' in the electron rest-frame:

$$\begin{aligned} C[f'(\epsilon', \hat{p}')] &\equiv \frac{df'}{d\tau'} = n_e \int d\hat{p}'_{in} \frac{d\sigma_T}{d\Omega} [f'(\epsilon', \hat{p}'_{in}) - f'(\epsilon', \hat{p}')] \\ &= n_e \sigma_T \left(-f'(\epsilon', \hat{p}') + \int \frac{d\hat{p}'_{in}}{4\pi} f'(\epsilon', \hat{p}'_{in}) \right) \end{aligned} \quad (3.67)$$

the first term in the integral account for incoming photon ($\hat{p}'_{in} \rightarrow \hat{p}'$) while the second describes outgoing photon ($\hat{p}' \rightarrow \hat{p}'_{in}$) and we see that the collision term vanish for isotropic radiation ($\hat{p}'_{in} = \hat{p}'$) confirming that the collision term arises only at linear order.

Now, we need to return to the background frame in which the electron is not at rest. This accounts for the bulk velocity of electrons \mathbf{v}_e . To obtain the distribution in this frame we need to perform a Lorentz boost of the distribution in the rest frame. First we note that, at zeroth order the proper time is the same in both frame. Then, using the Lorentz invariance of the distribution function ($f'(\epsilon', \hat{p}') = f(\epsilon, \hat{p})$), the scattering rate in the boosted frame is, up to second order terms:

$$C[f(\epsilon, \hat{p})] \equiv \frac{df(\epsilon, \hat{p})}{d\eta} = a \frac{df'(\epsilon', \hat{p}')}{d\tau} = a C'[f'(\epsilon', \hat{p}')] \quad (3.68)$$

Substituting Eq.(3.67) we get:

$$C[f(\epsilon, \hat{p})] = -\Gamma \left(f'(\epsilon', \hat{p}') + \int \frac{d\hat{p}'_{in}}{4\pi} f'(\epsilon', \hat{p}'_{in}) \right) \quad (3.69)$$

In the boosted frame, the photon energy is not conserved in the scattering due to the motion of the electron *i.e.* $\epsilon \neq \epsilon_{in}$. Infact a Lorentz transformation of the energy and of the distribution function gives:

$$\epsilon' = \gamma \epsilon (1 - \hat{p} \cdot \mathbf{v}_e) \quad (3.70)$$

$$\epsilon_{in} = \gamma \epsilon (1 - (\hat{p} - \hat{p}'_{in}) \cdot \mathbf{v}_e) \quad (3.71)$$

$$f'(\epsilon', \hat{p}') = f(\epsilon, \hat{p}) = \bar{f}(\epsilon) - \frac{d\bar{f}}{d\ln \epsilon} (\hat{p} - \hat{p}'_{in}) \cdot \mathbf{v}_e - \frac{df}{d\ln \epsilon} \Theta(\hat{p}_{in}) \quad (3.72)$$

Let us further discuss the terms of Eq.(3.72). The first term $\bar{f}(\epsilon)$ cancel out the contribution of the zeroth order term of $f(\epsilon, \hat{p}) \approx \bar{f}(\epsilon) + (d\bar{f}(\epsilon)/d\ln \epsilon)\Theta(\hat{p})$. The contribution of $\hat{p}'_{in} \cdot \mathbf{v}_e$ integrates to zero by parity. With these considerations, we can put all these into Eq.(3.67) to obtain:

$$C[f] = \Gamma \frac{d\bar{f}}{d\ln \epsilon} [\Theta(\hat{p}) - \Theta_0 - \hat{p} \cdot \mathbf{v}_e] \quad (3.73)$$

where $\Gamma = an_e\sigma_T$ and we have defined the *monopole* of the temperature anisotropy:

$$\Theta_0 = \frac{1}{4\pi} \int d\hat{p}_{in} \Theta(\hat{p}_{in}) \quad (3.74)$$

We conclude this part noting that in the Thomson cross section we have implicitly averaged over a polarization term. The more correct form of σ_T would be:

$$\frac{d\sigma}{d\Omega} = \frac{3\sigma_T}{16\pi} [1 + (\hat{p}'_{in} - \hat{p}')^2] \quad (3.75)$$

and the collision term will assume the form

$$C[f] = \Gamma \frac{d\bar{f}}{d\ln \epsilon} \left[\Theta(\hat{p}) - \hat{p} \cdot \mathbf{v}_e - \frac{3}{16\pi} \int d\hat{p}_{in} \Theta(\hat{p}_{in}) [1 + (\hat{p}_{in} - \hat{p})^2] \right] \quad (3.76)$$

The contribution from polarization is around the 1% in the collision term, however the dependence on polarization means that at a small level the CMB will be polarized due to Compton scattering. Interestingly the information carried by polarization is as valuable as that of the temperature spectrum. We will return on the polarization at the end of the next Section.

3.3.3 Photon Boltzmann equation

We obtain the Boltzmann equation for photons putting together Eq.(3.76) and Eq.(3.62):

$$\frac{d\Theta}{d\eta} = \frac{d\ln \epsilon}{d\eta} - \Gamma [\Theta - \Theta_0 - \hat{p} \cdot \mathbf{v}_e] \quad (3.77)$$

At early times the Thomson scattering was still efficient and electrons were tightly coupled to photons ($\Gamma \gg \mathcal{H}$). As we discussed previously scattering tends to make the photon distribution isotropic in the electron rest frame. In a general frame then the distribution has only a monopole and a dipole $\Theta \rightarrow \Theta_0 + \hat{p} \cdot \mathbf{v}_e$. Using Eq.(3.65) the Boltzmann equation becomes:

$$\Theta' + \hat{p}^i \partial_i \Theta = \Phi' - \hat{p}^i \partial_i \Psi - \Gamma [\Theta - \Theta_0 - \hat{p} \cdot \mathbf{v}_e] \quad (3.78)$$

It is now convenient to transform this equation into the Fourier space. We define the Fourier transform of a generic function $F(\eta, \mathbf{x})$ and the inverse transformation

3. THE INHOMOGENEOUS UNIVERSE

as:

$$F(\eta, \mathbf{k}) \equiv \int \frac{d^3x}{(2\pi)^{3/2}} F(\eta, \mathbf{x}) e^{-i\mathbf{k}\cdot\mathbf{x}} \quad F(\eta, \mathbf{x}) \equiv \int \frac{d^3k}{(2\pi)^{3/2}} F(\eta, \mathbf{k}) e^{i\mathbf{k}\cdot\mathbf{x}} \quad (3.79)$$

and Eq.(3.78) reads:

$$\Theta' + ik\mu\Theta = \Phi' - ik\mu\Psi - \Gamma[\Theta - \Theta_0 - i\mu v_e] \quad (3.80)$$

where $v_e \equiv iv_e \hat{\mathbf{k}}$ and $\mu \equiv \hat{\mathbf{k}} \cdot \hat{\mathbf{p}}$. It is worth stressing that due to the statistical isotropy of the Thomson scattering the evolution of the temperature fluctuations does not depends explicitly on $\hat{\mathbf{k}}$ and $\hat{\mathbf{p}}$ but only on their relative orientation μ . Furthermore, since for scalar fluctuations the perturbation from a single Fourier mode are axisymmetric it is convenient to expand the Fourier modes in terms of the Legendre polynomials, *i.e.*

$$\Theta(\eta, \hat{\mathbf{k}}, \hat{\mathbf{p}}) \equiv \sum_{\ell=0}^{\infty} (-i)^{\ell} \Theta_{\ell}(\eta, \hat{\mathbf{k}}) P_{\ell}(\mu) \quad (3.81)$$

The multipole expansion is really convenient in the tight-coupling limit since all moments $\ell \geq 2$ are suppressed. The evolution equation for the $\Theta_{\ell \geq 2}$ is obtained multiplying Eq.(3.80) by the Legendre polynomials $P_{\ell \geq 2}$ and integrating over μ . The remaining terms lead to the following equation:

$$\Theta' + k \left(\frac{\ell+1}{2\ell+3} \Theta_{\ell+1} - \frac{\ell}{2\ell-2} \Theta_{\ell-1} \right) = -\Gamma \Theta_{\ell} \quad (3.82)$$

which is an infinite hierarchy of coupled equation since each moment Θ_{ℓ} is coupled to the adjacent moments $\Theta_{\ell \pm 1}$. In the tight coupling limit ($\Gamma \gg k \geq \mathcal{H}$) it implies:

$$\Theta_{\ell} \sim \frac{k}{\Gamma} \Theta_{\ell-1} \ll \Theta_{\ell-1} \quad (3.83)$$

showing that moments with $\ell \geq 2$ are suppressed. We can derive the evolution equations for the monopole and the dipole as we have done for the higher order moments, this leads to:

$$\Theta'_0 = -\frac{k\Theta_1}{3} + \Phi' \quad (3.84a)$$

$$\Theta'_1 = k\Theta_0 - k\Phi - \Gamma(\Theta_1 - v_e) \quad (3.84b)$$

The monopole and the dipole are also related to the 00- and $i0$ - component of the perturbed stress-energy tensor for the photons in a simple way [44]:

$$\Theta_0 = \frac{\delta_{\gamma}}{4} \quad \Theta_1 = -v_{\gamma} \quad (3.85)$$

Using this relation, we can recast the evolution equation for the monopole and the dipole in a more familiar way:

$$\delta'_\gamma + \frac{4}{3} (\nabla \cdot \mathbf{v}_\gamma - 3\Phi') = 0 \quad (3.86)$$

$$\mathbf{v}'_\gamma + \frac{1}{4} \nabla \delta_\gamma + \nabla \Psi = -\Gamma(\mathbf{v}_\gamma - \mathbf{v}_e) \quad (3.87)$$

which are Eqs.(3.23) in the epoch of radiation domination with the addition of an interaction term. We notice that the first equation is the standard continuity equation for δ_γ which holds still since there is no energy exchange at linear order from Thomson scattering. The Euler equation instead receive a corrections due to exchange of momentum between photons and electrons caused by the scattering.

3.3.4 Neutrinos

We can trivially extended what we have found for Θ_0 and Θ_1 to derive the equation describing neutrino fluctuations. Neutrinos decouple from the rest of the plasma well before recombination, so they are described by the collisionless Boltzmann equation, *i.e.* by Eqs.(3.84) without the collision term. Defining the neutrino temperature fluctuation as \mathcal{N} we have:

$$\mathcal{N}'_0 = -\frac{k\mathcal{N}_1}{3} + \Phi' \quad (3.88a)$$

$$\mathcal{N}'_1 = k\mathcal{N}_0 - k\Phi \quad (3.88b)$$

where we have used the fact that the density contrast of neutrino is $\delta_v = 4\mathcal{N}_0$. When including neutrinos the equation for the evolution of the potential, Eqs(3.24a - 3.24b), assume the form:

$$\nabla^2 \Phi - 3\mathcal{H}(\Phi' + \mathcal{H}\Psi) = 4\pi G a^2 [\bar{\rho}_c \delta_c + \bar{\rho}_b \delta_b + 4\bar{\rho}_\gamma \Theta_0 + 4\bar{\rho}_v \mathcal{N}_0] \quad (3.89)$$

$$\nabla^2 (\Phi - \Psi) = -8\pi G a^2 (\bar{\rho}_\gamma \Theta_2 + \bar{\rho}_v \mathcal{N}_2) \quad (3.90)$$

where in the first equation we have explicitly written the contribution to the perturbed matter density $\rho_m \delta_m = \bar{\rho}_c \delta_c + \bar{\rho}_b \delta_b$ (accounting for cold dark matter and baryons respectively) and to the perturbed radiation density $\rho_r \delta_r = 4\bar{\rho}_\gamma \Theta_0 + 4\bar{\rho}_v \mathcal{N}_0$ (accounting for photons and neutrinos respectively). In Eq.(3.90) instead we have made use of the conservation equation for the stress-energy tensors spatial component (T^i_j) to relate the anisotropic stress σ to the quadrupole moments of neutrinos and photons perturbations which yields $\sigma_v = -3/5\mathcal{N}_2$ and $\sigma_\gamma = -3/5\Theta_2$. From Eq.(3.90) we see that the two potentials Φ and Ψ are equal and opposite unless neutrinos or photons have a non-negligible quadrupole moment. As we have discussed

3. THE INHOMOGENEOUS UNIVERSE

above, in the tight coupling limit photon quadrupole moment is suppressed however neutrinos are purely free-streaming and can therefore have a non-negligible quadrupole moment. In the next section we will see that the tight coupling limit approximation breaks for scale smaller than the photons mean free paths leading to the damping of perturbations at these scales.

3.4 CMB anisotropies

What we see in the sky as the CMB (Fig1.2) is a map of the cosmic microwave background which describe the variation of the CMB temperature as a function of the direction of photon propagation, $\hat{\mathbf{p}}$. However the temperature fluctuations are defined at every point in space and time, $\Theta(\eta, \mathbf{x}, \hat{\mathbf{p}})$, this mean that our only handle on the anisotropies is their dependence from the direction of the incoming photon $\hat{\mathbf{p}}$. The reason is that we only see a representation of the CMB map at fixed point in space ($x = x_0$) and time ($\eta = \eta_0$). Furthermore CMB maps are given in terms of the projection of $\hat{\mathbf{p}}$ in the sky *i.e.* in polar coordinates θ, ϕ .

To relate the anisotropies in the CMB with the fluctuations in the photon-baryon fluid we need therefore to expand the temperature fluctuations field in spherical harmonics, *i.e.*

$$\begin{aligned}\Theta(\eta, \hat{\mathbf{k}}, \hat{\mathbf{p}}) &= \sum_{\ell=1}^{\infty} \sum_{m=-\ell}^{\ell} a_{\ell m}(\eta, \hat{\mathbf{k}}) Y_{\ell m}(\hat{\mathbf{p}}) \\ &= \sum_{\ell=1}^{\infty} (-i)^{\ell} \Theta_{\ell}(\eta, \hat{\mathbf{k}}) P_{\ell}(\hat{\mathbf{k}} \cdot \hat{\mathbf{p}})\end{aligned}\quad (3.91)$$

where we have made use of the relation between spherical harmonics and Legendre polynomial,

$$P_{\ell}(\mathbf{a} \cdot \mathbf{b}) = \frac{4\pi}{2\ell + 1} \sum_{m=-\ell}^{\ell} Y_{\ell m}(\mathbf{b}) Y_{\ell m}^{\star}(\mathbf{a}) \quad (3.92)$$

and defined the $a_{\ell m}$ in terms of Θ_{ℓ} as:

$$a_{\ell m}(\eta, \hat{\mathbf{k}}) = (-i)^{\ell} \frac{4\pi}{2\ell + 1} \Theta_{\ell}(\eta, \hat{\mathbf{k}}) Y_{\ell m}^{\star}(\hat{\mathbf{k}}) \quad (3.93)$$

to make the relation with the moment of the temperature fluctuation manifest. With these relation the temperature map can be written as,

$$\begin{aligned}\Theta(\hat{\mathbf{p}}) &\equiv \frac{\delta T}{T}(\hat{\mathbf{p}}) = \Theta(\eta_0, x_0, \hat{\mathbf{p}}) \\ &= \int \frac{d^3 k}{(2\pi)^{3/2}} e^{i\hat{\mathbf{k}} \cdot \mathbf{x}_0} \sum_{\ell} (-)^{\ell} \Theta_{\ell}(k) \mathcal{R}(\hat{\mathbf{k}}) P_{\ell}(\hat{\mathbf{k}} \cdot \hat{\mathbf{p}})\end{aligned}\quad (3.94)$$

where \mathcal{R} is the comoving curvature perturbation and we have defined the transfer function $\Theta_\ell(k) \equiv \Theta_\ell(\eta_0, \hat{\mathbf{k}})/\mathcal{R}(\mathbf{k})$.

The background and homogeneity of the Universe require that the angular average of the $a_{\ell m}$ is zero but they have a non-zero variance. This variance is called C_ℓ and it is defined as:

$$\langle a_{\ell m} a_{\ell', m'}^* \rangle = \delta_{\ell\ell'} \delta_{mm'} C_\ell \quad (3.95)$$

Using the relation between $a_{\ell m}$ and Θ_ℓ , the C_ℓ coefficients can be related to the temperature fluctuation field *i.e.*

$$\langle \Theta(\hat{\mathbf{p}}) \Theta(\hat{\mathbf{p}}') \rangle = \sum_\ell \frac{2\ell + 1}{4\pi} C_\ell P_\ell(\hat{\mathbf{p}} \cdot \hat{\mathbf{p}}') \quad (3.96)$$

Using Eq.(3.94), it can be shown that the C_ℓ 's are defined as:

$$C_\ell = \frac{4\pi}{(2\ell + 1)^2} \int d \ln k \Theta_\ell^2(k) \Delta_{\mathcal{R}}^2(k) \quad (3.97)$$

where $\Delta_{\mathcal{R}}^2(k)$ is the spectrum of the curvature perturbation defined as:

$$\langle \mathcal{R}(\hat{\mathbf{k}}) \mathcal{R}^*(\hat{\mathbf{k}}') \rangle = \frac{2\pi^2}{k^3} \Delta_{\mathcal{R}}^2(k) \delta_D(\hat{\mathbf{k}} - \hat{\mathbf{k}}') \quad (3.98)$$

If the fluctuations are Gaussian the power spectrum (two-point correlation function) contains all the information of the CMB. This is in agreement with current data but the question on how Gaussian are the statistics of primordial perturbation is still open. Inflationary models infact predict that early time fluctuations may have some degree of non-Gaussianity; their detection would be therefore of great importance to better understand the physics of inflation [67].

3.4.1 Anisotropies from inhomogeneity

To connect the observed spectrum today with the fluctuations at recombination we need now to integrate back our equation to the time of recombination along the line of sight (LOS). It useful to introduce some auxiliary concepts:

- Optical depth

$$\tau(\eta) \equiv \int_\eta^{\eta_0} \Gamma(\eta') d\eta' \quad (3.99)$$

it describe the opacity of the Universe at a given time when seen from today. The probability of no scattering for a photon along the path to us scale as $e^{-\tau}$ therefore the Boltzmann equation can be rewritten :

$$\frac{d\Theta}{d\eta} + \Gamma\Theta = \frac{d}{d\eta}(e^{-\tau}\Theta) \quad (3.100)$$

3. THE INHOMOGENEOUS UNIVERSE

- Visibility function

$$g(\eta) \equiv -\tau'(\eta)e^{-\tau(\eta)} \quad (3.101)$$

it describe the probability density for a photon to last scatter at time η .

Using these new quantities the Boltzmann equation for scalar perturbations to the photon density can be written as:

$$\frac{d}{d\eta}[e^{-\eta}(\Theta + \Psi)] = e^{-\tau}(\Phi' + \Psi') + g(\tau)[\Theta_0 + \Psi - \hat{\mathbf{p}} \cdot \mathbf{v}_e] = S \quad (3.102)$$

integrating along the LOS we find:

$$\Theta(\eta_0, \mathbf{x}_0, \hat{\mathbf{p}}) = \int_0^{\eta_0} d\eta' S(\eta', \mathbf{x}_0 + (\eta_0 - \eta')\hat{\mathbf{p}}, \hat{\mathbf{p}}) \quad (3.103)$$

where we have used $\tau(\eta_0) = 0$ and $\tau(0) \approx \infty$ and dropped the unobservable monopole $\Psi(\eta_0, \mathbf{x}_0)$ (for a more detailed derivation see [44]). Assuming that the recombination occurs instantaneously we can set $g(\eta) = \delta_D(\eta - \eta_{\text{rec}})$ and $e^{-\tau} = \mathbf{H}(\eta - \eta_{\text{rec}})$ where δ_D and \mathbf{H} are the delta Dirac and the Heaviside functions respectively. Therefore we find:

$$\Theta(\hat{\mathbf{p}}) \approx (\Theta_0 + \Psi)|_{\eta_{\text{rec}}} - (\hat{\mathbf{p}} \cdot \mathbf{v}_e)|_{\eta_{\text{rec}}} + \int_{\eta_{\text{rec}}}^{\eta_0} d\eta' (\Psi' + \Phi') \quad (3.104)$$

We see then that $\Theta(\hat{\mathbf{p}})$ is made up of three contributions:

- *Sachs-Wolfe effect*(SW)

It is the relative frequency shift of photons induced by the difference in gravitational potential at emission and detection. More precisely is a combination of the intrinsic temperature fluctuation at the surface of last-scattering and an additional gravitational redshift arising when the photons climb out of a potential well at last-scattering.

- *Doppler effect*

The photon-baryon fluid moves w.r.t. the conformal Newtonian frame with a non-zero velocity \mathbf{v}_e . This leads to a shift in the photon energy.

- *Integrated Sachs-Wolfe effect* (ISW)

This term describes the effect of gravitational redshifting of the photon energy from the evolution of the potentials along the LOS. During the matter dominated era the potentials were constant but at early times the residual amount radiation gives a time variation of Φ leading to the early ISW effect. At late times, dark energy become relevant and again the potentials are not constant along the LOS leading to the so-called late ISW.

It is worth at this point to evaluate the Sachs-Wolfe term at large scales (where it dominates the CMB spectrum) to glance some of the physics behind this contribution. On super horizon scales and for adiabatic initial conditions we can write $-2\Psi = -2\Phi \approx \delta = \delta_c = \delta_b = 3/4\delta_\gamma$ (since recombination happens in the matter dominance) therefore we have that CMB anisotropies on large scales are:

$$\Theta \approx \left(\frac{1}{4}\delta_\gamma + \Psi \right) \Big|_{\eta_{\text{rec}}} = \frac{1}{3}\Psi(\eta_{\text{rec}}) = -\frac{1}{8}\delta_\gamma(\eta_{\text{rec}}) \quad (3.105)$$

At this scale gravitational redshift wins over temperature fluctuations, an overdensity at last scattering ($\delta_\gamma(\eta_{\text{rec}}) > 0$) corresponds to a potential well ($\Psi(\eta_{\text{rec}}) < 0$) and therefore to a cold spot in CMB map *i.e.* $\Theta(\eta_{\text{rec}}) < 0$. Conversely, hot spots corresponds to an underdensity.

Finally in order to find the transfer functions for each term we transform the LOS solution to Fourier space:

$$\Theta_\ell(k) = j_\ell(k\chi_{\text{rec}})(\Theta_0 + \Psi)|_{\eta_{\text{rec}}} - j'_\ell(k\chi_{\text{rec}})v_e|_{\eta_{\text{rec}}} + \int_{\eta_{\text{rec}}}^{\eta_0} d\eta'(\Psi' + \Phi')j_\ell(k\chi_{\text{rec}}) \quad (3.106)$$

in deriving this equation we have made use of the Rayleigh plane waves expansion,

$$e^{i\chi\mathbf{k}\cdot\hat{\mathbf{p}}} = \sum_{\ell} (-i)^\ell (2\ell + 1) j_\ell(k\chi) P_\ell(\hat{\mathbf{k}} \cdot \hat{\mathbf{p}}) \quad (3.107)$$

where j_ℓ are the Bessel function and we have defined $f|_{\eta_{\text{rec}}} \equiv f(\eta_{\text{rec}}, \mathbf{k})/\mathcal{R}(\mathbf{k})$ and $\chi(\eta) = \eta_0 - \eta$ as the conformal distance along the LOS. Putting Eq.(3.106) into Eq.(3.97) and neglecting for simplicity the cross spectra and the contribution of the ISW which are very small, we have:

$$\Theta_\ell(k) = T_{\text{SW}}(k)j_\ell(k\chi_{\text{rec}}) + T_{\text{D}}(k)j'_\ell(k\chi_{\text{rec}}) \quad (3.108)$$

with $T_{\text{SW}}(k) = (\Theta_0 + \Psi)|_{\eta_{\text{rec}}}/\mathcal{R}(\mathbf{k})$ and $T_{\text{D}}(k) = v_e|_{\eta_{\text{rec}}}/\mathcal{R}(\mathbf{k})$. Therefore the contribution to the C_ℓ 's of these terms can be find to be:

$$C_\ell^{\text{SW}} \sim T_{\text{SW}}^2(k)\Delta_{\mathcal{R}}^2(\mathbf{k})|_{k \sim \ell/\chi_{\text{rec}}} \quad (3.109)$$

$$C_\ell^{\text{D}} \sim T_{\text{D}}^2(k)\Delta_{\mathcal{R}}^2(\mathbf{k})|_{k \sim \ell/\chi_{\text{rec}}} \quad (3.110)$$

3.4.2 Transfer function

The last thing we need to do is to calculate the transfer function T_{D} and T_{SW} . This requires to evolve the coupled fluctuations of photons, baryons, electrons and dark matter in a perturbed spacetime. As we have already discussed, photons are tightly coupled to the electrons so that we can use the Boltzmann equation in the

3. THE INHOMOGENEOUS UNIVERSE

form derived in Section 3.3.3. This approximation breaks close to recombination (and below the diffusion damping scale, see below) but it is otherwise enough to describe photon dynamics with good accuracy. The coupling between baryons and electrons remains strong throughout so they form a single electron baryons fluid, for simplicity we will refer to this as the baryon fluid and denotes the bulk velocity of electrons and baryons as v_b .

What we need to do is to connect then Eqs.(3.84) with the equations describing the evolution of the baryon fluid. We start noting that the momentum density $q^i \equiv T_0^i$ can be written as:

$$q^i = (\bar{\rho}_\gamma + \bar{P}_\gamma)v_\gamma^i + (\bar{\rho}_b + \bar{P}_b)v_b^i = \frac{4}{3}\bar{\rho}_\gamma(v_\gamma^i + Rv_b^i) \quad (3.111)$$

where $R = 3\bar{\rho}_b/4\bar{\rho}_\gamma$ is the baryon to photon ratio. The total energy density perturbation can be then rewritten in terms of R as:

$$\delta\rho = \bar{\rho}_\gamma \left(\delta_\gamma + \frac{4}{3}R\delta_b \right) \quad (3.112)$$

Using these relations and $\nabla_\mu T_\nu^\mu = 0$ we obtain:

$$\delta'_b = -kv_b + 3\Phi' \quad (3.113a)$$

$$v'_b = -\mathcal{H}v_b - k\Psi - \frac{\Gamma}{R}(\Theta_1 + v_b) \quad (3.113b)$$

Let us now rearrange Eq.(3.113b) as:

$$v_b = -\Theta_1 - \frac{R}{\Gamma}[v'_b + \mathcal{H}v_b + k\Psi] \quad (3.114)$$

in the tight coupling limit $v_b \approx -\Theta_1$ but since it multiplied by Γ we need the next to leading order solution. We obtain this approximating $v_b \approx -\Theta_1$,

$$v_b \approx -\Theta_1 + \frac{R}{\Gamma}[\Theta'_1 + \mathcal{H}\Theta_1 - k\Psi] \quad (3.115)$$

Substituting Eq.(3.115) into the second of Eqs.(3.84) and using this into the first of Eqs.(3.84) to eliminate Θ_1 , we obtain an evolution equation for the monopole:

$$\Theta''_0 + \frac{\mathcal{H}R}{1+R}\Theta_0 + c_s^2 k^2 \Theta_0 = -\frac{1}{3}k^2\Psi + \Phi'' + \frac{R'}{1+R}\Phi' \quad (3.116)$$

Eq.(3.116) is the main equation in describing CMB phenomenology. Before moving on to discuss its solution it is worth mentioning which are the important scales in Eq.(3.116).

- *Hubble radius*

We have seen that metric perturbations are frozen outside the Hubble radius $r_H = (aH)^{-1}$. The perturbation modes then start to evolve only at horizon crossing when they reenter into the Hubble radius

- *Sound horizon*

Photon fluctuations remain frozen until they cross the sound horizon $r_s = \int_0^\eta c_s d\eta'$, then they start to oscillate. When $R \ll 1$, the sound speed $c_s = 1/\sqrt{3}$ and the sound horizon is nearly equal to the size of the horizon. Before decoupling however the baryon fraction becomes relevant and c_s goes to zero. At this moment the sound horizon is much smaller than the Hubble radius.

- *Diffusion scale*

The diffusion scale r_D is important in discussing the damping of CMB fluctuations. The tight coupling approximation in fact holds only above this scale. Below the diffusion scale we need a more careful treatment of the Boltzmann equation. For the moment, we define it as square root of the integral of the photon mean free path along the LOS *i.e.*

$$r_D^2 \sim \int_0^\eta \Gamma^{-1} \quad (3.117)$$

At early times the diffusion length is very small and so is the photon mean free path, but around recombination $\Gamma \rightarrow 0$ and diffusion scale becomes comparable to r_H . The longer a mode spends in the diffusive regime the more it gets damped by photons.

To capture much of the physics of Eq.(3.116), we can ignore the time variations of the potentials (which is a good approximation since recombination happens in matter dominance when the potential are approximately constant) and we ignore the evolution of the baryon ratio R compared to the oscillation frequency $c_s k$. Then, we can rewrite Eq.(3.116) as:

$$\Theta_0'' + c_s^2 k^2 \Theta_0 = -\frac{k^2}{3} \psi \quad (3.118)$$

which corresponds to a simple harmonic oscillator with a constant gravitational forcing term. The general solution is:

$$\Theta_0(\eta, \mathbf{k}) = [\Theta_0(\mathbf{k}) + (1 + R)\Psi(\mathbf{k})] \cos(kr_s) - (1 + R)\Psi(\mathbf{k}) \quad (3.119)$$

where we have used $\Theta_0'(0) = 0$ for adiabatic initial conditions. We conclude this section discussing the physical implications of Eq.(3.119).

3. THE INHOMOGENEOUS UNIVERSE

- When photons dominates the fluid $R \rightarrow 0$ and Eq.(3.119) becomes:

$$\Theta_0(\eta, \mathbf{k}) + \Psi(\mathbf{k}) = [\Theta_0(\mathbf{k}) + \Psi(\mathbf{k})] \cos(kr_s) \quad (3.120)$$

This represents a harmonic oscillator with a zero-point displaced by gravity. Photons oscillate in an out of the potential well, when they fall in the term $-\Psi > 0$ and photons gain energy. After decoupling photons have to climb out the potential and loose energy this precisely compensate the energy gain at infalling. Therefore Eq.(3.120) describe the observed temperature perturbation. Different modes will arrive in different phase of their evolution at the time of decoupling. A discrete sets of wavenumbers $k_n = n\pi/r_s(\eta_{\text{rec}})$ corresponds therefore to the oscillation peaks at decoupling *i.e.* the peaks that we observe in the CMB.

- Including the baryon ratio again but assuming it to be constant in time we get:

$$\Theta_0(\eta, \mathbf{k}) + \Psi(\mathbf{k}) = [\Theta_0(\mathbf{k}) + \Psi(\mathbf{k})] \cos(kr_s) - R\Psi(\mathbf{k}) \quad (3.121)$$

The displacement due to the gravitational potential is further enhanced by the presence of baryons *i.e.* the gravitational infall leads to a greater compression of the fluid in the potential well. Since the redshift is not affected by baryons this features remains in the spectrum and enhance all peaks from compression over those from rarefaction.

- During the radiation era the potential Ψ and Φ become time dependent inside the horizon. The decaying potentials act to enhance temperature fluctuations through a near resonant driving force. Since the potential Ψ decays after sound horizon crossing, it drives the first compression without a counterbalancing effect when photons exits the potential wells. The higher peaks began their oscillation during radiation dominance therefore are the more enhanced by this effect.
- For the approximate solution with constant R , the evolution of the dipole satisfy:

$$\Theta_1(\eta, \mathbf{k}) = -3[\Theta_0(\mathbf{k}) + (1 + R)\Psi(\mathbf{k})]c_s \sin(kr_s) \quad (3.122)$$

evaluating this and Eq.(3.119) at $\eta = \eta_{\text{rec}}$ the transfer function can be written as:

$$T_{\text{SW}}(k) = A(k) \cos(kr_{s,\text{rec}}) + B(k) \quad (3.123)$$

$$T_{\text{D}}(k) = -3c_s A(k) \sin(kr_{s,\text{rec}}) \quad (3.124)$$

with

$$A(k) \equiv \frac{\Theta_0(\mathbf{k}) + (1 + R)\Psi(\mathbf{k})}{\mathcal{R}(\mathbf{k})} \quad (3.125)$$

$$B(k) \equiv -R \frac{\Psi(\mathbf{k})}{\mathcal{R}(\mathbf{k})} \quad (3.126)$$

In our derivation of CMB anisotropies along with the contribution of the ISW term, we are not considering some important effects that contributes to shape the power spectra of CMB anisotropies :

- Photon decoupling does not happen instantaneously but actually takes quite sometimes as we have seen in Chapter 2. As a results instead of considering initial condition for the free-streaming evolution at η_{rec} one must convolve Φ , v_γ and δ_γ with the photon visibility function giving the probability that a photon last-scattered at redshift η . This in turn lead to an exponential suppression of the C_ℓ [65].
- At the reionization epoch, the light from the first stars, quasars and dwarf galaxies makes the Universe less transparent to CMB photons. Free electron density grows again and the probability for a photon to “live through” this epoch is given by the reionization optical depth $e^{-\tau_{\text{rei}}}$ with $\tau_{\text{rei}} = \tau(\eta_{\text{rei}})$. Photons that rescatter at $z = z_{\text{rei}}$ at given place in the Universe have last scattered at recombination anywhere on a sphere of coordinate radius $\approx \eta_{\text{rei}}$. Since the direction of photon propagation changes randomly, photons coming to an observer from a given direction gather from the whole of that sphere. Hence, the contribution of rescattered photons to anisotropy at angular scales smaller than $\Delta\theta_{\text{rei}} = \eta_{\text{rei}}/\eta_0$ is washed out, and the remaining anisotropy is due to photons that have not rescattered. On the other hand, the anisotropy at angular scales larger than $\Delta\theta_{\text{rei}}$ remains intact, since the regions of the coordinate size η_{rei} at recombination are not resolved at these angular scales. At the level of the angular power spectrum, this implies a suppression of the C_ℓ coefficients by $e^{2\tau_{\text{rei}}}$ for $\ell > \pi\eta_0/\eta_{\text{rei}}$
- We are not including (massive) neutrinos in our computation of CMB anisotropies. Their contribution (even if it is not dominant) as an important impact on CMB anisotropies has we have briefly discussed in Section 3.3.4.
- The ensemble average that define the C_ℓ should in principle be made over different Universe realizations. Since we have only one Universe to observe this cannot be done in reality. Therefore one must construct an estimator \hat{C}_ℓ of

3. THE INHOMOGENEOUS UNIVERSE

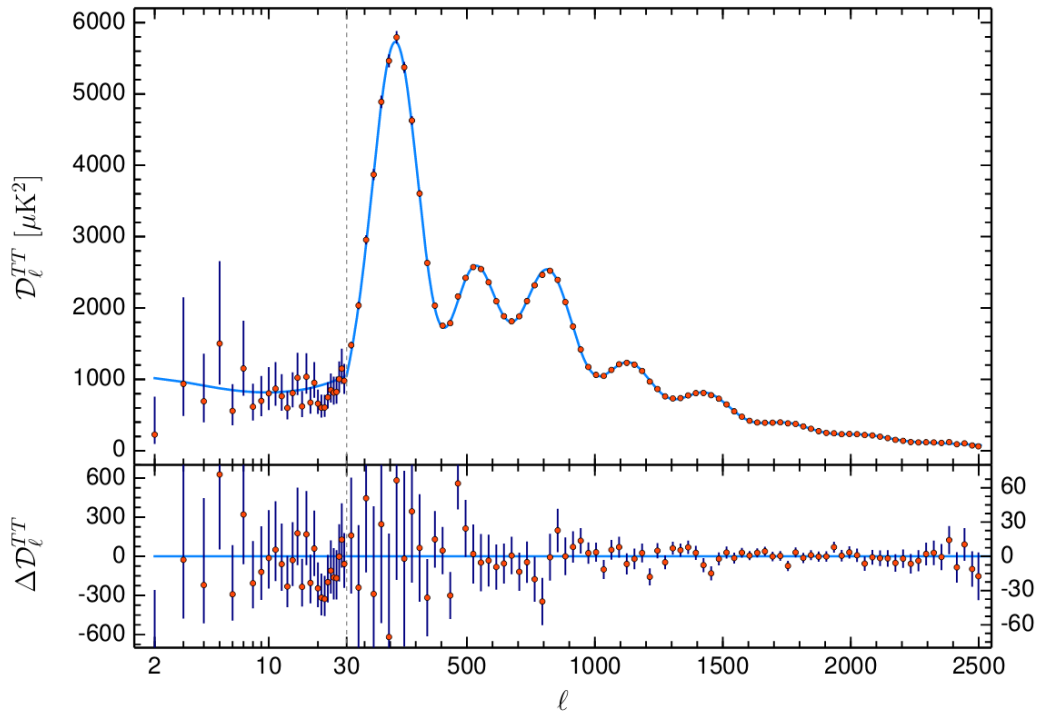


Figure 3.1: Planck 2018 temperature power spectrum (red points) with the 1σ error including cosmic variance. The base- Λ CDM theoretical spectrum best fit to the Planck likelihood is plotted in light blue. Residual w.r.t this model are showed in the lower panel. Note that $\mathcal{D}_\ell = \ell(\ell + 1)C_\ell$. The picture is adapted from [28].

the real C_ℓ assuming that each region at a certain multipole ℓ is an independent realization of the underlying stochastic field (ergodic hypothesis):

$$\hat{C}_\ell \equiv \frac{1}{2\ell + 1} \sum_{m=-\ell}^{\ell} |a_{\ell m}|^2 \quad (3.127)$$

The expected squared difference between \hat{C}_ℓ and C_ℓ is called the cosmic variance and for Gaussian anisotropies is:

$$\langle (\hat{C}_\ell - C_\ell)^2 \rangle = \frac{2C_\ell}{2\ell + 1} \quad (3.128)$$

Therefore, at large angular scales we do not have many different regions over which to sample the distribution from which the $a_{\ell, m}$ are drawn, and there will be an intrinsic uncertainty in our knowledge of the C_ℓ .

Current codes like the Boltzmann solver **CAMB** takes into account all these contributions along with solving the Boltzmann hierarchy to higher order than the dipole. In Fig.3.1 the Planck data points are showed with the best fit Λ CDM spectrum.

3.4.3 Diffusion Damping

By assuming perfect tight coupling (zero mean free path) our solution is missing some physics: the approximation of photons and baryons and electrons moving as a single fluid is not met in reality. Photons travels a finite distance between collisions $\lambda_{\text{mfp}} = (\sigma_T n_e)^{-1}$, in a Hubble time the number of photons scattering is $\sigma_T n_e H^{-1}$. The total distance traveled in the course of a random walk is the mean free path times the square root of the total number of steps $\lambda_D \sim \lambda_{\text{mfp}} \sqrt{\sigma_T n_e H^{-1}} = (\sigma_T n_e H)^{-1/2}$. Any perturbation on scales smaller than λ_D is washed out by the diffusion damping. In Fourier space this will corresponds to have a damping terms in Eq.(3.120) of the form:

$$\Theta_0 \propto e^{-k^2/k_D^2} \cos kr_s \quad (3.129)$$

with $k_D \sim \lambda_D^{-1}$. Since the tight coupling approximation breaks for scale smaller than k_D , we have to account also for the photons quadrupole moment Θ_2 . A detailed calculation of the damping scale involving the quadrupole moment in the Boltzmann equation gives:

$$k_D^{-2}(k) \equiv \int_0^\eta \frac{d\eta}{6(1+R)\Gamma(\eta)} \left[\frac{R^2}{1+R} + \frac{8}{9} \right] \quad (3.130)$$

we see that this is consistent with our naive definition of the damping scale Eq.(3.117) and with the approximate solution that we have found in this Section using the photon mean free path. The diffusion damping is sometimes called *Silk damping* and k_D is also known as the *Silk scale*.

3.4.4 CMB polarization

We conclude this Chapter with a note on CMB polarization. As we have discussed in deriving the photon Boltzmann equation, Thomson scattering can induce polarization if the incoming radiation field as a quadrupole moment (corresponding to Θ_2).

Polarization unfortunately is not a scalar field, so the expansion in spherical harmonics cannot be applied. We have instead to start from the anisotropic tensor $I_{ij}(\hat{\mathbf{p}})$ defined on the sky at the observation point $\{\eta_0, \mathbf{x}_0\}$. Starting from I_{ij} one can construct:

- the “Stokes parameters” Q and U (see also [44])

$$Q = \frac{1}{4}(I_{11} - I_{22}) \quad (3.131)$$

$$U = \frac{1}{2}I_{12} \quad (3.132)$$

3. THE INHOMOGENEOUS UNIVERSE

Q and U are related to the polarization magnitude and angle by:

$$P = \sqrt{Q^2 + U^2} \quad (3.133)$$

$$\alpha = \frac{1}{2} \arg(Q + iU) \quad (3.134)$$

- the scalar (spin-0) field $\frac{1}{4}(I_{11} + I_{22})$ which is nothing more than the temperature anisotropy itself.

Since Q and U are not invariant under rotation in the plane perpendicular to photon direction of propagation (\hat{p}) we cannot use the spherical harmonic expansion, instead we need to use the spin-2 spherical harmonics $Y_{\ell m}^{(\pm)}$. Q and U can then be written as [68, 69]:

$$Q(\hat{p}) \pm iU(\hat{p}) = \sum_{\ell=0}^{\infty} \sum_{m=-\ell}^{\ell} a_{\ell m}^{\pm} Y_{\ell m}^{\pm}(\hat{p}) \quad (3.135)$$

It is useful to introduce a linear combination of the $a_{\ell m}$:

$$a_{\ell m}^E = -\frac{1}{2}(a_{\ell m}^+ + a_{\ell m}^-) \quad (3.136)$$

$$a_{\ell m}^B = -\frac{1}{2i}(a_{\ell m}^+ - a_{\ell m}^-) \quad (3.137)$$

and from these one construct the following quantities:

$$E(\hat{p}) \equiv \sum_{\ell=0}^{\infty} \sum_{m=-\ell}^{\ell} a_{\ell m}^E Y_{\ell m}^{\pm}(\hat{p}) \quad (3.138)$$

$$B(\hat{p}) \equiv \sum_{\ell=0}^{\infty} \sum_{m=-\ell}^{\ell} a_{\ell m}^B Y_{\ell m}^{\pm}(\hat{p}) \quad (3.139)$$

The E field can be characterized as a divergence- and curl-free field (with $E < 0$ around cold spots in the sky and $E > 0$ around hot ones), instead the B field is a divergenceless but with a non-zero vorticity at every point in the sky. Along with the $a_{\ell m}$ (that we will from now on denotes with $a_{\ell m}^T$) are everything we need to know to compute the power spectra and cross-correlation of temperature and polarization fluctuations. Therefore Eq.(3.95) is generalized to:

$$\langle a_{\ell m}^X (a_{\ell', m'}^Y)^{\star} \rangle = \delta_{\ell \ell'} \delta_{m m'} C_{\ell}^{XY} \quad (3.140)$$

with $X, Y = T, E, B$. Given that temperature and polarization anisotropies are generated by density fluctuations we expect a non-zero cross correlation between

the temperature and the E fields while instead TB and EB are zero for parity reasons. This decomposition of the polarization in E- and B-modes is of great importance in modern cosmology as shown in [68, 69] (but see also [44]). In fact they have demonstrated that:

- scalar perturbations (fluctuations of the energy density) can lead to a quadrupole moment for the incoming radiation field. Then they can only source E-modes.
- vector perturbations (plasma vorticity) can also produce a quadrupole moment which results in the production of B-modes. But the expansion of the Universe wash out this kind of perturbations so their contribution is expected to be negligible
- tensor perturbations (gravity waves) stretch and squeeze the space in orthogonal directions thus they produce both E- and B-modes

Since gravitational waves are produced during inflation a detection of a B-modes signature in the CMB would represent the “smoking gun” for inflation. However foregrounds (such as dust and synchrotron radiation) can emit polarized radiation and must be taken into account carefully. Furthermore, gravitational lensing can rotate E-modes into B-modes and therefore acts as an additional source of contamination.

We conclude this brief review of the CMB polarization with the equivalent of Eq.(3.97) for XY different from TT. For XY = EE, TE, the E-modes power spectrum and its cross-correlation with the temperature field, the spectra are dominated by scalar fluctuations so that we can write:

$$C_\ell^{XY} \propto \int d \ln k \Delta_{\mathcal{R}}^2(k) \mathcal{T}_{X,\ell}(k) \mathcal{T}_{Y,\ell}(k) \quad (3.141)$$

where $\mathcal{T}_{Y,\ell}(k)$ and $\mathcal{T}_{X,\ell}(k)$ represent the transfer function of the X and Y fields and we have $\mathcal{T}_{T,\ell}(k) = \Theta_\ell(k)$. For XY = BB, B-modes power spectrum, we can instead write:

$$C_\ell^{BB} \propto \int d \ln k \Delta_h^2(k) \mathcal{T}_{B,\ell}(k) \mathcal{T}_{B,\ell}(k) \quad (3.142)$$

since this kind of polarization anisotropies are generated by tensor perturbations the power spectrum is the Fourier transform of the two-point correlation function of the spin-2 metric perturbation h_{ij} of Eq.(3.21).

PART III

SCIENTIFIC RESEARCH RESULTS

4 PMF IMPACT ON FUTURE CMB BOUNDS ON INFLATIONARY GRAVITATIONAL WAVES

In this Chapter we study the implications of including a primordial magnetic field (PMF) in the standard cosmological scenario and how this can lead to a bias inference of the tensor-to-scalar ratio for future experiments aiming at measuring this value with a sensitivity $\delta r \sim 10^{-3}$. Besides we provide also a forecast on the possibility of breaking the degeneracy using measurements of the Faraday rotation of CMB polarization.

This Chapter is mainly based on the work [Phys. Rev. D97 \(2018\) no.12, 123534](#)

Contents

4.1	Introduction	73
4.2	Primordial Magnetic Fields	75
4.2.1	Magnetic Parameters	75
4.2.2	Impact of PMFs on CMB spectra and fiducial model	78
4.3	Method	81
4.4	Results	84
4.4.1	Results from MCMC	84
4.4.2	Delensing	88
4.4.3	Importance of small-scale B-mode measurements	89
4.5	Constraints from Faraday rotation	91
4.6	Discussion and Conclusion	95

4.1 Introduction

One of the main goals of modern cosmology is the detection of Cosmic Microwave Background polarization B-modes produced by vacuum fluctuations of the metric during inflation. Their detection would provide a “smoking gun” for the inflationary paradigm and give hints towards the quantum nature of gravity.

In the past years the experimental bounds on the primordial B-mode component (parameterized by the tensor-to-scalar ratio r) have improved significantly. Indeed, since the constraints from the BICEP experiment of $r < 0.72$ at 95% C.L. [70] in 2010, the recent combined analysis of BICEP2, Keck Array IV and Planck B-mode measurements now provide $r < 0.07$ at 95% C.L. [31], showing an improvement by nearly one order of magnitude in about ~ 7 years (see also [71]). In the next years a further improvement by one order of magnitude, reaching a sensitivity in the range of $r \sim 10^{-2} - 10^{-3}$, is expected by several ongoing experiments such as BICEP3 and the Keck Array [72], CLASS [73], Advanced ACTPol [74], and SPT-3G [75]. Future experiments as the LiteBIRD [29] and CORE-M5 [76–78] satellite missions and the CMB-S4 ground based telescope [33] are expected to reach a sensitivity of $\delta r \sim 0.0001$, closing in on the prediction $r \approx 10^{-3}$ of the Starobinsky model [79].

It is however important to investigate if other mechanisms could generate a B-mode polarization signal that could lead to a wrong claim for a detection of vacuum fluctuations of the metric. For example, foregrounds as galactic dust are obviously an issue [80]. Topological defects (see e.g. [81]) can also produce B-modes (even from vector perturbations [82]). Finally, GWs can also be sourced during inflation in presence of anisotropic stress generated by quantum fluctuations of other fields, even if their energy density is much smaller than that of the dominant inflaton field (see e.g. [83, 84]). The common attribute to all these sources is the fact that they have some additional signature that allows to disentangle them from B-modes generated from vacuum fluctuations of the metric, be it the frequency dependence for galactic foregrounds (see e.g. [85, 86]), or the shape of the angular power spectrum for B-modes from topological defects or sourced tensor fluctuations during inflation.¹

B-mode polarization can also be produced by a primordial magnetic field (PMF) (see e.g. [94–96]). In the presence of PMFs, passive tensor and compensated vector modes give B-modes with angular spectra that are very similar in shape to those produced by primordial gravitational waves (GWs)² and lensing (see e.g. [94, 97–99]). Future CMB experiments like CMB-S4 will be extremely sensitive to PMFs, improving current constraints on the corresponding B-mode amplitude by nearly two orders of magnitude [100].

It is then important to investigate how well future CMB experiments could discriminate between inflationary GWs and PMFs in the generation of CMB polarization B-modes: *these experiments would be able to claim a detection of the*

¹ Moreover, sourced tensor fluctuations can be chiral [87–91] and highly non-Gaussian [92, 93].

² For simplicity, in the rest of the Chapter we will refer to vacuum fluctuations of the metric during inflation as primordial gravitational waves.

4. MAGNETIC FIELDS AND GRAVITATIONAL WAVES

quantum nature of tensor perturbations of the metric only if a potential contribution from PMFs can be identified and subtracted.

How can one distinguish between the two scenarios? One key difference between the two is that while GWs affect the CMB anisotropies on large angular scales, primordial magnetic fields affect also smaller angular scales through compensated perturbations (see e.g. [94, 97, 99, 101]). As we show later in this Chapter, CMB experiments sensitive mainly to large angular scales as the proposed PIXIE and LiteBIRD missions are essentially unable to discriminate between PMFs and primordial GWs at the level of $r \approx 10^{-3}$. Then, a clean and reliable detection of B-modes generated by the inflationary tensor fluctuations can be obtained only by considering also smaller scales, as planned by the CMB-S4 experiments, or by a satellite with improved angular resolution as the recent CORE-M5 proposal.

A second difference between these two scenarios is the fact that PMFs can be constrained also by measuring the Faraday rotation (FR) of CMB polarization (see e.g. [101] and references therein) considering maps at different frequencies and taking advantage of the fact that the frequency scaling of FR is $\sim \nu^{-2}$. Moreover, FR can be in principle measured either by considering the effect on CMB anisotropies angular spectra or by extracting the Faraday rotation angle through estimators that make use of the coupling between E- and B-modes induced by FR [102–105]. It is therefore important to evaluate whether future realistic CMB experiments, considering their sensitivities, angular resolution and frequency and sky coverages, would be able to use FR to differentiate PMFs from inflationary GWs.

This Chapter is structured as follows: in Section 4.2 we review how primordial magnetic fields affect CMB temperature and polarization anisotropies and discuss in what region of parameter space they give a B-mode signal degenerate with that from primordial GWs. In Section 4.3 we review our forecast method while in Section 4.4 we present our results. In Section 4.5 we discuss the impact of Faraday rotation on our forecasts. We finally conclude in Section 4.6.

4.2 Primordial Magnetic Fields

In this Section we present some definitions useful for our analysis: we refer the interested reader to [66, 94, 97, 98, 106, 107] for a more detailed discussion of the subject.

4.2.1 Magnetic Parameters

We consider a stochastic magnetic field $B^i(\eta, \vec{x})$ generated at a time η_B before the epoch of neutrino decoupling η_ν . We assume that PMFs are a statistically isotropic Gaussian field with no helicity (a review on the impact of helical field on CMB

physics can be found in [106]). The exact form of the power spectrum P_B of the PMF strongly depends on the mechanism generating it. Following the current literature, we define P_B as a power law with a cut-off scale k_D , i.e.

$$P_B(k) = \begin{cases} \mathcal{A} k^{n_B} & \text{for } k < k_D, \\ 0 & \text{otherwise,} \end{cases} \quad (4.1)$$

where a spectral index $n_B = -3$ denotes a scale-invariant spectrum and the cut-off scale k_D accounts for the damping of the magnetic field due to radiation viscosity on very small scales, where magnetic effects are suppressed by photon diffusion [108, 109]. From Eq. (4.1), then, we define the magnetic field amplitude in terms of the parameter B_λ , obtained by smoothing the magnetic energy density with a Gaussian filter over a comoving scale λ [94]. In what follows we take $\lambda = 1$ Mpc.¹ Moreover, we focus only on nearly scale-invariant spectra PMFs with $n_B = -2.9$, which we expect to be produced by inflationary magnetogenesis, where magnetic fields are generated on small scales and then stretched to cosmological scales by the accelerated expansion (see [111–113] for recent analyses). We refer to [66, 99, 106, 110, 114–116] for discussions about how values of n_B larger than -3 can be generated, and what are the current constraints on PMFs with blue-tilted spectra.

Depending on the generation epoch of the PMF three different class of magnetic perturbations can be distinguished: inflationary, passive and compensated. In this Chapter we focus only on passive and compensated mode which are sourced by every PMF independently of the magnetic generation history. Passive modes are generated before neutrino decoupling ($\eta < \eta_v$) [94, 97, 98, 117, 118]. When neutrinos decouple ($\eta \geq \eta_v$), they also produce an anisotropic stress that compensates the magnetic one leading to isocurvature-like perturbations, the so-called compensated modes [94, 97, 98, 117–119].

The amplitude of these modes is set by the comoving curvature perturbation ζ . The presence of a PMF sources the growth of ζ before neutrino decoupling through the anisotropic stress Π_B [94]. Once neutrino compensation on the PMF anisotropic stress is effective, the growth of ζ ceases. For scalar perturbations the final form of ζ is [94, 118]

$$\zeta \approx \zeta(\eta_B) - \frac{1}{3} R_Y \Pi_B \left[\ln(\eta_v/\eta_B) + \left(\frac{5}{8R_v} - 1 \right) \right], \quad (4.2)$$

where $\zeta(\eta_B)$ is the comoving perturbation at the time of PMF generation, $(\Pi_B)_j^i$ is the magnetic dimensionless anisotropic stress, and R_i represents the ratio between the total density and the density of the species i .

¹It is common to take this value for λ [110]: it corresponds to the size of a typical region at the time of last scattering that later collapses to form a galactic halo.

4. MAGNETIC FIELDS AND GRAVITATIONAL WAVES

$\Omega_b h^2$	$\Omega_c h^2$	τ	n_s	$100 \theta_{MC}$	$\ln [10^{10} A_s]$	r
0.02225	0.01198	0.055	0.9645	1.04077	3.094	0
<hr/>						
		$B_{1 \text{ Mpc}} [\text{nG}]$	$\log_{10} (\eta_v / \eta_B)$	n_B		
		1.08	12	-2.9		

Table 4.1: Cosmological (top) and magnetic field (bottom) parameters assumed for the fiducial model. The fiducial values for the PMF parameters are within the 95% C.L. limits from current CMB experiments such Planck [110] and Planck+SPT [99] (see [120, 121] for constraints from pre-Planck data).

From Eq. (4.2) we see that there are two main contributions to ζ . The first contribution which has amplitude proportional to the product $\Pi_B \ln(\eta_v/\eta_B)$ is the adiabatic-like passive mode (which, unlike the standard adiabatic mode, has non-Gaussian statistics). This mode grows logarithmically in time when $\eta_B \leq \eta \leq \eta_v$ and then freezes on super-horizon scales after neutrino decoupling. The value of η_B cannot be defined unless the generation mechanism of the PMF is known. In the following, we will allow η_v/η_B to range from 10^6 to 10^{17} [99], corresponding to a energy scale of PMF generation between 10^3 GeV and 10^{14} GeV.² From Eq. (4.2), we see that increasing η_v/η_B leads to an increase in the amplitude of the passive mode: as we are going to discuss in the following (see Section 4.4), on large scales this effect will be degenerate with changing the amplitude of the primordial magnetic field. The second scalar mode is the so-called compensated mode: it is proportional to Π_B but it also has a dependency on the magnetic contributions to the radiation density contrast, Δ_B , through the ratio R_γ/R_ν . This is a isocurvature-like mode sourced by the residual PMF stress-energy after neutrino compensation.

An expression similar to Eq. (4.2) can be derived for tensor perturbations, with Π_B replaced by the tensor part of the PMF anisotropic stress. There will be both passive and compensated tensor modes: however, compensated tensor modes are small in amplitude and can be safely neglected [118]. Finally, since vector perturbations rapidly decay when not sourced, there are no passive vector modes. Nevertheless, there is a compensated vector mode proportional to the vector part of the anisotropic stress. In conclusion, the CMB anisotropy spectra will receive contributions from four modes in total: a passive and a compensated scalar mode, a passive tensor mode, and a compensated vector mode. In the following sections we briefly discuss what are our fiducial parameters for the PMF power spectrum, and see what are the imprints of these four modes on CMB angular spectra.

²For inflationary magnetogenesis, this corresponds to considering instantaneous reheating at energies $T_{\text{reh}}^4 \approx H_{\text{inf}}^2 M_{\text{P}}^2/10$ between $T_{\text{reh}} = 10^3$ GeV and $T_{\text{reh}} = 10^{14}$ GeV [115].

4.2.2 Impact of PMFs on CMB spectra and fiducial model

We use the publicly available code MagCAMB³ [99], which is based on a modified version of the Boltzmann integrator CAMB [122], to compute the contributions to the CMB angular spectra of the four magnetic modes. The fiducial cosmological model that we are going to use for the forecasts in this Chapter is a flat Λ CDM model with parameters compatible with the recent Planck 2015 constraints [27, 110, 123]. Most importantly, since our aim is to investigate the impact of a PMF on the determination of the tensor-to-scalar ratio r from inflationary GWs, we have assumed a fiducial model with *no* primordial GWs (*i.e.* we fix $r = 0$), but with a non-zero PMF amplitude. More precisely, we choose a PMF amplitude $B_{1\text{ Mpc}} = 1.08\text{ nG}$ and a time $\eta_v/\eta_B = 10^{12}$ of generation of the PMF⁴ (compatible with the current Planck bounds coming from CMB anisotropies [110]): the reason for these choices is explained in detail at the end of this section. Besides, as discussed in the previous section, we choose a spectral index $n_B = -2.9$ for the PMF spectrum. For convenience of the reader, we list the values of the cosmological parameters and of the parameters describing the PMF in Tab. 4.1.

Fig. 4.1 shows the TT, EE, TE and BB angular spectra for our fiducial model (Tab. 4.1). We see that PMFs have a significant effect mainly on the BB power spectrum. On large scales, $\ell \lesssim 100$, the passive tensor mode of the PMF gives a scale-dependence similar to that from inflationary GWs. On small scales, magnetic vector perturbations dominate, and lead to an increase in power: this feature is not shared by inflationary tensor modes, and we expect that it will allow to break the degeneracy between the two mechanisms. We also notice that B-modes from lensing have a larger amplitude than those from the compensated vector mode: however, their scale dependence is different, so we can expect to be able to disentangle it.

In Fig. 4.2, instead, we plot the sum of the tensor passive and vector compensated contributions to the B-mode angular spectrum, together with lensing B-modes and the prediction for C_ℓ^{BB} given a tensor-to-scalar ratio $r = 0.0042$. This is the prediction of the Starobinsky R^2 model [79] for $N_\star \approx 53$ (N_\star being the number of e -folds of the observable part of the inflationary epoch), and is the main target of upcoming CMB experiments [33, 77]. We see that our fiducial values $B_{1\text{ Mpc}} = 1.08\text{ nG}$ for the magnetic field amplitude and $\eta_v/\eta_B = 10^{12}$ for the time of PMF generation give a large-scale B-mode spectrum very similar to that of the Starobinsky model. We take, then, these values of $B_{1\text{ Mpc}}$ and η_v/η_B as a case-study, using them to show how an unresolved PMF component can bias the constraints on the theoretically motivated class of inflationary models known as

³<https://alexzucca90.github.io/MagCAMB/>

⁴Corresponding to an energy scale of 10^9 GeV

4. MAGNETIC FIELDS AND GRAVITATIONAL WAVES

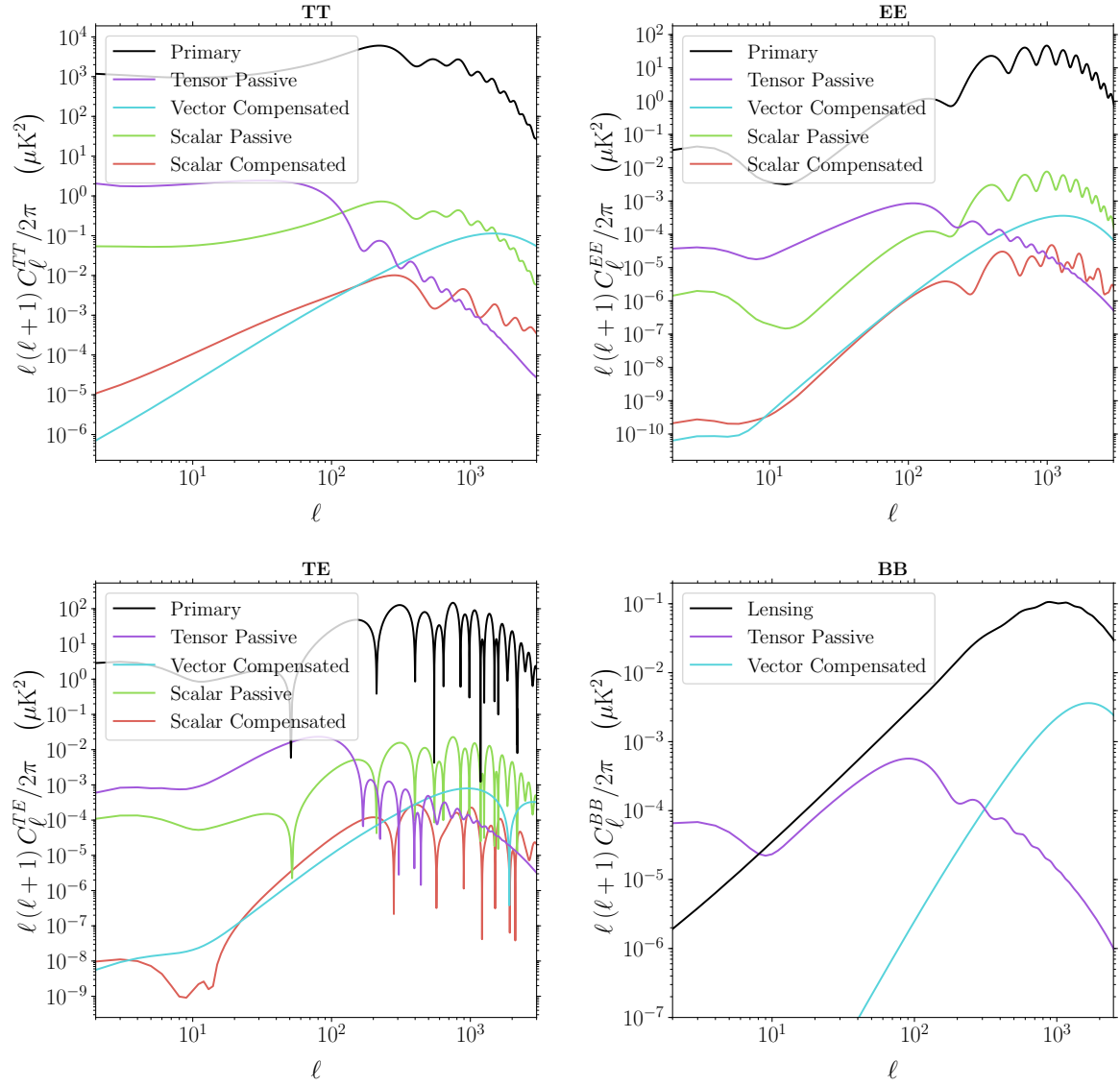


Figure 4.1: Comparison between primary and magnetic contributions to CMB angular correlation functions: the spectra have been computed with MagCAMB [99].

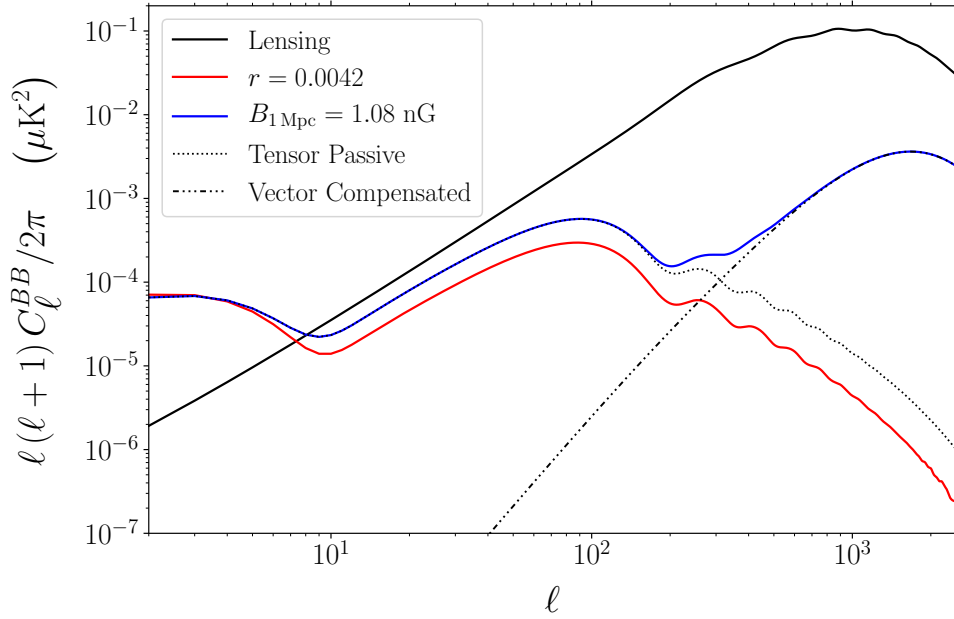


Figure 4.2: Comparison between the (tensor passive + vector compensated) B-mode angular power spectrum from PMFs (for $B_{1\text{Mpc}} = 1.08$ nG and $\eta_v/\eta_B = 10^{12}$) and the one from inflationary tensor modes (with tensor-to-scalar ratio equal to 0.0042). For this particular choice of parameters, we see that the inflationary and magnetic contributions are degenerate at very large scales, where both are about two orders of magnitude larger than lensing B-modes.

α -attractors [124].

Before proceeding, we comment on the degeneracy between $B_{1\text{Mpc}}$ and η_v/η_B : since the amplitude of the tensor passive mode, as that of the scalar mode, is proportional to η_v/η_B [94], we expect that increasing this parameter will result in more power in the BB spectrum at low ℓ . More precisely, for nearly scale-invariant PMF spectra the contribution of the tensor passive mode to C_ℓ^{BB} scales as:

$$C_\ell^{BB,\text{passive}} \sim B_{1\text{Mpc}}^4 [\ln(\eta_v/\eta_B)]^2.$$

Therefore, we could have equivalently reproduced the large-scale behavior of the Starobinsky model by choosing a larger $B_{1\text{Mpc}}$ and a smaller η_v/η_B . We stress, however, that for us the choice of the fiducial values of these parameters is not important: what is relevant is how a contribution to the B-mode power spectrum from PMFs could lead to a false claim of a detection at the level $r \approx 10^{-3}$. Moreover, choosing a larger $B_{1\text{Mpc}}$ and a smaller η_v/η_B would lead to a smaller contribution from the compensated vector mode. Therefore, breaking the degeneracy would be even more difficult for experiments that have access only to large scales. This makes our choice of parameters the most conservative one.⁵

⁵Of course, this point can be turned around. We can have the same large-scale tensor power by taking a larger η_v/η_B and a smaller $B_{1\text{Mpc}}$: in that case the contribution of the compensated vector mode could be large enough to be observable also on large scales. However, we stress that our point is that there

4. MAGNETIC FIELDS AND GRAVITATIONAL WAVES

Experiment	Beam [arcmin]	Power noise [$\mu\text{K} \cdot \text{arcmin}$]	ℓ_{max}	ℓ_{min}	f_{sky}
PIXIE	96	3.0	500	2	0.7
LiteBIRD	30	3.2	3000	2	0.7
CORE-M5	3.7	2.0	3000	2	0.7
Stage-3 (Deep)	1	4	3000	50	0.06
Stage-3 (Wide)	1.4	8	3000	50	0.4
CMB-S4	3	1	3000	5	0.4

Table 4.2: Experimental specifications for the several configurations considered in the forecasts. The power noise is defined as $w^{-1/2} = \sqrt{4\pi\sigma^2/N}$, where σ is the r.m.s. noise in each of the N pixels. We quote the power noise for temperature, and assume that for polarization it is simply enhanced by a factor of $\sqrt{2}$.

PIXIE	LiteBIRD	CORE-M5	Stage-3 (Deep)	Stage-3 (Wide)	CMB-S4
1	0.94	0.37	0.56	0.79	0.25

Table 4.3: Delensing factor α for the various experiments described in Tab. 7.1.

4.3 Method

In this Section we briefly illustrate the method we adopted to derive our forecasts for future CMB experiments.

We follow the same procedure (now standard practice) used in [125]. We produce synthetic realizations of future data given by

$$\hat{C}_\ell = C_\ell|_{\text{fid}} + N_\ell . \quad (4.3)$$

On the right-hand side, the $C_\ell|_{\text{fid}}$ are the angular power spectra of the fiducial model in μK^2 and

$$N_\ell = w^{-1} \exp(\ell(\ell + 1)\theta^2/8 \ln 2) \quad (4.4)$$

gives the experimental noise, where $w^{-1/2}$ is the experimental power noise expressed in $\mu\text{K} \cdot \text{rad}$ and θ is the experimental FWHM angular resolution in radians (we assume that pixel noise is uniform and uncorrelated). We have considered several future experiments with technical specifications listed in Tab. 7.1. More specifically we consider the PIXIE [126], LiteBIRD [29] and CORE-M5 [78] satellite missions, and the Stage-3 (see e.g. [127]) and CMB-S4 [33] ground-

is always a region in the currently available parameter space where the degeneracy cannot be broken unless we have access to small scales.

based experiments¹. The simulated data are then compared with theoretical C_ℓ obtained from the publicly available code MAGCAMB² [99], based on a modified version of the Boltzmann integrator CAMB [128]. Given a theoretical model, its likelihood \mathcal{L} is given by:

$$-2 \ln \mathcal{L} = \sum_{\ell} (2\ell + 1) f_{\text{sky}} \left(\frac{D}{|\bar{C}|} + \ln \frac{|\bar{C}|}{|\hat{C}|} - 3 \right), \quad (4.5)$$

where \hat{C}_ℓ are the fiducial spectra plus noise of Eq. (4.3), \bar{C}_ℓ are the theory spectra plus noise, and f_{sky} is the sky fraction observed by the experiment. Moreover, $|\bar{C}|$, $|\hat{C}|$ are given by:

$$|\bar{C}| = \bar{C}_\ell^{\text{TT}} \bar{C}_\ell^{\text{EE}} \bar{C}_\ell^{\text{BB}} - \left(\bar{C}_\ell^{\text{TE}} \right)^2 \bar{C}_\ell^{\text{BB}}, \quad (4.6)$$

$$|\hat{C}| = \hat{C}_\ell^{\text{TT}} \hat{C}_\ell^{\text{EE}} \hat{C}_\ell^{\text{BB}} - \left(\hat{C}_\ell^{\text{TE}} \right)^2 \hat{C}_\ell^{\text{BB}}, \quad (4.7)$$

while D is

$$\begin{aligned} D = & \hat{C}_\ell^{\text{TT}} \bar{C}_\ell^{\text{EE}} \bar{C}_\ell^{\text{BB}} + \bar{C}_\ell^{\text{TT}} \hat{C}_\ell^{\text{EE}} \bar{C}_\ell^{\text{BB}} + \bar{C}_\ell^{\text{TT}} \bar{C}_\ell^{\text{EE}} \hat{C}_\ell^{\text{BB}} \\ & - \bar{C}_\ell^{\text{TE}} \left(\bar{C}_\ell^{\text{TE}} \hat{C}_\ell^{\text{BB}} + 2 \hat{C}_\ell^{\text{TE}} \bar{C}_\ell^{\text{BB}} \right). \end{aligned} \quad (4.8)$$

In the following, we sample the likelihood using a MagCAMB-compatible [99] version of the Monte Carlo Markov Chain code CosmoMC³ [128], based on the Metropolis-Hastings algorithm with chains convergence tested by the Gelman and Rubin method. Since we assumed no correlation between primary adiabatic and magnetic modes, both theory and fiducial C_ℓ are obtained simply adding linearly together magnetic and non-magnetic contributions, i.e.

$$C_\ell = C_\ell^{\text{primary}} + C_\ell^{\text{passive}} + C_\ell^{\text{compensated}}. \quad (4.9)$$

We also study the impact of delensing on future constraints. In order to do this, we subtract from the total signal the lensed CMB B-modes using the ‘‘CMB×CMB’’ delensing procedure already proposed in [85, 129]. In fact, the CMB lensing is a contaminant of the primordial B-modes, that can be estimated and partially removed from the observed signal. For each future experiment considered in this paper, we rescale the BB power spectrum by using the corresponding delensing

¹Most of these experiments are still in the stage of a proposal. The above list should therefore be considered as an illustration of what a future CMB experiments could achieve.

²<https://alexzucca90.github.io/MagCAMB/>

³<http://cosmologist.info>

4. MAGNETIC FIELDS AND GRAVITATIONAL WAVES

factor [85, 130], that can be computed in the following way:

$$\alpha \equiv \frac{\sum_{\ell} C_{\ell}^{\text{BB,del}}}{\sum_{\ell} C_{\ell}^{\text{BB,len}}} \quad (4.10)$$

where $C_{\ell}^{\text{BB,del}} \equiv C_{\ell}^{\text{BB,len}} - C_{\ell}^{\text{BB,est}}$ is the delensed BB power spectrum and $C_{\ell}^{\text{BB,len}}$ is the original lensed one. The estimated lensing B-modes $C_{\ell}^{\text{BB,est}}$ can be obtained by computing [85, 129]

$$C_{\ell}^{\text{BB,est}} = \frac{1}{2\ell + 1} \sum_{\ell_1, \ell_2} |f_{\ell\ell_1\ell_2}^{\text{EB}}|^2 \times \frac{(C_{\ell_1}^{\text{EE}})^2}{C_{\ell_1}^{\text{EE}} + N_{\ell_1}^{\text{EE}}} \frac{(C_{\ell_2}^{\phi\phi})^2}{C_{\ell_2}^{\phi\phi} + N_{\ell_2}^{\phi\phi}}, \quad (4.11)$$

where $f_{\ell\ell_1\ell_2}^{\text{EB}}$ is the geometric coupling factor. Finally, the estimated noise will be computed as:

$$N_{\ell}^{\phi\phi} = \left[\frac{1}{2\ell + 1} \sum_{\ell_1, \ell_2} |f_{\ell\ell_1\ell_2}^{\text{EB}}|^2 \left[\times \frac{1}{C_{\ell_1}^{\text{BB}} + N_{\ell_1}^{\text{BB}}} \times \frac{(C_{\ell_2}^{\text{EE}})^2}{C_{\ell_2}^{\text{EE}} + N_{\ell_2}^{\text{EE}}} \right]^{-1} \right], \quad (4.12)$$

where the lensed B-modes appear. For this reason, we iterate this estimator until reaching the convergence criterion:

$$\left| \frac{N_{\ell}^{\phi\phi, i+1} - N_{\ell}^{\phi\phi, i}}{N_{\ell}^{\phi\phi, i+1}} \right| \leq 0.5 \% . \quad (4.13)$$

When delensing is included in the analysis, we do not carry out a full exploration of the parameter space: we consider the likelihood of Eq. (4.5) for the BB angular power spectrum only, and fix all parameters apart from r and B_1 Mpc. With these assumptions, Eq. (4.5) reduces to (for simplicity we drop the BB superscript on all power spectra, including noise):

$$-2 \ln \mathcal{L} = \sum_{\ell} (2\ell + 1) f_{\text{sky}} \left[\frac{\hat{C}_{\ell}}{\bar{C}_{\ell}} + \ln \left(\frac{\bar{C}_{\ell}}{\hat{C}_{\ell}} \right) - 1 \right], \quad (4.14)$$

where, following Eqs. (4.3, 4.5), we have

$$\hat{C}_{\ell} = C_{\ell}^{\text{t+PMF}}|_{\text{fid}} + \alpha \times C_{\ell}^{\text{lens}}|_{\text{fid}} + N_{\ell}, \quad (4.15)$$

$$\bar{C}_{\ell} = C_{\ell}^{\text{t+PMF}} + \alpha \times C_{\ell}^{\text{lens}} + N_{\ell}. \quad (4.16)$$

In the above equations, the “t+PMF” superscript labels the BB spectrum from primordial tensor modes plus the one from primordial magnetic fields (see Eq. (4.9)), and the “lens” superscript labels B-modes due to lensing. The values of the delensing parameter α for the different experiments of Tab. 4.2 are collected in Tab. 4.3.

4.4 Results

In what follows we analyze the simulated datasets for the fiducial of Tab. 4.1 and the experiments of Tab. 7.1. For r and $B_{1\text{Mpc}}$ we use a linear prior in the range $[0, 3]$ and $[0, 5]$, respectively. We instead sample logarithmically η_v/η_B in the range $[10^6, 10^{17}]$. The inflationary tensor spectral index is given by the consistency relation $n_t = -r/8$ while we consider only nearly scale-invariant PMFs with $n_B = -2.9$.

4.4.1 Results from MCMC

Let us start from the MCMC analysis. As a first step, we analyze the ability of future/planned CMB experiments (listed in Tab. 4.2) of recovering our fiducial values for the PMF parameters. The constraints on $B_{1\text{Mpc}}$ from our selection of future experiments are reported in Tabs. (4.4, 4.5). In the first row of these tables we report the results from our analysis without variation in η_v/η_B .

In this case, we see that large satellite experiments as PIXIE and LiteBIRD can recover $B_{1\text{Mpc}}$ with a very good precision of about $\sigma(B_{1\text{Mpc}}) \sim 0.06 - 0.03$ nG. Conversely, a satellite mission as CORE-M5, with improved angular resolution respect to PIXIE or LiteBIRD, would measure the PMF amplitude with an excellent accuracy of $\sigma(B_{1\text{Mpc}}) \sim 0.02$ nG. The same accuracy can be achieved by the CMB-S4 experiment. However it is important to note that we assumed a quite optimistic value of $\ell_{\min} = 5$ for CMB-S4. It may be possible that the final ℓ_{\min} will shift towards higher values given a more limited scanning strategy due to, for example, shorter observation time and high frequency foregrounds. The Stage-3 experiment in both configurations “wide” or “deep” will provide much weaker constraints. This is due to the fact that the Stage-3 experiment is less sensitive to large-scale B-modes. It is interesting to note that while experiments as CORE-M5 and CMB-S4 can constrain a PMF with amplitude of $B_{1\text{Mpc}} = 1.08$ nG with a $\sigma(B_{1\text{Mpc}}) \sim 0.02$ nG precision, the upper limit on $B_{1\text{Mpc}}$ achievable from CMB-S4 in case of no PMF is $B_{1\text{Mpc}} < 0.52$ nG at 68% C.L. (see e.g. [101]). This is due to the fact that, at fixed η_v/η_B , the amplitude of the B-mode polarization from PMF scales as $C_\ell \sim B_{1\text{Mpc}}^4$. This means that the CMB will be able to strongly constrain a PMF, if detected, but also that upper limits on $B_{1\text{Mpc}}$ will be only marginally improved by future experiments (by a factor four in case of CMB-S4 if we compare with the upper limit of 2 nG from Planck).

These constraints are obtained under the assumption of a perfect knowledge of the time of PMF generation, and this is obviously not a realistic case. As we see from the second row of both Tabs. 4.4, 4.5, letting also η_v/η_B free to vary weakens the constraints on $B_{1\text{Mpc}}$. The constraints on $B_{1\text{Mpc}}$ are relaxed by a

4. MAGNETIC FIELDS AND GRAVITATIONAL WAVES

	PIXIE	LiteBIRD	CORE-M5
$\log_{10}(\eta_v/\eta_B) = 12$			
$B_{1\text{ Mpc}} \text{ (nG)}$	1.07 ± 0.10	$1.078^{+0.034}_{-0.028}$	$1.080^{+0.037}_{-0.038}$
$\log_{10}(\eta_v/\eta_B) \text{ free}$			
$B_{1\text{ Mpc}} \text{ (nG)}$	$1.16^{+0.35}_{-0.31}$	$1.15^{+0.34}_{-0.28}$	$1.07^{+0.10}_{-0.11}$
$\log_{10}(\eta_v/\eta_B)$	unconstrained	unconstrained	$12.4^{+2.9}_{-2.5}$

Table 4.4: 95% C.L. constraints on $B_{1\text{ Mpc}}$ and $\log_{10}(\eta_v/\eta_B)$ for the PIXIE, LiteBIRD and CORE-M5 experiments. These runs are assume that inflationary gravitational waves are absent, i.e. $r = 0$.

factor $\sim 4 - 5$ for the PIXIE and LiteBIRD experiments, a factor ~ 2 for CORE-M5 and by $\sim 50\%$ for CMB-S4. Moreover, the posterior of η_v/η_B is tighter than the prior essentially just with the CORE-M5 and CMB-S4 experiments.

Let us now see how the degeneracy between PMFs and a possible primordial GW component can be resolved. To this goal, we perform three different additional analyses:

- in the first analysis, in contrast to our fiducial model, we wrongly assume no PMF and we let only r free to vary with a tensor spectral index n_t given by the inflationary consistency relation $n_t = -r/8$. Here we quantify how the assumption of no PMF could bias the determination of r and provide a misleading first detection of primordial GWs;
- in the second analysis we consider as free parameters both r and a $B_{1\text{ Mpc}}$, but again we fix the ratio η_v/η_B , to understand if a CMB experiment could discriminate between inflationary GWs and a PMF when the latter is described just by one parameter;
- in the third analysis we vary r , $B_{1\text{ Mpc}}$ and η_v/η_B . As noticed in [101] and discussed in Section 4.2.2, since the time ratio determines the amplitude of the passive tensor modes, it is mostly degenerate with r in the B-mode polarization.

The results of these three analysis are reported in Tabs. (4.6, 4.7). As we can see from the first row of both Tabs. (4.6, 4.7), analyzing a CMB dataset with the wrong assumption of no PMF and $B_{1\text{ Mpc}} = 0$ could lead to a bias on the tensor-to-scalar ratio r . An experiment as PIXIE could provide an indication at above three standard deviations for a primordial tensor amplitude of $r \sim 0.0065$. LiteBIRD, CORE-M5 and CMB-S4 will provide an even higher evidence for $r > 0$, with statistical significances that could reach (and also go over) about 10 standard

4. MAGNETIC FIELDS AND GRAVITATIONAL WAVES

	Stage-3 (Deep)	Stage-3 (Wide)	CMB-S4
$\log_{10}(\eta_v/\eta_B) = 12$			
$B_{1\text{ Mpc}}$ (nG)	< 1.2	< 1.2	1.079 ± 0.020
$\log_{10}(\eta_v/\eta_B)$ free			
$B_{1\text{ Mpc}}$ (nG)	< 1.3	< 1.3	$1.074^{+0.061}_{-0.065}$
$\log_{10}(\eta_v/\eta_B)$	unconstrained	unconstrained	12.2 ± 1.8

Table 4.5: As in Tab. 4.4 for the Stage-3 (deep and wide configurations) and CMB-S4 experiments.

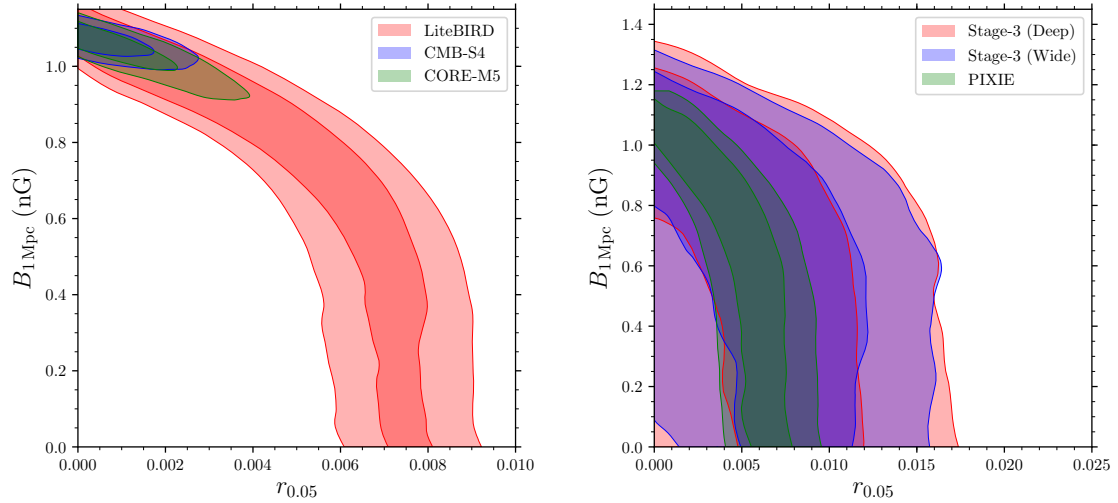


Figure 4.3: Forecasted constraints in the $B_{1\text{ Mpc}}$ vs. r plane from MCMC for LiteBIRD and CMB-S4 (left panel) and for PIXIE, Stage-3, and CORE-M5 (right panel). The fiducial model has $B_{1\text{ Mpc}} = 1.08$ nG, $\eta_v/\eta_B = 10^{12}$ and $r = 0$. Clearly the LiteBIRD, PIXIE and Stage-3 experiments are unable to distinguish the PMF from inflationary GWs. On the contrary, CMB-S4 and CORE-M5 can break the degeneracy thanks to better sensitivity to small scale B-modes.

4. MAGNETIC FIELDS AND GRAVITATIONAL WAVES

	PIXIE	LiteBIRD	CORE-M5
r	$0.0065^{+0.0029}_{-0.0028}$	$0.0073^{+0.0018}_{-0.0017}$	0.0072 ± 0.0011
r	$0.0050^{+0.0037}_{-0.0047}$	< 0.0082	< 0.0031
$B_{1\text{ Mpc}} \text{ (nG)}$	< 1.1	< 1.1	$1.034^{+0.079}_{-0.096}$
r	< 0.0083	$0.0051^{+0.0035}_{-0.0046}$	< 0.0057
$B_{1\text{ Mpc}} \text{ (nG)}$	< 1.2	< 1.3	$1.06^{+0.11}_{-0.12}$
$\log_{10}(\eta_v/\eta_B)$	unconstrained	unconstrained	< 13

Table 4.6: 95% C.L. constraints on $B_{1\text{ Mpc}}$, $\log_{10}(\eta_v/\eta_B)$ and r for the PIXIE, LiteBIRD and CORE-M5 experiments. Notice that these are one-dimensional marginalized constraints: given the strong degeneracy between r and $B_{1\text{ Mpc}}$, the detection of r when both parameters are varied is not significant.

deviations. The experimental evidence for $r > 0$ that these experiments obtain is therefore completely misleading and based on the wrong assumption of $B_{1\text{ Mpc}} = 0$.

The next step consists in letting also $B_{1\text{ Mpc}}$ free to vary and see if these future experiments will be able to discriminate between r and $B_{1\text{ Mpc}}$. The results of this analysis are on the second and third rows of both Tabs. (4.6, 4.7). As we can see, when $B_{1\text{ Mpc}}$ is included, the detection for $r > 0$ simply disappears or is rather weaker for all the experiments considered. Furthermore, for the PIXIE, LiteBIRD and Stage-3 experiments there is also no clear detection for $B_{1\text{ Mpc}}$. What is happening is clear by looking at Fig. 4.3: a degeneracy is present on the $B_{1\text{ Mpc}}$ vs. r plane and the experiments are simply unable to discriminate between a genuine primordial tensor component from GWs and PMFs. For PIXIE and LiteBIRD this is essentially due to the poor experimental angular resolution that does not allow to access small scales, $\ell \gtrsim 1000$, where the vector compensated PMF B-mode could be detected. Indeed, when we consider experiments with better angular resolution as CORE-M5 and CMB-S4 the degeneracy is broken, the PMF is well measured and just an upper limit is obtained for r . For the Stage-3 experiment a degeneracy between r and $B_{1\text{ Mpc}}$ is also present: this is essentially due to the lower experimental sensitivity that does not allow clear detection of the B-mode signal of the fiducial model. Finally, from the last three rows of Tabs. (4.6, 4.7) we see that the same conclusions hold when we let also η_v/η_B free to vary.

	Stage-3 (Deep)	Stage-3 (Wide)	CMB-S4
r	$0.0084^{+0.0079}_{-0.0084}$	$0.0084^{+0.0075}_{-0.0081}$	0.0072 ± 0.0014
r	< 0.015	< 0.015	< 0.0022
$B_{1\text{ Mpc}} \text{ (nG)}$	< 1.1	< 1.1	$1.058^{+0.053}_{-0.055}$
r	< 0.015	< 0.014	< 0.0059
$B_{1\text{ Mpc}} \text{ (nG)}$	< 1.2	< 1.2	$1.073^{+0.065}_{-0.069}$
$\log_{10}(\eta_v/\eta_B)$	unconstrained	unconstrained	< 12

Table 4.7: As in Tab. 4.6 for the Stage-3 (deep and wide configurations) and CMB-S4 experiments.

4.4.2 Delensing

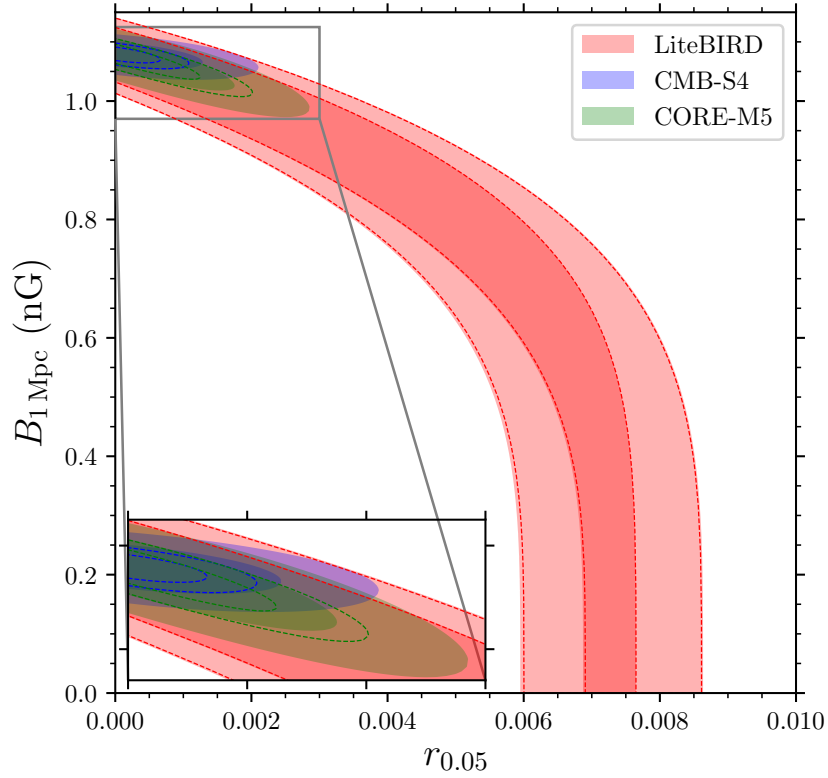


Figure 4.4: Impact of delensing for LiteBIRD, CMB-S4 and CORE-M5: dashed lines represent the 68% C.L. and 95% C.L. contours after delensing. Clearly, the delensing procedure affects the constraints on r and $B_{1\text{ Mpc}}$ only if the degeneracy between the two is broken.

In this Section we briefly study the impact of delensing on the forecasted constraints in the $B_{1\text{ Mpc}}$ vs. r plane from the simulated data for LiteBIRD, CMB-S4 and CORE-M5, using the BB exact likelihood and fixing all parameters apart from r and $B_{1\text{ Mpc}}$. To obtain the theoretical angular spectra we rescale two templates

4. MAGNETIC FIELDS AND GRAVITATIONAL WAVES

computed for $r = 0.1$, $B_{1\text{ Mpc}} = 0\text{ nG}$ and $r = 0$, $B_{1\text{ Mpc}} = 1.08\text{ nG}$ (fixing in both cases $\eta_v/\eta_B = 10^{12}$). We leave n_t fixed to $-0.1/8$, even if r is varied: at such low values of r as those probed by LiteBIRD, CMB-S4 and CORE-M5 the error is negligible (this is confirmed a posteriori by comparing Fig. 4.4 with Fig. 4.3).

The 68% C.L. and 95% C.L. contours are reported in Fig. 4.4. First, we notice that even fixing all parameters apart from $B_{1\text{ Mpc}}$ and r leads to only marginally more stringent constraints than those depicted in Fig. 4.3 (besides, recall that in this case we are not including the information coming from the TT, EE and TE spectra). Most importantly, we also see that delensing will not help to break the degeneracy between the two parameters for LiteBIRD. For CORE-M5 and CMB-S4, instead, delensing would shrink the 95% C.L. contours of roughly a factor of 2. We did not show the forecasts for Stage-3 or PIXIE in Fig. 4.4: as for LiteBIRD, also in this case delensing would not help in breaking the degeneracy between r and $B_{1\text{ Mpc}}$.

4.4.3 Importance of small-scale B-mode measurements

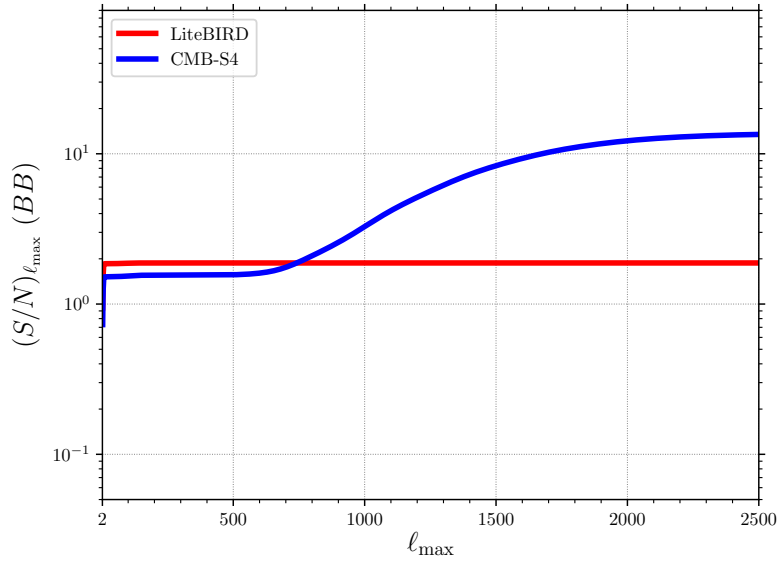


Figure 4.5: S/N of Eq. (4.17) at varying ℓ_{max} for the LiteBIRD and CMB-S4 experiments.

Finally, we investigate in more detail the differences between an experiment that cannot break the degeneracy between r and $B_{1\text{ Mpc}}$ (*i.e.* LiteBIRD) and one that can (*i.e.* CMB-S4). We consider two different models with roughly the same χ^2_{min} for the LiteBIRD simulated dataset, but with very different values of r and $B_{1\text{ Mpc}}$: the model “(1)” has ($r = 1.76 \times 10^{-5}$, $B_{1\text{ Mpc}} = 1.064\text{ nG}$), while the model “(2)” has ($r = 7.22 \times 10^{-3}$, $B_{1\text{ Mpc}} = 7.57 \times 10^{-2}\text{ nG}$). Then, we expect that for LiteBIRD

it will be impossible to distinguish between these two models, while CMB-S4 will be able to break the degeneracy between them.

We can estimate how well the two experiments are able to distinguish model (2) from model (1) by constructing a simple $\chi_\ell^2 \equiv (\Delta C_\ell / \sigma_\ell)^2$ for the difference $\Delta C_\ell \equiv C_\ell^{(2)} - C_\ell^{(1)}$. Thus, assuming uncorrelated multipoles, we can write the cumulative signal-to-noise ratio as

$$(S/N)_{\ell_{\max}}^2 = \sum_{\ell=2}^{\ell_{\max}} \frac{\left(C_\ell^{(2)} - C_\ell^{(1)}\right)^2}{\sigma_\ell^2}, \quad (4.17)$$

where we focus on B-modes only and σ_ℓ is given by noise plus cosmic variance, i.e. [131]

$$\sigma_\ell = \sqrt{\frac{2}{(2\ell + 1)f_{\text{sky}}}} \left(C_\ell^{(1)} + N_\ell\right). \quad (4.18)$$

We plot S/N for varying ℓ_{\max} in Fig. 4.5: we see that for LiteBIRD it remains of order 1 up to high ℓ_{\max} , while for CMB-S4 it becomes of order 10 at $\ell_{\max} \gtrsim 1000$.

We can show the importance of including small angular scales in a different way by using directly the full B-mode likelihood for the CMB-S4 experiment, as we did in our analysis of the impact of delensing. Varying ℓ_{\max} (having fixed the delensing parameter α to 1) we can see at which angular scale the degeneracy between r and $B_{1\text{ Mpc}}$ can be broken by this experiment. In Fig. 4.6, we see that this happens at $\ell_{\max} \gtrsim 900$: if CMB-S4 could not access higher multipoles, the constraints on r and $B_{1\text{ Mpc}}$ would be similar to those of LiteBIRD.

4. MAGNETIC FIELDS AND GRAVITATIONAL WAVES

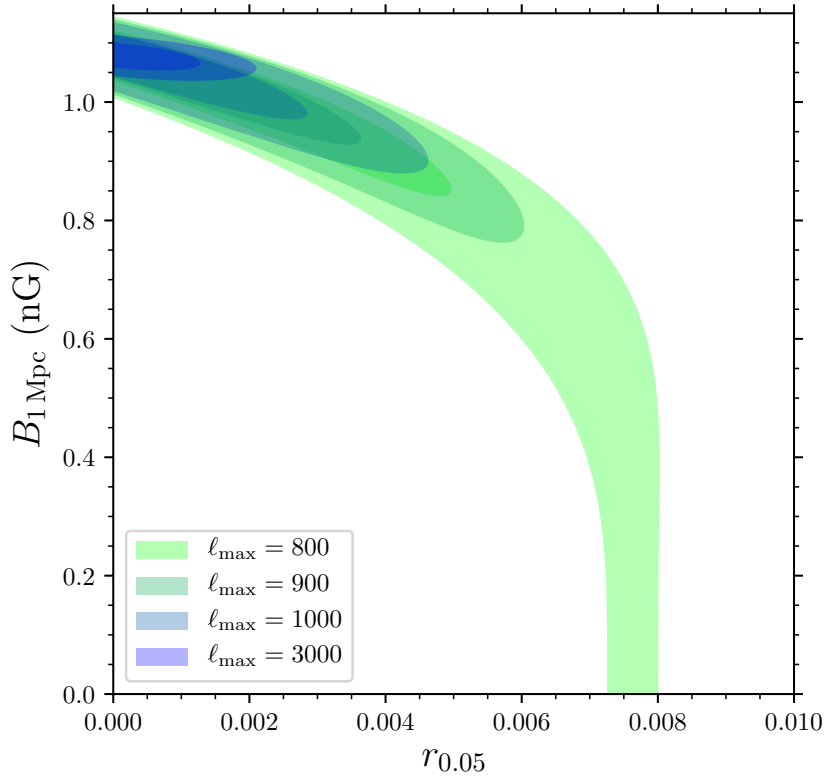


Figure 4.6: Impact of varying ℓ_{\max} on CMB-S4 constraints: we see that the degeneracy between r and $B_{1\text{Mpc}}$ is broken if B-mode anisotropies can be measured on scales $\ell \gtrsim 900$.

4.5 Constraints from Faraday rotation

PMFs also induce Faraday rotation (FR) of CMB polarization. It is therefore useful to evaluate the ability of future CMB experiments to detect a PMF with an amplitude of 1.08 nG through FR and break the possible degeneracies between r and $B_{1\text{Mpc}}$. FR of the linear polarization of CMB photons is described by the rotation angle α_F , defined in terms of the Stokes Q and U parameters by $(Q \pm iU)(\hat{n}) \rightarrow (Q \pm iU)(\hat{n})e^{\pm 2i\alpha_F(\hat{n})}$. An inhomogeneous magnetic field sources anisotropies in the rotation angle, whose angular power spectrum is related to the two-point correlation function of the magnetic field (see, e.g., [102–105, 132]). The angular power spectrum $C_\ell^{\alpha_F\alpha_F}$ of the rotation angle $\alpha_F(\hat{n})$ can be constrained directly by exploiting the fact that, at first order in α_F , the off-diagonal elements of the two-point correlation functions of E- and B-modes are proportional to the rotation field [133]. One can take advantage of this feature to build a quadratic estimator to measure the anisotropic rotation [133–135]. The rotation of E-modes into B-modes, moreover, leads to a contribution $C_\ell^{\text{BB,FR}}$ that should be in principle added to Eq. (4.9) (see [96] for an extensive review). However the angular spectrum $C_\ell^{\alpha_F\alpha_F}$, and then $C_\ell^{\text{BB,FR}}$, scales as ν^{-4} : thus we expect to have a larger signal for these FR-induced B-modes at lower frequencies (e.g. $\nu \sim 30$ GHz), that will not

be optimally sampled by the experiments considered here.

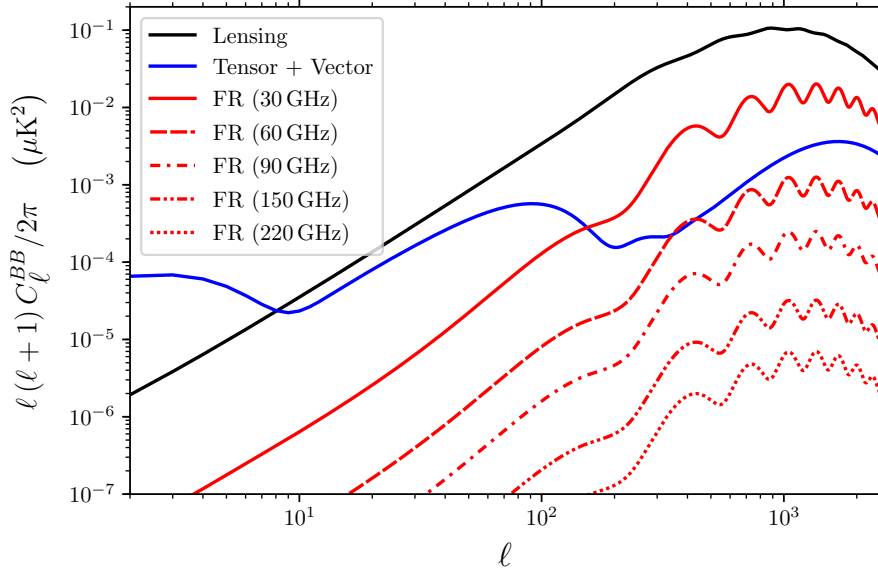


Figure 4.7: B-mode angular spectrum from Faraday rotation ($B_{1\text{ Mpc}} = 1.08\text{ nG}$ is assumed) at frequencies of 30 GHz, 60 GHz, 90 GHz, 150 GHz and 220 GHz. The B-modes from magnetic perturbations are also shown, together with the standard lensing prediction. Clearly the B-modes from FR are completely negligible for an experiment mostly sensitive to frequencies around 150 GHz as those considered in this Chapter. PIXIE will operate at lower frequencies, but it will have access only to very low multipoles, where the FR signal is negligible anyway.

Indeed, these experiments are not conceived for a measurement at these frequencies:

- lower frequencies are more contaminated by galactic foregrounds and are mostly used to identify and remove them rather than to extract genuine cosmological information;
- for a given experimental configuration, lower frequencies are limited by diffraction and have smaller angular resolution. Therefore, space experiments such as CORE-M5 or LiteBIRD have been designed with the largest number of detectors at frequencies around $\sim 150\text{ GHz}$ where the minimal foreground contamination is expected.

In Fig. 4.7 we plot the expected signal in the B-mode angular power spectrum from Faraday rotation generated by a magnetic field of 1.08 nG for various frequencies. The Faraday rotation B-modes are obtained using Eq. (38) of [102]. In Fig. 4.7 we also plot the lensing B-mode spectrum and the frequency-independent contribution of Eq. (4.9), i.e. the one generated by vector- and tensor-mode perturbations in the metric, sourced by the stress-energy in the PMF. As we can clearly see, the

4. MAGNETIC FIELDS AND GRAVITATIONAL WAVES

PIXIE	LiteBIRD	CORE-M5	Stage-3 (Deep)	Stage-3 (Wide)	CMB-S4
0.05	0.7	15	20	2	10^2

Table 4.8: S/N ratio for the detection of a nearly scale-invariant PMF of 1.08 nG through FR.

B-modes from Faraday rotation at 150 GHz are about four orders of magnitude smaller than the lensing signal, i.e. they will be undetectable by an experiment operating at those frequencies. At 30 GHz the signal is much larger, however none of the experiment considered in this Chapter will sample this frequency with the exception of PIXIE. In this case, however, the angular resolution will not be sufficient to detect the B-modes from Faraday rotation, since PIXIE can arrive at most at $\ell_{\max} = 500$. The LiteBIRD and CORE-M5 could produce full CMB sky maps at frequencies of 60 GHz. It is therefore interesting to investigate if these B-modes from FR could be detected by these experiments. Unfortunately, as we show in Fig. 4.8, neither of these two experiments will be able to detect them. Indeed, they will not have enough sensitivity and angular resolution at these frequencies. To summarize, the contribution $C_{\ell}^{\text{BB,FR}}$ to the B-mode angular power spectrum induced by a PMF of 1.08 nG is not detectable by the experiments considered here. For this reason, in the following we will focus on a forecast for the detection of anisotropies in the FR angle α_F of the E modes: clearly, a detection of α_F would allow to confirm whether a possible B-mode measurement is due to primordial GWs or to PMFs.

Then, to perform this forecast we consider the following approximated angular power spectrum of α_F induced by a nearly scale-invariant PMF of 1.08 nG (see e.g. Eq. (4) in [105]):

$$\frac{L(L+1)C_L^{\alpha_F\alpha_F}}{2\pi} = 4.2 \times 10^{-8} \text{ rad}^2, \quad (4.19)$$

where we have assumed a CMB observational frequency of $\nu \sim 150$ GHz. We have then estimated the experimental noise on $C_L^{\alpha_F\alpha_F}$ and computed the relevant signal-to-noise ratio using the quadratic estimator described in [134, 135] (see Appendix A). For simplicity we have neglected the contamination of “spurious” FR induced by magnetic fields in our galaxy and lensing. Our results (shown in Tab. 4.8) should therefore be considered as optimistic since the removal of these terms could lead to a significantly lower S/N (see [101]).

4. MAGNETIC FIELDS AND GRAVITATIONAL WAVES

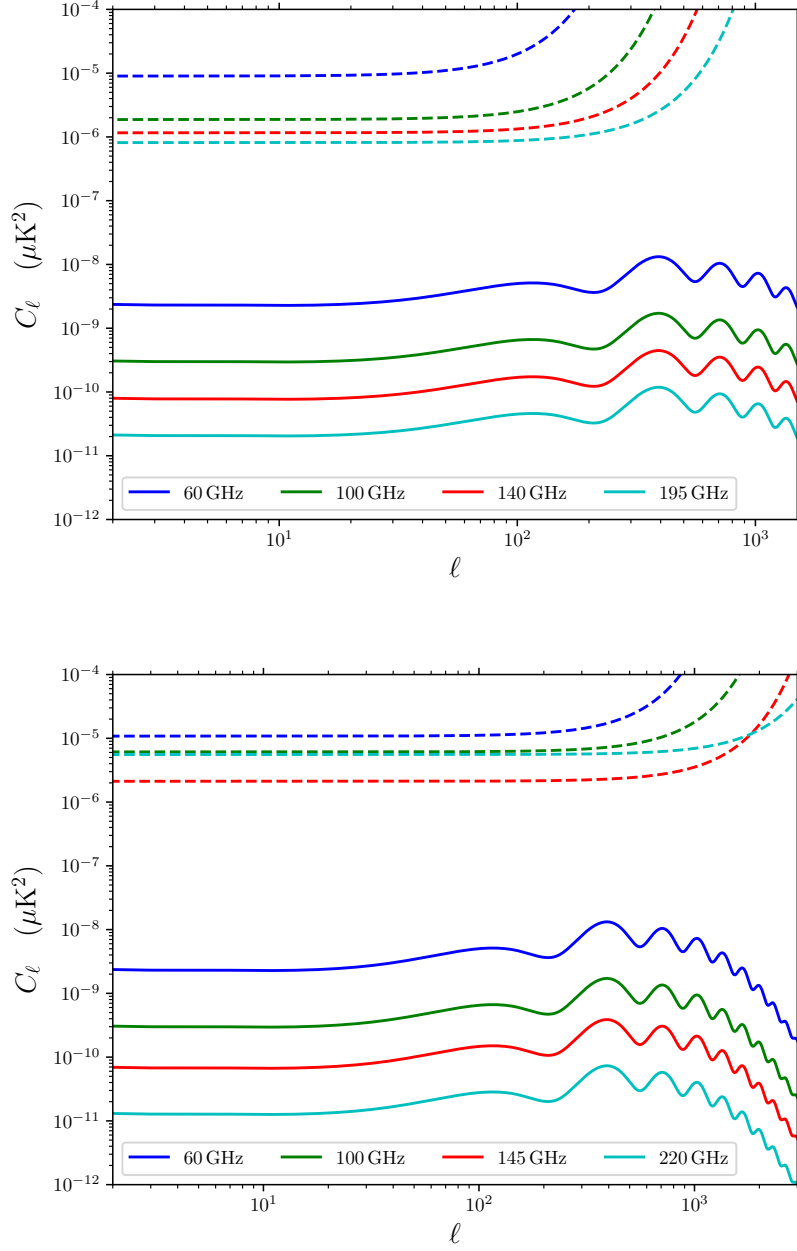


Figure 4.8: Expected experimental white noise for the lowest channels of LiteBIRD (top panel) and CORE-M5 (bottom panel), together with the expected signal from B-modes generated by Faraday rotation (for a PMF with $B_{1\text{ Mpc}} = 1.08\text{ nG}$) at the same frequencies. Clearly, the signal is undetectable in any frequency channel by any of the two experiments.

We see that experiments as PIXIE and LiteBIRD will essentially be unable to detect our fiducial PMF through FR. This is mainly due to the poor angular resolution that does not let these experiments measure E- and B-modes at $\ell \sim 1000$, i.e. at scales that are relevant for a measure of α_F . Including the frequency dependence of the signal will not change this result since at lower frequencies would correspond also an even lower angular resolution. On the contrary, the Stage-3 experiment, especially in the “deep” configuration, will be able to detect

the PMF via FR with high accuracy. While in this case r is poorly constrained, a combination with the LiteBIRD experiment could be extremely important. The CMB-S4 experiment will constrain a PMF with great accuracy, in agreement with the results presented in [101].

4.6 Discussion and Conclusion

Undoubtedly, one of the main goals of future CMB experiments is a detection of inflationary GWs through their effect on the B-mode polarization. Such a detection would be a strong hint towards the quantum nature of gravity. However, a simple detection of B-modes is not enough to confirm their primordial origin: primordial magnetic fields can cause a contamination of a possible signal from vacuum fluctuations of the metric. The goal of this Chapter was to show that future CMB experiments targeting inflationary GWs at the level of $r \approx 10^{-3}$ will not be able to claim a detection unless they are able to distinguish them from a PMF of amplitude ~ 1 nG.

Satellite missions as PIXIE or LiteBIRD, that are limited to large angular scales, will not be able to break such degeneracy. For experiments with better angular resolution, like CORE-M5 or CMB-S4, it will instead be possible to discriminate between the two mechanisms since they will be able to detect the compensated vector perturbations of the PMF. A second way to break the degeneracy is that of measuring the PMF through Faraday rotation of the CMB polarization. While B-modes induced by FR are practically undetectable by the experiments considered here, a better opportunity is offered by measurements of anisotropies in the FR angle. We find that also in this case PIXIE and LiteBIRD will not be able to significantly detect the PMF. However, we have found that the Stage-3 experiment could already put stringent constraints on it. A nice complementarity therefore exists between the LiteBIRD and Stage-3 experiments that could allow to break the degeneracy between the tensor-to-scalar ratio and the PMF amplitude.

Before concluding we note that there are other signatures typical of PMFs that could help in distinguishing them from inflationary GWs:

- the B-modes produced by PMFs are highly non-Gaussian, since they are proportional to the square of the field amplitude. Consequently, bispectrum and trispectrum measurements could also place strong constraints on them [110, 136, 137];
- PMFs are damped on small scales, leading to heating of baryons and electrons and producing Compton- γ distortions in the CMB (see [110]). This has been used to place an upper limit of 0.90 nG at 95% C.L on the magnetic field amplitude (recently [138] has improved this bound to 0.83 nG).

4. MAGNETIC FIELDS AND GRAVITATIONAL WAVES

Regarding the second of these signatures, we emphasize that uncertainties in the modeling of the heating and in the reionization process may affect the constraint [139]. Moreover, and most importantly, a PMF of $\sim 0.9 \text{ nG}$ would produce a B-mode spectrum essentially rescaled by a factor of 0.5 with respect to the template considered here. This could still bias future CMB polarization searches for primordial GWs at the level of $r \approx 10^{-3}$ if not accounted for.

In summary, future constraints at the level of 0.2 nG , as expected from FR measurements by the CMB-S4 experiment (see also [101]), will be crucial in limiting a spurious B-mode PMF contribution to sub-percent level respect to the value of $r \approx 10^{-3}$.

5 CORNERING THE PLANCK LENSING TENSION WITH FUTURE CMB DATA

In this Chapter we discuss the possibility of future experiments to confirm or rule out the present A_{lens} tension in Planck data. We also study how the tension will be seen in different frequency channels for the CMB-S4 experiment

The Chapter is mainly based on the work [Phys.Rev. D97 \(2018\) no.12, 123534](#)

Contents

5.1	Introduction	97
5.2	Current status of the A_{lens} anomaly	99
5.3	Method	100
5.4	Results	102
5.4.1	Future constraints on A_{lens}	102
5.4.2	Testing A_{lens} in different spectra and frequency channels .	104
5.4.3	Using B modes to test the A_{lens} anomaly.	105
5.4.4	Future constraints on angular scale dependence of A_{lens} . .	108
5.5	Conclusions	109

5.1 Introduction

The precise measurements of Cosmic Microwave Background (CMB) anisotropies made by the Planck satellite [27] have provided a wonderful confirmation of the standard cosmological model of structure formation based on inflation, dark matter and a cosmological constant. The predictions of acoustic oscillations in the CMB anisotropy angular power spectra have been fully confirmed with unprecedented accuracy. Nonetheless few, interesting, tensions are emerging hinting to systematics and/or possible extensions to the standard scenario (see e.g. [140–143]).

The most relevant anomaly, at least from the statistical point of view, concerns the amount of lensing in the CMB angular power spectra. Gravitational lensing

slightly redistributes the photon paths from the last scattering surface, smoothing the acoustic oscillations in the CMB anisotropy and polarization power spectra (see [144]). The amount of smearing due to CMB lensing, once the cosmological parameters are fixed, can be computed with great accuracy (see e.g. [145]) and the effect is included in all current parameter analyses. In [26] a phenomenological parameter, A_{lens} , was introduced that essentially rescales the lensing amplitude in the CMB spectra. This parameter has, in principle, no physical meaning and is mainly used as an effective parameter for testing theoretical assumptions and systematics. However, the value of this parameter from the latest Planck analysis of [123] is $A_{lens} = 1.15^{+0.13}_{-0.12}$ at 95% C.L., i.e. about 2.3σ larger than the expected value with a significant impact on parameter extraction.

Indeed, the inclusion of A_{lens} in the analysis shifts the constraints derived from Planck data on several cosmological parameters. Interestingly, some tension exists between the cosmological parameters derived from a combination of pre-Planck datasets and those obtained by the Planck satellite (see Table I in [146] and discussion in [141, 142]). As noted in [141, 142], the inclusion of A_{lens} significantly reduces this tension. Moreover, lensing in the CMB spectra is crucial in constraining neutrino masses. A larger value for A_{lens} , if not accounted for, could produce biased bounds on neutrino masses, stronger than those that realistically could be reached with the Planck specifications and experimental noise. Indeed, from simulated Planck angular spectra (assuming a neutrino mass of $\Sigma m_\nu \leq 0.06$ eV), one would expect a limit on the sum of neutrino masses of $\Sigma m_\nu \leq 0.59$ eV at 95% c.l., while the current limit from real Planck data is much stronger, at the level of $\Sigma m_\nu \leq 0.34$ eV at 95% c.l. (see [123]). These stronger than expected neutrino mass bounds from Planck are connected to the 2.3σ A_{lens} tension and should be treated with great care. Finally, A_{lens} anti-correlates with the amplitude of r.m.s. matter density fluctuations on $8h^{-1}\text{Mpc}$ scales, the so-called σ_8 parameter. Allowing A_{lens} to vary brings indeed the constraints on the $S_8 = \sigma_8(\Omega_m/0.3)^{0.5}$ parameter from $S_8 = 0.852 \pm 0.018$ at 68% C.L. to $S_8 = 0.808 \pm 0.034$, in better agreement with the constraints derived from cosmic shear data from the KiDS-450 [147] and DES [148, 149] surveys.

While A_{lens} seems to solve several current tensions, there are at least two puzzling aspects of the A_{lens} anomaly that should suggest some caution. First of all, there is no easy theoretical way to accommodate a value of A_{lens} *larger* than expected, even in an extended parameter space (see e.g. [5, 7, 25]). Proposals that can give a theoretical explanation to the A_{lens} anomaly include, for example, modified gravity [150], running of the running of the spectral index [151], closed universes [152], and compensated baryon isocurvature perturbations [153, 154]. These explanations are certainly all rather exotic and would hint for a significant

5. CORNERING THE PLANCK LENSING TENSION WITH FUTURE CMB DATA

change in the standard scenario. The second point is that an anomalous A_{lens} value, if related to lensing, must show up also in the CMB lensing measurements based on the trispectrum analysis of the Planck temperature and polarization maps. However Planck CMB lensing is in perfect agreement with the standard expectations. Combining the Planck angular power spectra with the CMB lensing yields $A_{lens} = 1.025^{+0.051}_{-0.058}$ [27], in agreement with the standard value even if at the price of an higher χ^2 value due to the relative inconsistency between the two datasets. This fact in practice, even if based on the assumption of Λ CDM, disfavors the hypothesis of $A_{lens} > 1$ due to gravitational lensing.

These two aspects could suggest that the A_{lens} anomaly is related to some systematics in the data. However, the anomaly survived the scrutiny of two Planck data releases and hints for its presence have already been reported, albeit at small statistical level, in pre-Planck data (see e.g. [155]). It is therefore timely to investigate the potential of future CMB experiments to confirm and/or rule out the A_{lens} anomaly. Several ground and space-based experiments are indeed proposed or expected in the next years that will sample the small scale region of the CMB angular spectrum. At the same time it is important to scrutinize the ability of these experiments in detecting a possible scale dependence of the effect. This is indeed the goal of the present chapter. While this kind of analysis is straightforward, none of the several recent papers that forecasted the ability of future experiments in constraining cosmological parameters (see e.g. [33, 76, 127]), as far as we know, considered the A_{lens} parameter.

In the next Section we briefly discuss the current status of the A_{lens} tension. In Section 5.3 we describe the data analysis method adopted for our forecasts. In Section 5.4 we show the obtained results and in Section 5.5 we present our conclusions.

5.2 Current status of the A_{lens} anomaly

In this section we discuss the current status of the A_{lens} anomaly and its impact on current cosmological parameter estimation. In Table 5.1 we compare the constraints presented in [146] with those derived from Planck 2015 temperature and polarization data assuming Λ CDM (third column) and a variation in A_{lens} (see fourth column of the table). We also show the effects of including cosmic shear data from CFHTLenS (named WL) as in [27] (fifth column). In the square brackets, on the right side of the constraint, we also report the shift S between the cosmological constraints from Planck and pre-Planck measurements defined as:

$$S = \frac{|\Pi_{pre-Planck} - \Pi_{Planck}|}{\sqrt{\sigma_{pre-Planck}^2 + \sigma_{Planck}^2}} \quad (5.1)$$

5. CORNERING THE PLANCK LENSING TENSION WITH FUTURE CMB DATA

Parameter	WMAP9 +ACT+SPT	Planck TTTEEE	Planck TTTEEE (A_{lens})	Planck TTTEEE +WL (A_{lens})
$100\Omega_b h^2$	2.242 ± 0.032	2.222 ± 0.015 [0.56]	2.239 ± 0.017 [0.08]	2.245 ± 0.017 [0.08]
$100\Omega_c h^2$	11.34 ± 0.36	12.03 ± 0.14 [1.79]	11.87 ± 0.16 [1.34]	11.78 ± 0.15 [1.13]
$10^4\theta_{MC}$	104.24 ± 0.10	104.069 ± 0.032 [1.63]	104.09 ± 0.033 [1.42]	104.10 ± 0.033 [1.32]
n_s	0.9638 ± 0.0087	0.9626 ± 0.0044 [0.12]	0.9675 ± 0.0049 [0.37]	0.9697 ± 0.0047 [0.59]
Ω_Λ	0.723 ± 0.019	0.6812 ± 0.0086 [2.00]	0.6920 ± 0.0096 [1.46]	0.6974 ± 0.0089 [1.22]
Ω_m	0.277 ± 0.019	0.3188 ± 0.0086 [2.00]	0.3080 ± 0.0096 [1.46]	0.3026 ± 0.0089 [1.22]
σ_8	0.780 ± 0.017	0.8212 ± 0.0086 [2.16]	0.806 ± 0.017 [1.08]	0.797 ± 0.016 [0.73]
t_0 [Gyrs]	13.787 ± 0.057	13.822 ± 0.025 [0.56]	13.790 ± 0.029 [0.05]	13.777 ± 0.028 [-0.20]
H_0 [km/s/Mpc]	70.3 ± 1.6	67.03 ± 0.61 [1.91]	67.84 ± 0.72 [1.4]	68.25 ± 0.69 [1.18]
A_{lens}	1	1	1.154 ± 0.076	1.194 ± 0.076

Table 5.1: Constraints at 68% c.l. on cosmological parameters from pre-Planck datasets (second column, see [146]), Planck TTTEEE in case of Λ CDM (third column), and Planck TTTEEE and Planck TTTEEE+WL varying A_{lens} (fourth and fifth column, respectively). In the square brackets we report the shift S , defined via Eq.(5.1), that quantifies the discrepancy in the constraint on the parameter Π between pre-Planck and Planck measurements. As we can see, when A_{lens} is included, the tensions on the value of the Hubble constant, the matter and cosmological constants densities and the value of σ_8 are significantly reduced, especially when including cosmic shear data (WL).

where Π and σ are the parameter mean value and uncertainty reported for the pre-Planck and Planck datasets. As we can see, the most relevant (at about $\sim 2\sigma$) shifts on the values of Ω_m , σ_8 and H_0 are relieved when a variation in A_{lens} is considered, especially when also the WL dataset is included. As we can see, we obtain a value for $A_{lens} > 1$ at about 2 sigma level from Planck TTTEEE and at about 2.6 sigma from Planck TTTEEE+WL. The inclusion of cosmic shear data therefore does not only improve the agreement with the WMAP constraints but also the statistical significance for A_{lens} .

5.3 Method

The goal of this paper is to investigate to what extent future CMB experiments will be able to constrain the value of A_{lens} and falsify/confirm the current anomaly. We have therefore simulated CMB anisotropy and polarization angular spectra data with a noise given by:

$$N_\ell = w^{-1} \exp(\ell(\ell + 1)\theta^2/8 \ln 2), \quad (5.2)$$

where w^{-1} is the experimental power noise expressed in $\mu\text{K-arcmin}$ and θ is the experimental FWHM angular resolution. We have considered several future experiments with technical specifications listed in Table 5.2. In particular, we have

5. CORNERING THE PLANCK LENSING TENSION WITH FUTURE CMB DATA

Experiment	Beam	Power noise w^{-1} [$\mu\text{K-arcmin}$]	ℓ_{max}	ℓ_{min}	f_{sky}
Pixie	96'	4.2	500	2	0.7
LiteBIRD	30'	4.5	3000	2	0.7
CORE	6'	2.5	3000	2	0.7
CORE-ext	4'	1.5	3000	2	0.7
Stage-III (Deep)	1'	4	3000	50	0.06
Stage-III (Wide)	1.4'	8	3000	50	0.4
Stage-IV	3'	1	3000	5, 50	0.4

Table 5.2: *Experimental specifications for the several configurations considered in the forecasts.*

Parameter	Value
$\Omega_b h^2$	0.02225
$\Omega_c h^2$	0.1198
τ	0.055
n_s	0.9645
$100\theta_{MC}$	1.04077
$\ln(10^{10} A_s)$	3.094
A_{lens}	1.00

Table 5.3: *Cosmological Parameters assumed for the fiducial model.*

considered three possible CMB satellite experiments as CORE [76, 78], LiteBIRD [156] and PIXIE [126]. A Stage-III experiment in two possible configurations as in [127], i.e. a 'wide' experiment similar to AdvACT and a 'deep' experiment similar to SPT-3G. Finally we consider the possibility of a 'Stage-IV' experiment as in [127] (but see also [33, 157]).

We have computed the theoretical CMB angular power spectra C_ℓ^{TT} , C_ℓ^{TE} , C_ℓ^{EE} , C_ℓ^{BB} for temperature, cross temperature-polarization and E and B modes polarization using the CAMB Boltzmann code [122]. The angular spectra are generated assuming a fiducial flat Λ CDM model with parameters compatible with the recent Planck 2015 constraints [123].

The theoretical C_ℓ 's are then compared with the simulations using the Monte

5. CORNERING THE PLANCK LENSING TENSION WITH FUTURE CMB DATA

Carlo Markow Chain code CosmoMC¹ [128] based on the Metropolis-Hastings algorithm. The convergence of the chains is verified by the Gelman and Rubin method. Given a simulated dataset, for each theoretical model we evaluate a likelihood \mathcal{L} given by

$$-2 \ln \mathcal{L} = \sum_l (2l+1) f_{\text{sky}} \left(\frac{D}{|\bar{C}|} + \ln \frac{|\bar{C}|}{|\hat{C}|} - 3 \right), \quad (5.3)$$

where \bar{C}_l are the fiducial spectra plus noise (i.e. our simulated dataset) while \hat{C}_l are the theory spectra plus noise. $|\bar{C}|$, $|\hat{C}|$ are given by:

$$|\bar{C}| = \bar{C}_\ell^{\text{TT}} \bar{C}_\ell^{\text{EE}} \bar{C}_\ell^{\text{BB}} - \left(\bar{C}_\ell^{\text{TE}} \right)^2 \bar{C}_\ell^{\text{BB}}, \quad (5.4)$$

$$|\hat{C}| = \hat{C}_\ell^{\text{TT}} \hat{C}_\ell^{\text{EE}} \hat{C}_\ell^{\text{BB}} - \left(\hat{C}_\ell^{\text{TE}} \right)^2 \hat{C}_\ell^{\text{BB}}, \quad (5.5)$$

with D defined as

$$\begin{aligned} D = & \hat{C}_\ell^{\text{TT}} \bar{C}_\ell^{\text{EE}} \bar{C}_\ell^{\text{BB}} + \bar{C}_\ell^{\text{TT}} \hat{C}_\ell^{\text{EE}} \bar{C}_\ell^{\text{BB}} + \bar{C}_\ell^{\text{TT}} \bar{C}_\ell^{\text{EE}} \hat{C}_\ell^{\text{BB}} \\ & - \bar{C}_\ell^{\text{TE}} \left(\bar{C}_\ell^{\text{TE}} \hat{C}_\ell^{\text{BB}} + 2 \hat{C}_\ell^{\text{TE}} \bar{C}_\ell^{\text{BB}} \right). \end{aligned} \quad (5.6)$$

In what follows we also test the possibility of a angular dependence for A_{lens} . Such scale dependence could arise from beyond standard model physics such as modified gravity, cold dark energy, or massive neutrinos. We therefore consider the following parametrization (see [6]):

$$A_{\text{lens}}(\ell) = A_{\text{lens},0} (1 + B_{\text{lens}} * \log(\ell/\ell_*)) \quad (5.7)$$

considering also the parameters $A_{\text{lens},0}$ and B_{lens} as free parameters and different values of the pivot scale ℓ_* .

5.4 Results

5.4.1 Future constraints on A_{lens}

The expected constraints on A_{lens} for several future CMB experiments are reported in Table 5.4. As we can see a satellite experiment as PIXIE, devoted mainly to the measurement of CMB spectral distortions, will not have enough angular

¹<http://cosmologist.info>

5. CORNERING THE PLANCK LENSING TENSION WITH FUTURE CMB DATA

Experiment	A_{lens}
Pixie	$1.016^{+0.09}_{-0.11}$
LiteBIRD	1.001 ± 0.025
CORE	1.001 ± 0.013
CORE-ext	1.002 ± 0.011
Stage-III (deep)	$0.92^{+0.13}_{-0.11}$
Stage-III (wide)	$0.97^{+0.11}_{-0.07}$
Stage-III (deep)+ τ -prior	$1.004^{+0.044}_{-0.048}$
Stage-III (wide)+ τ -prior	$1.001^{+0.026}_{-0.028}$
Stage-IV ($l_{min} = 50$)	0.998 ± 0.025
Stage-IV ($l_{min} = 5$)	0.999 ± 0.015

Table 5.4: Expected constraints on A_{lens} . The fiducial model assumes $A_{lens} = 1.000$. For Stage-III wide, deep and Stage-IV with $l_{min} = 50$ we have further imposed a Gaussian prior on the reionization optical depth corresponding to Planck 2015 results : $\tau = 0.055 \pm 0.010$.

resolution to constrain A_{lens} , conversely a satellite as LiteBIRD, despite the poorer angular resolution with respect to Planck, thanks to the precise measurement of CMB polarization, could reach an accuracy of $\Delta A_{lens} \sim 0.026$, enough to falsify the current value of $A_{lens} \sim 1.15$ at more than five standard deviations. A more ambitious space-based experiment as CORE, on the other hand, could test the A_{lens} anomaly at more than 10 standard deviations. Near future ground-based as Stage-III will not have enough sensitivity on A_{lens} unless the optical depth can be complementary measured by a different experiment. As we can see, considering an external prior on the optical depth as $\tau = 0.055 \pm 0.010$ (in agreement with the recent Planck constraint [123]) can improve the Stage-III (Deep) constraint to a level comparable with LiteBIRD, while Stage-III (Wide) can also improve but with an accuracy smaller by about a factor two. A Stage-IV experiment can measure A_{lens} with an accuracy about a factor ~ 4.5 better than the current Planck constraint, providing a large angular scale sensitivity from $l_{min} = 5$. In this case, the current indication for $A_{lens} \sim 1.15$ can be tested by a Stage=IV experiment at the level of ~ 10 standard deviations. In the less optimistic case of a smaller sensitivity from $l_{min} = 50$, the Stage-IV experiment is expected to constrain the A_{lens} parameter with a precision comparable with the one achievable by LiteBIRD.

5.4.2 Testing A_{lens} in different spectra and frequency channels

There are two, straightforward, ways for testing if the A_{lens} anomaly is due to a systematic in the data: checking for its presence in the temperature and polarization spectra separately and considering also the frequency dependence. Of course, if the A_{lens} anomaly is not simultaneously present in all the spectra and at all the frequencies this could better support the hypothesis of a systematic or a unresolved foreground. However when analyzing just one C_ℓ spectrum or just one frequency at time, the experimental noise is clearly larger and it is therefore interesting to investigate what kind of accuracy could be reached in this case.

As an example, we have considered the optimistic CMB-S4 configuration and considered the constraints on A_{lens} achievable when using just the TT and EE channels. We have found the following constraints at 68% C.L.: $A_{lens} = 1.000 \pm 0.044$ (TT) and $A_{lens} = 1.000 \pm 0.024$ (from EE). So, in practice, E polarization data alone from CMB-S4 could test the current $A_{lens} \sim 1.15$ anomaly at the level of 5 standard deviations. A complete configuration for the CMB-S4 experiment is clearly not yet finalized. In order to study the frequency sensitivity to A_{lens} we have however assumed three channels at 90, 150 and 220 GHz with angular resolutions of 5, 3, and 2 arcminutes and detector sensitivities of 2.2, 1.3 and 2.2 $\mu\text{Karcmin}$ respectively. We have found from TT data the constraints $A_{lens} = 1.003^{+0.044}_{-0.045}$, $A_{lens} = 1.002^{+0.041}_{-0.045}$, and $A_{lens} = 1.003^{+0.041}_{-0.046}$ for the 90, 150 and 220 GHz channels respectively. Using the EE data we have $A_{lens} = 1.003^{+0.028}_{-0.028}$, $A_{lens} = 1.002^{+0.023}_{-0.025}$, and $A_{lens} = 1.003^{+0.023}_{-0.025}$ again for the 90, 150 and 220 GHz channels respectively. In Figure 5.1, 5.2, and 5.3 we report the 2D forecasted constraints at 68% and 95% C.L. for A_{lens} and other cosmological parameters from a future CMB-S4 mission considering the frequency channels at 90, 150, and 220 GHz.

As we can see from the figures, polarization measurements will be crucial in improving the constraint on A_{lens} . In particular, polarization will somewhat reduce the degeneracy between A_{lens} and the baryon density parameter present in TT data. However, A_{lens} still strongly correlates with parameters as n_s , $\Omega_{cdm}h^2$, and H_0 even when the combined polarization+temperature measurements are considered. As we can see, therefore, with the assumed experimental configuration, the sensitivity to A_{lens} in each frequency channel will be essentially the same than the one achievable when all channels are combined. A frequency dependence of the A_{lens} anomaly as a power law $\sim \nu^n$ could be tested with spectral indexes of $n \sim 0.09$ at the level of three standard deviations.

5. CORNERING THE PLANCK LENSING TENSION WITH FUTURE CMB DATA

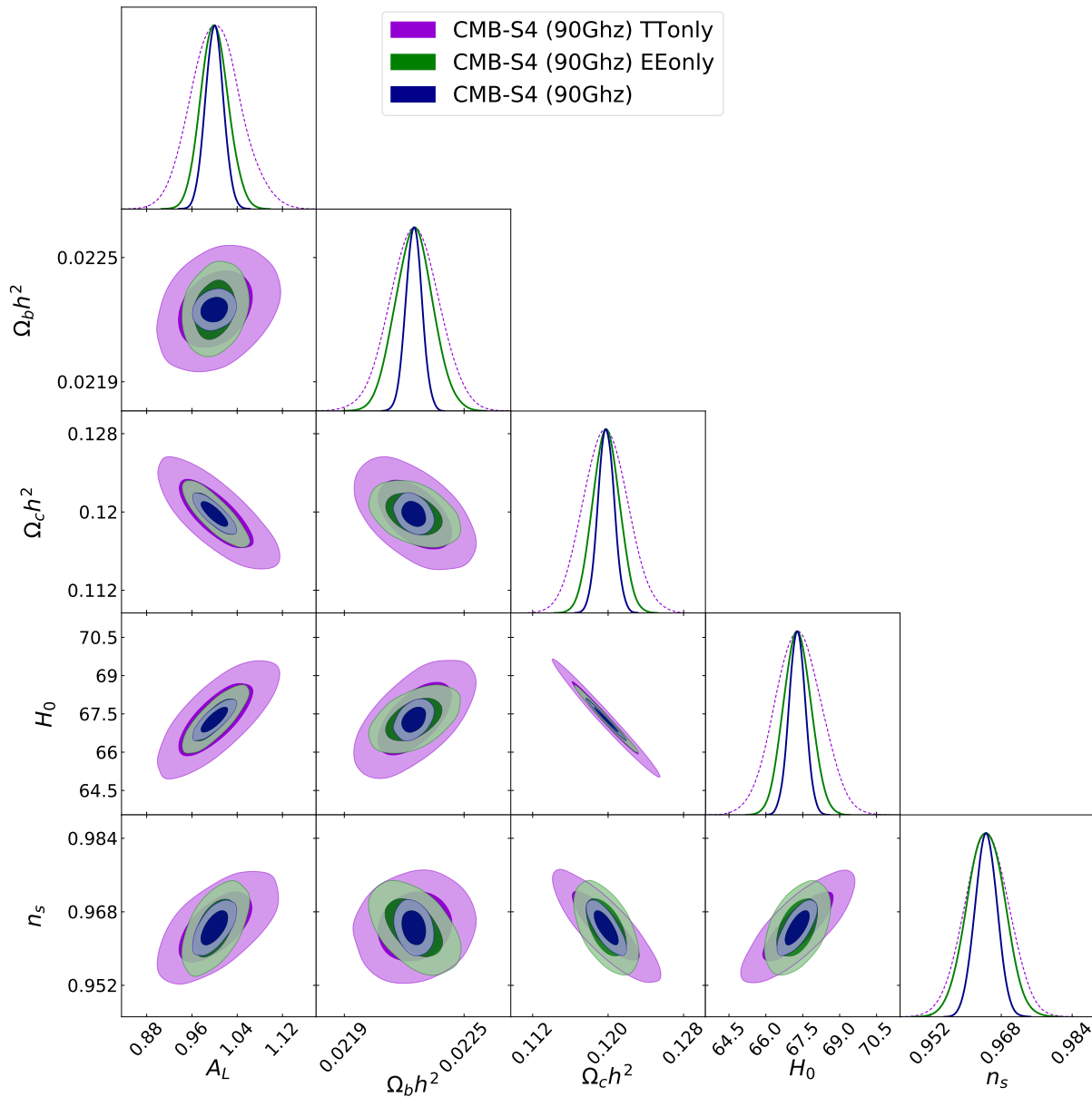


Figure 5.1: Forecasted constraints at 68% and 95% C.L. for A_{lens} and other cosmological parameters from a future CMB-S4 mission considering only the frequency channel at 90 GHz.

5.4.3 Using B modes to test the A_{lens} anomaly.

Future experiments as Stage-IV will measure with great accuracy the CMB polarization B mode that arises from lensing. The B mode spectra could therefore be in principle extremely useful for placing independent constraints on A_{lens} . In particular, an indication for an anomaly present in the TT, TE and EE angular spectra but not in the BB lensing spectrum would clearly confirm (once systematics or foregrounds are excluded) that the real physical nature of the anomaly is not connected to lensing but more to systematics or to new and unknowns processes possibly related to recombination or inflation that leave the small scale B mode signal as unaffected. Unfortunately the polarization B mode signal does not only

5. CORNERING THE PLANCK LENSING TENSION WITH FUTURE CMB DATA

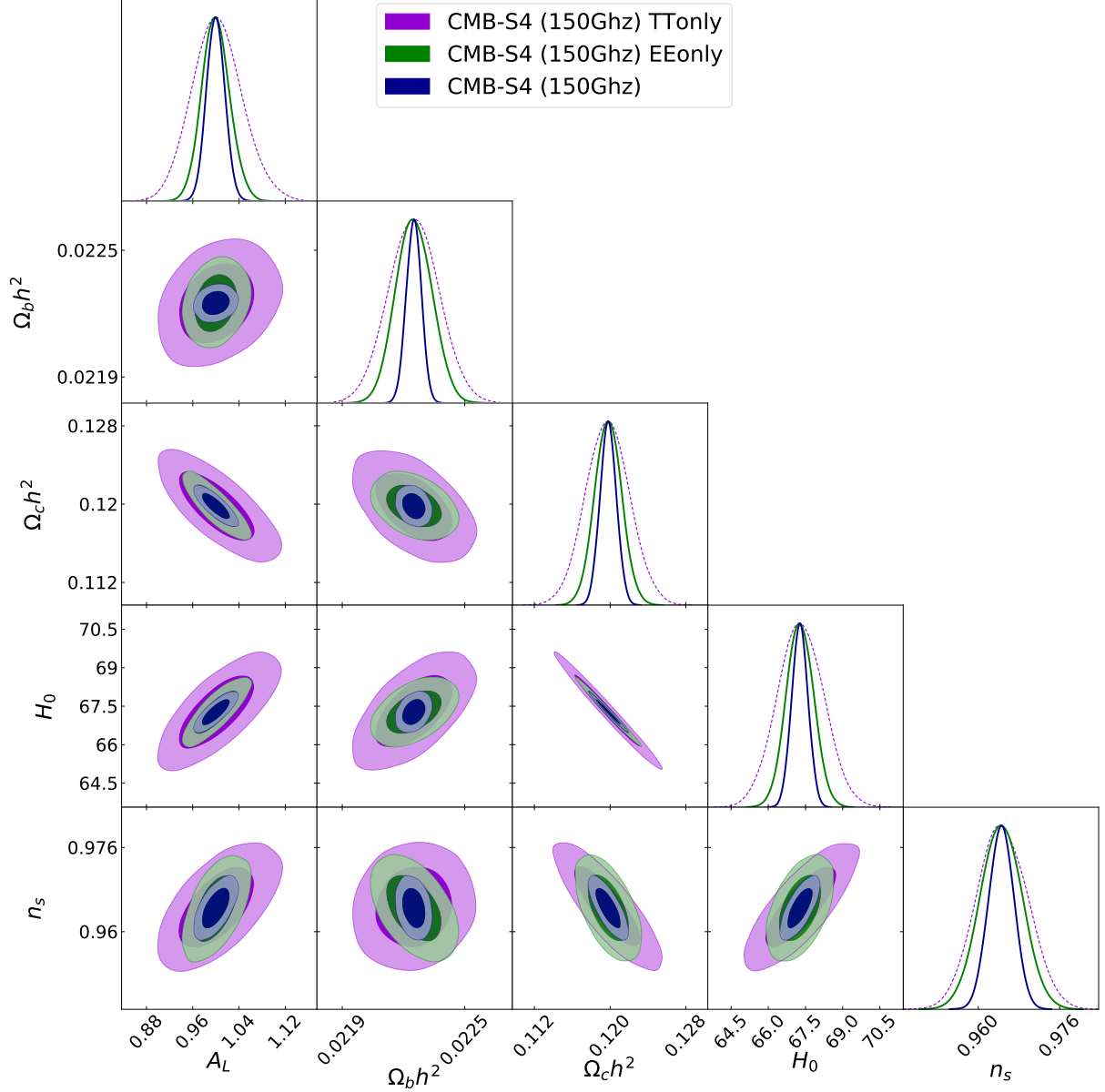


Figure 5.2: Forecasted constraints at 68% and 95% C.L. for A_{lens} and other cosmological parameters from a future CMB-S4 mission considering only the frequency channel at 150 GHz.

depends from A_{lens} . Degeneracies are indeed present between cosmological parameters and we have found that even with the Stage-IV experiment A_{lens} will be practically unbounded from just the B mode spectra, with a major degeneracy with the amplitude of primordial perturbations A_s . Including an external Gaussian prior of $\log(10^{10} A_s) = 3.094 \pm 0.005$ for the primordial inflationary density perturbation amplitude and of $\tau = 0.055 \pm 0.010$ for the reionization optical depth, we found that Stage-IV could reach the constraint $A_{lens} = 1.04^{+0.13}_{-0.19}$ at 68% c.l.. This would only marginally test the current anomaly and other complementary constraints will be needed to further test A_{lens} . In Figure 5.4, we plot the future constraints at 68% and 95% C.L. from the Stage-IV experiment (with $l_{min} = 5$) in the A_{lens} vs $\Omega_b h^2$,

5. CORNERING THE PLANCK LENSING TENSION WITH FUTURE CMB DATA

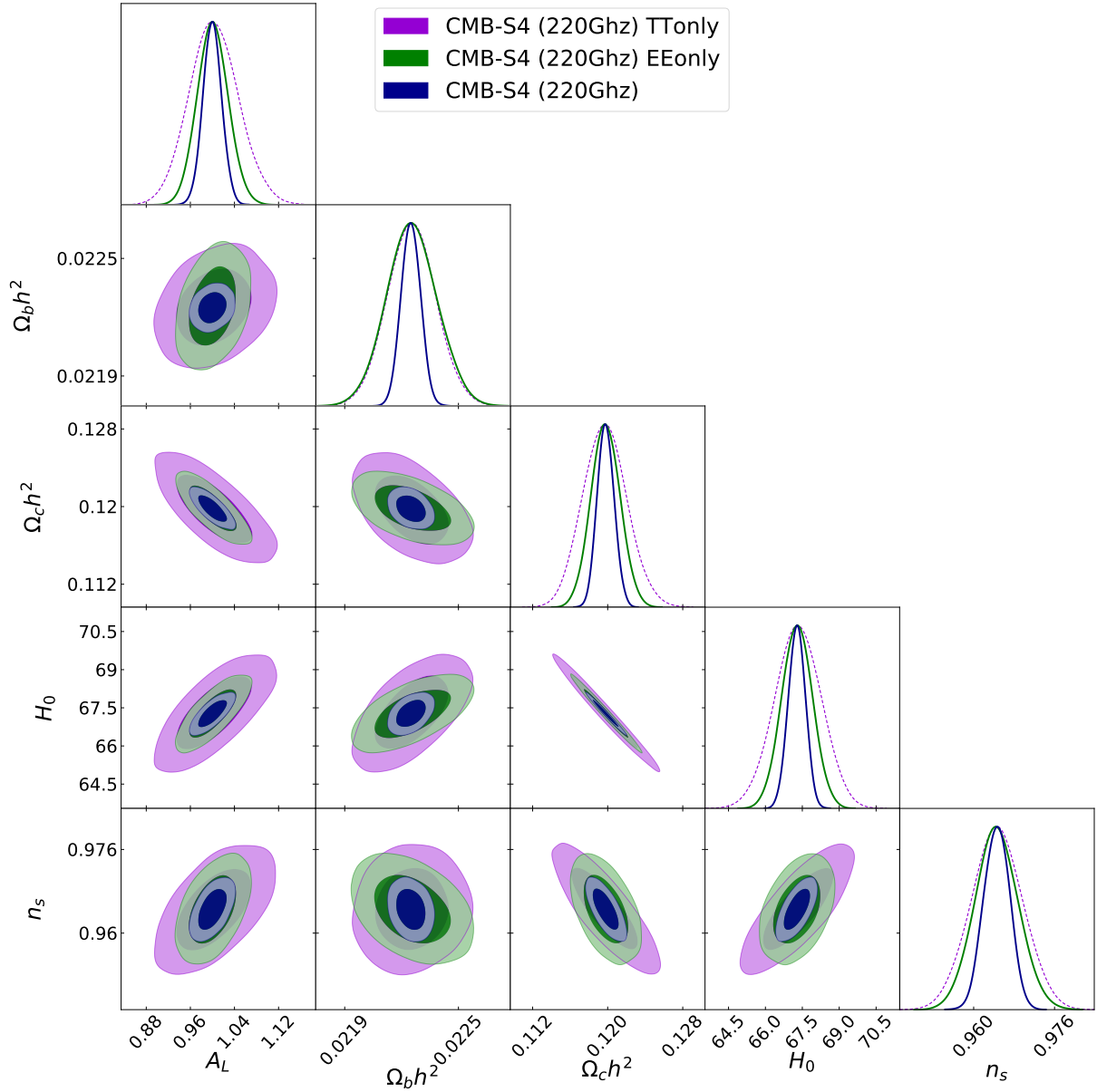


Figure 5.3: Forecasted constraints at 68% and 95% C.L. for A_{lens} and other cosmological parameters from a future CMB-S4 mission considering only the frequency channel at 220 GHz.

$\Omega_c h^2$, n_s , and $\ln[10^{10} A_s]$ planes. As we can see, the B modes are unable to bound A_{lens} due mainly to a degeneracy with the primordial amplitude A_s . However, when a prior on A_s is included, degeneracies are still present between A_{lens} and $\Omega_b h^2$, $\Omega_c h^2$, and n_s that prevent a precise determination of A_{lens} . In conclusion, the measurement of primordial B modes from lensing will not let to significantly improve the constraints on A_{lens} given the degeneracies between cosmological parameters.

5. CORNERING THE PLANCK LENSING TENSION WITH FUTURE CMB DATA

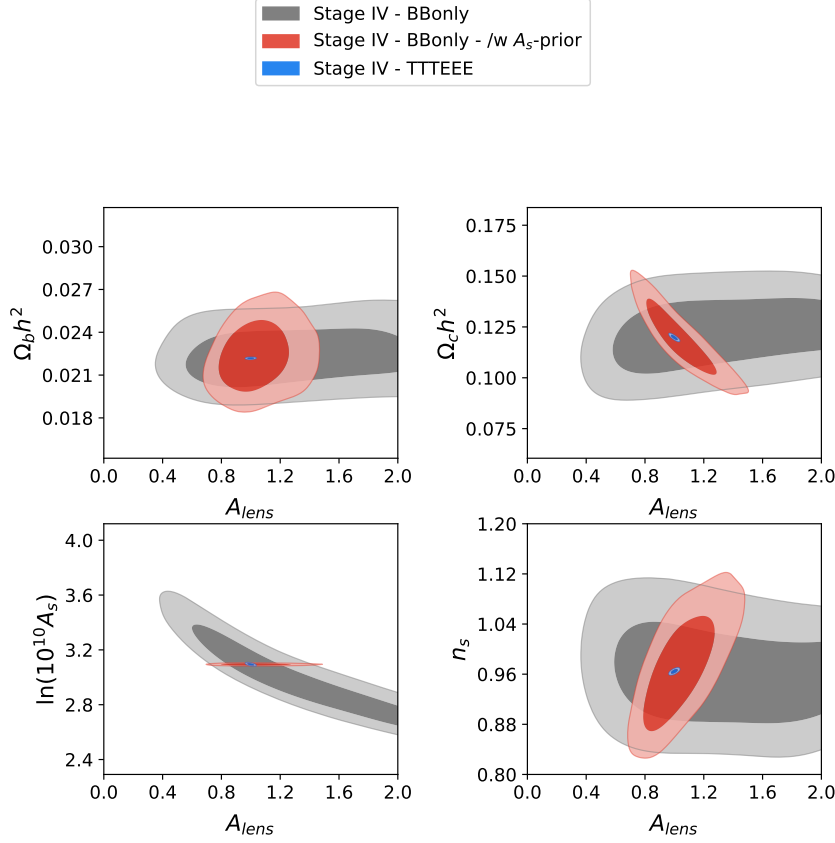


Figure 5.4: Future constraints at 68% and 95% C.L. from the Stage-IV experiment (with $l_{min} = 5$) in the A_{lens} vs $\Omega_b h^2$, $\Omega_c h^2$, n_s , and $\ln[10^{10} A_s]$ planes (clockwise from Top Left panel). The constraints from BB modes only (Grey) leave A_{lens} practically unbounded. Including a prior on the primordial amplitude improves the constraints on A_{lens} from B modes only (Red) but they are still far weaker than the constraints from TTTEEE (Blue).

5.4.4 Future constraints on angular scale dependence of A_{lens}

In Table 5.5 we report the constraints on the parameters of the angular scale dependency A_{lens} in the form of Eq.(5.7) for the Stage-IV configuration. For comparison, we also report the constraints using temperature and anisotropy spectra from the Planck 2015 release [27].

As we can see, while the current bounds from Planck are rather weak and there is no indication for a scale dependency of the A_{lens} anomaly (see also [6]), the Stage-IV experiment can provide constraints at $\sim 1\%$ level on B_{lens} , providing useful information on a possible scale dependence. As discussed in the previous section, we have considered different pivot scales ℓ_* . As we see from the results in Table 5.5, while the choice of the pivot can change significantly current constraints, the effect on the accuracy Stage-IV constraints is less significant.

5.5 Conclusions

While the agreement with the predictions of the Λ CDM model is impressive, the Planck data shows indications for a tension in the value of the lensing amplitude A_{lens} that clearly deserve further investigations. If future analyses of Planck data will confirm this tension then it will be the duty of new experiments to clarify the issue. In this brief paper we have shown that future proposed satellite experiments as LiteBIRD can confirm/rule out the A_{lens} tension at the level of 5 standard deviation. The same accuracy can be reached by near future ground based experiments as Stage-III providing an accurate measurement of the reionization optical depth τ as already reported by Planck. Future, more optimistic, experiments as Stage-IV can falsify the A_{lens} tension at the level of 10 standard deviations. The Stage-IV experiment will also give significant information on the possible scale dependence of A_{lens} , clearly shedding more light on its physical nature. A comparison between temperature and polarization measurements made at different frequencies could further identify possible systematics responsible for $A_{lens} > 1$. We have shown that, in the case of the CMB-S4 experiment, polarization data alone will have the potential of falsifying the current A_{lens} anomaly at more than five standard deviation and to strongly bound its frequency dependence.

5. CORNERING THE PLANCK LENSING TENSION WITH FUTURE CMB DATA

Parameter	Planck TTTEEE	Stage-IV
$\ell_*=50$		
$A_{lens,0}$	$1.157^{+0.116}_{-0.144}$	1.000 ± 0.016
B_{lens}	Unconstrained	0.0002 ± 0.0147
$\ell_*=300$		
$A_{lens,0}$	$1.150^{+0.111}_{-0.139}$	0.999 ± 0.016
B_{lens}	Unconstrained	$0.0002^{+0.0145}_{-0.0144}$
$\ell_*=900$		
$A_{lens,0}$	$1.220^{+0.181}_{-0.356}$	0.999 ± 0.019
B_{lens}	Unconstrained	-0.0004 ± 0.0144
$\ell_*=1500$		
$A_{lens,0}$	$1.269^{+0.209}_{-0.462}$	0.999 ± 0.021
B_{lens}	Unconstrained	-0.0005 ± 0.0150
$\ell_*=2100$		
$A_{lens,0}$	$1.313^{+0.223}_{-0.551}$	$0.999^{+0.022}_{-0.023}$
B_{lens}	Unconstrained	-0.0004 ± 0.0143

Table 5.5: Expected constraints on A_{lens} and B_{lens} from Planck real data and Stage-IV simulated data. The fiducial model for the simulated Stage-IV data has $A_{lens} = 1.00$ and $B_{lens} = 0.00$. We choose an hard flat prior $-0.4 < B_{lens} < 0.4$.

6 MAKE LENSING STRONG AGAIN

In this Chapter we study the constraints on simple extensions of the Λ CDM expansion history and on the value of H_0 coming from future observations of strongly lensed systems. We also study the impact of wrong assumptions about the background cosmological model on constraints from future surveys.

This Chapter is mainly based on the work [arXiv:1910.03566 \[astro-ph.CO\]](#)

Contents

6.1	Introduction	111
6.2	Cosmology with Time Delay Measurements	114
6.2.1	Theory of Gravitational Lensing Time Delays	114
6.2.2	Lens Mass Model and Mass-Sheet degeneracy	116
6.2.3	Stellar Dynamics Modelling	117
6.3	Analysis method and mock datasets	118
6.3.1	Mock Catalogues	121
6.4	Forecasts for cosmological parameters	123
6.4.1	Figure of Merit for Strong Lensing Time Delay	126
6.5	A smoking gun for dark energy?	128
6.6	Conclusions	130

6.1 Introduction

The phenomenon of cosmic acceleration, *i.e.* the late phase of accelerated expansion of the Universe, has posed a major challenge for Cosmology since it was first established in 1998 [158]. The standard cosmological model Λ CDM, with a cosmological constant Λ as the candidate mechanism responsible for cosmic acceleration, has so far been the most successful model in describing both early Universe observations, such as Cosmic Microwave Background (CMB), as well as the late time dynamics of the Universe, probed by observations of Baryon Acoustic Oscillations (BAO), galaxy clustering and weak lensing.

Despite the successes of Λ CDM, recent observations highlighted a discrepancy between the value of the Hubble constant today, H_0 , inferred from CMB observations and the local measurements performed through the distance ladder technique. While the former estimate of H_0 depends on the assumed cosmological model, the latter does not depend strongly on any cosmological assumption, as it relies on the observation of standard candles (type Ia supernovae) whose absolute luminosity is calibrated using Cepheids as an anchor. Recent estimates of H_0 obtained using the latter technique have been provided by the SHoES team [3], with their latest value achieved exploiting observations of Cepheids in the Large Magellanic Cloud from the Hubble Space Telescope, $H_0 = 74.03 \pm 1.42$ km/s/Mpc [4].

The CMB estimates of H_0 rely instead on constraints of the size of the sound horizon at the last scattering surface (θ_*) a measurement which allows to extrapolate bounds on the current expansion rate. This extrapolation however implies an assumption for the expansion history of the Universe. Assuming a Λ CDM background, measurements of the CMB from the Planck collaboration provide $H_0 = 67.36 \pm 0.54$ km/s/Mpc [28], a value which is in tension with the local measurement of the SHoES collaboration at 4.4σ .

There is currently no consensus on what is causing the discrepancy in the measure of the Hubble constant between low and high redshift data. One possibility is that the results are biased by neglected systematic effects on observational data (see e.g. [159–163]), while, on the other hand, this tension could indicate that we need to abandon the Λ CDM assumption when extrapolating results to present time. Investigations of the latter possibility have highlighted how early time deviations from standard physics have the potential to ease the tension (see e.g. [164–169]), while other studies have tried to solve this issue allowing for non standard late time evolution, which might be produced by dynamical dark energy (DE) models, modified theories of gravity or interactions between DE and dark matter (such as [22, 170–173]). In order to shed light on this tension, the value of H_0 has been determined also with other kind of observations. For example, the discovery of the first binary neutron stars merging event, GW170817 [174–177] and the detection of an associated electromagnetic counterpart have lead to the measurement $H_0 = 70^{+12}_{-8}$. Even though this constraint is much weaker than those obtained by SNe and CMB observations it is expected to significantly improve with the discovery of new merging events with an associated counterpart [178, 179].

Along with standard sirens (as gravitational wave events are called nowadays because of their analogy with standard candles), observations of the time delay between multiply imaged strongly lensed system has become a compelling method to obtain measurements of H_0 together with other cosmological parameters. The observational method of SLTD was first proposed in 1964 and it can now pro-

6. MAKE LENSING STRONG AGAIN

duce precise, although cosmology dependent, estimations of the Hubble constant thanks to accurate measurements of the time delays between multiple images of specific lensed quasar [180]. The analysis of four well-measured systems from the HoLiCOW lensing program [181] has recently provided a bound on the Hubble constant of $H_0 = 72.5 \pm 2.1$ assuming a flat Λ CDM cosmology [182]. While the HoLiCOW program is ambitiously aiming to bring the SLTD estimates of H_0 to the 1% precision (see e.g. [181] and [183] where a 2.4% constraints on H_0 is obtained combining six well-measured lensing systems), observations of lensed system from future surveys, such as the Large Synoptic Survey Telescope (LSST) which should start taking data in 2023 [184], are expected to significantly improve the number of well-measured strongly lensed systems [185]. The increase in the number of observed lensed sources will also open the possibility to constrain non standard cosmologies, *e.g.* extensions in the dark and neutrino sector (see [183] for recent constraints on these extended parameter space from SLTD). SLTD is sensitive to the cosmological model through a combination of distances, but unlike Type Ia SNe, SLTD measurements do not require any anchoring to known absolute distances.

Typically however, obtaining cosmological constraints with SLTD systems requires precise measurements and modeling of the mass profile and of the environment of the lens system in order to have systematics reasonably under control. Future surveys, like LSST, are also expected to provide enough well-measured systems to allow sufficient statistics with a selected subset of lenses for which a precise modelling of the lens properties can be obtained. This will certainly limit the impact on the cosmological constraints of the uncertainties in the modeling of lens mass and environment. LSST, for instance, has the advantage of having both the wide field-of-view to detect many quasars, and the frequent time sampling to monitor the lens systems for time delay measurements. Several thousand lensed quasar systems should be detectable with LSST, and, as shown in [186], around 400 of these should yield time delay measurements of high enough quality to obtain constraints on cosmological models [187].

It is timely to investigate the constraints on cosmological parameters that can be obtained from future observations of strongly lensed systems. In this Chapter we focus on simple extensions of the Λ CDM expansion history and forecast SLTD constraints on these, as well as on the current expansion rate H_0 . We do so, by creating synthetic mock catalogs of future survey with variable number of lenses up to 1000 and building a Gaussian likelihood to compare data with theory. We also include estimates of the lens galaxy stellar velocity dispersion in our analysis.

The Chapter is organized as follows. In Section 6.2 we outline the connection between the time delays and the cosmological model, describe the theoretical

modeling of the lens velocity dispersion and illustrate how it can improve the time delay constraints on DE parameters. In Section 6.3 we outline our analysis method, describing the likelihood expression used to infer the posterior distributions of cosmological parameters, and explaining the procedure used to generate mock datasets, which are used to forecast the constraints displayed in Section 6.4. In Section 6.4.1 we discuss the constraining power of SLTD on the DE models of interest, assessing at the same time how observational uncertainties on the lens model and on line of sight effects impact the Figure of Merit of future surveys. Section 6.5 contains our investigation of the possible bias brought on the inferred parameters by a wrong assumption of the underlying cosmological model. We also propose a consistency check that could be performed on future SLTD datasets to verify this possibility. Finally, we summarize our conclusions in Section 6.6.

6.2 Cosmology with Time Delay Measurements

We shall describe the connection between gravitational lensing time delay and the cosmological model, and how we account for the velocity dispersion of the lensing galaxy for our cosmological inference.

We also specify the lens and environment mass modeling used for our analysis and include a description of the mass-sheet degeneracy, which provides a transformation of the lens mass profile that has no observable effect other than to rescale the time delays [188].

6.2.1 Theory of Gravitational Lensing Time Delays

In strongly lensed systems, the time that light rays take to travel between the source and the observer depends sensibly both on their path and on the gravitational potential of the lens. For a given i -th light ray, the time delay with respect to its unperturbed path is given by [189, 190]):

$$t(\theta_i, \beta) = (1 + z_l) \frac{D_l D_s}{c D_{ls}} \left[\frac{(\theta_i - \beta)^2}{2} - \psi_{\perp}(\theta_i) \right], \quad (6.1)$$

where, as shown in Figure 6.1, β and θ_i stand, respectively, for the source and the image position, z_l is the redshift of the lens and $\psi_{\perp}(\theta_i)$ is the projected gravitational potential calculated on the lens plane. D_l , D_s and D_{ls} are, respectively, the angular diameter distance from the observer to the lens, from the observer to the source, and from the lens to the source; they satisfy the relation

$$D_{ls} = \frac{(1 + z_s)D_s - (1 + z_l)D_l}{1 + z_s}, \quad (6.2)$$

6. MAKE LENSING STRONG AGAIN

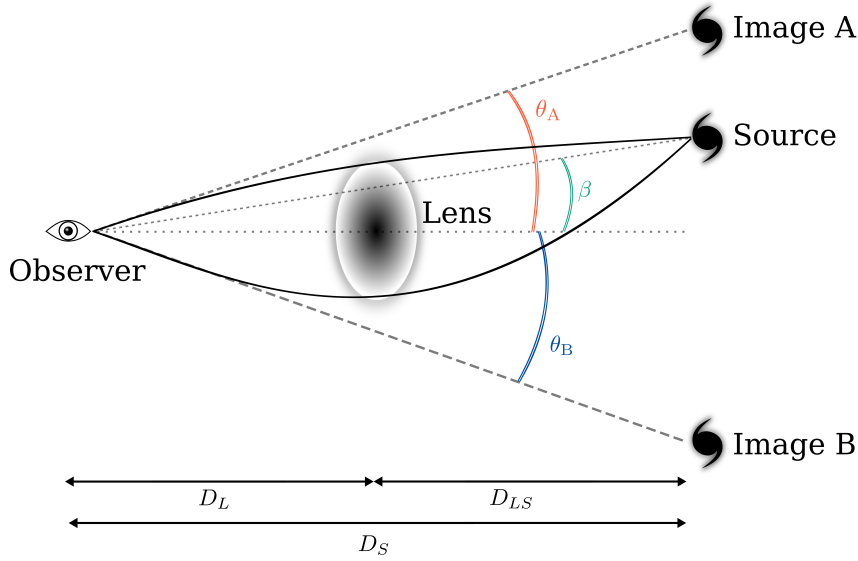


Figure 6.1: The schematic view of a strongly lensed system. D_L , D_S and D_{LS} are, respectively, the angular diameter distance from the observer to the lens, from the observer to the source, and from the lens to the source. The solid angles β and θ_i indicate the position of the source and the images, with respect to the lens plane.

where z_s is the redshift of the source. The Fermat principle provides us with a lens equation for the relative angle between the true position of the source and each of the, possibly multiple, images:

$$\theta_i - \beta = \nabla \psi_{\perp}(\theta_i), \quad (6.3)$$

where ∇ is the transverse gradient computed on the plane orthogonal to the direction of propagation of light. It can be shown [189, 190] that the combination $(\theta_i - \beta)^2/2 - \psi_{\perp}(\theta_i)$ in Eq. (6.1) is only dependent on the geometry and mass distribution of the deflectors; it is usually referred to as the *Fermat potential* $\phi(\theta_i, \beta)$.

As Eq. (6.1) shows, the background cosmological parameters impact the gravitational lensing time delays through the ratios of angular diameter distances. In a flat Universe the angular diameter distance can be written as

$$D(z) = \frac{c}{H_0(1+z)} \int_0^z \frac{dz'}{E(z')}, \quad (6.4)$$

where $E(z) = H(z)/H_0$ is the dimensionless Hubble rate, and c is the speed of light. The relative time delay between two images A and B of a lensed system is given by the difference in the excess time of the two images, which can be rewritten in a simple form using the Fermat potential

$$\Delta t_{AB} = (1 + z_l) \frac{D_L D_S}{c D_{LS}} [\phi(\theta_A, \beta) - \phi(\theta_B, \beta)], \quad (6.5)$$

where we can isolate the factor containing the dependence on cosmological pa-

rameters

$$D_{\Delta t} = (1 + z_l) \frac{D_l D_s}{c D_{ls}}, \quad (6.6)$$

which is referred to as the *time delay distance*.

6.2.2 Lens Mass Model and Mass-Sheet degeneracy

While assuming a cosmological model is enough to define $D_{\Delta t}$ through Eq. (6.6), in order to be able to obtain theoretical predictions for Δt_{AB} , the Fermat potential needs to be computed. This requires a modeling of the mass profile of the lens galaxy.

While an accurate description of the mass profile is challenging both experimentally and theoretically, the profiles of most discovered lens galaxies have been shown to be well fitted by a nearly elliptical power-law mass distribution [191]. Throughout this Chapter, when describing our lens systems, we will use a projected potential on the lens plane ψ_{\perp} obtained assuming the Softened Power-law Elliptical Potential (SPEP) [192]:

$$\psi_{\text{SPEP}}(\boldsymbol{\theta}) = \frac{2A^2}{(3 - \gamma')^2} \left[\frac{\theta_1^2 + \theta_2^2/q^2}{A^2} \right]^{(3-\gamma')/2}, \quad (6.7)$$

where q is the galaxy axis ratio, $A = \theta_E / [\sqrt{q} (\frac{3-\gamma'}{2})^{1/(1-\gamma')}]$ is an overall normalization factor depending on the Einstein radius θ_E and $\gamma' \approx 2$ is the slope of the mass profile [which we define in Eq. (6.11)]. θ_1 and θ_2 are the projections on the lens plane of the two dimensional image position $\boldsymbol{\theta}$.

Additionally, as common in the modeling of the mass profile of quadrupole lenses (see *e.g.* [189, 190]), we include in our modeling of the lens mass profile a constant external shear yielding a potential in polar coordinates of the form:

$$\psi_p(\theta, \phi) \equiv \frac{1}{2} \theta^2 \gamma_{\text{ext}} \cos 2(\phi - \phi_{\text{ext}}). \quad (6.8)$$

where γ_{ext} and ϕ_{ext} are the shear strength and angle. It is worth stressing that both ψ_p and ψ_{SPEP} contribute to the projected potential ψ_{\perp} .

When using time delay measurements in cosmology, a complicating factor arises from the so-called *mass-sheet degeneracy* (for a detailed discussion see *e.g.* [189, 190]). In fact, a transformation of the lens convergence $\kappa(\boldsymbol{\theta}) = \nabla^2 \psi_{\perp} / 2$ of the form:

$$\kappa'(\boldsymbol{\theta}) = \lambda \kappa(\boldsymbol{\theta}) + (1 - \lambda) \quad (6.9)$$

will result in the same dimensionless observables, *e.g.* image positions and shapes, but will rescale the time delays by a factor λ . The additional mass term can be due to perturbers that are very massive or close to the lens galaxy (which may need

6. MAKE LENSING STRONG AGAIN

to be included explicitly into the mass model and affects stellar kinematics) or to the structures that lie along the LOS (see *e.g.* [193–196]). Both effects can be summed up into a constant external convergence term, $\kappa_{\text{ext}} = 1 - \lambda$, due to the mass sheet transformation described by Eq.(6.9). The neat effect is a rescaling of the value of the observed time delay distance [197, 198]:

$$D'_{\Delta t} = \frac{D_{\Delta t}}{1 - \kappa_{\text{ext}}} \quad (6.10)$$

This degeneracy between the external convergence and the mass normalization of the lens galaxy, if not resolved, can lead to a biased inference of the cosmological parameters [199]. Such an effect can be reduced by the combination of lensing data with stellar kinematics measurements, tracing the internal mass distribution of the lens galaxy [200].

6.2.3 Stellar Dynamics Modelling

In order to model the measurable stellar velocity dispersion σ_v we need to model the 3D gravitational potential of the lens galaxy Φ , in which stars are orbiting. This potential will have contributions from the mass distributions of both the lens and the nearby galaxies physically associated with the lens. To model the stellar velocity dispersion we follow the analysis of [195, 196].

The overall mass density associated to Φ can be approximated as a spherically symmetric power law profile:

$$\rho_{\text{local}} = \rho_0 \left(\frac{r_0}{r} \right)^{\gamma'} \quad (6.11)$$

the overall normalization $\rho_0 r_0^{\gamma'}$ can be determined quite well by lensing measurements, since it is a function of the lens profile characteristic only, and can be written as [195]:

$$\rho_{\text{local}}(r) = \pi^{-1/2} (\kappa_{\text{ext}} - 1) \Sigma_{\text{cr}} R_E^{\gamma'-1} \frac{\Gamma(\gamma'/2)}{\Gamma\left(\frac{\gamma'-3}{2}\right)} r^{-\gamma'}, \quad (6.12)$$

where R_E is the Einstein radius and Σ_{cr} is the critical surface density. As in [195], to calculate the LOS velocity dispersion we follow [201].

The three-dimensional radial velocity dispersion σ_r is then found solving a spherical jeans equation:

$$\frac{\partial(\rho^* \sigma_r^2)}{\partial r} + \frac{2\beta_{\text{ani}}(r)\rho^* \sigma_r^2}{r} + \rho^* \frac{\partial \Phi}{\partial r} = 0, \quad (6.13)$$

where $\beta_{\text{ani}} = r^2/(r^2 + r_{\text{ani}}^2)$ is the anisotropy distribution of the stellar orbits in the lens galaxy and Φ is the galaxy gravitational potential associated to the overall

density of Eq.(6.11). For the modeling of the stellar distribution ρ^* , we have assumed the Hernquist profile [202]

$$\rho^*(r) = \frac{I_0 a}{2\pi r(r+a)^3}, \quad (6.14)$$

with I_0 being a normalization factor, $a = 0.551r_{\text{eff}}$ and r_{eff} being the effective radius of the lensing galaxy. The luminosity-weighted velocity dispersion σ_s is then given by :

$$I(R)\sigma_s^2 = 2 \int_R^\infty \left(1 - \beta_{\text{ani}} \left(\frac{R}{r}\right)^2\right) \frac{\rho^* \sigma_r^2 r dr}{\sqrt{r^2 - R^2}}. \quad (6.15)$$

Here R is the projected radius and $I(R)$ is the projected Hernquist profile. Finally, the luminosity-weighted LOS velocity dispersion within a measuring device aperture \mathcal{A} is :

$$(\sigma_v)^2 = \frac{\int_{\mathcal{A}} [I(R)\sigma_s^2 * \mathcal{P}] R dR d\theta}{\int_{\mathcal{A}} [I(R) * \mathcal{P}] R dR d\theta}. \quad (6.16)$$

where $*\mathcal{P}$ indicate convolution with the seeing (see also [195, 196]).

A prediction of the measurable velocity dispersion σ_v is therefore obtained accounting for the observational characteristics of the survey, i.e. through the convolution, over \mathcal{A} , of the product $I(R)\sigma_s^2$ with the seeing \mathcal{P} . Note that the cosmological dependence of σ_v is contained only in the combination $\Sigma_{cr} R_E^{\gamma'-1}$, therefore separate σ_v as:

$$(\sigma_v)^2 = (1 - \kappa_{\text{ext}}) \frac{D_s}{D_{ls}} \mathcal{F}(\gamma', \theta_E, \beta_{\text{ani}}, r_{\text{eff}}) \quad (6.17)$$

where the terms \mathcal{F} accounts for the computation of the integral in Eq.(6.16) without the cosmological terms, θ_E is the angle associated with the Einstein radius, and all the cosmological information is contained in the ratio D_s/D_{ls} .

In this work, we follow the spectral rendering approach of [196] to compute the luminosity-weighted LOS velocity dispersion from Eq.(6.16).

6.3 Analysis method and mock datasets

The final goal of this Chapter is to assess how well future surveys of strongly lensed systems will constrain cosmological parameters, with a particular focus on simple extensions to the Λ CDM model.

We do so by comparing the theoretical predictions of different cosmological models with forecasted datasets, based on mock catalogues. In practice we aim at calculating the *posterior distribution* $P(\vec{\pi}|\vec{d})$ for a set of cosmological parameters

6. MAKE LENSING STRONG AGAIN

$\vec{\pi}$ given the set of (forecasted) data \vec{d} . Using the Bayes theorem, this can be written as

$$P(\vec{\pi}|\vec{d}) \propto P(\vec{d}|\vec{\pi})P(\vec{\pi}), \quad (6.18)$$

where $P(\vec{d}|\vec{\pi})$ is the *likelihood* of \vec{d} given $\vec{\pi}$, and $P(\vec{\pi})$ is the prior distribution.

This expression for the posterior distribution does not include possible nuisance parameters which would account for uncertainties in the modeling of the lensed system, its environment and LOS effects. We will first generalize it to include these parameters and then marginalize over them in order to obtain the final distribution only for the cosmological parameters.

We consider the following nuisance parameters $\vec{\pi}_{\text{nuis}} = (r_{\text{ani}}, \kappa_{\text{ext}}, \gamma')$. The final posterior can be obtained as [195]

$$P(\vec{\pi}|\vec{d}) \propto \int dr_{\text{ani}} d\kappa_{\text{ext}} d\gamma' P(\vec{d}|\vec{\pi}, \vec{\pi}_{\text{nuis}}) P(\vec{\pi}) P(r_{\text{ani}}) P(\kappa_{\text{ext}}) P(\gamma'), \quad (6.19)$$

where $P(r_{\text{ani}})$, $P(\kappa_{\text{ext}})$ and $P(\gamma')$ are the prior distributions on each nuisance parameter. Notice that we do not include here as nuisance parameters, the other terms that enter in the lens model, e.g. the Einstein radius θ_E and the external shear γ_{ext} .

In this Chapter we assume these to be perfectly known, since we are mainly interested in analyzing the degeneracy between the H_0 and the parameters of the lens modeling that are expected to have the most important impact on its estimation, *i.e.* the slope of the power law profile and the external convergence (see *e.g.* [203]).

The degeneracy between H_0 , γ' and κ_{ext} may, in turn, also affect the constraints on DE equation of state through the well-known degeneracy between H_0 and DE parameters. We leave the study of the impact on our results of the inclusion of the whole parameter space of the lens model for a future work.

As discussed in Section 6.2, in order to break the mass-sheet degeneracy SLTD surveys combine measurements of the time delay between different images (Δt) and of the projected velocity dispersion within the lens (σ_v). The latter contains also a dependence on the cosmological parameters. Hence, our data vector will be therefore composed of this pair of measurements for each lensed system included in the dataset, with $\vec{d} = (\vec{\Delta t}, \vec{\sigma}_v)$. In order to constrain our cosmological models, these measurements need to be compared with the theoretical predictions $\vec{\Delta t}^{\text{th}}$ and $\vec{\sigma}^{\text{th}}$. Assuming a Gaussian likelihood, this can be written as

$$P(\vec{d}|\vec{\pi}) = \exp \left[-\frac{1}{2} \left(\sum_{i,j} \frac{(\Delta t_{i,j}^{\text{th}}(\vec{\pi}) - \Delta t_{i,j})^2}{\sigma_{\Delta t_{i,j}}^2} + \sum_i \frac{(\sigma_i^{\text{th}}(\vec{\pi}) - \sigma_{v,i})^2}{\sigma_{\sigma_{v,i}}^2} \right) \right], \quad (6.20)$$

where the index i runs over all the lensed systems in the dataset, j runs over the image pairs for each of the systems and we assume there is no correlation

between the measurements of different systems. For a given set of cosmological ($\vec{\pi}$) and lens model ($\vec{\pi}_{\text{nuis}}$) parameters, the theoretical predictions $\Delta t_{i,j}^{\text{th}}$ and $\sigma_{v,i}^{\text{th}}$ can be obtained from Eq. (6.1) and Eq. (6.16) respectively. We compute the angular diameter distances that appear in these equations using EFTCAMB [204, 205], a public patch to CAMB [122, 206].

With these predictions we can then reconstruct the posterior distribution $P(\vec{\pi}|\vec{d})$ sampling the parameter space and computing the likelihood of Eq. (6.20) for each sampled point. The parameter space is sampled through the public Monte-Carlo Markov-Chain (MCMC) code CosmoMC [128], with the parameter vector $\vec{\pi}$ including the total matter density Ω_m , the Hubble constant H_0 and w_0 and w_a , which parameterize the DE equation of state via the CPL form [207, 208]

$$w(z) = w_0 + w_a \frac{z}{1+z}. \quad (6.21)$$

Using this parameterization, the dimensionless Hubble rate $E(z)$ appearing in Eq. (6.4) can be written as

$$E(z) = \sqrt{\Omega_m(1+z)^3 + \Omega_{\text{DE}}(1+z)^{3(1+w_0+w_a)} \exp \left[-w_a \frac{z}{1+z} \right]}. \quad (6.22)$$

In the following, we will explore three different DE models and this will determine whether or not we sample w_0 and w_a . The cases we investigate are:

- Λ CDM, where both parameters are fixed to $w_0 = -1$ and $w_a = 0$, recovering the standard cosmological constant equation of state $w(z) = -1$;
- w CDM, where $w_a = 0$, but we keep w_0 free to vary, obtaining a constant equation of state which might however deviate from -1 ;
- $w_0 w_a$ CDM, where both w_0 and w_a are free to vary and we explore the possibility of a DE with a time dependent equation of state.

We always assume a flat Universe, with the DE density set by the relation $\Omega_{\text{DE}} = 1 - \Omega_m$. As stated above, sampling only over the parameters $\vec{\pi}$, while keeping the nuisance parameters $\vec{\pi}_{\text{nuis}}$ fixed to their fiducial values, implicitly assumes that the lensed system is perfectly known: we label such cases as *ideal*.

We consider also a *realistic* cases, where the nuisance parameters are allowed to vary. In Table 6.1 we show the prior distributions assumed for all the parameters, with the cosmological ones always sampled using a uniform prior $[\pi_{\text{min}}^i, \pi_{\text{max}}^i]$.

In the w CDM and $w_0 w_a$ CDM cases, we additionally impose an *acceleration prior*, which limits the DE equation of state to $w(z) < -1/3$. In the realistic case, we additionally sample the nuisance parameters using Gaussian priors \mathcal{G} for κ_{ext} and γ' and a uniform prior for r_{ani} . Keeping the nuisance parameters fixed, like in

6. MAKE LENSING STRONG AGAIN

the ideal case, effectively amounts to using Dirac δ_D distributions as their priors. As stated by [195], we stress that the uncertainty in r_{eff} has a negligible effect on the velocity dispersion modeling.

Parameter	Ideal case	Realistic case
Ω_m	[0, 1]	[0, 1]
H_0	[40, 140]	[40, 140]
w_0	[-3, 0]	[-3, 0]
w_a	[-4, 4]	[-4, 4]
κ_{ext}	$\delta_D(-0.03)$	$\mathcal{G}(-0.03, 0.05)$
γ'	$\delta_D(1.93)$	$\mathcal{G}(1.93, 0.02)$
$r_{\text{ani}} (")$	$\delta_D(3.5)$	[0.665, 6.65]

Table 6.1: Prior ranges on the cosmological and nuisance parameters sampled in our analysis.

6.3.1 Mock Catalogues

The last ingredient that we need in order to compute the likelihood, is the data vector \vec{d} . We generate three mock catalogues containing different numbers of observed systems, i.e. with $N_{\text{lenses}} = 10, 100, 1000$ lenses, uniformly distributed in the redshift range $0 < z \leq 1$. Furthermore, we assume all the systems in the dataset to be identical to each other, adopting for all of them the mass profile described in Eq. (6.7), with the fiducial values of the model parameters set to those of the HoLiCOW resolved quadruply lensed system HE0435-1223 [209], listed in Table 6.2.

We also assume that the redshift difference between the lens and the background source is the same for all the systems, with $\Delta z = 1.239$.

Parameter	$\theta_E (")$	q	$\theta_q (^\circ)$	γ'	γ_{ext}	$\varphi_{\text{ext}} (^\circ)$	κ_{ext}	$r_{\text{eff}} (")$	$r_{\text{ani}} (")$
Value	1.18	0.8	-16.8	1.93	0.03	63.7	-0.03	1.33	3.5

Table 6.2: Fiducial values for the mock lens parameters.

Apart for being one of the currently best observed system, HE0435-1223 has the advantage of being almost symmetric in terms of the image configuration,

which itself implies that the image separations are more than the observational threshold of $1''$ [210].

Moreover, the amount of external shear induced from the environment of this lens is consistent with the shear parameter of most of the studied lens systems in the assumed redshift range (see *e.g.* the catalogue of [186]).

Our assumptions on the redshift range of the dataset are justified by the constraints on source quasar redshifts from current surveys such as SDSS [211], as well as the predicted peak lens and source redshift ranges for the LSST survey [185]. Notice that our modeling of the mock catalogue implies also that we assume the same external convergence κ_{ext} for all systems. We fix the value of the external convergence on the best fit value of the distribution of κ_{ext} estimated by the analysis of the environment of the lens HEO435-1223 [212]. Since κ_{ext} is a LOS effect, this assumption might easily break down for surveys with an extended redshift range, for which a redshift dependence of this nuisance parameters could be included.

The external convergence might also carry cosmological information, in particular if one wants to explore deviations from General Relativity; the different evolution of Large Scale Structures in modified gravity theories might indeed imprint characteristic features in the effect that these structures have on SLTD measurements, which can in principle be exploited to constrain departure from the standard General Relativity description [199].

In addition to the lens parameters, in order to generate our mock datasets we also need to assume a fiducial cosmology. We choose two different fiducials, thus creating two classes of mock data:

- Λ -mock, where the DE equation of state parameter is constant in time and equal to $w(z) = -1$ (thus assuming $w_0 = -1$ and $w_a = 0$), and the cosmological parameters are chosen to be in agreement with the constraints obtained by the Planck collaboration [28], i.e. $\Omega_m = 0.295$, $H_0 = 67.3$ Km/s/Mpc.
- w -mock, which differs from the Λ -mock only in the value of the DE equation of state parameter, which is again constant but set to $w(z) = -0.9$.

In both cases, we assume a flat Universe, with $\Omega_{\text{DE}} = 1 - \Omega_m$. Once the lens and fiducial cosmological parameters are assumed, the relative time delays and the velocity dispersion can be computed following Eq. (6.5) and Eq.(6.16). Computing these for each of the N_{lens} lensed system contained in our dataset allows us to create our simulated data points; for each of these we assume that the time delays are observed with an error of $\sigma_{\Delta t} = 0.8$ days¹, while for the

¹Based on our generated time delay values, this estimate fulfills the requirement of 0.2% level time delay accuracy which, as pointed out by [213], is needed for a low biased cosmological inference.

6. MAKE LENSING STRONG AGAIN

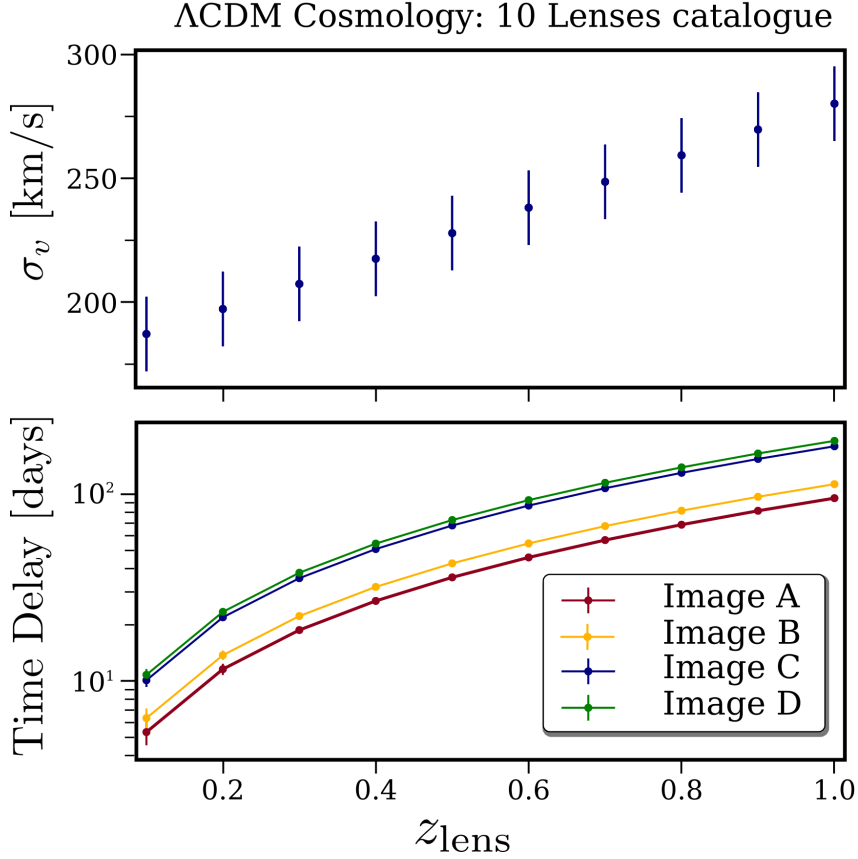


Figure 6.2: Λ CDM for a survey with $N_{\text{lens}} = 10$. The upper panel shows the velocity dispersion of the lens galaxies projected along the line of sight. The bottom panel shows the absolute time delay differences between image A and the other three images.

velocity dispersion measurements we assume a constant error $\sigma_{\sigma_v} = 15$ km/s. As an example, we show in Figure 6.2 the Λ -mock obtained for a forecasted survey of $N_{\text{lens}} = 10$ lensed systems.

6.4 Forecasts for cosmological parameters

In this Section we present the forecasted bounds on cosmological parameters obtained following the analysis procedure and the mock datasets described in Section 6.3. We focus on the Λ -mocks, containing $N_{\text{lens}} = 10, 100, 1000$ lensed systems, and we analyse them, both in the ideal and realistic cases, using the three DE models we introduced: Λ CDM, w CDM and $w_0 w_a$ CDM.

Λ CDM - In a standard Λ CDM scenario, we find that future strong lensing surveys will be able to constrain H_0 at the same level of Planck [28], $\sigma_{H_0} \sim 1\%$, already with $N_{\text{lens}} = 10$ in the ideal case; this result is consistent with what was found in [214] for a catalogue of 55 lenses. Increasing the number of systems to $N_{\text{lens}} = 100$, improves the bound on H_0 by a factor of ~ 3 , while with our most optimistic dataset ($N_{\text{lens}} = 1000$) we find that H_0 could be constrained with an error of $\sim 0.1\%$. These

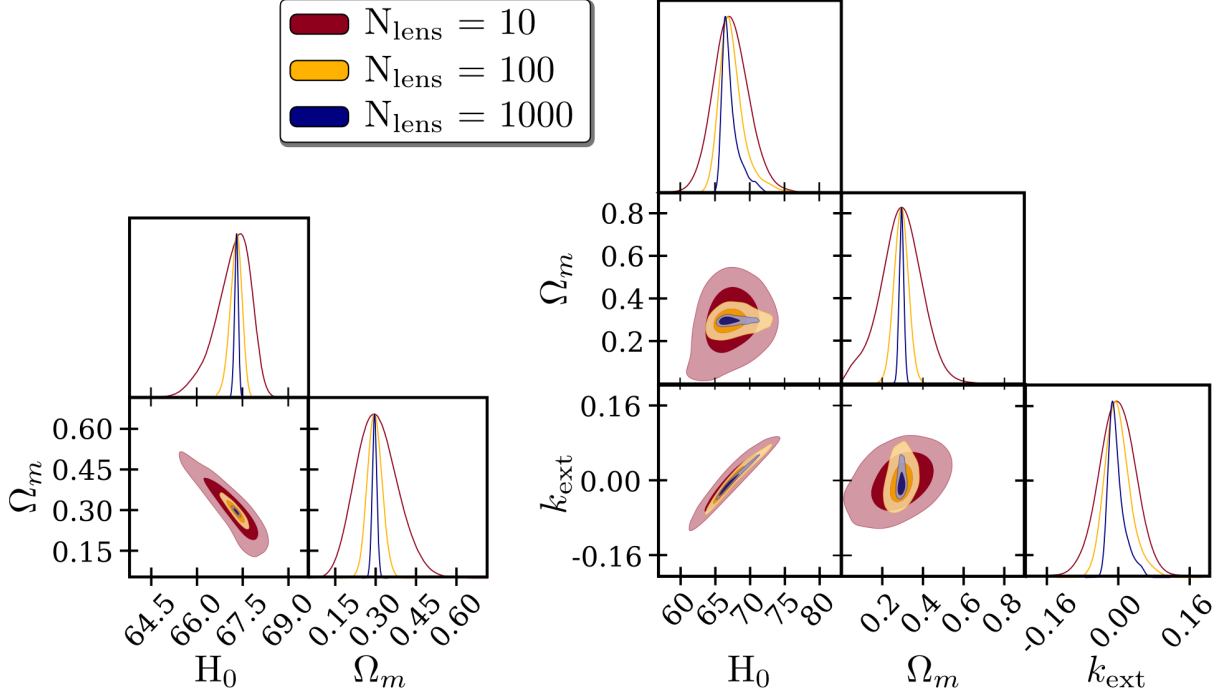


Figure 6.3: Constraints on the Λ CDM cosmological model obtained using the Λ -mock datasets with $N_{\text{lens}} = 10$ (red contours), 100 (yellow contours) and 1000 (blue contours). The left panel shows the results for the ideal case, with nuisance parameters fixed to their fiducial values, while the right panel refers to the realistic case where these parameters are free. We show here only κ_{ext} as this is the only nuisance parameter with a significant degeneracy with the cosmological ones.

results are shown in the left panel of Figure 6.3 and in the Λ CDM entries of Table B.1 shown in Appendix B.

In the realistic cases, where the nuisance parameters are let free to vary, the constraints on the Hubble rate are worsened by a factor of ~ 4 for $N_{\text{lens}} = 10$. This worsening is mainly due to the strong degeneracy between H_0 and κ_{ext} described by Eq. (6.10), which is clearly visible in the right panel of Figure 6.3. Increasing the number of lenses improves the bounds on both parameters, and we reach a $\sim 2\%$ constraint on H_0 when $N_{\text{lens}} = 1000$. All the results for the realistic cases are shown in Table B.2 in Appendix B.

w CDM - Using the mock datasets to constrain this simple extended DE model, we find that in the ideal case with $N_{\text{lens}} = 10$, H_0 can now be measured with an error of $\sim 4\%$, which is improved to $\sim 1\%$ and $\sim 0.3\%$ for $N_{\text{lens}} = 100$ and $N_{\text{lens}} = 1000$ respectively. The parameter determining the equation of state for DE, w_0 , is constrained at the level of $\sim 34\%$ for the 10 lenses case, while moving to the optimistic 1000 lenses configuration boosts the constraining power on this parameter up to $\sim 2\%$, thanks to the breaking of the degeneracy between H_0 and w_0 . Such a result highlights how the improvement of SLTD measurements will significantly impact the investigation of DE alternatives to Λ CDM. These results

6. MAKE LENSING STRONG AGAIN

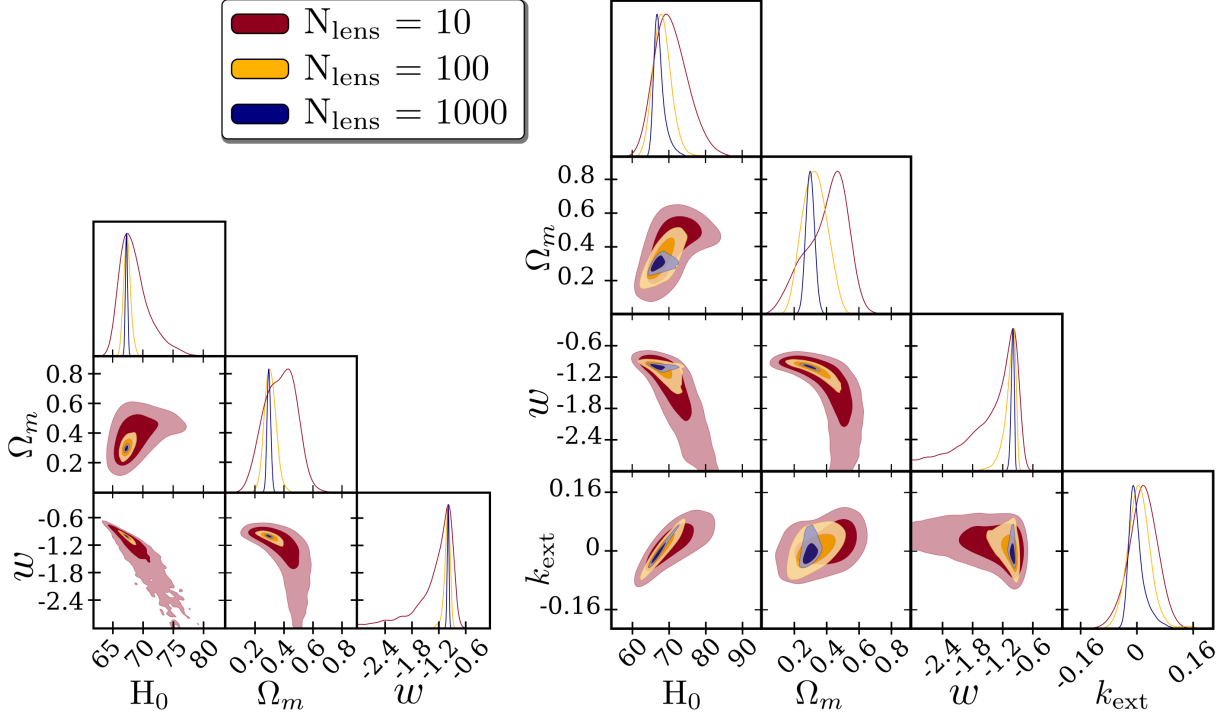


Figure 6.4: Constraints on the w CDM cosmological model obtained using the Λ -mock datasets with $N_{\text{lens}} = 10$ (red contours), 100 (yellow contours) and 1000 (blue contours). The left panel shows the results for the ideal case, with nuisance parameters fixed to their fiducial values, while the right panel refers to the realistic case where these parameters are free. We show here only κ_{ext} as this is the only nuisance parameter with a significant degeneracy with the cosmological ones.

are shown in Figure 6.4, while the constraints on all the sampled parameters are included in Appendix B in Table B.1.

When considering the realistic case (see right panel of Figure 6.4 and Table B.2), the worsening of the constraints due to the nuisance parameters has a different trend with respect to the Λ CDM model; in the 10 lenses case, the additional degeneracy introduced by κ_{ext} worsen the bounds on H_0 only by a factor ~ 2 (with respect to the factor ~ 4 of the Λ CDM case), due to the already existing degeneracy between H_0 and w_0 , while in the 100 and 1000 lens cases, when this degeneracy is broken, the constraints become looser by a factor ~ 5 and ~ 7 respectively.

As κ_{ext} affects w_0 only through its degeneracy with H_0 , moving from the ideal to the realistic case does not have an extreme impact on the DE parameter, with the constraints getting worse by a factor of ~ 2 for $N_{\text{lens}} = 10, 100, 1000$

$w_0 w_a$ CDM - In this case, we find that due to the degeneracies between H_0 and the DE parameters w_0 and w_a , the constraints on H_0 are significantly worsened. We see that a strong lensing survey could reach a $\sim 1\%$ level bound on the Hubble parameter only with the most optimistic configuration of this Chapter, i.e. $N_{\text{lens}} = 1000$ in the ideal case. Due to their degeneracy, w_0 and w_a are not efficiently constrained solely with SLTD data; the best constraint is of the order of

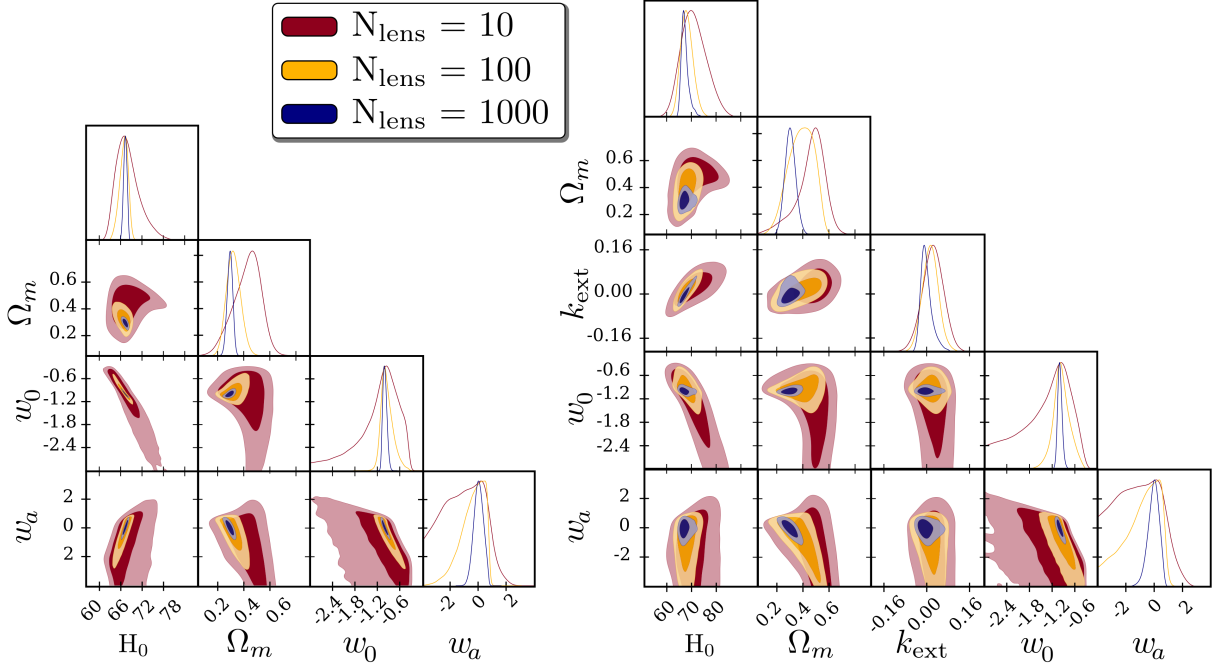


Figure 6.5: Constraints on the w_0w_a CDM cosmological model obtained using the Λ -mock datasets with $N_{\text{lens}} = 10$ (red contours), 100 (yellow contours) and 1000 (blue contours). The left panel shows the results for the ideal case, with nuisance parameters fixed to their fiducial values, while the right panel refers to the realistic case where these parameters are free. We show here only κ_{ext} as this is the only nuisance parameter with a significant degeneracy with the cosmological ones.

$\sim 5\%$ on w_0 and $\sigma_{w_a} \sim 0.3$ on w_a , in the most optimistic case. Of course, possible synergies of future SLTD surveys with other background probes, such as SNIa or BAO, would significantly improve this situation, breaking the degeneracy between the DE parameters and allowing to obtain again a bound on H_0 competitive with respect to CMB or local measurements.

The effect of nuisance parameters when considering the realistic case is similar to what is found for the w CDM case, with the additional parameters affecting mainly the bounds on H_0 , whose error reaches now $\sim 2\%$ for $N_{\text{lens}} = 1000$, while not showing significant impact on the DE parameters.

The results for the w_0w_a case are shown in Figure 6.5, while numerical constraints are reported in Tables B.1 and B.2 shown in Appendix B.

6.4.1 Figure of Merit for Strong Lensing Time Delay

We would like to quantify the constraining power of SLTD surveys, and its improvement with the number of observed systems, in a general way that allows to directly compare the performance of different surveys. For this purpose, we rely on the commonly used *Figure of Merit* (FoM) [215]. For two parameters α and β the FoM is

$$\text{FoM}_{\alpha\beta} = \sqrt{\det \tilde{F}_{\alpha\beta}}, \quad (6.23)$$

6. MAKE LENSING STRONG AGAIN

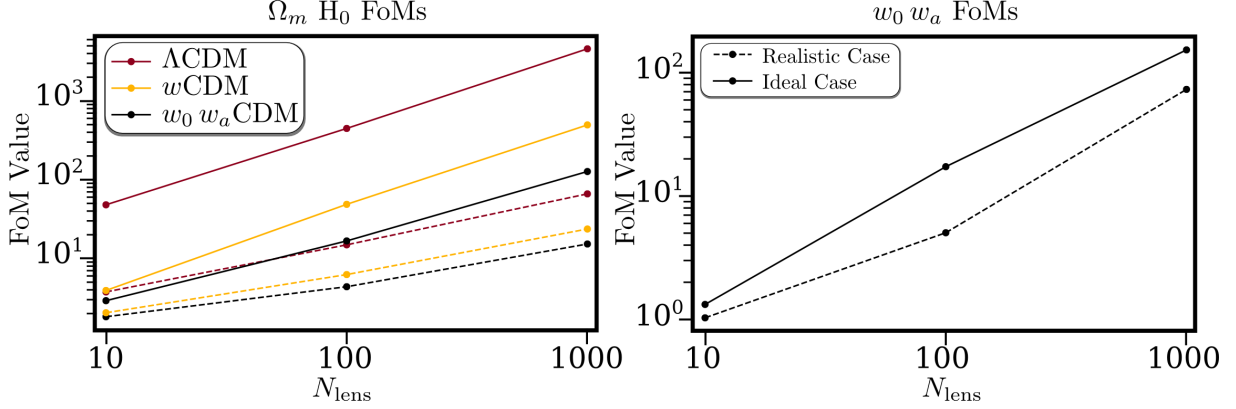


Figure 6.6: FoM for the Ω_m, H_0 (left panel) and w_0, w_a (right panel) as a function of N_{lens} when analysing ΛCDM (red lines), $w\text{CDM}$ (yellow lines) and $w_0 w_a \text{CDM}$ (black lines). The solid lines refer to the ideal case, while the dashed lines account for free nuisance parameters (realistic case).

where F is the *Fisher information matrix* for a generic number of parameters and $\tilde{F}_{\alpha\beta}$ is the Fisher matrix marginalized over all the parameters except for α and β . Given its definition, the FoM gives an estimate of the area of the confidence contours for two parameters, thus quantifying the constraining power of an experiments on them, taking also into account their correlation. It is important to remember that such a definition implies approximating the posterior distribution $P(\vec{\pi}|\vec{d})$ to a Gaussian.

From our MCMC analysis we derived a covariance matrix $C = F^{-1}$, which contains all the sampled parameters. Let us focus on two cosmological parameters of interest that are common to all the models investigated in this work: Ω_m and H_0 . We shall marginalize the covariance matrices over all the other parameters and then compare the constraining power of our mock datasets in each of the cases analysed, using the FoM for Ω_m and H_0 :

$$\text{FoM}_{\Omega_m H_0} = \sqrt{\det \tilde{C}_{\Omega_m H_0}^{-1}}. \quad (6.24)$$

The posterior for Ω_m and H_0 is very close to a Gaussian one when the parameters are tightly constrained, e.g. in the ΛCDM case with $N_{\text{lens}} = 1000$; however, the gaussian approximation becomes less and less efficient as the number of lenses in the dataset decreases. Hence, the FoM values for the less constraining cases might be overestimated.

In the left panel of Figure 6.6 we show the trend of the FoM for the ideal (solid lines) and realistic (dashed lines) cases as a function of N_{lens} . Comparing these two cases, we can notice how the improvement in constraining power brought by the number of lenses is less significant when the nuisance parameters are let free to vary. We also notice that the FoM for the ideal and realistic cases become more similar to each other as we go from ΛCDM to the more general DE parametrized by CPL. This is consistent with the trends that we have discussed in Section 6.4.

In the right panel of Figure 6.6 we also show the FoM for the w_0 and w_a parameters, $\text{FoM}_{w_0w_a}$. Such quantity is commonly used when quantifying the expected sensitivity of future experiment to the DE sector. We find that SLTD surveys can reach values of $\text{FoM}_{w_0w_a} \approx 100$ for $N_{\text{lens}} = 1000$ (in the ideal case), which is comparable with other future surveys, such as Euclid, expected to reach $\text{FoM}_{w_0w_a} \approx 400$ with its primary probes, [216] or the $\text{FoM}_{w_0w_a} \approx 100$ reached by the combination of Weak Lensing measurements from SKA1 and DES, together with Planck observations [217].

6.5 A smoking gun for dark energy?

In Section 6.4 we used the Λ -mock and constrained three DE models which contained the assumed fiducial cosmology as a limiting case. However, when real data will be available, we will have no a priori knowledge of the underlying cosmological model, and assumptions about the latter might affect the results.

In this Section we test the impact of wrong assumptions about the underlying cosmology on constraints from future surveys. To this extent, we consider the w -mocks, generated with a fiducial $w_0 = -0.9$, and fit the data assuming instead a Λ CDM cosmology. Given that the latter does not contain the true fiducial as a limiting case, we can quantify the sensitivity of future surveys on this assumption by computing the shift of the mean values obtained for cosmological parameters. In particular, for H_0 we have

$$S(H_0) = \frac{|H_0 - H_0^{\text{fid}}|}{\sigma_{H_0}}, \quad (6.25)$$

where the fiducial value is the one used to generate the mock data, i.e. $H_0^{\text{fid}} = 67.3$ km/s/Mpc, and we assume that the H_0 distributions obtained through our analysis can be approximated by a Gaussian of width σ_{H_0} .

In Figure 6.7 we show the bounds on H_0 and the values of $S(H_0)$ changing the sample size, both for the ideal and realistic cases, when fitting the w -mocks with a Λ CDM cosmology. In the realistic case, the shift on this parameter is never statistically significant and reaches the maximum of $S(H_0) = 1.4$ for the 1000 lenses mock. However, in the ideal case the shift can be as high as 10σ . This implies that, if mass modelling of lenses reaches extreme accuracy with future surveys, the assumption of wrong cosmology could lead to significant tensions on H_0 value between SLTD observations and other independent cosmological measurements (e.g. from SHoES [4]).

Interestingly, it might be possible to exploit this shift effect, to build a consistency check of the assumed cosmological model. Using a dataset of N_{lens} observed

6. MAKE LENSING STRONG AGAIN

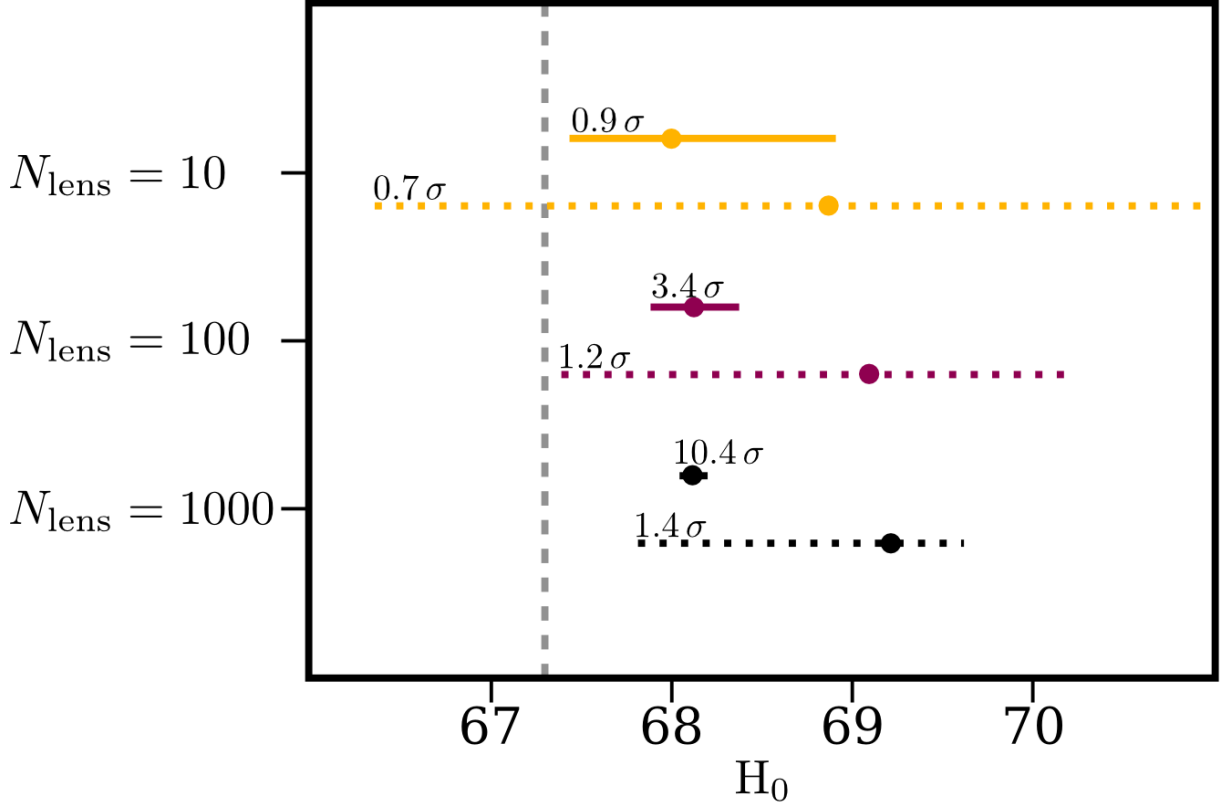


Figure 6.7: Marginalized means and error estimates on the value of the Hubble constant using the w -mocks ($w_0 \neq -1$) analysed keeping the w fixed to the Λ CDM value. The solid lines represent the ideal cases, while the dashed lines show the results of the realistic cases. The numbers above each line correspond to $S(H_0)$ computed following Eq. (6.25).

systems, we can split it in N_{bin} redshift bins and use the resulting datasets separately to constrain the parameters of a given cosmological model, e.g. Λ CDM. Should this model differ from the “true” cosmology (or the fiducial one in the case of forecasts), the results obtained analysing separately the three datasets will be in tension with each other. As a test case, we split the w -mock, both for $N_{\text{lens}} = 100$ and $N_{\text{lens}} = 1000$, in $N_{\text{bin}} = 3$ redshift bins and we fit these with a Λ CDM cosmology.

In Figure 6.8 we show the constraints on H_0 and Ω_m obtained through this analysis for $N_{\text{lens}} = 100$ (top panels) and $N_{\text{lens}} = 1000$ (bottom panels), with the left (right) panels showing the results in the ideal (realistic) case. While for 100 overall lenses both the ideal and realistic case show no tensions on the cosmological parameters, in the ideal case with $N_{\text{lens}} = 1000$ a tension between the results on H_0 appears, with a $\sim 2\sigma$ significance between the first and the third bin. Such a result highlights how, with a sufficient number of observed systems, the assumption of a Λ CDM cosmology could be checked internally using only this observable; a statistically significant tension on the measured parameters in different redshift bins would then provide a smoking gun for the breakdown of Λ CDM, after internal systematics effect are excluded.

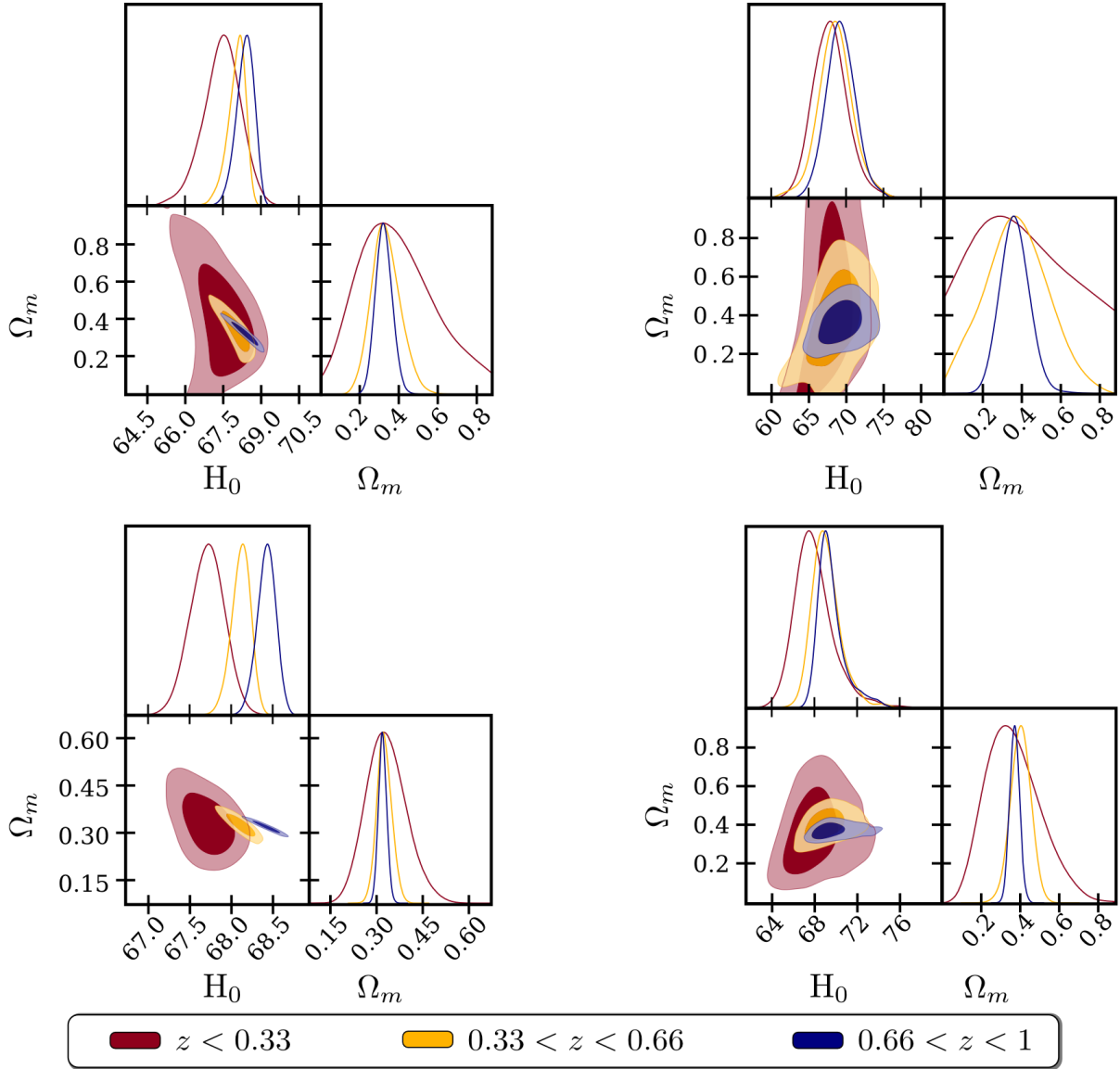


Figure 6.8: Comparison of the constraints on H_0 and Ω_m from the analysis of the three datasets obtained splitting the original mock data in three redshift bins. Top panels refer to the $N_{\text{lens}} = 100$ dataset, while the bottom panels to the $N_{\text{lens}} = 1000$. Left panels do not include nuisance parameters (ideal case), while the right panels refer to the realistic case.

6.6 Conclusions

In this Chapter we explored constraints on the nature of Dark Energy (DE) from future Strong Lensing Time Delay (SLTD) measurements. We simulated SLTD datasets starting from a fiducial cosmological model and a description of the lens profile. For the latter, we assumed a common lens profile for all the systems. We distributed the lenses uniformly in the redshift range $0 < z_{\text{lens}} < 1$, and we simulated the time delay that these would generate among different images of a background source, always placed at a $\Delta z = 1.239$ from the lens, assuming different cosmologies. In the ideal case, in which the lens profile and external

6. MAKE LENSING STRONG AGAIN

environment parameters are perfectly known, SLTD measurements can provide constraints that are competitive with other upcoming cosmological observations; H_0 can be constrained with an error as small as $\sim 0.1\%$ assuming a Λ CDM model and an optimistic dataset of $N_{\text{lens}} = 1000$ observed systems, while this error increases up to $\sim 1\%$ when the DE equation of state is allowed to vary.

We also evaluated the Figure of Merit (FoM) for the w_0 and w_a in the Chevallier-Polarski-Linder parametrization of DE. We found that in our most optimistic case, the FoM can reach a value of ~ 100 , which is competitive with what is expected from upcoming Large Scale Structure surveys. When considering a more realistic case, with the lens profile and lens environment parameters not perfectly known, the constraints worsen significantly. In particular H_0 is strongly degenerate with the nuisance parameter κ_{ext} , that encodes the external convergence brought by additional structures along the line of sight between the observer and the lens. When we allow κ_{ext} to vary (according to a prior), we find that H_0 can be constrained only up to $\sim 2\%$ both in the Λ CDM and w_0w_a CDM cases. In the latter case, the FoM on w_0, w_a can reach only ~ 60 .

Furthermore we quantified the bias on cosmological parameters arising from a wrong assumption on the cosmological model in the analysis of future data. We analysed the mock dataset generated assuming $w = -0.9$ with a Λ CDM cosmology, i.e. with a fixed $w = -1$, and computed the shift $S(H_0)$ on the Hubble constant with respect to the fiducial value used to obtain the mock data. Interestingly, we found that in the ideal case this shift can reach 10σ , highlighting how comparing the results obtained from SLTD observations with other measurements of H_0 could produce significant tensions on this parameter. Such a shift is however almost completely washed out in the realistic case, where $S(H_0)$ never exceeds $\sim 1.5\sigma$.

The study of the shift in H_0 , suggested an interesting, and potentially powerful, consistency check of the cosmological model, entirely based on SLTD data. We split our mock datasets constructed with a w CDM cosmology, with $w = -0.9$, and analysed the three resulting datasets separately, (wrongly) assuming Λ CDM cosmology. In the ideal case with $N_{\text{lens}} = 1000$, we found that the measurements of H_0 in the different bins would be in tension with each other up to $\sim 2\sigma$. This result shows how, with an accurate modeling of the observed lenses, future SLTD datasets can be used to internally test the assumptions on the cosmological model.

The future of SLTD looks bright; measurements are reaching the same accuracy of other, more traditional probes of background cosmology. As we have shown with our analysis, in the upcoming years, SLTD will provide competitive and complementary constraints on dark energy. It would be of great interest to not only further explore SLTD in the context of extended theories of gravity [218–220], but also in combination with other cosmological probes. This work represents a

first step in all these directions. In particular, the likelihood pipeline that we have built in CosmoMC will be of great use to explore complementarity of SLTD with other cosmological probes.

7

STANDARD SIRENS IMPACT ON FUTURE HUBBLE PARAMETER CONSTRAINTS

In the previous Chapter, we showed that strong lensing time delay will be a powerful method to test cosmological models in the coming future. With a large dataset of strong lensing events it would also be possible to put tight constraints on the equation of state of the dark energy. However, the number of gravitational wave events measured is also expected to increase significantly. Many of them might also have an electromagnetic counterpart (*i.e.* they might be standard sirens) and it would be possible to measure H_0 from them. In this Chapter we are going to study the impact that a measurement of the Hubble constant, H_0 , coming from gravitational wave observations would have on future bounds from CMB and BAO experiments in extended cosmological models.

This Chapter is mainly based on the work [Phys. Rev. D98 \(2018\) no.8, 083523](#)

Contents

7.1	Introduction	134
7.2	Method	136
7.2.1	Extended Models	136
7.2.2	Forecasts for CMB	137
7.2.3	Forecasts for BAO	139
7.2.4	Forecast for gravitational wave standard sirens	140
7.3	Results	142
7.3.1	Λ CDM + Ω_k + Σm_ν + N_{eff} + w model	142
7.3.2	Λ CDM + Ω_k + Σm_ν + w_0 + w_a model	149
7.3.3	Figure of Merit	153
7.4	Conclusions	155

7.1 Introduction

We have briefly discuss in Section 6.1 that gravitational-wave standard sirens (GWSS) have been posed as a powerful and new method for the determination of Hubble constant (but see also [179, 221–228]) .

While the constraint on H_0 from GWSS is much weaker than those currently obtained from measurements of luminosity distances of standard sirens or observations of the CMB anisotropies, it is expected to significantly improve in the coming years with the discovery of additional standard siren events. Moreover, this kind of measurement is clearly of particular interest given the current discrepancy on the value of H_0 between standard candle luminosity distances of Cepheids and Type Ia supernovae [3, 229]

Clearly an independent and accurate future determination of H_0 from GWSS will play a key role in confirming or rejecting the possibility of new physics beyond Λ CDM. It is to emphasized that an accurate measurement of the Hubble constant, even though it is a low-redshift quantity, can have important consequences for other higher-redshift cosmological parameters such as the dark energy equation of state [230]. The possibility of constraining cosmology with GWSS has been already considered in several different work (see *e.g.* [19, 223, 231–239]). Some of these studies analyzed “far future” experiments such as the LISA satellite mission [240] expected to be launched in 2034 or third generation interferometers such as the Einstein telescope [233, 241] or the Cosmic Explorer [242].

However, recently, in [179] it has been estimated that, depending on the discovery rate of binary neutron stars, a sub-percent determination of the Hubble constant from GWSS could be achieved by the Hanford-Livingston-Virgo (HLV) network as early as during the second year of operation at design sensitivity (~ 2023 [243]). Given the rate uncertainties, a sub-percent measurement may have to wait for two years of Hanford-Livingston-Virgo-Japan-India (HLVJI) network, which is expected to commence operations $\sim 2024+$.

On the other hand, a significant improvement in the observational data is expected from the next CMB and BAO experiments. Future satellite missions such as LiteBIRD [29, 156] and ground based experiments such as CMB-S4 [33] will improve the Planck results thanks to cosmic variance limited measurement of CMB polarization. The LiteBIRD satellite is a JAXA strategic large mission candidate in Phase-A1 (concept development) and is currently scheduled for launch around 2026 – 2027 . A complementary groundbased CMB experiment with the sensitivity of CMB-S4 is at the moment planned after 2023 .

Similarly, galaxy spectroscopic surveys such as DESI ([244], expected to be completed by 2023) will observe BAO with unprecedented precision. The level of

7. STANDARD SIRENS IMPACT ON FUTURE HUBBLE PARAMETER CONSTRAINTS

accuracy on the Hubble constant expected from future CMB+BAO observations can reach the 0.15% level (see *e.g.* [76]). This could naively appear as an order of magnitude more accurate than future projections for standard sirens constraints. However the CMB + BAO constraint is obtained under the assumption of Λ CDM and, as we are going to show in the following sections, can easily be more than one order of magnitude weaker in extended cosmological scenarios.

These extended scenarios are of particular interest as they may offer a solution to the existing tension between different measurements of H_0 . We emphasize that standard sirens constitute a direct measurement of the luminosity distance, obviating the need for a distance ladder. The absolute calibration of the source is provided by the theory of general relativity. The possible systematics associated with standard siren measurements are expected to reside primarily with the instrument, and in particular, with the calibration of the photodetectors which lead directly to the measurement of the amplitude of the gravitational waves [245, 246]. This calibration is expected to be achieved to better than 1% in the near future [247]. Gravitational wave standard siren measurements thus have the potential to provide a particularly clean and robust probe to the sub-percent level.

This is to be compared with the case of Type Ia supernovae standard candle measurements, which involve astronomical calibrators such as Cepheids, and multiple rungs of the distance ladder. It remains unclear whether the supernova systematics can be reduced to the $\sim 1\%$ level (see *e.g.* [3, 248, 249]). However, if supernovae achieve this level of accuracy on the measurement of H_0 then our results apply directly to them as well. Of course, supernovae also offer the opportunity to probe to much higher redshifts than GWSS, and therefore offer additional cosmological constraints.

It is therefore timely to investigate what kind of additional constraints a direct determination of H_0 with $\sim 1\%$ accuracy from GWSS can bring, with the expected completion of new CMB and BAO surveys within the coming decade. In this Chapter we address this question by forecasting the cosmological constraints from future CMB and BAO surveys in extended cosmological scenarios and by discussing the implications of an additional independent and direct H_0 measurement at the level of 1% from upcoming GWSS sources. This Chapter is structured as follows: in the next section we discuss how we produced our forecasts for CMB, BAO and GWSS data, in section 7.3 we present the constraints coming from our analysis combining together our mock datasets, and in section 7.4 we present our conclusions.

7.2 Method

In this section we describe our forecasting method. We start with a description of the assumed theoretical framework, and then discuss the generation of forecasts for CMB, BAO and standard sirens constraints.

7.2.1 Extended Models

As discussed in the previous section, in this chapter we consider parameter extension to the standard Λ CDM model. These models, as we discussed below, are physically plausible, compatible with current observations, and able to solve in some cases the current observed tensions between cosmological datasets.

The standard flat Λ CDM model is based on just 6 parameters: the baryon ω_b and cold dark matter ω_c physical energy densities, the amplitude A_s and the spectral index n_s of scalar primordial perturbations, the angular size of the sound horizon at decoupling θ_s and the optical depth at reionization τ . Following [25, 254], we consider variations with the addition of 4 additional parameters:

- Curvature, Ω_k . Most of the recent analyses assume a flat universe with $\Omega_k = 0$ since this is considered as one of the main predictions of inflation. However inflationary models with non-zero curvature can be conceived (see *e.g.* [255]). Moreover the recent results from Planck prefer a closed model $\Omega_k > 0$ at more than two standard deviations [27]. Including further data from BAO strongly constraints curvature with $\Omega_k = 0.0002 \pm 0.0021$ at 68% C.L. and perfectly compatible with a flat universe [27]. However this result is obtained in the framework of Λ CDM + Ω_k *i.e.* in one single parameter extension while here we want to analyze a larger parameter space, varying ten parameters at the same time. In this scenario the current Planck + BAO constraints on Ω_k are weaker.
- Neutrino mass, Σm_ν . Neutrino oscillation experiments have demonstrated that neutrinos undergo flavor oscillations and must therefore have small but non-zero masses. However the neutrino absolute mass scale and the mass hierarchy are not yet determined (see *e.g.* [34] for a recent review). Usually, as in [27], the total neutrino mass scale is fixed to $\Sigma m_\nu = 0.06$ eV corresponding to the minimal value expected in the normal hierarchy scenario. There is clearly no fundamental reason to limit current analyses to this value and the neutrino mass should be let free to vary.
- Neutrino effective number, N_{eff} . Any particle that decouples from primordial thermal plasma before the QCD transition could change the number of relativistic particles at recombination increasing N_{eff} from its standard value

of 3.046 (see *e.g.* [256]). An increased value of N_{eff} can help in solving the Hubble constant tension (see *e.g.* [3]). Reheating at energy scale close to the epoch of neutrino decoupling could on the contrary lower the value of N_{eff} [37].

- Dark energy equation of state, w . While current data are in agreement with a cosmological constant, the possibility of having dark energy equation of state different from -1 is certainly open (see *e.g.* [7]). Moreover, a time evolution for w helps in solving the coincidence problem of why dark energy and dark matter have similar densities today. In this Chapter we consider two parametrization, either w constant with time or the Chevalier-Polarski-Linder parametrization (hereafter CPL) [207, 208]:

$$w(a) = w_0 + (1 - a)w_a \quad (7.1)$$

where a is the scale factor, w_0 is the equation of state today ($a = 1$) and w_a parametrizes its time evolution. This should be considered as a minimal extension since dark energy time dependences could be more complicated as, for example, in the case of rapid transition. We consider dark energy perturbations following the approach of [257].

In this chapter we consider the following 10 parameter extension : $\Lambda\text{CDM} + \Omega_k + N_{\text{eff}} + \Sigma m_\nu + w$ and $\Lambda\text{CDM} + \Omega_k + \Sigma m_\nu + w_0 + w_a$.

While we study extended models, for our simulated data we assume as a fiducial (true) model the standard ΛCDM model with parameters in agreement with the most recent Planck constraints [27]: $\omega_b = 0.02225$, $\omega_c = 0.1198$, $\tau = 0.055$, $100\theta_s = 1.0477$, $n_s = 0.9645$, $\Sigma m_\nu = 0.06$ eV, $N_{\text{eff}} = 3.046$, $\Omega_k = 0$, $w_0 = -1$ and $w_a = 0$. The corresponding derived value of H_0 in this model is $H_0 = 67.3 \text{ km s}^{-1} \text{ Mpc}^{-1}$.

The theoretical models and the simulated data are computed with the latest version of the Boltzmann integrator CAMB [122]. Given a simulated dataset and a likelihood that compares data with theory, we extract the constraints on cosmological parameters using the Monte Carlo Markow Chain (MCMC) code CosmoMC¹ [128].

7.2.2 Forecasts for CMB

We produce forecasts on cosmological parameters for future CMB experiments with a well established and common method (see *e.g.* [41, 76, 157]). Under the assumption of the fiducial model described previously, we compute the theoretical

¹<http://cosmologist.info>

7. STANDARD SIRENS IMPACT ON FUTURE HUBBLE PARAMETER CONSTRAINTS

Experiment	Beam	Power noise $W^{-1/2}$ [$\mu\text{K-arcmin}$]	ℓ_{\max}	ℓ_{\min}	f_{sky}
LiteBIRD	30'	4.5	3000	2	0.7
S3deep	1'	4	3000	50	0.06
S3wide	1.4'	8	3000	50	0.4
CMB-S4	3'	1	3000	5	0.4

Table 7.1: Specifications for the different experimental configurations considered in this chapter. In case of polarization spectra the noise W^{-1} is multiplied by a factor 2.

CMB angular spectra for temperature, C_ℓ^{TT} , E and B modes polarization C_ℓ^{EE} and C_ℓ^{BB} , and cross temperature-polarization C_ℓ^{TE} , using the Boltzmann code [122].

Given an experiment with FWHM angular resolution θ and experimental sensitivity W^{-1} (expressed in [$\mu\text{K-arcmin}$] 2), we can introduce an experimental noise for the temperature angular spectra of the form (see e.g. [125]):

$$N_\ell = W^{-1} \exp(\ell(\ell + 1)\theta^2/8 \ln 2) \quad (7.2)$$

A similar expression is used to describe the noise for the polarization spectra with $W_p^{-1} = 2W^{-1}$ (one detector measures two polarization states). We have then produced synthetic realizations of CMB data assuming different possible future CMB experiments with technical specifications as listed in Table 7.1.

In particular, we have considered a possible future CMB satellite experiments such as LiteBIRD [156] and three possible configurations for ground-based telescopes as Stage-III 'wide' (S3wide), Stage-III 'deep' (S3deep) (see [127]), and CMB-S4 (see e.g. [33, 41, 157]). The simulated experimental spectra are then compared with the theoretical spectra using a likelihood \mathcal{L} given by

$$-2 \ln \mathcal{L} = \sum_l (2l + 1) f_{\text{sky}} \left(\frac{D}{|\bar{C}_\ell|} + \ln \frac{|\bar{C}_\ell|}{|\hat{C}_\ell|} - 3 \right), \quad (7.3)$$

where \hat{C}_l are the theoretical spectra plus noise, while \bar{C}_l are the fiducial spectra plus noise (i.e. our simulated dataset). The quantities $|\bar{C}_\ell|$, $|\hat{C}_\ell|$ are :

$$|\bar{C}_\ell| = \bar{C}_\ell^{\text{TT}} \bar{C}_\ell^{\text{EE}} \bar{C}_\ell^{\text{BB}} - \left(\bar{C}_\ell^{\text{TE}} \right)^2 \bar{C}_\ell^{\text{BB}}, \quad (7.4)$$

$$|\hat{C}_\ell| = \hat{C}_\ell^{\text{TT}} \hat{C}_\ell^{\text{EE}} \hat{C}_\ell^{\text{BB}} - \left(\hat{C}_\ell^{\text{TE}} \right)^2 \hat{C}_\ell^{\text{BB}}, \quad (7.5)$$

where D is defined as

$$D = \hat{C}_\ell^{TT} \bar{C}_\ell^{EE} \bar{C}_\ell^{BB} + \bar{C}_\ell^{TT} \hat{C}_\ell^{EE} \bar{C}_\ell^{BB} + \bar{C}_\ell^{TT} \bar{C}_\ell^{EE} \hat{C}_\ell^{BB} - \bar{C}_\ell^{TE} \left(\bar{C}_\ell^{TE} \hat{C}_\ell^{BB} + 2 \hat{C}_\ell^{TE} \bar{C}_\ell^{BB} \right) \quad (7.6)$$

In what follows we do not consider information from CMB lensing derived from trispectrum data.

7.2.3 Forecasts for BAO

For the future BAO dataset we consider the DESI experiment [244]. If D_V is the volume averaged distance, this is defined as:

$$D_V(z) \equiv \left[\frac{(1+z)^2 D_A(z)^2 c z}{H(z)} \right]^{\frac{1}{3}} \quad (7.7)$$

where D_A is the angular diameter distance and $H(z)$ the expansion rate. Under the assumption of the fiducial model described previously, we compute the theoretical values of the ratio r_s/D_V , where r_s is the sound horizon at the drag epoch when photons and baryons decouple, for the different redshifts in the range $z = [0.15 - 1.85]$ listed in Table 7.2.

Given the forecast uncertainties reported in [1] for D_A/r_s and $H(z)$, we then compute the uncertainties on r_s/D_V and we show them in Table 7.2. The simulated BAO dataset is finally compared with the theoretical r_s/D_V values through a Gaussian prior. As a consistency test, we have checked that by using directly the D_A/r_s value and the corresponding uncertainties reported in [1] instead of r_s/D_V , we obtain very similar results with constraints about $\sim 30\%$ weaker on H_0 when combined with CMB-S4 data in agreement with the results of [258].

In principle it would be possible to forecast BAO data considering D_A/r_s and $H(z)$ as independent measurements. However some small tension (around 1 sigma level) is present between the current constraints from D_A/r_s and $H(z)$ (see e.g. [258], Figure 2 contours in the Top Left and Bottom Left panels for $\Omega_m \sim 0.3$). It is clearly difficult to properly take into account a possible small tension between future D_A/r_s and $H(z)$ measurements that could improve/reduce future BAO constraints. We therefore follow the approach of [127] deriving the expected fractional uncertainties on r_s/D_V for DESI from the fractional errors on D_A/r_s and $H(z)$ forecasted in [1].

7. STANDARD SIRENS IMPACT ON FUTURE HUBBLE PARAMETER CONSTRAINTS

Redshift	$\sigma(r_s/D_V)D_V/r_s$	$\sigma(r_s/D_V)$
0.15	2.57%	0.00595
0.25	1.71%	0.00246
0.35	1.32%	0.00141
0.45	1.08%	0.00093
0.55	0.91%	0.00067
0.65	0.79%	0.00051
0.75	0.70%	0.00040
0.85	0.68%	0.00036
0.95	0.75%	0.00037
1.05	0.77%	0.00036
1.15	0.76%	0.00034
1.25	0.76%	0.00032
1.35	0.83%	0.00033
1.45	0.96%	0.00037
1.55	1.21%	0.00046
1.65	1.89%	0.00069
1.75	2.91%	0.00104
1.85	3.87%	0.00134

Table 7.2: Specifications for the forecast DESI data, obtained by [1].

7.2.4 Forecast for gravitational wave standard sirens

As stated in the introduction, in this chapter we address the question of what kind of cosmological information can be obtained from GWSS systems within the coming decade (i.e. by ~ 2028) when complementary measurements from CMB and BAO surveys will be available. We therefore focus our attention on GW experiments that could be completed in this time-scale: the Hanford-Livingston-Virgo (HLV) network of interferometers during the second year of operation at design sensitivity (~ 2023) and the the Hanford-Livingston-Virgo-Japan-India (HLVJI) network two years after the start of operations (~ 2026) [243].

We do not consider longer-term experiments such as the LISA [240] or DECIGO [259] missions or proposed third generation interferometers such as the Einstein Telescope [241] or the Cosmic Explorer [242] that would presumably

7. STANDARD SIRENS IMPACT ON FUTURE HUBBLE PARAMETER CONSTRAINTS

start operations no sooner than 2030. Moreover, these experiments will be able to determine the luminosity distance of GWSS at higher redshift, opening the possibility to test the acceleration of the universe (i.e. the deceleration parameter), while here we only limit our discussion to the Hubble constant (although black holes standard sirens would probe these high redshifts earlier [260]).

Considering HLV or HLVJI and assuming the optimistic case that all binary neutron star (BNS) systems have detected optical counterparts and associated redshift measurements, the major uncertainty on the projected constraint on H_0 from GWSS comes from the BNS detection rate. The current best estimate of the BNS rate is $R = 1540^{+3200}_{-1220} \text{ Gpc}^{-3} \text{ yr}^{-1}$ [175] (median and 90% credible interval); it is very poorly constrained given that only one BNS event has been detected to date. Following [179] we forecast 4%, 2%, and 1% uncertainties on the measurement of H_0 for the HLV network after two years at design sensitivity (~ 2023) and assuming lower, mean, and upper BNS rates of $R = 320 \text{ Gpc}^{-3} \text{ yr}^{-1}$, $R = 1540 \text{ Gpc}^{-3} \text{ yr}^{-1}$, and $R = 4740 \text{ Gpc}^{-3} \text{ yr}^{-1}$. The corresponding accuracy for the HLVJI network operating after one year of operation (~ 2025) reaches 3%, 1.4%, and 0.8% on H_0 , while after two years it arrives at 2.8%, 1.2%, and 0.7% (see Figure 3 in [179]). By 2028 the HLVJI network would have an additional two years of operation, leading *very roughly* to a factor of $\sqrt{2}$ improvement to 2%, 0.85%, and 0.5%. It is therefore possible that standard siren measurements will reach an accuracy of 1% by 2028 (under the assumption that a majority of BNS mergers have detectable electromagnetic counterparts).

Considering that our fiducial model has $H_0 = 67.3 \text{ km/s/Mpc}$, we therefore assume a Gaussian prior of $H_0 = 67.3 \pm 0.673 \text{ km/s/Mpc}$. In what follows we will refer to this (optimistic) prior as GWSS67. On the other hand, we also consider the significantly more pessimistic H_0 prior of 4% ($H_0 = 67.3 \pm 2.7 \text{ km/s/Mpc}$). This prior, just a factor of ~ 4 smaller than the current GW constraint based on a single event, is clearly extremely conservative but may happen if the BNS rate ends up on the low side (see e.g. [175, 179, 261, 262]). In what follows we will refer to this prior as PGWSS67.

These priors on H_0 are introduced by importance sampling on the models (samples) drawn from our MCMC simulations [128]. In our case this translates into multiplying each sample weight by a Gaussian function, with mean and variance defined by the assumed H_0 prior, evaluated at the value of H_0 in the sample itself. For this to work it is only necessary that the obtained weights are significant for a large fraction of the re-weighted samples; this is a direct consequence of the requirement that the distribution from which the samples are drawn and the importance distribution are not too dissimilar.

7.3 Results

7.3.1 Λ CDM + Ω_k + Σm_ν + N_{eff} + w *model*

We first forecast the constraints on cosmological parameters from future CMB data only, assuming the extended 10 parameter model Λ CDM + Ω_k + Σm_ν + N_{eff} + w . The constraints on cosmological parameters for the experimental configurations listed in Table 7.1 are reported in Table 7.3, while 2D contour plots at 68% C.L. and 95% C.L. between the extra parameters are reported in Figure 7.1. We find that future experiments, including CMB-S4, will be unable to provide significant additional constraints on geometrical parameters such as H_0 , Ω_k , and w . This is due to the well known geometrical degeneracy that affects CMB observables (see, e.g., [263–265]).

CMB-S4 will improve the constraints on n_s , N_{eff} , $\Omega_b h^2$, and $\Omega_c h^2$ by a factor of ~ 2 – 5 with respect to LiteBIRD. These parameters are less affected by the geometrical degeneracy, and can thus be better constrained with an improvement in the angular resolution of the experiment. Constraints on neutrino masses will also only see marginal improvement (i.e. $\Sigma m_\nu < 0.32$ eV at 95% C.L. for the strongest case from CMB-S4), which falls short of the sensitivity of $\Delta \Sigma m_\nu \sim 0.05$ eV needed to test the inverted neutrino mass hierarchy at two standard deviations. The neutrino effective number will be, on the contrary, less affected and interesting constraints at the $\Delta N_{\text{eff}} \sim 0.045$ level can be achieved with CMB-S4 even in the case of a very extended parameter space. It is interesting to investigate how the inclusion of future BAO surveys, such as DESI, can break the geometrical degeneracy and improve the constraints derived from CMB data.

Assuming the same Λ CDM fiducial model, we report the CMB+DESI constraints in Table 7.4 and we show the 2D confidence level contours at 68% C.L. and 95% C.L. in Figure 7.2. The geometrical parameters are constrained almost equally by all configurations, indicating that the additional constraining power arises from the inclusion of DESI. Curvature is now determined with a 0.1–0.2% accuracy, while the equation of state can be determined with a $\sim 5\%$ accuracy. It is interesting to note that a degeneracy is present between Ω_k , w , and Σm_ν , i.e. the introduction of a neutrino mass limits the CMB+BAO constraints on curvature and w . In addition, after the inclusion of DESI, CMB-S4+DESI provides better constraints by a factor ~ 2 – 4 on parameters such as n_s and N_{eff} with respect to LiteBIRD+DESI. The bounds on the sum of neutrino masses are however still affected by the remaining extra parameters (mostly by the anti-correlation with w and the correlation with Ω_k), resulting in a limit of $\Sigma m_\nu < 0.126$ eV at 95% C.L. for the CMB-S4+DESI configuration and $\Sigma m_\nu < 0.202$ eV at 95% C.L. for LiteBIRD+DESI. However the key result for our analysis is the constraint on the

7. STANDARD SIRENS IMPACT ON FUTURE HUBBLE PARAMETER CONSTRAINTS

Hubble parameter. Again, between the several configurations we consider, CMB-S4+DESI provides the best constraint of $H_0 = 67.4^{+1.0}_{-1.1} \text{ km s}^{-1} \text{ Mpc}^{-1}$, i.e. an uncertainty on the value of the Hubble constant of the order of $\sim 1.5\%$, while LiteBIRD+DESI gives $H_0 = 67.8^{+1.3}_{-1.5} \text{ km s}^{-1} \text{ Mpc}^{-1}$ with an uncertainty of $\sim 2\%$.

As discussed in the previous section, a similar uncertainty can be reached by the HLVJI network after one year of observations (~ 2025) with a BNS detection rate of $R \geq 1540 \text{ Gpc}^{-3} \text{ yr}^{-1}$ or by HLV after two years of observations (~ 2023) if the rate is $R \geq 2800 \text{ Gpc}^{-3} \text{ yr}^{-1}$. For simplicity we have assumed that the standard siren accuracy on H_0 scales as $1/\sqrt{N_{\text{BNS}}}$ where N_{BNS} is the number of observed BNS systems, which is a good approximation for $N \gtrsim 20$ [179]. A first conclusion is that by 2025–2030 standard sirens may offer constraints on H_0 that are comparable in accuracy to those achievable from future CMB+BAO missions at a similar epoch.

Furthermore, given existing estimates of the BNS event rate, an even higher H_0 accuracy may be expected from GWSS. In Table 7.5 and in Figure 7.3 we report the future constraints achievable by a combination of the CMB data and a prior on the Hubble constant with a 1% accuracy (GWSS67). This GWSS67 prior, with respect to the CMB data alone, breaks the geometrical degeneracy and improves significantly the constraints on the corresponding parameters, now producing strong bounds on cosmological parameters such as curvature (0.3% accuracy from CMB-S4+GWSS67) and w (7% accuracy from CMB-S4+GWSS67). The bound on neutrino masses is improved by $\sim 30\%$, while there is no significant improvement on the remaining parameters (N_{eff} , n_s , and the cold dark matter and baryon densities).

How would the inclusion of a GWSS measurement of H_0 impact cosmological constraints derived from a CMB+DESI?

We answer to this question in Table 7.6 and Figure 7.4 where we report the constraints achievable from the full combined dataset. We find that the combined analysis (in the case of CMB-S4) would constrain the Hubble constant with an accuracy of $\sim 0.5 \text{ km/s/Mpc}$, i.e. nearly a factor of two better than the CMB-S4+DESI case. A similar improvement is present with respect to LiteBIRD+DESI. Constraints on the dark energy equation of state are also significantly improved, by 30–40%, reaching an accuracy of about 3% with CMB-S4+DESI and 4% with LiteBIRD+DESI. It is interesting to note that the constraints on H_0 , Ω_k , and w coming from a combined analysis of DESI, GWSS, and a CMB mission such as LiteBIRD, S3deep, or S3wide, will be comparable or in some cases even better than the corresponding constraints coming from a CMB-S4+DESI dataset. For example, a 0.1% accuracy on curvature or a 3% accuracy on w can be reached by a S3wide+DESI+GWSS67 configuration instead of CMB-S4+DESI. Alternatively,

the GWSS measurement would also provide an interesting consistency check between different CMB+BAO datasets. We also consider the possibility that future standard siren measurements of H_0 will confirm the current tension on the Hubble constant between CMB+BAO and local measurements from supernovae. It is interesting to evaluate at how many standard deviations a CMB+DESI measurement of H_0 will disagree with a GWSS determination of $H_0 = 73.30 \pm 0.73$ km/s/Mpc. From Table 7.4, we find that the standard siren measurement would be 4 standard deviations from the expected LiteBIRD+DESI constraint, and at roughly 5 standard deviations from the CMB-S4+DESI value. This is a significant improvement, since in an extended parameter space such the one we are considering the existing tension is at about 2 standard deviations (see e.g. [5]). Finally, let us consider a significantly more pessimistic GW prior on H_0 with a $\sim 4\%$ accuracy (PGWSS67). In Table 7.7 we report the constraints achievable from a combination of this prior with future CMB data. As expected, the constraints on curvature and w are relaxed with respect to the previous analyses of CMB+GWSS67 but only by a $\sim 10 - 20\%$. In practice, the geometrical degeneracies between cosmological parameters present in CMB data only can be already sufficiently broken with a, pessimistic, PGWSS67 prior. An improvement of a factor four in the determination of H_0 will result in a, more modest, 10% improvement in the parameters. A first conclusion is therefore that in this theoretical framework, the GWSS67 and the PGWSS67 prior produce very similar constraints when combined with CMB data. On the other hand, combining the PGWSS67 prior with CMB+DESI data has a small effect in improving the constraints on w . We have found that in this case the constraints on w improve just by $\sim 5\%$ while, as discussed above, the improvement in case of GWSS67 is larger than $\sim 20\%$. The 4% PGWSS67 prior will clearly provide little help in solving the current tension on the value of the Hubble parameter.

7. STANDARD SIRENS IMPACT ON FUTURE HUBBLE PARAMETER CONSTRAINTS

Parameter	LiteBIRD	S3deep	S3wide	CMB-S4
$\Omega_b h^2$	0.02214 ± 0.00023	0.02222 ± 0.00016	$0.02220 \pm 9 \times 10^{-5}$	$0.02219 \pm 5 \times 10^{-5}$
$\Omega_c h^2$	0.1203 ± 0.0042	0.1199 ± 0.0030	0.1198 ± 0.0013	0.1199 ± 0.0010
$100\theta_{MC}$	1.04075 ± 0.00078	1.04065 ± 0.00033	1.04071 ± 0.00016	1.04071 ± 0.00012
τ	0.054 ± 0.002	0.054 ± 0.010	0.053 ± 0.010	0.055 ± 0.003
H_0	64^{+8}_{-18}	59^{+7}_{-19}	61^{+7}_{-17}	60^{+8}_{-11}
Ω_K	$-0.014^{+0.018}_{-0.005}$	$-0.027^{+0.033}_{-0.010}$	$-0.016^{+0.020}_{-0.006}$	$-0.012^{+0.016}_{-0.004}$
$\log(10^{10} A_S)$	3.092 ± 0.011	3.090 ± 0.021	3.090 ± 0.021	3.093 ± 0.006
n_S	$0.9629^{+0.0073}_{-0.0074}$	0.9656 ± 0.0112	$0.9650^{+0.0048}_{-0.0046}$	0.9648 ± 0.0038
w	$-1.069^{+0.638}_{-0.297}$	$-0.896^{+0.661}_{-0.279}$	$-0.911^{+0.506}_{-0.243}$	$-0.846^{+0.283}_{-0.234}$
N_{eff}	$3.069^{+0.243}_{-0.246}$	3.082 ± 0.141	3.063 ± 0.070	$3.060^{+0.046}_{-0.045}$
Σm_ν	$< 0.594 \text{ eV}$	$< 0.584 \text{ eV}$	$< 0.405 \text{ eV}$	$< 0.322 \text{ eV}$

Table 7.3: Forecasted constraints at 68% C.L. (upper limits at 95% C.L.) from future CMB experiments with specifications listed in Table 7.1 in an extended Λ CDM + Ω_k + Σm_ν + N_{eff} + w 10 parameters analysis. A 6 parameters Λ CDM model is assumed as fiducial model. Parameters as H_0 and w are practically unbounded. Ω_k and Σm_ν are also weakly constrained.

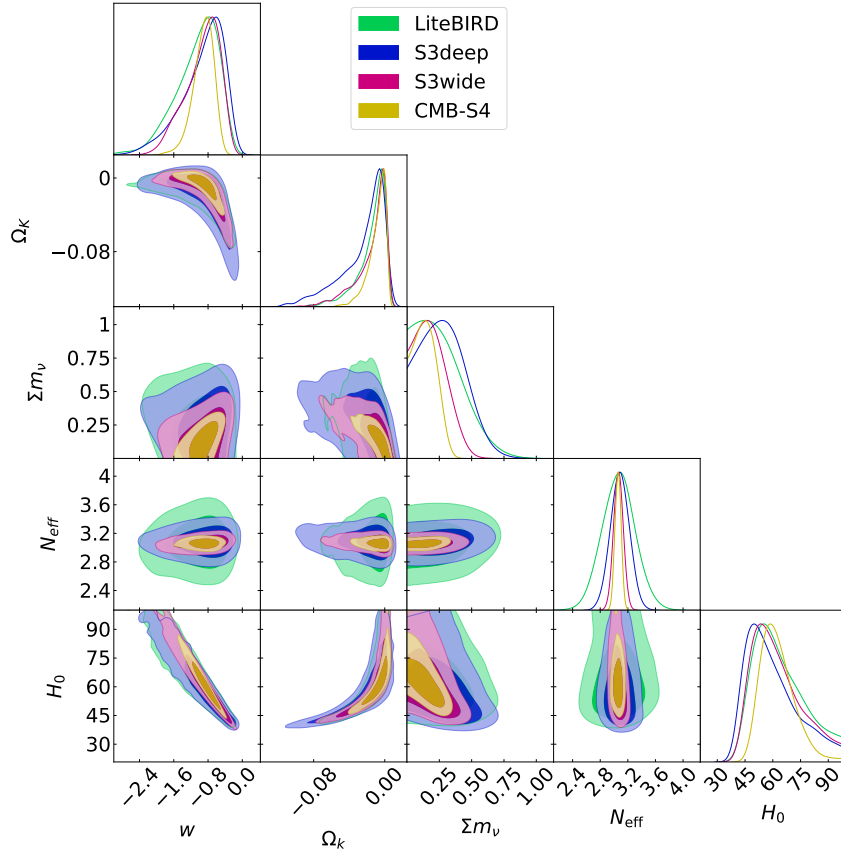


Figure 7.1: Forecasted future constraints at 68% and 95% C.L. from future CMB data for the experimental configurations in Table 7.1 in case of the Λ CDM + Ω_k + Σm_ν + N_{eff} + w extended model. Clearly in this extended parameter space CMB data alone will be unable to significantly constrain geometrical parameters as H_0 , Ω_k or w .

7. STANDARD SIRENS IMPACT ON FUTURE HUBBLE PARAMETER CONSTRAINTS

Parameter	LiteBIRD+DESI	S3deep+DESI	S3wide+DESI	CMB-S4+DESI
$\Omega_b h^2$	0.02219 ± 0.00022	0.02219 ± 0.00016	$0.02218 \pm 9 \times 10^{-5}$	$0.02218 \pm 5 \times 10^{-5}$
$\Omega_c h^2$	$0.1212^{+0.0033}_{-0.0041}$	0.1208 ± 0.0027	0.1199 ± 0.0013	0.1199 ± 0.0010
$100\theta_{\text{MC}}$	$1.04058^{+0.00071}_{-0.00070}$	1.04069 ± 0.00031	1.04075 ± 0.00015	1.04076 ± 0.00011
τ	0.055 ± 0.002	0.057 ± 0.009	0.057 ± 0.008	$0.055^{+0.002}_{-0.003}$
H_0	$67.8^{+1.3}_{-1.5}$	$67.7^{+1.2}_{-1.3}$	$67.4^{+1.0}_{-1.2}$	$67.4^{+1.0}_{-1.1}$
Ω_K	$0.000^{+0.001}_{-0.002}$	0.001 ± 0.002	0.000 ± 0.001	0.000 ± 0.001
$\log(10^{10} A_S)$	3.097 ± 0.009	3.101 ± 0.018	3.099 ± 0.016	$3.095^{+0.005}_{-0.006}$
n_s	$0.9656^{+0.0069}_{-0.0068}$	0.9637 ± 0.0104	$0.9645^{+0.0046}_{-0.0047}$	$0.9647^{+0.0037}_{-0.0036}$
w	$-1.013^{+0.054}_{-0.047}$	$-1.022^{+0.057}_{-0.047}$	$-1.010^{+0.051}_{-0.045}$	$-1.005^{+0.047}_{-0.043}$
N_{eff}	$3.118^{+0.206}_{-0.237}$	$3.065^{+0.136}_{-0.138}$	3.049 ± 0.067	3.051 ± 0.044
Σm_ν	$< 0.202 \text{ eV}$	$< 0.253 \text{ eV}$	$< 0.186 \text{ eV}$	$< 0.126 \text{ eV}$

Table 7.4: Forecasted constraints at 68% C.L. (upper limits at 95% C.L.) from future CMB experiments with specifications listed in Table 7.1 plus information from the BAO DESI galaxy survey in an extended $\Lambda\text{CDM} + \Omega_k + \Sigma m_\nu + N_{\text{eff}} + w$, 10 parameters, analysis. A 6 parameters ΛCDM model is assumed as fiducial model. When comparing the results with those in the CMB alone case reported in Table 7.3 we can notice a significant improvement in geometrical parameters as H_0 , w and Ω_k . Constraints on neutrino masses are also improved.

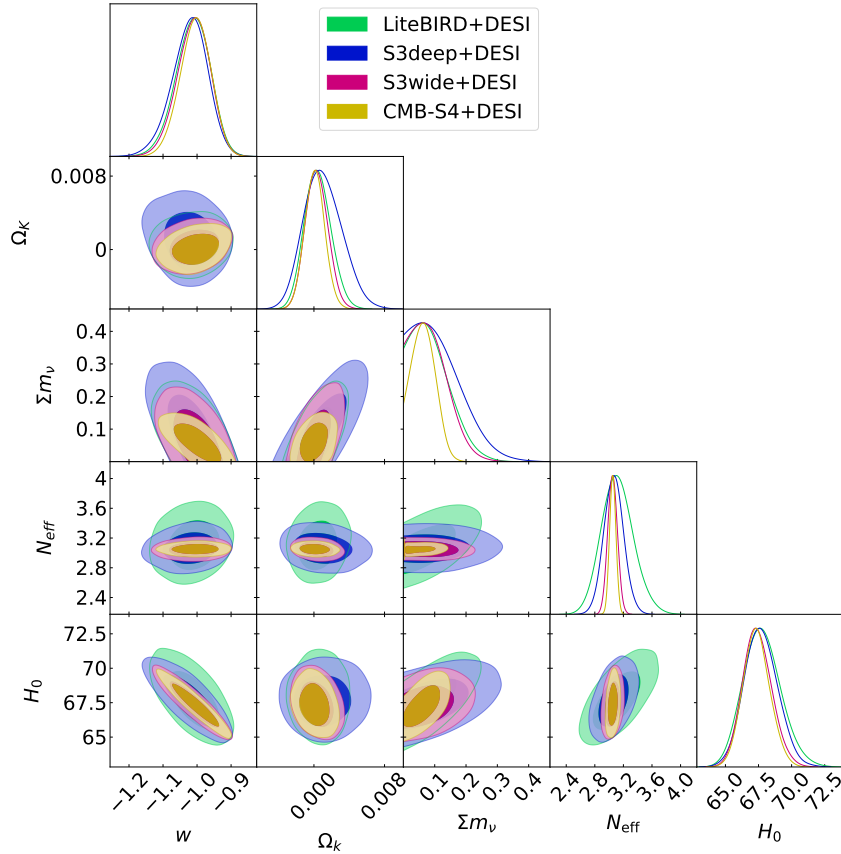


Figure 7.2: Forecasted constraints at 68% and 95% C.L. from CMB+DESI data for the experimental configurations in Table 7.1 in case of the $\Lambda\text{CDM} + \Omega_k + \Sigma m_\nu + N_{\text{eff}} + w$ extended model.

7. STANDARD SIRENS IMPACT ON FUTURE HUBBLE PARAMETER CONSTRAINTS

Parameter	LiteBIRD+GWSS67	S3deep+GWSS67	S3wide+GWSS67	CMB-S4+GWSS67
$\Omega_b h^2$	0.02215 ± 0.00023	0.02221 ± 0.00017	$0.02220 \pm 9 \times 10^{-5}$	$0.02219 \pm 5 \times 10^{-5}$
$\Omega_c h^2$	$0.1204^{+0.0042}_{-0.0043}$	$0.1199^{+0.0032}_{-0.0030}$	$0.1198^{+0.0014}_{-0.0013}$	$0.1200^{+0.0010}_{-0.0009}$
$100\theta_{MC}$	1.04075 ± 0.00080	$1.04068^{+0.00031}_{-0.00035}$	$1.04074^{+0.00015}_{-0.00016}$	1.04075 ± 0.00011
τ	0.055 ± 0.002	0.054 ± 0.010	0.053 ± 0.011	$0.055^{+0.002}_{-0.003}$
H_0	$67.30^{+0.67}_{-0.68}$	$67.30^{+0.65}_{-0.67}$	$67.26^{+0.66}_{-0.63}$	67.27 ± 0.65
Ω_K	$-0.005^{+0.007}_{-0.005}$	$-0.006^{+0.007}_{-0.008}$	-0.004 ± 0.005	-0.001 ± 0.003
$\log(10^{10} A_S)$	3.093 ± 0.010	$3.091^{+0.022}_{-0.023}$	3.090 ± 0.022	$3.095^{+0.005}_{-0.006}$
n_s	$0.9631^{+0.0072}_{-0.0074}$	$0.9658^{+0.0117}_{-0.0104}$	$0.9653^{+0.0049}_{-0.0047}$	$0.9649^{+0.0035}_{-0.0037}$
w	$-1.199^{+0.260}_{-0.112}$	$-1.208^{+0.241}_{-0.142}$	$-1.100^{+0.126}_{-0.086}$	$-1.032^{+0.070}_{-0.046}$
N_{eff}	$3.073^{+0.243}_{-0.255}$	$3.076^{+0.147}_{-0.141}$	3.059 ± 0.070	$3.055^{+0.044}_{-0.043}$
Σm_ν	$< 0.587 \text{ eV}$	$< 0.536 \text{ eV}$	$< 0.326 \text{ eV}$	$< 0.206 \text{ eV}$

Table 7.5: Forecasted constraints at 68% C.L. (upper limits at 95% C.L.) from CMB+GWSS67 data for the experimental configurations in Table 7.1 in case of the Λ CDM + Ω_k + Σm_ν + N_{eff} + w extended model.

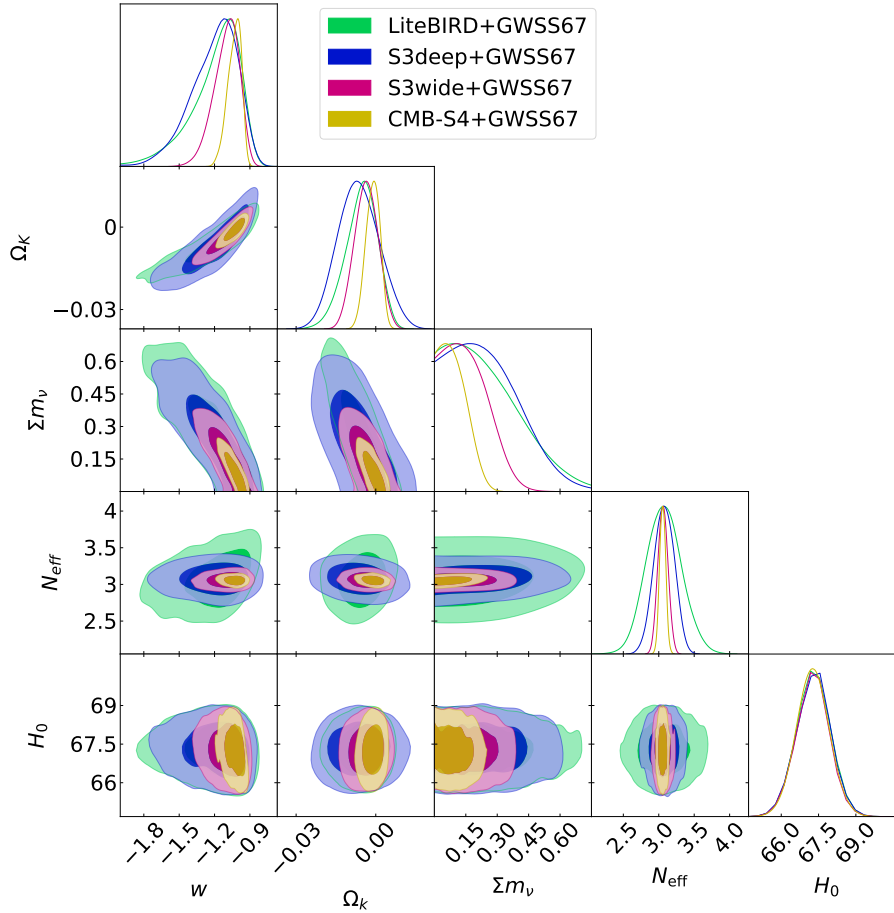


Figure 7.3: Forecasted constraints at 68% and 95% C.L. from CMB+GWSS67 data for the experimental configurations in Table 7.1 in case of the Λ CDM + Ω_k + Σm_ν + N_{eff} + w extended model.

7. STANDARD SIRENS IMPACT ON FUTURE HUBBLE PARAMETER CONSTRAINTS

Parameter	LiteBIRD+DESI+GWSS67	S3deep+DESI+GWSS67	S3wide+DESI+GWSS67	CMB-S4+DESI+GWSS67
$\Omega_b h^2$	0.02218 ± 0.00021	$0.02218^{+0.00015}_{-0.00016}$	$0.02218 \pm 9 \times 10^{-5}$	$0.02218 \pm 5 \times 10^{-5}$
$\Omega_c h^2$	$0.1205^{+0.0028}_{-0.0031}$	0.1205 ± 0.0024	0.1199 ± 0.0013	0.1199 ± 0.0010
$100\theta_{MC}$	$1.04069^{+0.00064}_{-0.00063}$	1.04072 ± 0.00030	1.04075 ± 0.00015	1.04076 ± 0.00011
τ	0.055 ± 0.002	0.057 ± 0.009	0.057 ± 0.008	$0.055^{+0.002}_{-0.003}$
H_0	$67.37^{+0.60}_{-0.61}$	$67.36^{+0.58}_{-0.59}$	67.32 ± 0.57	$67.31^{+0.54}_{-0.55}$
Ω_K	$0.000^{+0.001}_{-0.002}$	0.001 ± 0.002	0.000 ± 0.001	0.000 ± 0.001
$\log(10^{10} A_S)$	3.096 ± 0.008	3.100 ± 0.018	3.099 ± 0.016	$3.095^{+0.005}_{-0.006}$
n_s	0.9648 ± 0.0061	0.9635 ± 0.0100	0.9645 ± 0.0046	0.9648 ± 0.0036
w	$-1.003^{+0.043}_{-0.039}$	$-1.009^{+0.038}_{-0.035}$	-1.007 ± 0.030	-1.003 ± 0.028
N_{eff}	$3.076^{+0.176}_{-0.178}$	$3.053^{+0.124}_{-0.123}$	$3.048^{+0.065}_{-0.066}$	$3.052^{+0.043}_{-0.044}$
Σm_ν	$< 0.164 \text{ eV}$	$< 0.226 \text{ eV}$	$< 0.180 \text{ eV}$	$< 0.120 \text{ eV}$

Table 7.6: Forecasted constraints at 68% C.L. (upper limits at 95% C.L.) from CMB+DESI+GWSS67 data for the experimental configurations in Table 7.1 in case of the Λ CDM + Ω_k + Σm_ν + N_{eff} + w extended model.

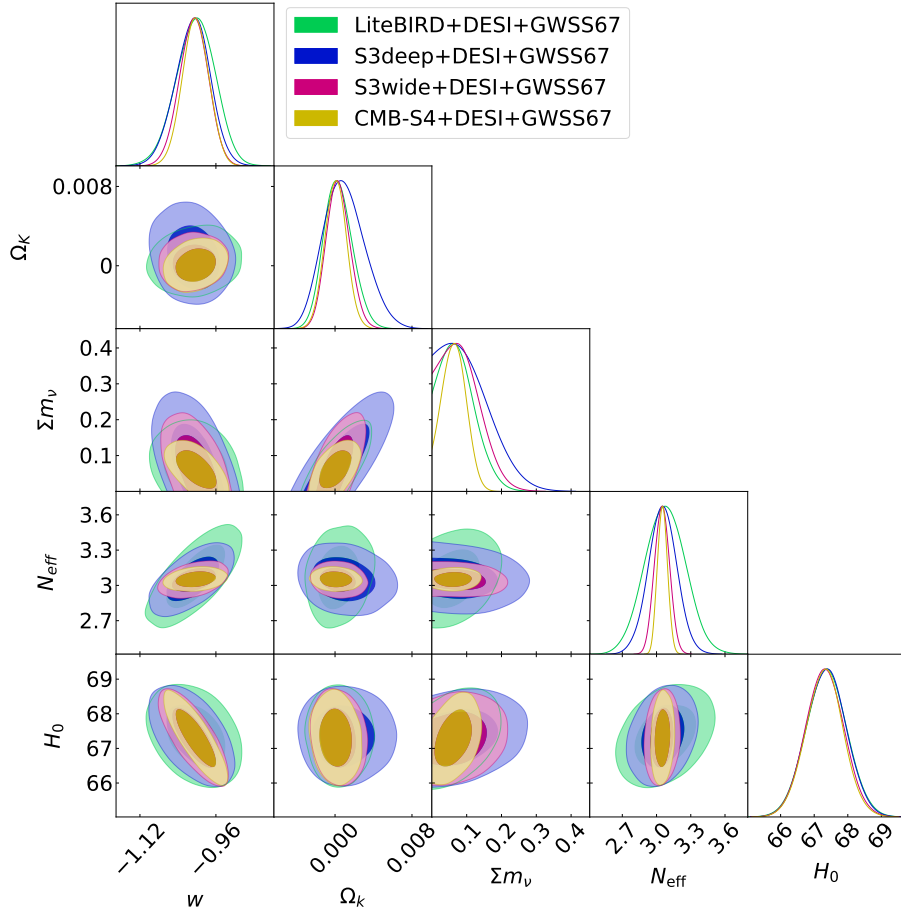


Figure 7.4: Forecasted constraints at 68% and 95% C.L. from CMB+DESI+GWSS67 data for the experimental configurations in Table 7.1 in case of the Λ CDM + Ω_k + Σm_ν + N_{eff} + w extended model.

7. STANDARD SIRENS IMPACT ON FUTURE HUBBLE PARAMETER CONSTRAINTS

Parameter	LiteBIRD+PGWSS67	S3deep+PGWSS67	S3wide+PGWSS67	S4+PGWSS67
$\Omega_b h^2$	0.02215 ± 0.00023	0.02222 ± 0.00017	$0.02219 \pm 9 \times 10^{-5}$	$0.02219 \pm 5 \times 10^{-5}$
$\Omega_c h^2$	$0.1204^{+0.0040}_{-0.0044}$	$0.1199^{+0.0031}_{-0.0029}$	$0.1198^{+0.0014}_{-0.0013}$	$0.1200^{+0.0010}_{-0.0011}$
$100\theta_{\text{MC}}$	$1.04073^{+0.00079}_{-0.00078}$	$1.04068^{+0.00034}_{-0.00033}$	1.04074 ± 0.00015	1.04075 ± 0.00012
τ	0.055 ± 0.002	0.054 ± 0.010	0.053 ± 0.011	$0.055^{+0.002}_{-0.003}$
H_0	67.03 ± 2.68	$66.95^{+2.65}_{-2.69}$	$66.86^{+2.80}_{-2.69}$	$66.72^{+2.52}_{-2.55}$
Ω_K	$-0.006^{+0.007}_{-0.005}$	-0.007 ± 0.008	$-0.004^{+0.005}_{-0.004}$	-0.002 ± 0.003
$\log(10^{10} A_s)$	3.093 ± 0.010	3.090 ± 0.022	3.090 ± 0.021	$3.094^{+0.005}_{-0.006}$
n_s	$0.9631^{+0.0073}_{-0.0074}$	$0.9662^{+0.0109}_{-0.0111}$	$0.9651^{+0.0046}_{-0.0049}$	$0.9652^{+0.0040}_{-0.0039}$
w_0	$-1.188^{+0.274}_{-0.130}$	$-1.191^{+0.254}_{-0.151}$	$-1.087^{+0.148}_{-0.112}$	$-1.022^{+0.088}_{-0.079}$
N_{eff}	$3.073^{+0.244}_{-0.247}$	$3.078^{+0.142}_{-0.140}$	$3.056^{+0.068}_{-0.069}$	$3.058^{+0.047}_{-0.048}$
m_ν	$< 0.580 \text{ eV}$	$< 0.531 \text{ eV}$	$< 0.338 \text{ eV}$	$< 0.208 \text{ eV}$

Table 7.7: Forecasted constraints at 68% C.L. (upper limits at 95% C.L.) from CMB+PGWSS67 data for the experimental configurations in Table 7.1 in case of the $\Lambda\text{CDM} + \Omega_k + \Sigma m_\nu + N_{\text{eff}} + w$ extended model.

7.3.2 $\Lambda\text{CDM} + \Omega_k + \Sigma m_\nu + w_0 + w_a$ model

As shown in the previous section, the neutrino effective number N_{eff} will be measured with good accuracy even in extended parameter spaces. The main reason for this is due to the lack of the so-called early integrated Sachs Wolfe effect in polarization data. The inclusion of polarization helps in determining the amplitude of the EISW and N_{eff} . Since we are interested in evaluating the impact of a future GWSS measurement of H_0 , it makes sense to further extend the number of geometric parameters. In what follows we substitute N_{eff} with w_a , considering therefore a dynamical dark energy equation of state described by a CPL form.

In Table 7.8 we report the constraints at 68% C.L. on cosmological parameters from the combination of future CMB and DESI data while in Figure 7.5 we report the corresponding 2D contours for the 68% and 95% confidence levels. If we compare with the results in Table 7.8 and in Figure 7.5 with those previously obtained assuming $w = \text{constant}$ in Table 7.4 and in Figure 7.2 there is now a substantial increase (about a factor two!) in the error on H_0 . Indeed, now the combination of CMB-S4+DESI data is able to constrain the Hubble constant to only $\sim 2 \text{ km s}^{-1} \text{ Mpc}^{-1}$ error, i.e. to a $\sim 3\%$ accuracy. LiteBIRD+DESI constrains H_0 to $\sim 3.5\%$ accuracy. These weaker constraints are due to the geometrical degeneracy between H_0 , w_a , and w_0 . The two dark energy parameters are now weakly determined, with uncertainties of the order of $\sim 20\%$ for w_0 and $\sim 60\text{--}70\%$ for w_a . H_0 , w_a , and w_0 are also determined to similar accuracy by different CMB experiments, indicating that the constraining power in this case is coming primarily

from DESI.

The constraint on Ω_k is virtually unchanged with respect to Table 7.4, and varies with the CMB experiment considered. The inclusion of w_a weakens the future constraint on the sum of neutrino masses, Σm_ν . Other parameters, such as n_s , that are degenerate with N_{eff} , are, on the contrary, now better constrained. Given the strong degeneracy in the w_0 – w_a plane for these future experiments, it is clearly interesting to study the impact of a future GWSS determination of H_0 . As discussed in the previous section, a 3% accuracy on H_0 can be reached by the HLV network after two years of operation if the BNS detection rate is $R > 3500 \text{ Gpc}^{-3} \text{ yr}^{-1}$, a value well inside current limits. The same accuracy can be achieved by the HLVI network after just one year of observation even assuming the lowest BNS rate of $R = 320 \text{ Gpc}^{-3} \text{ yr}^{-1}$. We found that including a 3% GWSS prior to the CMB+DESI constraints reported in Table 7.8 the constraints on H_0 and on the dark energy parameters could be already improved at the level of 10 – 30%.

However, a $\sim 1\%$ accuracy on H_0 is also directly attainable by future GWSS measurements, and it is interesting to discuss the impact of this improved determination on future combined cosmological parameter measurements. We report the constraints on cosmological parameters for CMB+DESI+GWSS67 in Table 7.9 and the corresponding 2D confidence levels in Figure 7.6.

The measured value of the Hubble constant is practically identical to the assumed prior from the standard sirens (GWSS67), indicating that the standard siren measurements are contributing to the combined constraints on all related cosmological parameters. In particular, the constraints on the dark energy parameters w_0 and w_a are substantially improved, by a factor ~ 1.6 – 2.8 , with the inclusion of the standard siren measurements.

Finally, in Table 7.10 we report the expected constraints when combining future CMB data with a, pessimistic, PGWSS67 prior on the Hubble parameter. As we can see, including the PGWSS67 prior will improve the constraints on the dark energy parameters by ~ 20 – 30% respect to CMB+DESI data. A $\sim 4\%$ determination of the Hubble parameter can be therefore useful in this theoretical framework even when considering the CMB+DESI dataset.

However the constraints achievable with the PGWSS67 prior on w_0 will be about a factor two larger than those achievable with the GWSS67 prior.

7. STANDARD SIRENS IMPACT ON FUTURE HUBBLE PARAMETER CONSTRAINTS

Parameter	LiteBIRD+DESI	S3wide+DESI	S3deep+DESI	CMB-S4+DESI
$\Omega_b h^2$	0.02214 ± 0.00018	$0.02218 \pm 6 \times 10^{-5}$	0.02217 ± 0.00011	$0.02218 \pm 3 \times 10^{-5}$
$\Omega_c h^2$	0.1201 ± 0.0011	0.1199 ± 0.0009	$0.1207^{+0.0018}_{-0.0020}$	0.1198 ± 0.0008
$100\theta_{MC}$	1.04072 ± 0.00049	1.04075 ± 0.00013	1.04070 ± 0.00028	1.04077 ± 0.00010
τ	0.055 ± 0.002	0.057 ± 0.009	0.057 ± 0.009	$0.055^{+0.002}_{-0.003}$
H_0	66.2 ± 2.3	66.3 ± 2.3	66.4 ± 2.4	$66.4^{+2.2}_{-1.9}$
Ω_K	0.000 ± 0.002	0.000 ± 0.002	0.001 ± 0.003	0.000 ± 0.001
$\log(10^{10} A_S)$	3.095 ± 0.004	3.098 ± 0.017	3.100 ± 0.018	3.094 ± 0.005
n_S	0.9638 ± 0.0042	0.9644 ± 0.0026	$0.9626^{+0.0060}_{-0.0059}$	0.9645 ± 0.0023
w_0	$-0.859^{+0.202}_{-0.259}$	$-0.883^{+0.203}_{-0.252}$	$-0.872^{+0.225}_{-0.269}$	$-0.901^{+0.149}_{-0.228}$
w_a	$-0.470^{+0.795}_{-0.540}$	$-0.390^{+0.749}_{-0.549}$	$-0.456^{+0.818}_{-0.616}$	$-0.306^{+0.661}_{-0.372}$
Σm_ν	$< 0.212 \text{ eV}$	$< 0.216 \text{ eV}$	$< 0.289 \text{ eV}$	$< 0.150 \text{ eV}$

Table 7.8: Forecasted constraints at 68% C.L. (upper limits at 95% C.L.) from CMB+DESI data for the experimental configurations in Table 7.1 in case of the Λ CDM + Ω_k + Σm_ν + w_0 + w_a extended model. Note the significant increase in the error on H_0 (about a factor two) with respect to the Λ CDM + Ω_k + Σm_ν + w_0 + w_a scenario reported before.

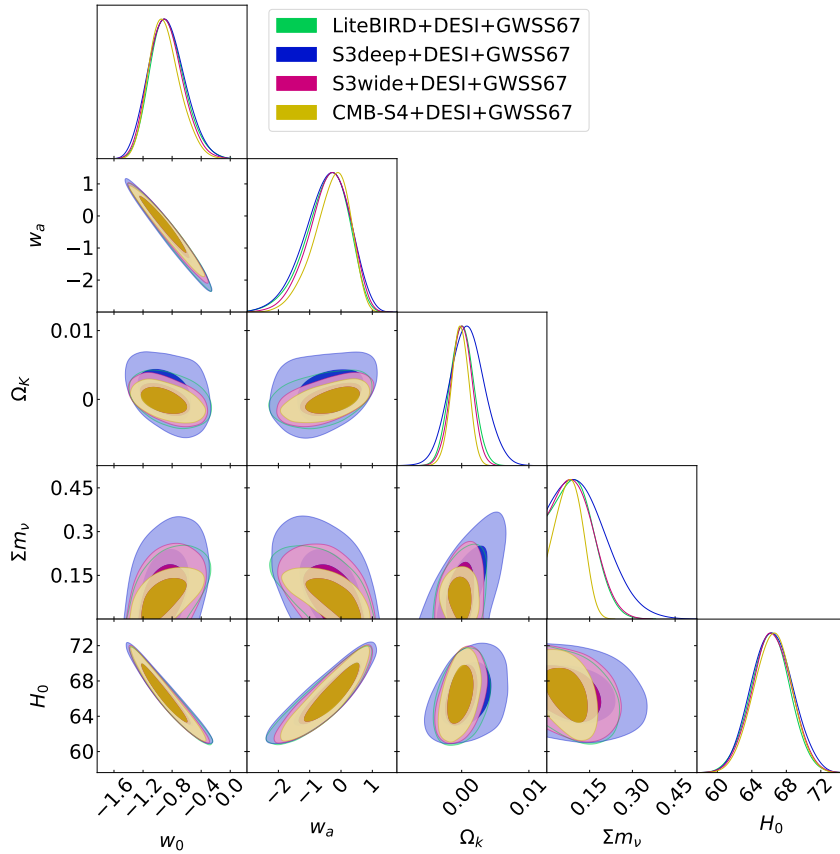


Figure 7.5: Forecasted constraints at 68% and 95% C.L. from CMB+DESI data for the experimental configurations in Table 7.1 in case of the Λ CDM + Ω_k + Σm_ν + w_0 + w_a extended model.

7. STANDARD SIRENS IMPACT ON FUTURE HUBBLE PARAMETER CONSTRAINTS

Parameter	LiteBIRD+DESI+GWSS67	S3wide+DESI+GWSS67	S3deep+DESI+GWSS67	CMB-S4+DESI+GWSS67
$\Omega_b h^2$	0.02214 ± 0.00017	$0.02218 \pm 5 \times 10^{-5}$	0.02217 ± 0.00012	$0.02218 \pm 3 \times 10^{-5}$
$\Omega_c h^2$	$0.1202^{+0.0010}_{-0.0011}$	0.1200 ± 0.0009	$0.1207^{+0.0017}_{-0.0020}$	0.1198 ± 0.0008
$100\theta_{MC}$	1.04074 ± 0.00048	1.04075 ± 0.00013	1.04070 ± 0.00028	1.04077 ± 0.00010
τ	0.055 ± 0.002	0.057 ± 0.008	0.057 ± 0.009	0.055 ± 0.002
H_0	$67.21^{+0.62}_{-0.63}$	$67.23^{+0.67}_{-0.63}$	67.24 ± 0.64	$67.23^{+0.63}_{-0.64}$
Ω_K	0.000 ± 0.002	0.000 ± 0.001	0.001 ± 0.002	0.000 ± 0.001
$\log(10^{10} A_S)$	3.095 ± 0.004	$3.098^{+0.016}_{-0.017}$	3.100 ± 0.018	3.095 ± 0.005
n_s	0.9638 ± 0.0043	0.9642 ± 0.0026	0.9625 ± 0.0058	0.9644 ± 0.0022
w_0	$-0.974^{+0.078}_{-0.089}$	$-0.978^{+0.081}_{-0.089}$	$-0.969^{+0.084}_{-0.095}$	$-0.985^{+0.066}_{-0.082}$
w_a	$-0.147^{+0.377}_{-0.282}$	$-0.127^{+0.360}_{-0.304}$	$-0.188^{+0.404}_{-0.320}$	$-0.080^{+0.319}_{-0.225}$
Σm_ν	$< 0.196 \text{ eV}$	$< 0.205 \text{ eV}$	$< 0.278 \text{ eV}$	$< 0.140 \text{ eV}$

Table 7.9: Forecasted constraints at 68% C.L. (upper limits at 95% C.L.) from CMB+DESI+GWSS67 data for the experimental configurations in Table 7.1 in case of the Λ CDM + Ω_k + Σm_ν + w_0 + w_a extended model. Note the significant improvement in accuracy on H_0 and on the dark energy parameters w_0 and w_a with respect to the CMB+DESI case.

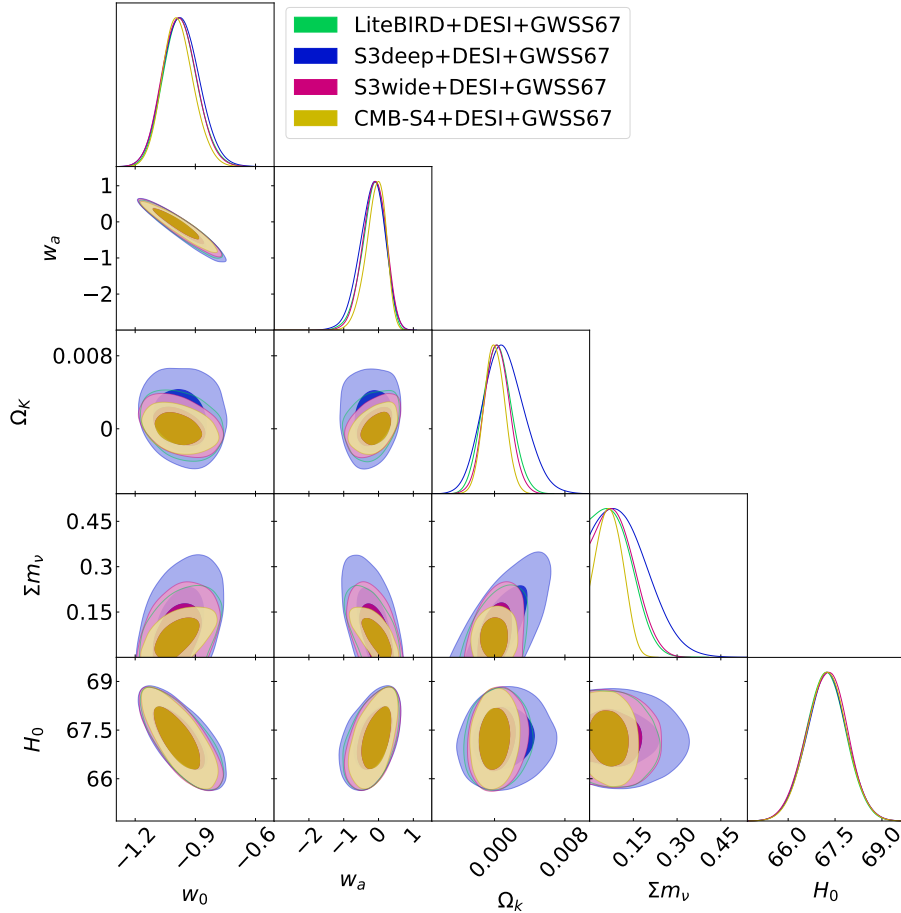


Figure 7.6: Forecasted constraints at 68% and 95% C.L. from CMB+DESI+GWSS67 data for the experimental configurations in Table 7.1 in case of the Λ CDM + Ω_k + Σm_ν + w_0 + w_a extended model.

7. STANDARD SIRENS IMPACT ON FUTURE HUBBLE PARAMETER CONSTRAINTS

Parameter	LiteBIRD+DESI+PGWSS67	S3wide+DESI+PGWSS67	S3deep+DESI+PGWSS67	CMB-S4+DESI+PGWSS67
$\Omega_b h^2$	0.02214 ± 0.00017	0.02217 ± 0.00011	$0.02218 \pm 6 \times 10^{-5}$	$0.02218 \pm 3 \times 10^{-5}$
$\Omega_c h^2$	$0.1201^{+0.0010}_{-0.0011}$	$0.1207^{+0.0018}_{-0.0020}$	0.1199 ± 0.0009	0.1199 ± 0.0008
$100\theta_{MC}$	1.04073 ± 0.00048	1.04070 ± 0.00028	1.04075 ± 0.00013	1.04076 ± 0.00010
τ	0.055 ± 0.002	0.057 ± 0.009	0.057 ± 0.008	$0.055^{+0.002}_{-0.003}$
H_0	$66.64^{+1.71}_{-1.72}$	$66.76^{+1.82}_{-1.83}$	$66.74^{+1.74}_{-1.72}$	$66.79^{+1.69}_{-1.71}$
Ω_K	0.000 ± 0.002	$0.001^{+0.002}_{-0.003}$	0.000 ± 0.001	0.000 ± 0.001
$\log(10^{10} A_S)$	3.095 ± 0.004	3.100 ± 0.018	3.098 ± 0.017	3.095 ± 0.005
n_s	0.9638 ± 0.0042	$0.9625^{+0.0059}_{-0.0058}$	0.9643 ± 0.0026	0.9643 ± 0.0022
w_0	$-0.912^{+0.159}_{-0.195}$	$-0.918^{+0.172}_{-0.204}$	$-0.926^{+0.163}_{-0.190}$	$-0.938^{+0.142}_{-0.182}$
w_a	$-0.323^{+0.619}_{-0.444}$	$-0.330^{+0.643}_{-0.497}$	$-0.271^{+0.588}_{-0.460}$	$-0.213^{+0.548}_{-0.375}$
m_ν	$< 0.205 \text{ eV}$	$< 0.284 \text{ eV}$	$< 0.211 \text{ eV}$	$< 0.148 \text{ eV}$

Table 7.10: Forecasted constraints at 68% C.L. (upper limits at 95% C.L.) from CMB+DESI+GWSS67 data for the experimental configurations in Table 7.1 in case of the Λ CDM + Ω_k + Σm_ν + w_0 + w_a extended model. Note the significant improvement in accuracy on H_0 and on the dark energy parameters w_0 and w_a with respect to the CMB+DESI case.

7.3.3 Figure of Merit

Model	Dataset	LiteBIRD	S3deep	S3wide	CMB-S4
Λ CDM + Ω_k + Σm_ν + N_{eff} + w	CMB	5	1	398	29236
	CMB+PGWSS67	110	40	12732	2.2×10^6
	CMB+GWSS67	262	104	50929	1.2×10^7
	CMB+DESI	6659	2415	383240	3.74×10^7
	CMB+DESI+PGWSS67	7735	2807	422008	4.06×10^7
	CMB+DESI+GWSS67	16928	5484	752879	7.39×10^7
Λ CDM + Ω_k + Σm_ν + w_0 + w_a	CMB	7	1	170	9223
	CMB+PGWSS67	111	18	2732	14402
	CMB+GWSS67	291	43	9231	589791
	CMB+DESI	13335	2394	227590	1.04×10^7
	CMB+DESI+PGWSS67	19458	3577	323789	1.6×10^7
	CMB+DESI+GWSS67	57928	11735	1.01×10^6	5.7×10^7

Table 7.11: Improvement with respect to simulated CMB data of the global Figure of Merit for the two theoretical scenarios considered in this chapter and for different combination of datasets. The FoM is normalized to the S3deep CMB alone case that provides the less constraining results.

It is interesting to quantify the improvement of a GWSS prior by comparing the overall Figure of Merit for the cases considered. Given an experimental configuration and a set of N parameters p_i with $i = (1, \dots, N)$, we can define the FoM from the covariance matrix of uncertainties on p_i as (see e.g. [76, 266]):

$$\text{FoM} = (\det[\text{cov } p_i])^{-1/2} \quad (7.8)$$

that is proportional to the inverse of the volume of the constrained parameters

7. STANDARD SIRENS IMPACT ON FUTURE HUBBLE PARAMETER CONSTRAINTS

space. It is important to stress that this FoM considers the whole parameter space and not just the dark energy parameters as in [250]. In Table 7.11 we report the FoM for the two theoretical scenarios considered in this Chapter and for different combinations of datasets.

The FoM are normalized to the S3deep, CMB only, value. As we can see, in the case of $\Lambda\text{CDM} + \Omega_k + \Sigma m_\nu + N_{\text{eff}} + w$ there is a significant improvement in FoM when the GWSS67 prior is included with the CMB data. The improvement is significant (between a factor ~ 50 and ~ 400) and larger in the case of the CMB-S4 dataset. A smaller but still significant improvement is present when the PGWSS67 prior is considered. This clearly shows that, once the geometrical degeneracies are broken by the introduction of the GWSS prior, there is a significantly improved parameter determination with this dataset. It is interesting also to note that the S3wide configuration has a constraining power that is superior to LiteBIRD+GWSS67 and S3deep+GWSS67. When the DESI dataset is included there is an improvement by a factor ~ 1000 and ~ 2400 . In this case the CMB dataset that would better benefit by the inclusion of the DESI data is S3deep. Both S3deep+DESI and LiteBIRD+DESI have a smaller FoM than S3wide+GWSS67, and S3wide+DESI has less constraining power than CMB-S4+GWSS67.

When further including the GWSS67 prior the improvement in FoM is about a factor 2–3 with respect to the CMB+DESI case, clearly showing that GWSS will be useful in further constraining the parameter space. However, when considering the more pessimistic PGWSS67 prior the improvement with respect to the CMB+DESI case is just $\sim 10 - 20\%$. In the case of the $\Lambda\text{CDM} + \Omega_k + \Sigma m_\nu + w_0 + w_a$ model the improvement in the FoM obtained by the inclusion of the GWSS67 prior in the case of the CMB data is about a factor of ~ 50 . With the DESI dataset the improvement is a factor of $\sim 1000-2400$. As we can see these improvements are smaller if compared to the $\Lambda\text{CDM} + \Omega_k + \Sigma m_\nu + N_{\text{eff}} + w$ scenario, showing that in this case the parameter degeneracies are more severe. When the GWSS67 prior is included the improvement is about a factor $\sim 4-6$, larger if compared with the similar data combination for the $\Lambda\text{CDM} + \Omega_k + \Sigma m_\nu + N_{\text{eff}} + w$ scenario. The combination of LiteBIRD, S3deep, and S3wide with DESI data has less constraining power than CMB-S4+GWSS67. The inclusion of a PGWSS67 prior can improve by a $\sim 60\%$ the FoM of CMB-S4 and CMB-S4+DESI.

Finally, in order to better visualize the impact of a future prior on H_0 , we plot in Figure 7.7 the values of the FoM in function of 4 different expected accuracies on the Hubble constant: 4%, 3%, 2%, and 1%. We can firstly clearly see that the FoM will be in general larger in case of the " $w_0 + w_a$ " scenario with respect to the " $w_0 + N_{\text{eff}}$ " for any experimental configuration (with the exception of LiteBIRD). The inclusion of an external prior on the Hubble parameter is therefore

7. STANDARD SIRENS IMPACT ON FUTURE HUBBLE PARAMETER CONSTRAINTS

more efficient in improving the constraints in the case of a " $w_0 + w_a$ " model, where dynamical dark energy is considered. Secondly, while in the CMB only scenario an improvement in the accuracy of H_0 is always reflected in a substantial increase in the FoM, it seems that in the case of CMB+DESI and for the " $w_0 + N_{\text{eff}}$ " model (the red lines in the figure) a significant increase is expected when moving to an accuracy below 2%. An improved accuracy in H_0 from 4% to 2% produces larger improvements in the FoM for the CMB+DESI dataset in the case of the " $w_0 + w_a$ " scenario.

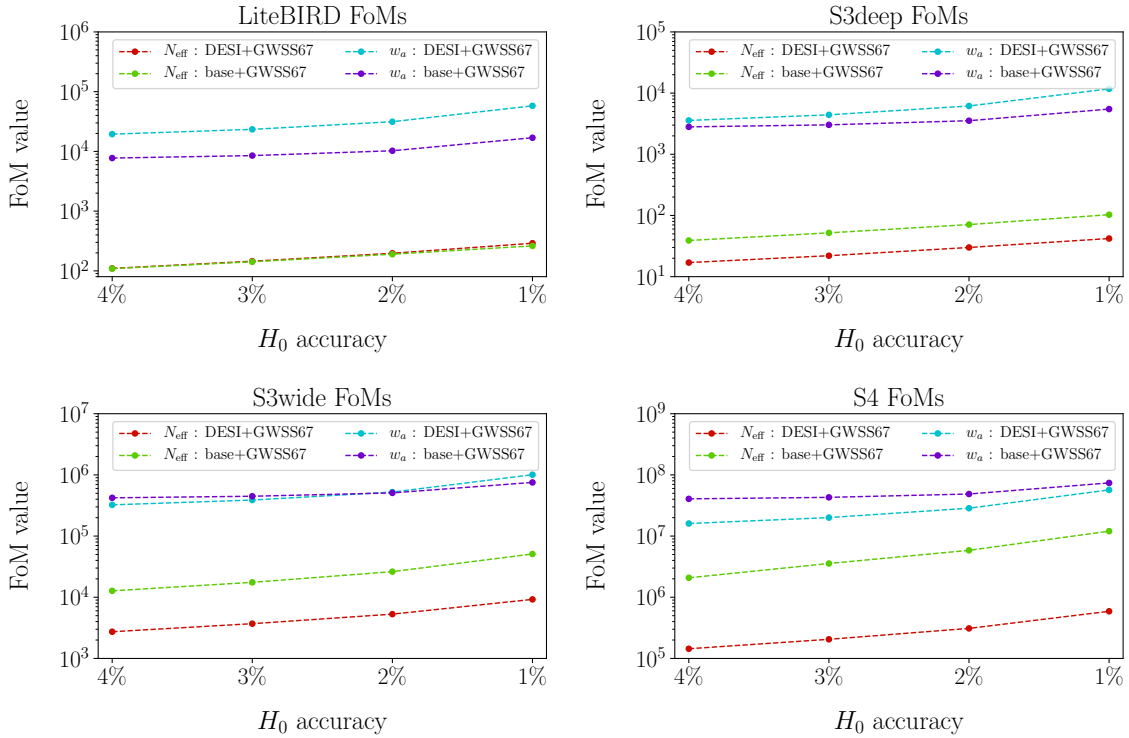


Figure 7.7: Figures of Merit for the theoretical models and experimental configurations considered in function of different priors on the Hubble parameter with a 4%, 3%, 2%, and 1% accuracy respectively. The assumed CMB datasets are LiteBIRD (Top Left), S3deep (Top Right), S3wide (Bottom Left), and CMB-S4 (Bottom Right).

7.4 Conclusions

The recent observations of gravitational waves and electromagnetic emission produced by the merger of the binary neutron-star system GW170817 has introduced a complementary and direct method for measuring the Hubble constant. In the coming decade GW standard sirens are expected to produce constraints on H_0 with $\sim 1\%$ accuracy. At the same time, improved constraints are expected from CMB experiments and from BAO surveys.

In an extended Λ CDM parameter space, where we have considered variations in curvature, neutrino mass, and the dark energy equation of state, we have found that

7. STANDARD SIRENS IMPACT ON FUTURE HUBBLE PARAMETER CONSTRAINTS

a combination of future CMB and BAO data can constraint the Hubble constant at the level of 1.5–2%. A similar accuracy may be reached by the HLV network in the second year of observations if the the BNS rate is $R \geq 2800 \text{ Gpc}^{-3}\text{yr}^{-1}$, in agreement with current limits on R , or by the HLVJI network after one year of observations with a more conservative BNS detection rate of $R \geq 1540 \text{ Gpc}^{-3}\text{yr}^{-1}$. Gravitational wave standard sirens may reach a 1% measurement of H_0 within the decade, which when combined with future CMB data would constrain curvature to 0.3% and the dark energy equation of state to $\sim 5\%$. A GWSS measurement of the Hubble constant would also improve the constraints on these geometrical parameters coming from future CMB+BAO data by 30–40%. In addition, the current 2σ Hubble tension between CMB+BAO and supernova data could be strengthened to 5σ with the inclusion of standard siren constraints.

When we further include time variations in the dark energy equation of state, parameterizing its evolution with a CPL function, we find that future CMB+BAO data will constrain the Hubble constant to $\sim 3\%$. This level of accuracy on H_0 can be independently reached by the HLV network of interferometers after the second year of operation if the BNS detection rate is $R > 3500 \text{ Gpc}^{-3}\text{yr}^{-1}$, a value again well inside current limits, or by the HLVJI network after one year of observations even considering a low BNS detection rate of $R = 320 \text{ Gpc}^{-3}\text{yr}^{-1}$. This standard siren measurement would therefore improve the CMB+BAO constraints on this model at the level of 10 – 30%. Assuming a future H_0 accuracy of $\sim 1\%$ from standard sirens, as to be expected within the decade, we find that the constraints on the dark energy equation of state parameters w_0 and w_a from future CMB+BAO datasets can be improved by a factor 1.6–2.8. We conclude that standard siren measurements by the HLV and HLVJI gravitational-wave detector networks over the coming decade may significantly improve our understanding of cosmology. We have also found that even a more pessimistic determination of H_0 , with a $\sim 4\%$ accuracy can significantly improve the constraints from CMB alone data in case of a $\Lambda\text{CDM} + \Omega_k + \Sigma m_\nu + N_{\text{eff}} + w$ model and from CMB alone and CMB+DESI data in case of a $\Lambda\text{CDM} + \Omega_k + \Sigma m_\nu + w_0 + w_a$ model.

Finally it is clearly worth mentioning that similar constraints on H_0 and dark energy parameters could come by combining CMB and BAO data with other complementary probes such as supernovae and cosmic shear (see e.g. [239, 267]). In this case future constraints from GWSS will play a crucial role in confirming these results and cross-validating the different approaches. In addition, these comparisons offer the exciting possibility of discovering new physics beyond the ΛCDM scenario.

THESIS SUMMARY

The goal of my Ph.D. thesis was to forecast the constraints that would come from future experiments on cosmological parameters in non- Λ CDM cosmologies in order to study the possibility to test new physics beyond the standard model in the upcoming decades. In the following we summarize the results drawn by the research I carried out:

- One of the main goals of future CMB experiments is undoubtedly to detect the signature of inflationary gravitational waves in the polarization B-modes. It is well known that such a detection would be a strong hint towards the validity of inflation and of the quantum nature of gravity. However, primordial magnetic fields can contaminate a possible signal from inflationary tensor modes. In [40] we showed that CMB experiments targeting inflationary GWs with amplitude $\sim 10^{-3}$ will not be able to claim any detection unless they are able to disentangle them from a nearly scale invariant magnetic field with amplitude ~ 1 nG. However, magnetic fields produce vector perturbations that source a B-mode signature peaked around $\ell \sim 1000$ [94, 97, 98]: measuring this feature of the magnetic spectrum would be enough to break the degeneracy with CMB spectra alone. Therefore we showed that experiments with enough angular resolution, such as CORE-M5 and CMB-S4, will be able to distinguish a B-mode signal produced during inflation from that of a primordial magnetic field. Conversely experiments limited to large angular scales, like LiteBIRD or PIXIE will not be able to break the degeneracy. Finally we discussed the possibility of breaking the degeneracy using the Faraday rotation of CMB polarization induced by the magnetic field showing that this could be a complementary way to distinguish a primordial magnetic field from inflationary gravitational waves.
- Even though the agreement with Λ CDM is impressive, Planck data shows a tension in the value of the lensing amplitude A_{lens} at $\sim 2\sigma$ (grown to 3σ in the 2018 Planck release [28]) that clearly need to be understood. In [41] we showed that experiments such as LiteBIRD and Stage-III would be able to confirm or falsify the current tension at the level of 5 standard deviations while a CMB-S4 like experiment can falsify the tension at the incredible level

of 10 standard deviations. Furthermore we showed that CMB-S4 would be able to identify a possible scale or frequency dependence of A_{lens} providing new insight into its physical nature.

- In the next decades, gravitational waves are expected to provide a measurement of the Hubble constant with an accuracy comparable with the constraints from CMB and standard candles [179, 224] and possibly leading to solve the current tension between late and early time observations. In [42] we discussed the impact of a 1% measurement of the Hubble constant coming from gravitational wave standard sirens on CMB+BAO constraints on extended cosmologies. In particular we considered non-flat cosmologies with varying neutrino sector and dark energy parameter. We showed that the major improvement brought by GWSS will be on the dark energy equation of state. For a constant equation of state, a combination of CMB, BAO and GWSS will lead to a 3% bound on w in the most optimistic case (a factor ~ 2 with respect to CMB+BAO alone). When considering a time varying dark energy equation of state instead the improvement is more significant. w is now constrained only to 7%, a factor of 2 worst than with constant w but around 3 times better than CMB+BAO constraints. We conclude therefore that GWSS measurements will indeed improve our understanding of cosmology in the coming decade.
- The HoLiCOW program has recently shown that strong lensing time delay (SLTD) measurements is becoming a compelling method to test cosmology [181, 183]. Even though only 6 lensed systems have been measured with enough accuracy in the mass model to be suitable for cosmological constraints, in the upcoming decade experiments like LSST are expected to bring this number up to 400. In [43] we simulated strong lensing time delay datasets starting from a fiducial cosmology and a description of the lens mass profile. We showed that already with 10 lenses, the Hubble parameter will be measured with a 1% accuracy in Λ CDM closing the gap with CMB and Supernovae Ia constraints (has was found also in [214]). We further address the possibility of SLTD surveys of constraining dark energy. We showed that for a constant equation of state, w can be constrained to the 7% with 100 lenses and to an impressive 2% in the most optimistic case (1000 lenses). When considering a time varying dark energy parameter instead only a 5% constraints is reached in the most optimistic scenario of 1000 well-measured lensing systems. In conclusion, we showed that future lensing surveys has the possibility to rapidly achieve constraints comparable or even better than CMB and standard candles current constraints provided enough

well-measured lenses are observed.

To conclude, upcoming CMB experiments and lensing surveys will play a great deal towards a better understanding of our Universe with the possibility of shedding light on many questions that have been left open after the conclusion of the Planck mission. The way ahead of us promises to bring new discoveries which may lead to a new level of comprehension of our Universe. This thesis has deal with some of these questions showing that future experiments would be able to shed light on many of them, however it also showed that significant improvements on parameter constraints may be achieved when combining different and independent measures together to take advantage of their peculiar features. In this respect, gravitational waves and strong lensing time delay are expected to play the most important role both in solving the H_0 tension and in shedding light on the physics of dark energy.

PART IV

APPENDIX

A MEASURING ANISOTROPIES IN THE FARADAY ROTATION ANGLE

In this appendix we describe how we calculate the signal-to-noise ratio for Faraday rotation measurements introduced in Chapter 4.

Following [134] we compute the signal-to-noise ratio using:

$$\frac{S}{N} = \sqrt{\sum_L \left(\frac{C_L^{\alpha_F \alpha_F}}{\Delta C_L^{\alpha_F \alpha_F}} \right)^2 \frac{f_{sky}(2L+1)}{2}}. \quad (\text{A.1})$$

where $C_L^{\alpha_F \alpha_F}$ is the spectrum reported in Eq.(4.19) and

$$\Delta C_L^{\alpha_F \alpha_F} = \left[\sum_{ll'} \frac{(2l+1)(2l'+1)(F_{ll'}^{L, \text{BE}})^2}{4\pi C_l^{\text{BB, map}} C_{l'}^{\text{EE, map}}} \right]^{-1}. \quad (\text{A.2})$$

with

$$F_{ll'}^{L, \text{BE}} \equiv 2C_{l'}^{\text{EE}} \begin{pmatrix} l & L & l' \\ 2 & 0 & -2 \end{pmatrix} W_l W_{l'}, \quad F_{ll'}^{L, \text{EB}} \equiv F_{l'l}^{L, \text{BE}}. \quad (\text{A.3})$$

Here, the objects in parentheses are Wigner-3j symbols, W_l is Gaussian window function of full-width half-maximum θ (in radians): $W_l(\theta) \equiv \exp[-l^2 \theta^2 / (16 \ln 2)]$, $C_l^{\text{EE, map}}$, and $C_l^{\text{BB, map}}$ are, respectively, the power spectra for the E and B modes from the map (we assume for simplicity just instrumental noise for the B modes),

$$C_l^{\text{EE, map}} \equiv C_l^{\text{EE}} |W_l|^2 + 2w^{-1}, \quad (\text{A.4})$$

$$C_l^{\text{BB, map}} \equiv 2w^{-1}. \quad (\text{A.5})$$

B CONSTRAINTS ON COSMOLOGICAL PARAMETERS FROM SLTD

In this Appendix we show the constraints obtained on all free cosmological parameters when the Λ -mock is analysed. In Table B.1 we show the results obtained in the ideal case, when the nuisance parameters are assumed to be perfectly known, while Table B.2 shows the constraints in the realistic case, where also the κ_{ext} , r_{ani} and γ' are free. In these tables, for each parameter, we show the results obtained assuming different DE models, i.e. Λ CDM, w CDM and w_0w_a CDM.

Parameter	DE model	10 lenses	100 lenses	1000 lenses
Ω_m	Λ CDM	$0.304^{+0.069}_{-0.085}$	0.296 ± 0.027	0.2949 ± 0.0086
	w CDM	$0.37^{+0.12}_{-0.10}$	$0.305^{+0.037}_{-0.042}$	0.296 ± 0.012
	w_0w_a CDM	$0.425^{+0.12}_{-0.083}$	0.322 ± 0.053	$0.294^{+0.022}_{-0.020}$
H_0	Λ CDM	$67.16^{+0.70}_{-0.41}$	$67.28^{+0.21}_{-0.17}$	$67.299^{+0.063}_{-0.057}$
	w CDM	$68.1^{+2.1}_{-4.0}$	$67.42^{+0.51}_{-0.62}$	67.31 ± 0.18
	w_0w_a CDM	$68.3^{+3.0}_{-3.8}$	$66.9^{+1.4}_{-1.2}$	$67.33^{+0.52}_{-0.47}$
w_0	Λ CDM	—	—	—
	w CDM	$-1.30^{+0.47}_{-0.10}$	$-1.021^{+0.073}_{-0.046}$	$-1.002^{+0.020}_{-0.018}$
	w_0w_a CDM	$-1.19^{+0.74}_{-0.21}$	$-0.94^{+0.15}_{-0.19}$	$-1.001^{+0.045}_{-0.063}$
w_a	Λ CDM	—	—	—
	w CDM	—	—	—
	w_0w_a CDM	$-1.1^{+1.8}_{-1.3}$	$-0.43^{+1.0}_{-0.79}$	0.02 ± 0.34

Table B.1: Mean marginalized values and their 68% confidence level bounds for the three DE model considered. We show here the results for the ideal case for 10, 100 and 1000 lenses.

Parameter	DE model	10 lenses	100 lenses	1000 lenses
Ω_m	Λ CDM	$0.292^{+0.11}_{-0.096}$	0.293 ± 0.035	0.295 ± 0.011
	w CDM	$0.401^{+0.15}_{-0.091}$	0.327 ± 0.075	0.299 ± 0.027
	w_0w_a CDM	$0.460^{+0.13}_{-0.065}$	$0.388^{+0.11}_{-0.084}$	0.304 ± 0.042
H_0	Λ CDM	$67.3^{+2.3}_{-2.7}$	$67.5^{+1.1}_{-2.1}$	$67.26^{+0.43}_{-1.5}$
	w CDM	$70.8^{+3.6}_{-5.4}$	$68.3^{+2.1}_{-2.8}$	$67.51^{+0.77}_{-1.9}$
	w_0w_a CDM	$71.1^{+4.4}_{-5.8}$	$68.2^{+2.2}_{-2.8}$	$67.48^{+0.82}_{-1.8}$
w_0	Λ CDM	—	—	—
	w CDM	$-1.44^{+0.62}_{-0.20}$	$-1.07^{+0.15}_{-0.050}$	$-1.007^{+0.036}_{-0.024}$
	w_0w_a CDM	$-1.41^{+0.89}_{-0.37}$	-0.96 ± 0.23	$-0.997^{+0.050}_{-0.064}$
w_a	Λ CDM	—	—	—
	w CDM	—	—	—
	w_0w_a CDM	$-1.2^{+1.9}_{-1.6}$	$-0.93^{+1.7}_{-0.64}$	$-0.07^{+0.46}_{-0.33}$
κ_{ext}	Λ CDM	-0.001 ± 0.041	$-0.001^{+0.023}_{-0.032}$	$-0.0040^{+0.0092}_{-0.023}$
	w CDM	0.017 ± 0.041	0.006 ± 0.034	$-0.001^{+0.011}_{-0.027}$
	w_0w_a CDM	0.023 ± 0.040	0.011 ± 0.030	$-0.001^{+0.013}_{-0.025}$
r_{ani}	Λ CDM	> 3.06	> 3.45	4.1 ± 1.5
	w CDM	> 3.46	> 3.33	4.2 ± 1.4
	w_0w_a CDM	> 3.57	> 3.55	$4.2^{+1.9}_{-1.3}$
γ'	Λ CDM	1.930 ± 0.018	1.930 ± 0.013	1.9301 ± 0.0052
	w CDM	1.927 ± 0.018	1.930 ± 0.012	1.9301 ± 0.0052
	w_0w_a CDM	1.926 ± 0.018	1.929 ± 0.013	1.9300 ± 0.0052

Table B.2: Mean marginalized values and their 68% confidence level bounds for the three DE model considered. We show here the results for the realistic case for 10, 100 and 1000 lenses.

REFERENCES

- [1] A. Font-Ribera, P. McDonald, N. Mostek, B. A. Reid, H.-J. Seo, and A. Slosar, *JCAP* **1405**, 023 (2014), [arXiv:1308.4164 \[astro-ph.CO\]](#) .
- [2] L. Verde, T. Treu, and A. G. Riess, in *Nature Astronomy 2019* (2019) [arXiv:1907.10625 \[astro-ph.CO\]](#) .
- [3] A. G. Riess *et al.*, *ApJ*. **826**, 56 (2016), [arXiv:1604.01424 \[astro-ph.CO\]](#) .
- [4] A. G. Riess, S. Casertano, and W. t. Yuan, .
- [5] E. Di Valentino, A. Melchiorri, and J. Silk, *Phys. Lett. B* **761**, 242 (2016), [arXiv:1606.00634 \[astro-ph.CO\]](#) .
- [6] E. Di Valentino, E. V. Linder, and A. Melchiorri, *Phys. Rev. D* **97**, 043528 (2018), [arXiv:1710.02153 \[astro-ph.CO\]](#) .
- [7] E. Di Valentino, A. Melchiorri, E. V. Linder, and J. Silk, *Phys. Rev. D* **96**, 023523 (2017), [arXiv:1704.00762 \[astro-ph.CO\]](#) .
- [8] M.-M. Zhao, D.-Z. He, J.-F. Zhang, and X. Zhang, *Phys. Rev. D* **96**, 043520 (2017), [arXiv:1703.08456 \[astro-ph.CO\]](#) .
- [9] W. Yang, R. C. Nunes, S. Pan, and D. F. Mota, *Phys. Rev. D* **95**, 103522 (2017), [arXiv:1703.02556 \[astro-ph.CO\]](#) .
- [10] V. Prilepina and Y. Tsai, *JHEP* **09**, 033 (2017), [arXiv:1611.05879 \[hep-ph\]](#) .
- [11] B. Santos, A. A. Coley, N. C. Devi, and J. S. Alcaniz, *JCAP* **1702**, 047 (2017), [arXiv:1611.01885 \[astro-ph.CO\]](#) .
- [12] S. Kumar and R. C. Nunes, *Phys. Rev. D* **94**, 123511 (2016), [arXiv:1608.02454 \[astro-ph.CO\]](#) .
- [13] T. Karwal and M. Kamionkowski, *Phys. Rev. D* **94**, 103523 (2016), [arXiv:1608.01309 \[astro-ph.CO\]](#) .
- [14] M. Benetti, L. L. Graef, and J. S. Alcaniz, *JCAP* **1807**, 066 (2018), [arXiv:1712.00677 \[astro-ph.CO\]](#) .
- [15] P. Ko and Y. Tang, *Phys. Lett. B* **762**, 462 (2016), [arXiv:1608.01083 \[hep-ph\]](#) .
- [16] M. Archidiacono, S. Gariazzo, C. Giunti, S. Hannestad, R. Hansen, M. Laveder, and T. Tram, *JCAP* **1608**, 067 (2016), [arXiv:1606.07673 \[astro-ph.CO\]](#) .
- [17] Q.-G. Huang and K. Wang, *Eur. Phys. J. C* **76**, 506 (2016), [arXiv:1606.05965 \[astro-ph.CO\]](#) .
- [18] Y. Zhang, H. Zhang, D. Wang, Y. Qi, Y. Wang, and G.-B. Zhao, *Res. Astron. Astrophys.* **17**, 050 (2017), [arXiv:1703.08293 \[astro-ph.CO\]](#) .
- [19] G.-B. Zhao *et al.*, *Nat. Astron.* **1**, 627 (2017), [arXiv:1701.08165 \[astro-ph.CO\]](#) .
- [20] J. Solà Peracaula, J. d. C. Perez, and A. Gomez-Valent, *MNRAS* **478**, 4357 (2018), [arXiv:1703.08218 \[astro-ph.CO\]](#) .
- [21] C. Brust, Y. Cui, and K. Sigurdson, *JCAP* **1708**, 020 (2017), [arXiv:1703.10732 \[astro-ph.CO\]](#) .
- [22] E. Di Valentino, A. Melchiorri, and O. Mena, *Phys. Rev. D* **96**, 043503 (2017), [arXiv:1704.08342 \[astro-ph.CO\]](#) .
- [23] E. Di Valentino, C. Bøehm, E. Hivon, and F. R. Bouchet, *Phys. Rev. D* **97**, 043513 (2018), [arXiv:1710.02559 \[astro-ph.CO\]](#) .
- [24] W. Yang, S. Pan, E. Di Valentino, R. C. Nunes, S. Vagnozzi, and D. F. Mota, *JCAP* **1809**, 019 (2018), [arXiv:1805.08252 \[astro-ph.CO\]](#) .
- [25] E. Di Valentino, A. Melchiorri, and J. Silk, *Phys. Rev. D* **92**, 121302 (2015), [arXiv:1507.06646 \[astro-ph.CO\]](#) .
- [26] E. Calabrese, A. Slosar, A. Melchiorri, G. F. Smoot, and O. Zahn, *Phys. Rev. D* **77**, 123531 (2008), [arXiv:0803.2309 \[astro-ph\]](#) .
- [27] P. A. R. Ade *et al.* (Planck), *A&A* **594**, A13 (2016), [arXiv:1502.01589 \[astro-ph.CO\]](#) .
- [28] N. Aghanim *et al.* (Planck), (2018), [arXiv:1807.06209 \[astro-ph.CO\]](#) .
- [29] A. Suzuki *et al.*, *17th International Workshop on Low Temperature Detectors (LTD 17) Kurume City, Japan, July 17-21, 2017*, *J. Low. Temp. Phys.* **193**, 1048 (2018), [arXiv:1801.06987 \[astro-ph.IM\]](#) .
- [30] Y. Akrami *et al.* (Planck), (2018), [arXiv:1807.06205 \[astro-ph.CO\]](#) .

- [31] P. A. R. Ade *et al.* (BICEP2, Keck Array), *Phys. Rev. Lett.* **116**, 031302 (2016), [arXiv:1510.09217 \[astro-ph.CO\]](#) .
- [32] Y. Akrami *et al.* (Planck), (2018), [arXiv:1807.06211 \[astro-ph.CO\]](#) .
- [33] K. N. Abazajian *et al.* (CMB-S4), (2016), [arXiv:1610.02743 \[astro-ph.CO\]](#) .
- [34] F. Capozzi, E. Di Valentino, E. Lisi, A. Marrone, A. Melchiorri, and A. Palazzo, *Phys. Rev. D* **95**, 096014 (2017), [arXiv:1703.04471 \[hep-ph\]](#) .
- [35] M. Lattanzi and M. Gerbino, *Front.in Phys.* **5**, 70 (2018), [arXiv:1712.07109 \[astro-ph.CO\]](#) .
- [36] S. Vagnozzi, E. Giusarma, O. Mena, K. Freese, M. Gerbino, S. Ho, and M. Lattanzi, *Phys. Rev. D* **96**, 123503 (2017), [arXiv:1701.08172 \[astro-ph.CO\]](#) .
- [37] P. F. de Salas, M. Lattanzi, G. Mangano, G. Miele, S. Pastor, and O. Pisanti, *Phys. Rev. D* **92**, 123534 (2015), [arXiv:1511.00672 \[astro-ph.CO\]](#) .
- [38] S. Gariazzo, M. Archidiacono, P. F. de Salas, O. Mena, C. A. Ternes, and M. Tórtola, *JCAP* **1803**, 011 (2018), [arXiv:1801.04946 \[hep-ph\]](#) .
- [39] Y. Akrami *et al.* (Planck), (2019), [arXiv:1905.05697 \[astro-ph.CO\]](#) .
- [40] F. Renzi, G. Cabass, E. Di Valentino, A. Melchiorri, and L. Pagano, *JCAP* **1808**, 038 (2018), [arXiv:1803.03230 \[astro-ph.CO\]](#) .
- [41] F. Renzi, E. Di Valentino, and A. Melchiorri, *Phys. Rev. D* **97**, 123534 (2018), [arXiv:1712.08758 \[astro-ph.CO\]](#) .
- [42] E. Di Valentino, D. E. Holz, A. Melchiorri, and F. Renzi, *Phys. Rev. D* **98**, 083523 (2018), [arXiv:1806.07463 \[astro-ph.CO\]](#) .
- [43] B. Shiralilou, M. Martinelli, G. Papadomanolakis, S. Peirone, F. Renzi, and A. Silvestri, (2019), [arXiv:1910.03566 \[astro-ph.CO\]](#) .
- [44] S. Dodelson, *Modern Cosmology* (Elsevier, 2002).
- [45] D. Baumann, in *Cosmology* (2011) <http://cosmology.amsterdam/education/cosmology/> .
- [46] D. Baumann, in *Advanced Cosmology* (2011) <http://cosmology.amsterdam/education/cosmology/> .
- [47] D. Baumann, in *TASI Lectures on Inflation* (2011) pp. 523–686, [arXiv:0907.5424 \[hep-th\]](#) .
- [48] A. A. Penzias and R. W. Wilson, *ApJ* **142**, 419 (1965).
- [49] J. C. Mather *et al.*, *ApJ* **354**, L37 (1990).
- [50] J. C. Mather *et al.*, *ApJ* **420**, 439 (1994).
- [51] N. W. Boggess *et al.*, *ApJ* **397**, 420 (1992).
- [52] P. A. R. Ade *et al.* (Planck), *A&A* **571**, A1 (2014), [arXiv:1303.5062 \[astro-ph.CO\]](#) .
- [53] K. S. Dawson *et al.*, *AJ* **151**, 44 (2016), [arXiv:1508.04473 \[astro-ph.CO\]](#) .
- [54] G. Zasowski *et al.*, *ApJ* **154**, 198 (2017), [arXiv:1708.00155 \[astro-ph.GA\]](#) .
- [55] K. Bundy *et al.*, *ApJ* **798**, 7 (2015), [arXiv:1412.1482 \[astro-ph.GA\]](#) .
- [56] M. R. Blanton *et al.* (SDSS), *AJ* **154**, 28 (2017), [arXiv:1703.00052 \[astro-ph.GA\]](#) .
- [57] S. Weinberg, *Gravitation and Cosmology* (John Wiley and Sons, New York, 1972).
- [58] C. W. Misner, K. S. Thorne, and J. A. Wheeler, *Gravitation* (San Francisco: W.H. Freeman and Co., 1973, 1973).
- [59] R. M. Wald, *General Relativity* (University of Chicago Press, Chicago, 1984).
- [60] S. M. Carroll, *Spacetime and Geometry: An Introduction to General Relativity* (San Francisco, USA: Pearson, 2003).
- [61] A. Goobar and B. Leibundgut, *Annual Review of Nuclear and Particle Science* **61**, 251 (2011), [arXiv:1102.1431 \[astro-ph.CO\]](#) .
- [62] D. Eisenstein, *New Astronomy Reviews* **49**, 360–365 (2005), wide-Field Imaging from Space.
- [63] A. G. Riess *et al.* (Supernova Search Team), *Astron. J.* **116**, 1009 (1998), [arXiv:astro-ph/9805201 \[astro-ph\]](#) .
- [64] S. Perlmutter *et al.* (Supernova Cosmology Project), *Astrophys. J.* **517**, 565 (1999), [arXiv:astro-ph/9812133 \[astro-ph\]](#) .
- [65] V. A. Rubakov and D. S. Gorbunov, *Introduction to the Theory of the Early Universe* (World Scientific, Singapore, 2017).
- [66] R. Durrer and A. Neronov, *A&ARv* **21**, 62 (2013), [arXiv:1303.7121 \[astro-ph.CO\]](#) .

- [67] N. Bartolo, E. Komatsu, S. Matarrese, and A. Riotto, *Phys. Rept.* **402**, 103 (2004), [arXiv:astro-ph/0406398 \[astro-ph\]](#) .
- [68] M. Zaldarriaga and U. Seljak, *Phys. Rev.* **D55**, 1830 (1997), [arXiv:astro-ph/9609170 \[astro-ph\]](#) .
- [69] M. Kamionkowski, A. Kosowsky, and A. Stebbins, *Phys. Rev.* **D55**, 7368 (1997), [arXiv:astro-ph/9611125 \[astro-ph\]](#) .
- [70] H. C. Chiang *et al.*, *ApJ* **711**, 1123 (2010), [arXiv:0906.1181 \[astro-ph.CO\]](#) .
- [71] G. Cabass, E. Pajer, and F. Schmidt, *JCAP* **1701**, 003 (2017), [arXiv:1612.00033 \[hep-th\]](#) .
- [72] J. A. Grayson *et al.* (BICEP3), *Proceedings, SPIE Astronomical Telescopes + Instrumentation 2016 : Millimeter, Submillimeter, and Far-Infrared Detectors and Instrumentation for Astronomy VIII: Edinburgh, United Kingdom, June 28-July 1, 2016*, *Proc. SPIE Int. Soc. Opt. Eng.* **9914**, 99140S (2016), [arXiv:1607.04668 \[astro-ph.IM\]](#) .
- [73] T. Essinger-Hileman *et al.*, *Proceedings, SPIE Astronomical Telescopes + Instrumentation 2014: Millimeter, Submillimeter, and Far-Infrared Detectors and Instrumentation for Astronomy VII: Montreal, Quebec, Canada, June 24-27, 2014*, *Proc. SPIE Int. Soc. Opt. Eng.* **9153**, 91531I (2014), [arXiv:1408.4788 \[astro-ph.IM\]](#) .
- [74] S. W. Henderson *et al.*, *Proceedings, 16th International Workshop on Low Temperature Detectors (LTD 16): Grenoble, France, July 20-24, 2015*, *J. Low. Temp. Phys.* **184**, 772 (2016), [arXiv:1510.02809 \[astro-ph.IM\]](#) .
- [75] B. A. Benson *et al.* (SPT-3G), *Proceedings, SPIE Astronomical Telescopes + Instrumentation 2014: Millimeter, Submillimeter, and Far-Infrared Detectors and Instrumentation for Astronomy VII: Montreal, Quebec, Canada, June 24-27, 2014*, *Proc. SPIE Int. Soc. Opt. Eng.* **9153**, 91531P (2014), [arXiv:1407.2973 \[astro-ph.IM\]](#) .
- [76] E. Di Valentino *et al.* (CORE), *JCAP* **1804**, 017 (2018), [arXiv:1612.00021 \[astro-ph.CO\]](#) .
- [77] F. Finelli *et al.* (CORE), *JCAP* **1804**, 016 (2018), [arXiv:1612.08270 \[astro-ph.CO\]](#) .
- [78] J. Delabrouille *et al.* (CORE), *JCAP* **1804**, 014 (2018), [arXiv:1706.04516 \[astro-ph.IM\]](#) .
- [79] A. A. Starobinsky, *Phys. Lett. B* **91**, 99 (1980).
- [80] Y. Akrami *et al.* (Planck), (2018), [arXiv:1801.04945 \[astro-ph.GA\]](#) .
- [81] J. Lizarraga, J. Urrestilla, D. Daverio, M. Hindmarsh, M. Kunz, and A. R. Liddle, *Phys. Rev. Lett.* **112**, 171301 (2014), [arXiv:1403.4924 \[astro-ph.CO\]](#) .
- [82] A. Moss and L. Pogosian, *Phys. Rev. Lett.* **112**, 171302 (2014), [arXiv:1403.6105 \[astro-ph.CO\]](#) .
- [83] E. Pajer and M. Peloso, *CQG* **30**, 214002 (2013), [arXiv:1305.3557 \[hep-th\]](#) .
- [84] R. Namba, M. Peloso, M. Shiraishi, L. Sorbo, and C. Unal, *JCAP* **1601**, 041 (2016), [arXiv:1509.07521 \[astro-ph.CO\]](#) .
- [85] J. Errard, S. M. Feeney, H. V. Peiris, and A. H. Jaffe, *JCAP* **1603**, 052 (2016), [arXiv:1509.06770 \[astro-ph.CO\]](#) .
- [86] M. Remazeilles *et al.* (CORE), *JCAP* **1804**, 023 (2018), [arXiv:1704.04501 \[astro-ph.CO\]](#) .
- [87] A. Lue, L.-M. Wang, and M. Kamionkowski, *Phys. Rev. Lett.* **83**, 1506 (1999), [arXiv:astro-ph/9812088 \[astro-ph\]](#) .
- [88] S. Saito, K. Ichiki, and A. Taruya, *JCAP* **0709**, 002 (2007), [arXiv:0705.3701 \[astro-ph\]](#) .
- [89] V. Gluscevic and M. Kamionkowski, *Phys. Rev. D* **81**, 123529 (2010), [arXiv:1002.1308 \[astro-ph.CO\]](#) .
- [90] M. Gerbino, A. Gruppuso, P. Natoli, M. Shiraishi, and A. Melchiorri, *JCAP* **1607**, 044 (2016), [arXiv:1605.09357 \[astro-ph.CO\]](#) .
- [91] B. Thorne, T. Fujita, M. Hazumi, N. Katayama, E. Komatsu, and M. Shiraishi, *Phys. Rev. D* **97**, 043506 (2018), [arXiv:1707.03240 \[astro-ph.CO\]](#) .
- [92] A. Agrawal, T. Fujita, and E. Komatsu, (2017), [arXiv:1707.03023 \[astro-ph.CO\]](#) .
- [93] A. Agrawal, T. Fujita, and E. Komatsu, (2018), [arXiv:1802.09284 \[astro-ph.CO\]](#) .
- [94] J. R. Shaw and A. Lewis, *Phys. Rev. D* **81**, 043517 (2010), [arXiv:0911.2714 \[astro-ph.CO\]](#) .
- [95] C. Bonvin, R. Durrer, and R. Maartens, *Phys. Rev. Lett.* **112**, 191303 (2014), [arXiv:1403.6768 \[astro-ph.CO\]](#) .
- [96] M. Giovannini, *CQG* **35**, 084003 (2018), [arXiv:1712.07598 \[astro-ph.CO\]](#) .

- [97] F. Finelli, F. Paci, and D. Paoletti, *Phys. Rev. D* **78**, 023510 (2008), arXiv:0803.1246 [astro-ph] .
- [98] D. Paoletti, F. Finelli, and F. Paci, *MNRAS* **396**, 523 (2009), arXiv:0811.0230 [astro-ph] .
- [99] A. Zucca, Y. Li, and L. Pogosian, *Phys. Rev. D* **95**, 063506 (2017), arXiv:1611.00757 [astro-ph.CO] .
- [100] D. R. Sutton, C. Feng, and C. L. Reichardt, *ApJ* **846**, 164 (2017), arXiv:1702.01871 [astro-ph.CO] .
- [101] L. Pogosian and A. Zucca, (2018), 10.1088/1361-6382/aac398, arXiv:1801.08936 [astro-ph.CO] .
- [102] L. Pogosian, A. P. S. Yadav, Y.-F. Ng, and T. Vachaspati, *Phys. Rev. D* **84**, 043530 (2011), [Erratum: *Phys. Rev. D* **84**, 089903(2011)], arXiv:1106.1438 [astro-ph.CO] .
- [103] S. De, L. Pogosian, and T. Vachaspati, *Phys. Rev. D* **88**, 063527 (2013), arXiv:1305.7225 [astro-ph.CO] .
- [104] P. A. R. Ade *et al.* (POLARBEAR), *Phys. Rev. D* **92**, 123509 (2015), arXiv:1509.02461 [astro-ph.CO] .
- [105] P. A. R. Ade *et al.* (Keck Array, BICEP2), *Phys. Rev. D* **96**, 102003 (2017), arXiv:1705.02523 [astro-ph.CO] .
- [106] K. Subramanian, *Rept. Prog. Phys.* **79**, 076901 (2016), arXiv:1504.02311 [astro-ph.CO] .
- [107] D. Grasso and H. R. Rubinstein, *Phys. Rep.* **348**, 163 (2001), arXiv:astro-ph/0009061 [astro-ph] .
- [108] A. Mack, T. Kahniashvili, and A. Kosowsky, *Phys. Rev. D* **65**, 123004 (2002), arXiv:astro-ph/0105504 [astro-ph] .
- [109] K. Subramanian and J. D. Barrow, *Phys. Rev. Lett.* **81**, 3575 (1998), arXiv:astro-ph/9803261 [astro-ph] .
- [110] P. A. R. Ade *et al.* (Planck), *A&A* **594**, A19 (2016), arXiv:1502.01594 [astro-ph.CO] .
- [111] T. Kobayashi, *JCAP* **1405**, 040 (2014), arXiv:1403.5168 [astro-ph.CO] .
- [112] T. Kobayashi and N. Afshordi, *JHEP* **10**, 166 (2014), arXiv:1408.4141 [hep-th] .
- [113] D. Green and T. Kobayashi, *JCAP* **1603**, 010 (2016), arXiv:1511.08793 [astro-ph.CO] .
- [114] C. Caprini and R. Durrer, *Phys. Rev. D* **65**, 023517 (2001), arXiv:astro-ph/0106244 [astro-ph] .
- [115] C. Bonvin, C. Caprini, and R. Durrer, *Phys. Rev. D* **D88**, 083515 (2013), arXiv:1308.3348 [astro-ph.CO] .
- [116] S. Camera, C. Fedeli, and L. Moscardini, *JCAP* **1403**, 027 (2014), arXiv:1311.6383 [astro-ph.CO] .
- [117] M. Giovannini, *Phys. Rev. D* **70**, 123507 (2004), arXiv:astro-ph/0409594 [astro-ph] .
- [118] A. Lewis, *Phys. Rev. D* **70**, 043011 (2004), arXiv:astro-ph/0406096 [astro-ph] .
- [119] K. Kojima, T. Kajino, and G. J. Mathews, *JCAP* **1002**, 018 (2010), arXiv:0910.1976 [astro-ph.CO] .
- [120] D. Paoletti and F. Finelli, *Phys. Rev. D* **83**, 123533 (2011), arXiv:1005.0148 [astro-ph.CO] .
- [121] D. Paoletti and F. Finelli, *Phys. Lett. B* **726**, 45 (2013), arXiv:1208.2625 [astro-ph.CO] .
- [122] A. Lewis, A. Challinor, and A. Lasenby, *ApJ* **538**, 473 (2000), arXiv:astro-ph/9911177 [astro-ph] .
- [123] N. Aghanim *et al.* (Planck), *A&A* **596**, A107 (2016), arXiv:1605.02985 [astro-ph.CO] .
- [124] R. Kallosh, A. Linde, and D. Roest, *JHEP* **11**, 198 (2013), arXiv:1311.0472 [hep-th] .
- [125] L. Perotto, J. Lesgourgues, S. Hannestad, H. Tu, and Y. Y. Y. Wong, *JCAP* **0610**, 013 (2006), arXiv:astro-ph/0606227 [astro-ph] .
- [126] A. Kogut *et al.*, *JCAP* **1107**, 025 (2011), arXiv:1105.2044 [astro-ph.CO] .
- [127] R. Allison, P. Caucal, E. Calabrese, J. Dunkley, and T. Louis, *Phys. Rev. D* **92**, 123535 (2015), arXiv:1509.07471 [astro-ph.CO] .
- [128] A. Lewis and S. Bridle, *Phys. Rev. D* **66**, 103511 (2002), arXiv:astro-ph/0205436 [astro-ph] .
- [129] K. M. Smith, D. Hanson, M. LoVerde, C. M. Hirata, and O. Zahn, *JCAP* **1206**, 014 (2012), arXiv:1010.0048 [astro-ph.CO] .
- [130] B. D. Sherwin and M. Schmittfull, *Phys. Rev. D* **92**, 043005 (2015), arXiv:1502.05356 [astro-ph.CO] .

- [131] M. Tegmark, *Phys. Rev. D* **56**, 4514 (1997), [arXiv:astro-ph/9705188 \[astro-ph\]](#) .
- [132] A. Kosowsky, T. Kahniashvili, G. Lavrelashvili, and B. Ratra, *Phys. Rev. D* **71**, 043006 (2005), [arXiv:astro-ph/0409767 \[astro-ph\]](#) .
- [133] A. P. S. Yadav, R. Biswas, M. Su, and M. Zaldarriaga, *Phys. Rev. D* **79**, 123009 (2009), [arXiv:0902.4466 \[astro-ph.CO\]](#) .
- [134] V. Gluscevic, M. Kamionkowski, and A. Cooray, *Phys. Rev. D* **80**, 023510 (2009), [arXiv:0905.1687 \[astro-ph.CO\]](#) .
- [135] R. R. Caldwell, V. Gluscevic, and M. Kamionkowski, *Phys. Rev. D* **84**, 043504 (2011), [arXiv:1104.1634 \[astro-ph.CO\]](#) .
- [136] H. J. Hortúa and L. Castañeda, *JCAP* **1706**, 020 (2017), [arXiv:1511.02991 \[astro-ph.CO\]](#) .
- [137] P. Trivedi, K. Subramanian, and T. R. Seshadri, *Phys. Rev. D* **89**, 043523 (2014), [arXiv:1312.5308 \[astro-ph.CO\]](#) .
- [138] D. Paoletti, J. Chluba, F. Finelli, and J. A. Rubino-Martin, (2018), [arXiv:1806.06830 \[astro-ph.CO\]](#) .
- [139] J. Chluba, D. Paoletti, F. Finelli, and J.-A. Rubiño-Martín, *MNRAS* **451**, 2244 (2015), [arXiv:1503.04827 \[astro-ph.CO\]](#) .
- [140] N. Aghanim *et al.* (Planck), *A&A* **594**, A11 (2016), [arXiv:1507.02704 \[astro-ph.CO\]](#) .
- [141] N. Aghanim *et al.* (Planck), *A&A* **607**, A95 (2017), [arXiv:1608.02487 \[astro-ph.CO\]](#) .
- [142] G. E. Addison, Y. Huang, D. J. Watts, C. L. Bennett, M. Halpern, G. Hinshaw, and J. L. Weiland, *ApJ* **818**, 132 (2016), [arXiv:1511.00055 \[astro-ph.CO\]](#) .
- [143] P. Motloch and W. Hu, *Phys. Rev. D* **97**, 103536 (2018), [arXiv:1803.11526 \[astro-ph.CO\]](#) .
- [144] U. Seljak, *ApJ* **463**, 1 (1996), [arXiv:astro-ph/9505109 \[astro-ph\]](#) .
- [145] A. Lewis and A. Challinor, *Phys. Rep.* **429**, 1 (2006), [arXiv:astro-ph/0601594 \[astro-ph\]](#) .
- [146] E. Calabrese *et al.*, *Phys. Rev. D* **95**, 063525 (2017), [arXiv:1702.03272 \[astro-ph.CO\]](#) .
- [147] F. Köhlinger *et al.*, *MNRAS* **471**, 4412 (2017), [arXiv:1706.02892 \[astro-ph.CO\]](#) .
- [148] T. M. C. Abbott *et al.* (DES), *Phys. Rev. D* **98**, 043526 (2018), [arXiv:1708.01530 \[astro-ph.CO\]](#) .
- [149] M. A. Troxel *et al.* (DES), *Phys. Rev. D* **98**, 043528 (2018), [arXiv:1708.01538 \[astro-ph.CO\]](#) .
- [150] E. Di Valentino, A. Melchiorri, and J. Silk, *Phys. Rev. D* **93**, 023513 (2016), [arXiv:1509.07501 \[astro-ph.CO\]](#) .
- [151] G. Cabass, E. Di Valentino, A. Melchiorri, E. Pajer, and J. Silk, *Phys. Rev. D* **94**, 023523 (2016), [arXiv:1605.00209 \[astro-ph.CO\]](#) .
- [152] J. Ooba, B. Ratra, and N. Sugiyama, *ApJ* **864**, 80 (2018), [arXiv:1707.03452 \[astro-ph.CO\]](#) .
- [153] J. B. Muñoz, D. Grin, L. Dai, M. Kamionkowski, and E. D. Kovetz, *Phys. Rev. D* **93**, 043008 (2016), [arXiv:1511.04441 \[astro-ph.CO\]](#) .
- [154] J. Valiviita, *JCAP* **1704**, 014 (2017), [arXiv:1701.07039 \[astro-ph.CO\]](#) .
- [155] E. Di Valentino, S. Galli, M. Lattanzi, A. Melchiorri, P. Natoli, L. Pagano, and N. Said, *Phys. Rev. D* **88**, 023501 (2013), [arXiv:1301.7343 \[astro-ph.CO\]](#) .
- [156] T. Matsumura *et al.*, (2013), [10.1007/s10909-013-0996-1](#), [*J. Low. Temp. Phys.*176,733(2014)], [arXiv:1311.2847 \[astro-ph.IM\]](#) .
- [157] L. Capparelli, E. Di Valentino, A. Melchiorri, and J. Chluba, *Phys. Rev. D* **97**, 063519 (2018), [arXiv:1712.06965 \[astro-ph.CO\]](#) .
- [158] P. C. t. Adam G. Riess, Alexei V. Filippenko, **116**, 1009 (1998).
- [159] S. Dhawan, S. W. Jha, and B. Leibundgut, *A&A* **609**, A72 (2018), [arXiv:1707.00715 \[astro-ph.CO\]](#) .
- [160] W. D. Kenworthy, D. Scolnic, and A. Riess, *ApJ* **875**, 145 (2019), [arXiv:1901.08681 \[astro-ph.CO\]](#) .
- [161] B. M. Rose, P. M. Garnavich, and M. A. Berg, *ApJ* **874**, 32 (2019), [arXiv:1902.01433 \[astro-ph.CO\]](#) .
- [162] E. O. Colgáin, (2019), [arXiv:1903.11743 \[astro-ph.CO\]](#) .
- [163] M. Martinelli and I. Tutusaus, (2019), [arXiv:1906.09189 \[astro-ph.CO\]](#) .
- [164] J. L. Bernal, L. Verde, and A. G. Riess, *JCAP* **2016**, 019 (2016), [arXiv:1607.05617 \[astro-ph.CO\]](#)

- [165] E. Di Valentino, E. V. Linder, and A. Melchiorri, *Phys. Rev. D* **97**, 043528 (2018).
- [166] S. Adhikari and D. Huterer, arXiv e-prints , arXiv:1905.02278 (2019), arXiv:1905.02278 [astro-ph.CO] .
- [167] V. Poulin, T. L. Smith, T. Karwal, and M. Kamionkowski, *Phys. Rev. Lett.* **122**, 221301 (2019), arXiv:1811.04083 [astro-ph.CO] .
- [168] P. Agrawal, F.-Y. Cyr-Racine, D. Pinner, and L. Randall, arXiv e-prints , arXiv:1904.01016 (2019), arXiv:1904.01016 [astro-ph.CO] .
- [169] M.-X. Lin, G. Benevento, W. Hu, and M. Raveri, (2019), arXiv:1905.12618 [astro-ph.CO] .
- [170] P. Agrawal, G. Obied, and C. Vafa, (2019), arXiv:1906.08261 [astro-ph.CO] .
- [171] R. E. Keeley, S. Joudaki, M. Kaplinghat, and D. Kirkby, (2019), arXiv:1905.10198 [astro-ph.CO] .
- [172] F. Gerardi, M. Martinelli, and A. Silvestri, (2019), arXiv:1902.09423 [astro-ph.CO] .
- [173] M. Martinelli, N. B. Hogg, S. Peirone, M. Bruni, and D. Wands, (2019), arXiv:1902.10694 [astro-ph.CO] .
- [174] B. P. Abbott *et al.* (LIGO Scientific, Virgo, 1M2H, Dark Energy Camera GW-E, DES, DLT40, Las Cumbres Observatory, VINROUGE, MASTER), *Nature* **551**, 85 (2017), arXiv:1710.05835 [astro-ph.CO] .
- [175] B. P. Abbott *et al.* (LIGO Scientific, Virgo), *Phys. Rev. Lett.* **119**, 161101 (2017), arXiv:1710.05832 [gr-qc] .
- [176] B. P. Abbott *et al.* (Virgo, Fermi-GBM, INTEGRAL, LIGO Scientific), *ApJ* **848**, L13 (2017), arXiv:1710.05834 [astro-ph.HE] .
- [177] D. A. Coulter *et al.*, *Science* (2017), 10.1126/science.aap9811, [Science358,1556(2017)], arXiv:1710.05452 [astro-ph.HE] .
- [178] K. Hotokezaka, E. Nakar, and O. t. Gottlieb, .
- [179] H.-Y. Chen, M. Fishbach, and D. E. Holz, *Nature* **562**, 545 (2018), arXiv:1712.06531 [astro-ph.CO] .
- [180] V. Bonvin, F. Courbin, S. H. Suyu, P. J. Marshall, C. E. Rusu, D. Sluse, M. Tewes, K. C. Wong, T. Collett, C. D. Fassnacht, T. Treu, M. W. Auger, S. Hilbert, L. V. E. Koopmans, G. Meylan, N. Rumbaugh, A. Sonnenfeld, and C. Spiniello, *MNRAS* **465**, 4914 (2017), arXiv:1607.01790 [astro-ph.CO] .
- [181] S. H. Suyu *et al.*, *MNRAS* **468**, 2590 (2017), arXiv:1607.00017 [astro-ph.CO] .
- [182] S. Birrer *et al.*, *MNRAS* **484**, 4726 (2019), arXiv:1809.01274 [astro-ph.CO] .
- [183] K. C. Wong, S. H. Suyu, and G. C. F. t. Chen, .
- [184] Ž. Ivezić, S. M. Kahn, and J. A. t. Tyson, *ApJ* **873**, 111 (2019), arXiv:0805.2366 [astro-ph] .
- [185] M. Oguri and P. J. Marshall, *MNRAS* **405**, 2579 (2010), arXiv:1001.2037 [astro-ph.CO] .
- [186] M. Oguri and P. J. Marshall, *MNRAS* **405**, 2579 (2010), arXiv:1001.2037 [astro-ph.CO] .
- [187] K. Liao, T. Treu, and P. t. Marshall, *ApJ* **800**, 11 (2015), arXiv:1409.1254 [astro-ph.IM] .
- [188] E. E. Falco, M. V. Gorenstein, and I. I. Shapiro, *ApJ* **289**, L1 (1985).
- [189] P. Schneider, J. Ehlers, and E. Falco, *Gravitational Lenses* (Springer, 1992).
- [190] P. Schneider, C. S. Kochanek, and J. Wambsganss, *Gravitational Lensing: Strong, Weak and Micro* (Springer, 2006).
- [191] L. V. E. Koopmans, T. Treu, and A. S. t. Bolton, *ApJ* **649**, 599 (2006), arXiv:astro-ph/0601628 [astro-ph] .
- [192] R. Barkana, *ApJ* **502**, 531–537 (1998).
- [193] P. Saha, C. Lobo, A. Iovino, D. Lazzati, and G. Chincarini, *AJ* **120**, 1654 (2000), arXiv:astro-ph/0006432 [astro-ph] .
- [194] O. Wucknitz, *MNRAS* **332**, 951 (2002), arXiv:astro-ph/0202376 [astro-ph] .
- [195] S. H. Suyu, P. J. Marshall, and M. W. Auger, *ApJ* **711**, 201 (2010), arXiv:0910.2773 [astro-ph.CO] .
- [196] S. Birrer, A. Amara, and A. Refregier, *JCAP* **2016**, 020 (2016), arXiv:1511.03662 [astro-ph.CO] .

- [197] C. R. Keeton, *ApJ* **584**, 664 (2003), [arXiv:astro-ph/0209040 \[astro-ph\]](#) .
- [198] C. McCully, C. R. Keeton, K. C. Wong, and A. I. Zabludoff, *MNRAS* **443**, 3631 (2014), [arXiv:1401.0197 \[astro-ph.CO\]](#) .
- [199] U. Seljak, *ApJ* **436**, 509 (1994), [arXiv:astro-ph/9405002 \[astro-ph\]](#) .
- [200] S. H. Suyu *et al.*, *ApJ* **788**, L35 (2014), [arXiv:1306.4732 \[astro-ph.CO\]](#) .
- [201] J. Binney and S. Tremaine, *Galactic Dynamics* (Princeton University press, 2008).
- [202] L. Hernquist, *ApJ* **356**, 359 (1990).
- [203] P. Schneider and D. Sluse, *A&A* **559**, A37 (2013), [arXiv:1306.0901 \[astro-ph.CO\]](#) .
- [204] B. Hu, M. Raveri, N. Frusciante, and A. Silvestri, *Phys. Rev. D* **89**, 103530 (2014), [arXiv:1312.5742 \[astro-ph.CO\]](#) .
- [205] M. Raveri, B. Hu, N. Frusciante, and A. Silvestri, *Phys. Rev. D* **90**, 043513 (2014), [arXiv:1405.1022 \[astro-ph.CO\]](#) .
- [206] C. Howlett, A. Lewis, A. Hall, and A. Challinor, *JCAP* **1204**, 027 (2012), [arXiv:1201.3654 \[astro-ph.CO\]](#) .
- [207] M. Chevallier and D. Polarski, *Int. J. Mod. Phys. D* **10**, 213 (2001), [arXiv:gr-qc/0009008 \[gr-qc\]](#) .
- [208] E. V. Linder, *Phys. Rev. Lett.* **90**, 091301 (2003), [arXiv:astro-ph/0208512 \[astro-ph\]](#) .
- [209] K. C. Wong, S. H. Suyu, and M. W. t. Auger, *MNRAS* **465**, 4895 (2017), [arXiv:1607.01403 \[astro-ph.CO\]](#) .
- [210] M. Oguri, *MNRAS* **367**, 1241 (2006), [arXiv:astro-ph/0508528 \[astro-ph\]](#) .
- [211] I. Pâris, P. Petitjean, and É. t. Aubourg, *A&A* **613**, A51 (2018), [arXiv:1712.05029 \[astro-ph.GA\]](#) .
- [212] C. E. Rusu, C. D. Fassnacht, and D. t. Sluse, *MNRAS* **467**, 4220 (2017), [arXiv:1607.01047 \[astro-ph.GA\]](#) .
- [213] A. Hojjati and E. V. Linder, *Phys. Rev. D* **90**, 123501 (2014), [arXiv:1408.5143 \[astro-ph.CO\]](#) .
- [214] I. Jee, E. Komatsu, S. Suyu, and D. Huterer, *JCAP* **2016**, 031 (2016).
- [215] A. Albrecht, G. Bernstein, and R. t. Cahn, *arXiv e-prints*, [astro-ph/0609591](#) (2006), [arXiv:0609591 \[astro-ph\]](#) .
- [216] R. Laureijs, J. Amiaux, and S. t. Arduini, *arXiv e-prints*, [arXiv:1110.3193](#) (2011), [arXiv:1110.3193 \[astro-ph.CO\]](#) .
- [217] D. J. Bacon *et al.* (SKA), Submitted to: *Publ. Astron. Soc. Austral.* (2018), [arXiv:1811.02743 \[astro-ph.CO\]](#) .
- [218] T. E. Collett, L. J. Oldham, and R. J. t. Smith, *Science* **360**, 1342 (2018), [arXiv:1806.08300 \[astro-ph.CO\]](#) .
- [219] T. L. Smith, *arXiv e-prints*, [arXiv:0907.4829](#) (2009), [arXiv:0907.4829 \[astro-ph.CO\]](#) .
- [220] D. Jyoti, J. B. Muñoz, R. R. Caldwell, and M. Kamionkowski, *Phys. Rev. D* **100**, 043031 (2019), [arXiv:1906.06324 \[astro-ph.CO\]](#) .
- [221] B. F. Schutz, *Nature* **323**, 310 (1986).
- [222] D. E. Holz and S. A. Hughes, *ApJ* **629**, 15 (2005), [arXiv:astro-ph/0504616 \[astro-ph\]](#) .
- [223] N. Dalal, D. E. Holz, S. A. Hughes, and B. Jain, *Phys. Rev. D* **74**, 063006 (2006), [arXiv:astro-ph/0601275 \[astro-ph\]](#) .
- [224] S. Nissanke, D. E. Holz, N. Dalal, S. A. Hughes, J. L. Sievers, and C. M. Hirata, (2013), [arXiv:1307.2638 \[astro-ph.CO\]](#) .
- [225] A. Nishizawa, *Phys. Rev. D* **96**, 101303 (2017), [arXiv:1612.06060 \[astro-ph.CO\]](#) .
- [226] N. Seto and K. Kyutoku, *MNRAS* **475**, 4133 (2018), [arXiv:1710.06424 \[astro-ph.CO\]](#) .
- [227] R. Nair, S. Bose, and T. D. Saini, *Phys. Rev. D* **98**, 023502 (2018), [arXiv:1804.06085 \[astro-ph.CO\]](#) .
- [228] S. Vitale and H.-Y. Chen, *Phys. Rev. Lett.* **121**, 021303 (2018), [arXiv:1804.07337 \[astro-ph.CO\]](#) .
- [229] A. G. Riess *et al.*, *ApJ* **861**, 126 (2018), [arXiv:1804.10655 \[astro-ph.CO\]](#) .
- [230] W. Hu, *ASP Conf. Ser.* **339**, 215 (2005), [arXiv:astro-ph/0407158 \[astro-ph\]](#) .
- [231] C. L. MacLeod and C. J. Hogan, *Phys. Rev. D* **77**, 043512 (2008), [arXiv:0712.0618 \[astro-ph\]](#) .
- [232] C. Cutler and D. E. Holz, *Phys. Rev. D* **80**, 104009 (2009), [arXiv:0906.3752 \[astro-ph.CO\]](#) .

- [233] B. S. Sathyaprakash, B. F. Schutz, and C. Van Den Broeck, *CQG* **27**, 215006 (2010), [arXiv:0906.4151 \[astro-ph.CO\]](#) .
- [234] W. Zhao, C. Van Den Broeck, D. Baskaran, and T. G. F. Li, *Phys. Rev. D* **83**, 023005 (2011), [arXiv:1009.0206 \[astro-ph.CO\]](#) .
- [235] W. Del Pozzo, *Phys. Rev. D* **86**, 043011 (2012), [arXiv:1108.1317 \[astro-ph.CO\]](#) .
- [236] A. Nishizawa, K. Yagi, A. Taruya, and T. Tanaka, *Phys. Rev. D* **85**, 044047 (2012), [arXiv:1110.2865 \[astro-ph.CO\]](#) .
- [237] S. R. Taylor and J. R. Gair, *Phys. Rev. D* **86**, 023502 (2012), [arXiv:1204.6739 \[astro-ph.CO\]](#) .
- [238] E. Belgacem, Y. Dirian, S. Foffa, and M. Maggiore, *Phys. Rev. D* **98**, 023510 (2018), [arXiv:1805.08731 \[gr-qc\]](#) .
- [239] S. M. Feeney, H. V. Peiris, A. R. Williamson, S. M. Nissanke, D. J. Mortlock, J. Alsing, and D. Scolnic, *Phys. Rev. Lett.* **122**, 061105 (2019), [arXiv:1802.03404 \[astro-ph.CO\]](#) .
- [240] H. Audley *et al.* (LISA), (2017), [arXiv:1702.00786 \[astro-ph.IM\]](#) .
- [241] B. Sathyaprakash *et al.*, *Gravitational waves. Numerical relativity - data analysis. Proceedings, 9th Edoardo Amaldi Conference, Amaldi 9, and meeting, NRDA 2011, Cardiff, UK, July 10-15, 2011*, *CQG* **29**, 124013 (2012), [Erratum: *Class. Quant. Grav.*30,079501(2013)], [arXiv:1206.0331 \[gr-qc\]](#) .
- [242] B. P. Abbott *et al.* (LIGO Scientific), *CQG* **34**, 044001 (2017), [arXiv:1607.08697 \[astro-ph.IM\]](#) .
- [243] B. P. Abbott *et al.* (KAGRA, LIGO Scientific, VIRGO), *Living Rev. Rel.* **21**, 3 (2018), [arXiv:1304.0670 \[gr-qc\]](#) .
- [244] M. Levi *et al.* (DESI), (2013), [arXiv:1308.0847 \[astro-ph.CO\]](#) .
- [245] B. P. Abbott *et al.* (LIGO Scientific), *Phys. Rev. D* **95**, 062003 (2017), [arXiv:1602.03845 \[gr-qc\]](#) .
- [246] B. P. Abbott *et al.* (LIGO Scientific, VIRGO), *Phys. Rev. Lett.* **118**, 221101 (2017), [Erratum: *Phys. Rev. Lett.*121,no.12,129901(2018)], [arXiv:1706.01812 \[gr-qc\]](#) .
- [247] S. Karki *et al.*, *Rev. Sci. Instrum.* **87**, 114503 (2016), [arXiv:1608.05055 \[astro-ph.IM\]](#) .
- [248] D. Huterer and D. L. Shafer, *Rept. Prog. Phys.* **81**, 016901 (2018), [arXiv:1709.01091 \[astro-ph.CO\]](#) .
- [249] S. A. Uddin, J. Mould, C. Lidman, V. Ruhlmann-Kleider, and B. R. Zhang, *ApJ* **848**, 56 (2017), [arXiv:1709.05830 \[astro-ph.CO\]](#) .
- [250] D. H. Weinberg, M. J. Mortonson, D. J. Eisenstein, C. Hirata, A. G. Riess, and E. Rozo, *Phys. Rept.* **530**, 87 (2013), [arXiv:1201.2434 \[astro-ph.CO\]](#) .
- [251] R. Laureijs *et al.* (EUCLID), (2011), [arXiv:1110.3193 \[astro-ph.CO\]](#) .
- [252] R. Mandelbaum *et al.*, *ApJSuppl.* **212**, 5 (2014), [arXiv:1308.4982 \[astro-ph.CO\]](#) .
- [253] Z.-M. Ma, W. Hu, and D. Huterer, *ApJ* **636**, 21 (2005), [arXiv:astro-ph/0506614 \[astro-ph\]](#) .
- [254] E. Di Valentino and A. Melchiorri, *Phys. Rev. D* **97**, 041301 (2018), [arXiv:1710.06370 \[astro-ph.CO\]](#) .
- [255] A. D. Linde, *5th International Conference on Particle Physics and the Early Universe (COSMO 2001) Rovaniemi, Finland, August 30-September 4, 2001*, *JCAP* **0305**, 002 (2003), [arXiv:astro-ph/0303245 \[astro-ph\]](#) .
- [256] D. Baumann, D. Green, and B. Wallisch, *Phys. Rev. Lett.* **117**, 171301 (2016), [arXiv:1604.08614 \[astro-ph.CO\]](#) .
- [257] W. Hu, *Phys. Rev. D* **71**, 047301 (2005), [arXiv:astro-ph/0410680 \[astro-ph\]](#) .
- [258] G. E. Addison, D. J. Watts, C. L. Bennett, M. Halpern, G. Hinshaw, and J. L. Weiland, *ApJ* **853**, 119 (2018), [arXiv:1707.06547 \[astro-ph.CO\]](#) .
- [259] S. Sato *et al.*, *Proceedings, 11th International LISA Symposium: Zurich, Switzerland, September 5-9, 2016*, *J. Phys. Conf. Ser.* **840**, 012010 (2017).
- [260] M. Fishbach, D. E. Holz, and W. M. Farr, *ApJ* **863**, L41 (2018), [*Astrophys. J. Lett.*863,L41(2018)], [arXiv:1805.10270 \[astro-ph.HE\]](#) .
- [261] N. Gupte and I. Bartos, (2018), [arXiv:1808.06238 \[astro-ph.HE\]](#) .
- [262] D. Scolnic *et al.* (DES), *ApJ* **852**, L3 (2018), [arXiv:1710.05845 \[astro-ph.IM\]](#) .
- [263] J. R. Bond, G. Efstathiou, and M. Tegmark, *MNRAS* **291**, L33 (1997), [arXiv:astro-ph/9702100 \[astro-ph\]](#) .

- [264] M. Zaldarriaga, D. N. Spergel, and U. Seljak, *ApJ* **488**, 1 (1997), [arXiv:astro-ph/9702157](#) [astro-ph] .
- [265] A. Melchiorri and L. M. Griffiths, *New Astron. Rev.* **45**, 321 (2001), [arXiv:astro-ph/0011147](#) [astro-ph] .
- [266] C. L. Bennett *et al.* (WMAP), *ApJSuppl.* **208**, 20 (2013), [arXiv:1212.5225](#) [astro-ph.CO] .
- [267] E. Aubourg *et al.*, *Phys. Rev. D* **92**, 123516 (2015), [arXiv:1411.1074](#) [astro-ph.CO]